Investigation and Validation of FDTD Weighting Function Modelling for Microwave Radiometric Temperature Measurement

Marie L. Smith

Department of Physics and Astronomy

University of Glasgow

Presented for the degree of

Doctor of Philosophy

at the University of Glasgow

August 2003

To Mum, Dad and Fraser.

"It is not enough that you should understand about applied science in order that your work may increase man's blessings. Concern for the man himself and his fate must always form the chief interest of all technical endeavors; concern for the great unsolved problems of the organisation of labor and the distribution of goods in order that the creations of our mind shall be a blessing and not a curse to mankind. Never forget this in the midst of your diagrams and equations."

- Albert Einstein, speech at the California Institute of Technology, Pasadena, California, February 16, 1931 [1].

Acknowledgements

With greatest thanks to my supervisors, Dr. D. Land and Dr. A. Watt, and to the other members of the group, Patrick Harrison and Feng Chen, for their invaluable assistance. Thanks also to Prof. F. Bardati and Dr. G. Marrocco for their time and generosity.

Special thanks to my parents and to Fraser and Gordon for all of their support and encouragement. Thanks also to Kate, my PhD colleague, for her companionship and for making the office a fun place to be. Finally thanks to all the friends and colleagues who have helped me out over the last few years.

This work was jointly funded by the Northern Foods Group plc and the University of Glasgow. The BEST program was developed and loaned by Dr G. Marrocco at the Dipartmento di Informatica Sistemi e Produzione, Universita di Roma, Tor Vergata.

Glasgow
August, 2003

Marie L. Smith

Declaration

This thesis has been composed by the undersigned. It has not been accepted in any previous application for a degree. The work of which it is a record has been done by myself, unless indicated otherwise in the text. I further state that no part of this has already been or is being concurrently submitted for any such degree or qualification at any other university.

Marie L. Smith

Summary

Microwave radiometry can provide a non-invasive, non-destructive and inherently safe method of temperature measurement suitable for a range of medical and industrial applications [2]. The measured radiometric signal is formed by a convolution of the actual material temperature distribution with a coupling spatial response, or weighting function, over the viewed volume of material. The form of this weighting function depends on both the electromagnetic coupling structure (either antenna or cavity) and on the geometry and dielectric properties of the material. Through reciprocity, the weighting function can be found by computation or measurement of the power dissipation distribution (also known as the specific absorption rate (SAR)) when the coupling structure is actively excited. Knowledge of the weighting function is used to interpret the measured radiometric temperature. Chapter 1 introduces the method of microwave radiometry, its range of applications and considers the key features of weighting function determination.

The suitability and validity of finite difference time domain (FDTD) SAR and weighting function modelling was investigated for the largely travelling - wave fields appropriate to surface contact antennas. An FDTD simulator, the Basic Electromagnetic Simulation Tool [3], was used to computationally model a range of antenna configurations that could then be compared directly with experimental results. Chapter 2 introduces several numerical techniques and justifies the choice of FDTD modelling. An introduction to the theory of the FDTD technique and a description of the BEST software is also given.

Simulations of systems where electromagnetic field distributions are known (or can be

determined experimentally) allowed the direct comparison of simulation results with theoretical predictions. Chapters 3 and 4 consider various validation examples; a monopole radiator above ground plane and TE_{01} waveguide in chapter 3, experimental field determination in lossy dielectrics using the non-resonant perturbation method in chapter 4. In all cases considered, simulation and experiment agree within a reasonable magnitude of error.

With the successful validation of its microwave modeling capabilities, the BEST program was then used to predict the weighting functions expected for practical radiometer antennas for microwave temperature measurement. Of primary importance are the variations of the effective coupling distance into the viewed material with dielectric changes, particularly those due to water content, and with measurement frequency. Knowledge of this behaviour is essential for estimating, at one extreme, relatively small but physiologically important temperature gradients within the human body, and at the other extreme, the large and rapidly varying temperature patterns induced during industrial processes.

By measuring the microwave temperature at different microwave frequencies, it is possible to retrieve information on the temperature at varying depths within the material. To aid in the interpretation of these measurements, the BEST program was used to ascertain the form of the weighting function at two frequencies, 1.35 GHz and 3.2 GHz, for a specific dual - frequency antenna in a range of phantom materials. The phantom materials were composed of a mixture of water, protein and salts, with the intention being to simulate common biological materials. To consider foodstuffs a mashed potato phantom was used.

Chapter 5 includes the design of this dual frequency antenna and its application to measuring the radiometric temperature of non-isothermal mashed potato mixtures. The specific manipulation of the potato mixture (through heating and cooling) to produce known temperature profiles (quasi-linear and quasi-quadratic) is also considered in this chapter. Further validation of the BEST weighting function determination is possible by comparison with these experimental temperature measurements.

Chapter 6 initially covers the modelling of the dielectric properties of the mashed potato and protein / saline mixtures. In particular, a model of the variation of the dielectric constant and loss factor of the mashed potato material, covering a wide range of temperatures at 1.35GHz and 3.2GHz, is presented and shown to agree with published literature. The effects on the computed weighting function of variation of several key factors, including measurement frequency and material temperature, are then considered for both phantom types. Further, limitations in the computational modelling in terms of finite bounds and the modelling of layers are investigated.

Finally, techniques for obtaining the physical temperature distribution from multi - frequency microwave readings are considered in chapter 7 and their applicability at two frequencies is discussed. By making use of the data collected from the dual - frequency antenna and simulated microwave temperatures, the various methods of temperature profile retrieval are compared.

Table of Contents

List of Tables

List of Figures

Chapter 1

Microwave Radiometry for Thermometry

Microwave radiometry provides a non-invasive method for the determination of temperature from a wide range of biological and organic materials. The radiometric temperature of a volume of material is measured by coupling to its thermal radiation field through a suitable antenna-type structure, and measuring the equivalent temperature of the coupled signal with a radiometer receiver [9, 10, 11]. At frequencies below about 6 GHz, human and animal tissues and many natural materials are partially transparent to electromagnetic radiation. This allows the generation and transmission of microwave thermal radiation over distances approximately equal to the radiation wavelength in the material allowing temperature information to be obtained over depths of up to several centimetres in human tissues [12, 13]. Many applications both clinical and industrial in nature have been developed to make use of this technique.

On the clinical side microwave radiometry has been employed to give objective, site-specific information which can be advantageous in disease and injury detection and in diagnosis and treatment of certain conditions. Since its invention in the mid 1970s [14, 15, 16] passive microwave sensing of human tissues has been applied to the detection of various cancers, in particular breast cancer [11, 16, 17, 18, 19, 20] and many other medical conditions including arthritis [18]. The detection of cancer is made possible due

to the temperature differential between normal and the enhanced perfusion environment of many tumours.

Microwave thermometry has also become an established technique in the treatment of these conditions by means of hyperthermia [21, 22, 23]. In this procedure the damaged tissue (generally cancerous area) is heated by radio-frequency or microwaves with the intention of destroying the growth. Using a microwave radiometry system allows non-invasive detection of the induced changes in tissue temperature as heating progresses. A review of the major clinical applications of microwave thermometry can be found in the review paper of Leroy *et al* [24].

In more recent years research on the medical applications of microwave thermometry has moved to the determination of thermal gradients in tissues. By measuring the microwave temperature at more than one frequency it is possible to obtain information on the variation of temperature with depth below the skin surface. This has applications in the treatment of newborn infants [25, 26] and for industrial thermometry. Multi-frequency radiometry is considered in more detail in section 1.5.2 of this chapter and in chapter 7.

Applications of microwave radiometry in the industrial sector have focused on the food industry in areas including food safety and quality control. The major benefit of this method is that reliable average temperature measurements can be achieved in a completely non destructive manner, unlike present invasive thermometry practices which cost thousands of pounds in damaged goods. In addition to this saving in cost, microwave radiometry may also give more accurate temperature measurements.

1.1 Why Microwave Radiometry?

Microwave radiometry is a measurement technique which is made possible due to the fact that all electromagnetically lossy material objects at a temperature greater than absolute zero emit natural radiation. This radiation is a result of electromagnetic thermal noise, i.e. random thermal motion of atoms, and takes the form of electromagnetic waves. The intensity and frequency distribution of the emitted radiation is dependent on the

absolute temperature of the source material. Thermal radiation emitted at around room temperature occurs in the region of the electromagnetic spectrum from infra red to radio frequencies. Microwave Thermometry measures the microwave component of this natural thermal radiation.

The depth from which a thermally related electromagnetic signal can be detected by a radiometer receiver at the surface of the emitting body is principally determined by the frequency at which the measurement is made, by the properties of the tissue and by the structure of the receiver antenna. By the antenna reciprocity principle [5] and the thermodynamic principle of detailed balancing, the pattern of microwave thermal radiation passively emitted at a particular frequency must be identical to the active absorption of microwave radiation by the same tissue when the same antenna is used in active and passive mode [27].

This pattern of microwave absorption (and thus emission) depends primarily on the dielectric properties of the material under investigation and on the physical structure of the operating antenna. As the dielectric behaviour and the electric field properties of a specific receiver depend on the measurement frequency, this frequency dependence is of vital importance to the method. In determining the particular frequency or frequency range to use, it is essential to consider both penetration depth and lateral spatial resolution.

1.1.0.1 Depth of Penetration

The depth of penetration (D) of a plane electromagnetic wave in a lossy dielectric given by [28]:

$$D = \frac{c}{2\pi f}(2\epsilon_r')^{-\frac{1}{2}}\left(\sqrt{1+\left(\frac{\epsilon_r''}{\epsilon_r'}\right)^2}-1\right)^{-\frac{1}{2}} \tag{1.1}$$

where f is the frequency, ϵ_r' is the relative dielectric constant and ϵ_r'' is the relative dielectric loss factor. The dielectric loss factor can be related to an equivalent conductivity of the dielectric material. This depth corresponds to the distance into the material at which the intensity falls to 1/e of its original value. This depth is the "ideal" situation where there are no near-fields effects as a result of diffraction of the signal by the edges of

the antenna. Additionally this relation (1.1) does not apply for multi-layered or inhomogeneous dielectric materials. In reality these effects can account for 20-50% of the total signal [29] thus the actual penetration depth can be considerably less. Matching the permittivity of the antenna aperture and viewed material, however, can reduce near field effects [29].

Using the standard relation between frequency and wavelength:

$$c = f\lambda \tag{1.2}$$

where c is the speed of light in vacuo ($3x10^8$ ms^{-1}) which holds for all electromagnetic waves, equation 1.1 can be re-written in terms of wavelength (λ). As the frequency increases, wavelength decreases, the depth of penetration rapidly becomes very small leading to surface only penetration. To ensure that the measured radiation comes from a useful depth of material, given the presence of near field effects, the chosen frequency must be kept at a reasonable value ($\leq$ 6GHz).

As an illustration of this we can consider infra-red imaging. In this technique the radiation emitted in the 10^{10}Hz region of the spectrum is detected. Although accurate detection of the position of radiating bodies (e.g. as used by the police force) is possible, the depth from which this radiation is detected is approximately 0.1mm. As a result it is only possible to determine surface temperature information hence limiting its application in medical or industrial situations.

Another factor that can influence the location of the source of the signal is the use of a bolus with hyperthermia apparatus. The introduction of this cooling liquid in a microwave transparent container between the source and antenna works by cooling the surface of the source and thus reduces the contribution to the total signal from the surface. This allows for a greater penetration depth into the tissue and thus the measurement of a signal from deeper volumes of tissue [24].

1.1.0.2 Spatial Resolution

The second important consideration is that of the lateral spatial resolution. In order to view the thermal features of interest within the material the wavelength used must be smaller than the smallest features to be detected. The spatial resolution (S) can be approximated by [30]:

$$S \approx \frac{\lambda}{2\sqrt{\epsilon_r'}} = \frac{1}{2}\lambda_m \tag{1.3}$$

where λ_m is the wavelength in the material. To ensure that the spatial resolution is such that the areas of interested can be adequately viewed requires that the chosen wavelength must not be too large conflicting with the requirement of a low frequency (hence large wavelength) for adequate depth penetration. This sets a lower frequency limit of approximately 1 to 2GHz for the applications of interest.

1.1.0.3 Choice of Frequency

The optimum frequency clearly will be a compromise between these two independent needs for a low and high frequency. Simplifying equation 1.1 by considering the innermost square-root term and using a Taylor series expansion (assuming $(\epsilon_r'/\epsilon_r'')$ to be small) leads to the approximated equation for the penetration depth:

$$D \approx \frac{\lambda\sqrt{\epsilon_r'}}{\pi\epsilon_r.''} \tag{1.4}$$

Given this the ratio of spatial resolution to depth penetration is approximately:

$$\frac{S}{D} \approx \frac{\pi}{2}\frac{\epsilon_r''}{\epsilon_r'}. \tag{1.5}$$

This is then proportional to the loss tangent, $tan\delta$, of the material:

$$loss\,tangent = \tan\delta = \frac{\epsilon_r''}{\epsilon_r.'} \propto \frac{S}{D} \tag{1.6}$$

A minimum in the loss tangent against frequency curve will indicate an optimum frequency measurement region [27]. Considering the variation in loss tangent with frequency for several common body tissues, Figure 1.1 [4] , this minimum occurs at around 3GHz.

In fact the range of frequencies, 0.9-4 GHz, corresponding to the broad minimum in this curve have been found to be suitable for microwave radiometry. At these frequencies internal body structures and tissue thermal patterns are comparable in size to the radiation

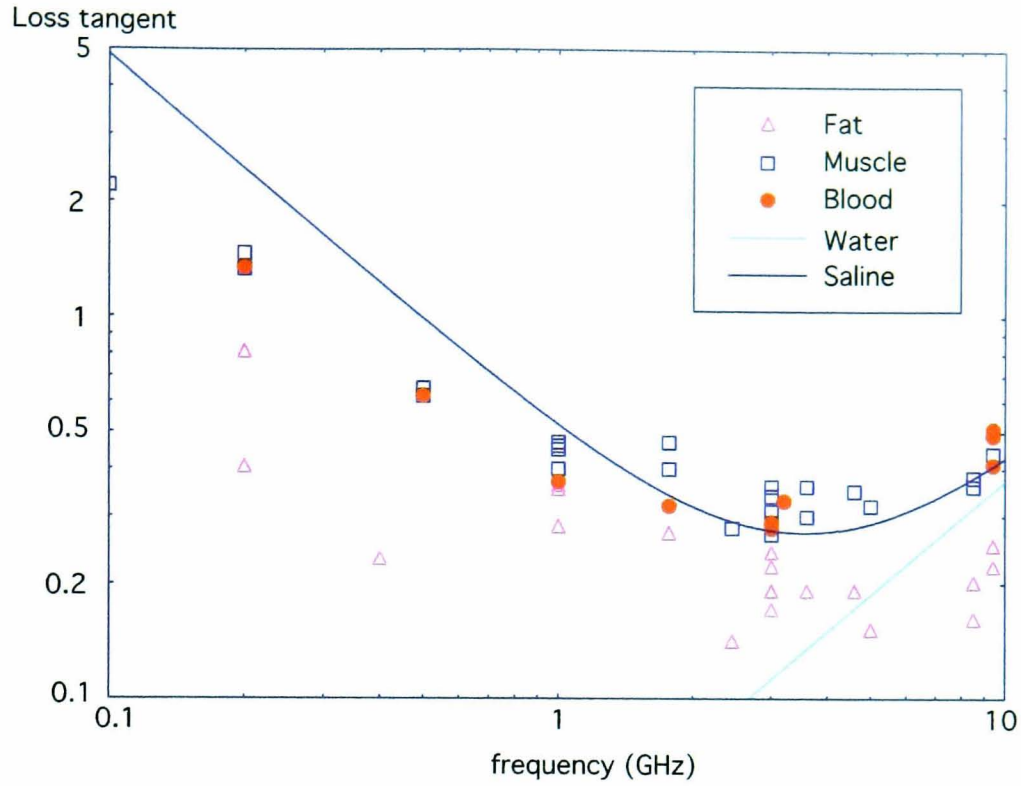

Figure 1.1: *Plot of loss tangent against frequency for the major body tissue components. Figure reproduced from [4].*

wavelengths [27] hence satisfying the spatial resolution condition. Fortuitously this corresponds to a frequency which gives a depth of penetration suitable to measuring thermal distributions at depths of several centimetres.

Although only body tissues have been considered the situation is the same for most organic materials, e.g. foodstuffs, due to the similarity in their constituents. In general, both organic and biological materials are considered to be partially transparent to microwaves. Microwave thermal radiation in these types of material can come from depths of around 5-50mm depending of the dielectric property specifics.

1.2 Radiometry System

A complete temperature measurement system consists of a source material, an antenna structure which is electromagnetically coupled to this radiating body, and a receiver as shown in Figure 1.2. This radiometer system measures the *equivalent noise temperature*

of the source [9, 10, 11]. Since the radiation is white, the received power is dependent not on the measurement frequency but on the measurement bandwidth.

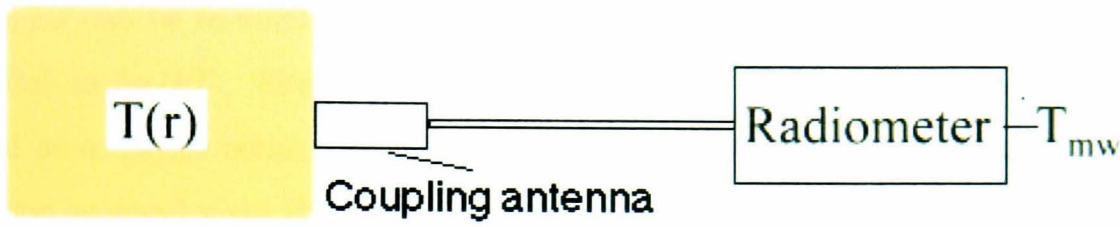

Figure 1.2: *The complete temperature measurement system, consisting of a source material at temperature T(r) coupled to a direct contact antenna. The antenna then connects to the radiometer which measures the equivalent noise temperature and produces a Celsius temperature.*

The intensity variation of emitted radiation with wavelength at a particular source temperature was first described by Planck. At human body temperatures ($\sim$ 310K) this curve has a maximum in the infra red wavelength region with a much smaller intensity contribution in the microwave region. In fact at microwave wavelengths the intensity within a wavelength window varies directly with the temperature of the material. As a result the measured microwave temperature is directly proportional to the absolute source temperature [18], giving an additional advantage to using the microwave frequency region for measurement.

1.2.1 Microwave model

From Planck's theory of black body radiation the measured microwave noise power can be expressed in terms of T, the microwave temperature of the source, B, the pre-detection bandwidth of the radiometer and k, Boltzmann's constant. Planck's equation for the energy density of thermal electromagnetic blackbody radiation from a source at absolute temperature T in the range λ to $\lambda + d\lambda$ is:

$$\rho_t d\lambda = \frac{8\pi hc}{\lambda^5 \left(e^{\frac{hc}{\lambda kT}} - 1 \right)} d\lambda \tag{1.7}$$

where h is Planck's constant ($6.6\text{x}10^{-34}$ Js), c is the speed of light in vacuo, k is Botlzman's constant ($1.381\text{x}10^{-23}$ JK^{-1}) and ρ_t is the energy density.

Equation 1.7 can be re-written in terms of the frequency (ν) to give the argument of the exponential as $h\nu/kT$. Then in the classical limit ($h\nu \ll kT$) the exponential can be expanded as a Taylor series, the Rayleigh-Jeans approximation. Neglecting the second order terms as small gives the energy density as:

$$\frac{8\pi kT}{c\lambda^2}d\nu \tag{1.8}$$

The power density (P) is then simply equation 1.8 multiplied by the speed of light, c.

If the power received by an antenna is W_r then in terms of the power density this is:

$$W_r = A_e P \tag{1.9}$$

where A_e is the effective area of the antenna. For a 'small' antenna, (where conductor dimensions $\ll \lambda$) the effective area for unpolarised radiation is given by:

$$A_e = \frac{\lambda^2}{8\pi} \tag{1.10}$$

The power received by the antenna is then $kTd\nu$, usually written in the form:

$$W_r = kTB \tag{1.11}$$

where B is the noise power bandwidth of the source.

This is the maximum thermal power which can be measured and occurs when source and antenna are impedance matched. From equation 1.11 it can be seen that the received power is independent of the actual frequency used in the long wavelength (classical) limit. Thus the power received is not dependent on the position of the bandwidth just on its size. The bandwidth, however, is a property of the measuring instrument and must be determined to maximise the signal to noise ratio of the system.

If the source and antenna impedances are not matched then there can be a reflection of the outgoing signal. This leads to a reduced value of transmitted power as given by:

$$W_r = (1 - |\rho|^2)kTB. \tag{1.12}$$

where ρ is the power reflection coefficient. Termed the emissivity effect, this reflection can be reduced by attempting to match the impedances of the source and the antenna by filling the antenna with a dielectric and by ensuring that there are no air gaps between them. It is still essential, however, that the radiometer be capable of measuring the matched impedance power temperatures in the presence of reflections if source temperatures are to be intercompared.

1.2.2 Dickie Radiometer

The total measured power from the microwave source in all cases is small (approximately $10x10^{-11}$W) [18]. Thus in order to use the microwave thermography technique it is necessary to use an amplifier to boost the signal and then to separate the signal from any amplifier noise. To achieve an appropriate level of accuracy in the temperature readings (e.g. 0.1K at 300K) and to reduce the effects of the amplifier gain drift the Dickie technique [31] is employed [32]. This technique involves comparing the measured source temperature (T_S) with a matched impedance reference temperature (T_R) by means of a switch in order to eliminate the presence of any radiometer noise and minimise the effect of gain changes. From Land [32] the resultant signal, independent of amplifier noise is:

$$(1 - \rho)(T_S - T_R)G \tag{1.13}$$

where G is the system gain constant and ρ is the power reflection at the antenna aperture. By ensuring the reference temperature is close to the source temperature the effect of gain and reflection variations can be kept low. Making use of an improved Dickie configuration with two reference temperatures it is possible to measure the source microwave temperature independently of the gain and reflection coefficient. In this configuration, commonly refereed to as radiation balance mode, the measured microwave temperature is equal to the material microwave temperature independent of any reflection at the antenna / material interface. The reader is referred to [32] for more information on this improvement and a full discussion of the design of the radiometers used in this work.

1.2.3 Gabor Limit

The nature of thermal radiation signals is such that they are inherently subject to random fluctuations about a mean value. Signal averaging ('smoothing') reduces these fluctuations at the expense of a long measurement time. The theoretically smallest detectable temperature fluctuation, i.e. the temperature resolution achievable, is given by the Gabor relation modified for the Dickie configuration [24]:

$$\Delta T = \frac{2(T_{source} + T_{rad})}{(\Delta t B)^{\frac{1}{2}}} \tag{1.14}$$

where T_{source} is the temperature of the material, T_r is the effective noise temperature of the receiver, Δt is the response time and B is the (pre-detection) bandwidth of the radiometer.

For the two reference comparator radiometer, [32], temperature resolutions equal to that of the single reference Dickie radiometer are achieved when the source temperature falls near to the mean of the reference temperatures. For a radiometer operating at 3.0-3.4GHz over the range of 25 to 40 °C a measurement accuracy of 0.2°C and temperature resolution of 0.1°C are achieved.

1.2.4 Types of Radiometer System

To date two basic categories of microwave radiometer system, total power and correlation radiometers have been developed. Both work by measuring the microwave temperature of a volume of material. The radiation reaching the antenna at the surface of the material is generated over the entire depth on the material. In other words the signal is built up with distance towards the measuring surface and it is the whole integrated contribution over the viewed volume that is measured.

The actual radiometer is only one part of a complete temperature measurement system. Also required are the source material (which is emitting the microwaves) and a structure (antenna) which is electromagnetically coupled to the radiating material body, see Figure 1.2. Two forms of coupling structure, a direct contact probe and a cavity are discussed

in the following sections.

In the case of total power systems the thermal noise power of the source is measured directly by the antenna. In the case of the correlation radiometer more than one antenna is used and a correlation between each of the signals is produced. Correlation radiometry will not be considered further in this work but more detail can be found in [24, 33, 34].

1.2.4.1 Direct contact radiometer

Open antennas are used primarily in medical applications as they allow direct contact with the area of interest. The signal measured comes from the tissue directly below the antenna aperture thus allowing the measurement to be site (though not depth) specific. This site specificity is of prime importance in the detection and monitoring of disease. Open antennae, however, have some important disadvantages. They have low immunity to other sources of electromagnetic noise in the vicinity (e.g. mobile telephones, computer screens) leading to spurious readings. There is also the need for the aperture to be applied directly to the skin surface, as any air gaps can result in a large reflection of the signal. Clearly such antennae are also susceptible to any product packaging and thus of minimal use in industrial applications. A review of some of the many direct contact antennas used in both total and correlation systems can be found in the review paper of Leroy *et al* [24].

1.2.4.2 Cavity Radiometers

In cavity radiometry the source material is surrounded by the walls of a microwave cavity, within which the material is the principal source of thermal radiation. A cavity wall probe or loop couples the cavity thermal signal to the radiometer receiver as with the open antennas. This method has the advantage that radiation from all around the source is detected and also with the cavity there is a much greater immunity to external sources of electromagnetic noise. This type of coupling is obviously unsuitable for use in the medical field and is clearly more appropriate than the direct contact system for use in the food industry. A further advantage of the cavity radiometer is that the spatial dependence of coupling between the source signal and the radiometer can be well controlled [35].

1.3 Weighting Functions

For a non-isothermal source material the effective microwave source temperature is found by integrating the contribution from each sub-volume coupled to the probe. This process requires the use of a weighting function w(**r**), where **r** is the position in the source material, to describe the relative radiation coupling of the subvolumes to the antenna. The weighting function can also be considered as corresponding to the three dimensional form of the penetration depth.

The weighting function is determined by the properties of both the antenna and the sample material. Factors influencing this weighting function include the geometry, size relative to wavelength and modes of excitation of the coupling antenna, and the geometry and attenuation length of the source material. The development and application of weighting function computation and its experimental verification define the core of this research work.

In the case of a thermal distribution T(**r**) in a matched source material the signal equivalent temperature, T_e, is given by [36]:

$$T_e = \oint_{vol} w(\mathbf{r})T(\mathbf{r})dv \tag{1.15}$$

The weighting function normalises to one as:

$$\oint_{vol} w(\mathbf{r})dv = 1 \tag{1.16}$$

The idea of a weighting function and of the coupling of sub-volumes to the antenna was first suggested by Robillard *et al* [37] and then further specified by Leroy *et al* [9] and Bocquet *et al* [38].

More recently, Leroy *et al* (1998) [24] and Lasri *et al* [39] have proposed the absolute weighting function (AWF). The AWF is the contribution in radiometric degrees to the signal from a subvolume of $1mm^3$ subject to a temperature rise of 1K. Although this definition is of interest as it expresses the variation in radiometric degrees directly to the variation in temperature, it is not considered further in this work.

1.3.1 Calculation of the Weighting Function

The loss of high frequency electromagnetic power in (organic) materials as heat can be represented by two processes, ohmic heating by conduction currents and dielectric absorption losses. For the power levels found in microwave radiography the effects of these two loss mechanisms are linear and the heating power density is given by [27, 28]:

$$\frac{1}{2}(\sigma + \omega\epsilon'')\mathbf{E}^2 \tag{1.17}$$

where $\mathbf{E}$ is the electric field strength, σ is the conductivity and ω is the angular frequency.

Thus an excited antenna operating at a specific frequency coupled to a tissue deposits a power density distribution dependent on the antenna and tissue properties and on the radiated power. Using reciprocity, an antenna at the same frequency would receive an electromagnetic signal proportional to this distribution and to the source temperature. Thus this power normalised distribution is an expression of the weighting function [27].

The general equation for the weighting function is then:

$$\frac{w(x,y,z)}{1-|\rho|^2} = \frac{\frac{1}{2}\sigma|E(x,y,z)|^2}{W_o} \tag{1.18}$$

where W_o is the power normalisation factor, and is equal to the power input in the active process. For some applications it can be useful to simplify the calculation of the weighting function to a one dimensional case. For this it is necessary to reduce the weighting function to one dimensional form by integrating over two space dimensions as:

$$w(z) = \int\int w(x,y,z)dxdy \qquad \text{with} \qquad T_{mw} = \int_z w(z)T(z)dz. \tag{1.19}$$

1.3.2 Form of the Weighting Function

The simplest form of weighting function is found for plane wave propagation normal to the surface of a uniform semi-infinite region of material [4]. In this case for a matched antenna, the one dimensional weighting function expression is given as:

$$T_e = 2\alpha \int_0^\infty e^{-2\alpha z}T(z)dz \tag{1.20}$$

where α is the attenuation coefficient. The three dimensional case requires the inclusion of a normalised lowest order Bessel function to describe the field behaviour in the remaining two space dimensions [40].

Weighting function examples can be given for both antenna and cavity coupling systems. In the case of the open ("medical") antenna system the radiometer system has a weighting function of approximately 60% plane wave contribution and the rest near field losses (higher order terms in 1/r) [27]. Any air gaps etc. present in the system, however, can drastically alter the composition of the weighting function and it becomes ill controlled.

In the case of the cavity antenna much more control over the weighting function is possible. It is possible to construct the cavity so that any losses from its interior are small compared with that from the source material. The weighting function within the cavity can be relatively easily controlled by varying the measurement frequency and the cavity shape. In general the cavity weighting function will be composed of quasi plane wave functions inward from sample surfaces with the field standing wave patterns which exist over the whole bandwidth [27]. The position and type of the cavity coupling can be chosen to couple to particular modes or combinations of modes within the cavity.

This research work will focus on the weighting functions for the direct contact antenna systems. For more information on the cavity antenna systems see Barrie [41].

1.4 Determination of the Weighting Function

Determination of the weighting function relies both on accurate determination of the near field ($\mathbf{E(r)}$) of the antenna and on having an accurate knowledge of the distribution of conductivity of the material of interest ($\sigma(\mathbf{r})$). A direct consequence of antenna reciprocity is that the modelling of power absorption and power dissipation in tissues are identical problems. Thus the determination of the near field of the antenna is accomplished by consideration of the active process.

In particular the general form of the weighting function is directly proportional to the

specific absorption rate (SAR) electromagnetic waves by tissues:

$$SAR = \frac{1}{2}\sigma\rho_m\mathbf{E}^2 \propto \frac{1}{2}\sigma\mathbf{E}^2 = w(\mathbf{r}). \tag{1.21}$$

where ρ_m is the density of the tissue / material. Thus the sizeable literature considering methods of finding the SAR in human and animal tissues is directly relevant to finding the weighting functions for microwave radiometric applications.

Computational methods in particular are readily applicable to this type of problem and as computational speeds increase and costs decrease these methods are employed more and more. The FDTD method in particular can be applied with relative ease to model the absorption of electromagnetic waves from a radiating antenna by a variety of materials and geometries. One of the first instances of applying the finite difference time domain (FDTD) method to the absorption of electromagnetic radiation was by Taflove (1975) [42] in the problem of microwave heating of the human eye. The specific application of FDTD to bioelectromagnetic problems is discussed by Sullivan *et al* [43].

FDTD has since been used to calculate the near field for radiometric applications by many authors including Wu *et al* [44], Abe *et al* [45] and more recently Maruyma *et al.* [25], Hand *et al.* [26] and Van Leuween *et al.* [46].

Alternative modelling methods have also been applied for SAR computation. Mamouni *et al* [47] employ a modal method involving analytical solutions to determine the near field in homogeneous lossy materials. This method has since been expanded to consider inhomogeneous and layered structures, Bocquet *et al* [38] and Ridaoui *et al* [48]. Other methods include those of Cheever *et al* [49] who use the mode matching technique of Harrington to determine depth of penetration into various materials and Bardati *et al* [50] who use a multimode two dimensional model.

In this research work the FDTD technique is employed to determine the weighting functions. Due to the large effect of near field losses in the situations of interest it is essential to have a thorough and accurate representation of the fields. A full explanation of the FDTD approach along with information on its implementation to this specific subset of problems is presented in the following chapter. Chapter 2 also presents information on the various experimental approaches to determination of the antenna near field including

the non-resonant perturbation method.

In all of the methods of determination of the electric field distribution, knowledge of the complex permittivity of the material in which the field propagates is vital. Thus for complete weighting function computation it is essential to know the dielectric behaviour, permittivity and conductivity, of the material under investigation. In particular, in calculation of the weighting functions, care has to be taken when considering multilayered materials [38].

1.4.1 Dielectric Properties

To gain a full understanding of the weighting function and thus the microwave radiometric signal it is necessary to consider in some detail the dielectric properties of the source materials. In body tissues, these properties are highly dependent on the water content of the particular tissue being discussed. Dielectrically there are two distinct types of tissues, low permittivity low loss fats and proteins, and the high permittivity high loss water component. Dielectric properties of organic materials are primarily dependent on frequency, temperature and the physical state of the material [51].

1.4.1.1 The Complex Permittivity

In response to an applied electric field, a dielectric material may respond in several ways. In response to a static field charges may move freely within the material leading to 'static' conductivity. Further to this, minute movements of positive and negative charges on atoms and non-polar molecules may occur. These movements will result in the generation of a dipole moment for each of the atoms and molecules involved. In response to an applied field polar molecules, which have a permanent dipole moment, will tend to orient with the applied filed in such a way that their dipole moment is parallel to the field. The vector sum of each individual dipole moment gives the macroscopic dielectric polarisation $\mathbf{P}$ of the material. For a more detailed description of the polarisation of dielectric materials the reader is referred to Ramo *et al.* [28].

The generation of the dielectric polarisation takes a finite amount of time after initial application of the applied field as it requires the physical displacement of charges, atoms or molecules. Upon removal of the field the polarisation decays exponentially with time, with the time to reduce to 1/e of its initial amplitude termed the relaxation time, τ. For an applied alternating field the polarisation builds up and relaxes at a rate approximately equal to the rate at which the field alternates but the polarisation lags behind the field [40]. If the polar molecules in the material under consideration are large or the frequency of the applied field is large then the materials cannot rotate quickly enough to keep up with the field. In this case the polarisation and field lose phase and a thermal dissipation of energy results.

The behaviour of lossy dielectrics of this type is represented by the complex relative permittivity in the form:

$$\epsilon_r = \epsilon_r' - i\epsilon_r''. \tag{1.22}$$

The real part, the dielectric constant ϵ_r', represents the storage of energy and the imaginary part, the relative dielectric loss factor ϵ_r'', represents the dissipation of energy in the material. Rewritten in polar form this becomes:

$$\epsilon_r = |\epsilon_r| e^{-i\delta} \tag{1.23}$$

where $\tan\delta$ is the loss tangent as given by:

$$\tan\delta = \frac{\epsilon_r''}{\epsilon_r'}. \tag{1.24}$$

The total loss factor for the material is composed of contributions from both the dielectric relaxation (ϵ_d'') and from the ionic conductivity as:

$$\epsilon_t'' = \epsilon_d'' + \epsilon_i'' = \frac{\sigma_d}{\omega} + \frac{\sigma_i}{\omega} \tag{1.25}$$

where σ_i is the ionic conductivity, σ_d is the effective dielectric conductivity and ω is the angular frequency of the applied field. In a similar way a total effective conductivity for the material can be stated ($\sigma = \sigma_i + \sigma_d$).

1.4.1.2 Dielectric properties of biological and organic materials

The microwave properties of biological and organic materials are dominated by their water content with salts and minerals having a smaller effect. Water, a polar molecule, has a high dielectric constant (≈ 81 Fm^{-1} at 15°C) a result primarily of its orientational polarisability. The dielectric behaviour of pure water at microwave frequencies is well described by a Cole-Cole [52] relationship [40]:

$$\epsilon_r'(f) = \frac{\epsilon_s - \epsilon_m}{1 + (f/f_r)^2} + \epsilon_m \tag{1.26}$$

$$\epsilon_r''(f) = \left(\frac{f}{f_r}\right) \frac{\epsilon_s - \epsilon_m}{1 + (f/f_r)^2} \tag{1.27}$$

where ϵ_s is the static permittivity, ϵ_m is the millimetre permittivity and f_r is the Debye resonance frequency. The Debye resonance occurs at a particular frequency in the microwave range where there is a marked peak in the loss value and an associated fall in the real permittivity for a material. Various other resonances occur in other frequency ranges.

In body tissues the dielectric behaviour is dominated by interstitial solutions which can be considered to be weak (0.9%) saline solutions [40]. The ionic conductivity and the Debye relaxation of the polar water molecules are the principal contributors to the dielectric behaviour of saline solutions. At physiological concentrations this conductivity (a result of the presence of electrolyte ions) only slightly affects the real part of the permittivity [40] but contributes primarily to the loss factor, in the form of an effective loss contribution.

Fats, oils and proteins have fairly low dielectric constants and so are relatively transparent to microwaves, producing a weak microwave signal. In a mixed material product the material with the higher water content will be the main source of the microwave signal.

The modelling of the dielectric properties of biological and organic materials is considered in some depth in chapter 5. This discussion includes a fuller account of the Cole-Cole approximation for water solutions along with more details on the methods of modelling the dielectric properties of mixtures.

1.5 Interpretation of radiometric temperatures

Objective, qualitative interpretation of the radiometric data is vital to the applicability of this technique. Realtime measurement allows scanning of the microwave temperature of a particular location in a linear manner giving a temperature profile which can be applied to detect breast carcinoma and arthritic joints [18]. The use of many antennae in parallel can reduce the measurement time to allow production of a two dimensional temperature map. It is not possible in these ways, however, to give any information on the variation of the temperature with depth into the material. To achieve this information it is necessary either to measure at more than one frequency and reconstruct the temperature profile or to use a-priori information on the expected temperature distributions.

1.5.1 Thermal Model Approach

A combined model linking the microwave temperature to the surface, arterial and ambient temperatures is a means of providing a useful interpretation of the radiometric data in the case of medical applications [53]. The thermal and microwave models of heating can be combined as a result of the shared anatomy and the interdependence of the propagation constant ($2\omega\alpha$) and the thermal conductivity (K) through their dependence on the tissue water content. The field attenuation coefficient, α, is equivalent to the depth of penetration of an electromagnetic field.

By assuming the Pennes heat transfer model (in which arterial blood is considered to reach equilibrium with the bulk tissue at the capillary level) and linearised Newtonian cooling at the skin surface Land *et al.* [53] present a thermal model for tissues.

For the simplified limiting condition of a semi-infinite region of uniform tissue, (where T_{mw}, is given by equation 1.20):

$$T_a - T_{mw} = \frac{H}{\left(\sqrt{w_b C_b K} + w_b C_b/2\alpha\right)} \left(T_s - T_{amb}\right), \tag{1.28}$$

where w_b is the arterial blood perfusion, K is the thermal conductivity, H is the surface conductivity (heat loss coefficient) and C_b is the specific heat capacity of the tissues.

In this equation the ambient temperature T_{amb}, microwave temperature T_{mw}, surface temperature T_s and arterial temperature T_a are either known or can be easily measured.

In the case of the thermal modelling of food products several key differences exist. The main principles, however, are still applicable as water is the dominant microwave and thermal constituent. The surface heat loss will be by similar methods. During heating or cooling, however, there is no natural response as in living tissue to maintain an equilibrium temperature.

1.5.2 Multifrequency Radiometry

By measuring the microwave temperature at more than one frequency it is possible to obtain data generated over a variety of depths within the source material. As the range over which measurements can be made is approximately 2.5GHz and the bandwidth required at each specific frequency is about 400MHz a maximum of 7 independent measurement frequencies can be used. The method of inverting the radiometric data and returning a valid temperature profile is termed the inverse problem. In effect the inverse problem requires determining T(r) given that $T_{mw}(i,r)$ and w(i,r), where i is each measurement frequency, are known and related as:

$$T_{mw}(i,r) = \int_{vol} w(i,r)T(i,r)dr. \tag{1.29}$$

An important consideration in solving this inverse problem results from the fact that the data suffers from a high degree of measurement uncertainties. This type of inverse problem is ill posed as the solution is not stable with respect to small variations in the data [54].

Several different techniques have been considered to solve the inverse problem. Bardati *et al* [50, 55, 56, 57, 58] consider the temperature profile to be retrieved in terms of singular functions, the coefficients of which are determined from the radiometric data. In this way they have been able to reconstruct two dimensional temperature profiles of a small hot object inside a cooler liquid with a temperature differential of several degrees.

Another popular approach is that of using a-priori information on the temperature profile

and using various statistical methods to fit the radiometric data to that profile as considered by Maruyma *et al.* [25], Hand *et al.* [26] and Van Leeuwen *et al.* [46]. Model fitting combined with the Monte Carlo technique to simulate random variations in the data has been considered by Mizushina *et al* [36, 59].

Finally correlation radiometry can be applied to the determination of temperature gradients in materials without the need for measurement at more than one frequency [60]. Problems of sensitivity with this approach, however, have limited its applicability so far [24].

Chapter 7 considers in more detail several of the approaches to solving this inverse problem and presents results for a dual frequency system.

Chapter 2

Modelling of Electromagnetic Radiation Systems

One of the main aims of this research work is accurate determination of weighting functions for specific antenna configurations. Although there exist many approaches to this problem by far the most flexible is the use of computational modelling techniques. This chapter will introduce several of these methods, considering their advantages and disadvantages, and then focus on the finite difference time domain (FDTD) method as the most suitable method. Finally it will conclude with a description of the basic electromagnetic simulation tool (BEST) [3] and the application of this modeller to weighting function computation.

2.1 Numerical Modelling Techniques

Many numerical techniques exist for the modelling of electromagnetic radiation problems, each particularly suited to specific types of problem, large scattering bodies, small antennae, inhomogenous materials etc. As some problems can be of various types, hybrid methods combining the benefits of two or more techniques have also been developed. In choosing a particular method there is a necessary compromise between accuracy, speed and computational requirements.

Computational techniques for modelling electromagnetic problems also include analytical techniques and expert systems [61]. These methods involve making *a-priori* assumptions and / or generalisations about the problem. Although these methods can give a guide to the solution relatively quickly, they are of little use where specific detail is required.

In the particular case of determining the power deposition in biological or in-homogeneous lossy dielectric structures three main numerical techniques have been employed [62]. These approaches are the method of moments (MoM), the finite element method (FEM) and the finite difference time domain (FDTD) technique. In addition several hybrid methods combining the strengths of two or more of these methods have been proposed. More recently the finite integration technique (FIT) has also been applied for research of this nature [63, 64]. Hubing [61] provides a good general review of some of the most popular numerical techniques and their implementation.

2.1.1 Method of Moments (MoM)

One of the most popular and long standing numerical techniques is the Method of Moments (MoM). Introduced by Harrington [65] in the late 1960's this technique has been applied to a wide range of applications. The method of moments, also known as the method of weighted residuals, reduces a complex integral equation derived from Maxwell's equations to a series of linear equations [61, 66]. The difference between an initial estimated solution and the true solution, the residual, is then minimised by a matrix inversion process.

This technique is good for analysing conductors and homogeneous dielectrics but can have problems with inhomogeneous, non-linear dielectrics or complex geometries [61]. The method of moments technique works best in situations where the scattering/radiating body is (electrically) large. Several disadvantages exist with this approach though. The derivation of the set of linear equations may be time consuming for complex inhomogeneous scattering objects and once found these equations would only be applicable to the one particular problem. For complex inhomogeneous objects the matrix to be inverted may grow to sizes which make accurate computation difficult [67].

Many other weighted residual techniques exist, including the Conjugate Gradient Method [68], Generalised Multipole Technique and Boundary Element Method [69], and have their own set of advantages and disadvantages over the general moment method.

Some early applications of the method of moments to determining the fields in biological bodies has been performed by Livesay [70] and Chen [71]. More recently the technique has been applied by Chuang [72] with coupled integral equations to the effect of fat layers on power absorption in full body human models. Using the moment method for this application, however, places severe limits on the accuracy with which the human body can be modelled. In general the use of moment methods is limited to problems of electromagnetic scattering from large bodies and not to the power absorption problems of microwave radiometry.

2.1.2 Finite element methods (FEM)

The finite element method is a time domain technique that requires modelling of not only the structure of interest (as in MoM) but must also include the area around the structure. Finite element techniques are based on splitting the whole configuration into a number of homogeneous elements. As the FEM is not a time stepping procedure the elements can be of varying size so that more detailed regions can have smaller elements than elsewhere. The corners of the elements are called nodes and this method calculates the field quantities at these nodes. In general FEM are based on variational techniques, in which the unknown field quantities are determined by minimising an energy function [61].

Finite element methods are good for inhomogeneous configurations as the electrical and geometric properties of the elements can be defined independently [61]. The FEM allows generality of programming in that one general purpose program can be used for many wide-ranging simulation situations [73]. This technique, however, is not as good for open unbounded problems requiring an absorbing boundary to truncate the computational mesh. Another disadvantage is that the method and programming in this technique are also quite complex and so require more time [28].

Applications of FEM to hyperthermia and power deposition in lossy dielectrics have been considered by Lynch, Paulsen and Strohbehn [69, 74].

2.1.3 Finite difference time domain (FDTD) technique

The finite difference time domain method is a direct solution of Maxwell's time dependent equations. There also exists the finite difference frequency domain (FDFD) method based on the time harmonic form of Maxwell's equations. The FDFD method is more similar in form to the finite element method than the FDTD technique, and so has similar advantages and disadvantages to it [61].

As a time domain method the FDTD technique is well suited to modelling transient fields. In the FDTD method the electromagnetic problem is dealt with as an initial value problem. The simulation begins with the application of a wave source at time t=0 and ends when all waves achieve steady state variation or converge to zero. In between the waves are propagated by solving the finite difference form of Maxwell's time dependent equations at a series of lattice points called nodes [67]. The FDTD method requires that the entire computational domain be modelled leading to the necessity for an absorbing boundary condition (ABC) to mimic free space and absorb without reflection any outgoing waves.

The FDTD technique has several advantages over the other numerical techniques. Firstly the nature of the FDTD method allows modelling of anisotropic, non-linear materials. This is made possible because the dielectric properties are independently defined at each of the lattice points. The FDTD method also has the advantage that the results of the modelling can be easily visualised. As the FDTD technique directly calculates the electric and magnetic fields, an advantage in itself, it is possible using visualisation tools to watch animation displays of the changes in the field distributions as they progress with time. There is also the advantage of not having to invert a large matrix to achieve the desired solution as is the case for moment and finite element methods [73].

The major disadvantage with this method is that computational requirements may grow to unreasonable sizes for complex geometries. This problem occurs for example in simulations

involving long thin structures and in simulations where field values a considerable distance away from the object are desired. Other disadvantages include a lower degree of accuracy than some of the other numerical techniques and the fact that the field quantities are only found at the nodes of the grid [73].

The application of the finite difference time domain method to the determination of the patterns of power dissipation and calculation of weighting functions is considered further in section 2.3.

2.1.4 Computational Requirements of Numerical Techniques

The various computational techniques discussed in this section have differing computational needs. The term computational requirements encompasses both the necessary computer storage space and the computational run time. For the method of moments technique the storage space is proportional to $(3N)^2$ and the run time to $(3N)^3$, where N is the total number of cells used in the simulation [43]. The FDTD technique, however, has storage requirements and a run time directly proportional to N [75], so that both the computational storage and run time are proportional to the volume modelled.

It is important to note though that the size of N is much larger for the FDTD technique than for the MoM. This is a result of the need for the entire region to be modelled for the FDTD method where as the MoM requires that only the surface of interested be simulated. Hence an increased value of N due to the inclusion of many free space cells. Albeit, the FDTD method is considered to be an appropriate alternative to other techniques due to its linear and not geometrical increase in computational requirements with N [43].

2.1.5 Choice of technique

The decision to use the finite difference time domain approach as opposed to the others came about as a result of several factors. Firstly this technique is well established in the field of computationally determining the specific absorption rate [42, 43, 76, 77, 78, 79, 80, 81, 82, 83, 84, 85] and weighting functions in general [25, 26, 44, 45, 46]. Additionally

the algorithm is relatively straightforward to program directly or using generally available software. Finally the ease with which non-isotropic media can be modelled, a requirement for the structures of interest in this research work (e.g body tissues, food stuffs), further strengthens the case for FDTD. It has been noted that frequency domain methods (MoM, FEM etc.) suffer from badly conditioned material matrices as a result of the highly inhomogeneous nature of biological tissues [64]. The major limiting factor of FDTD in that it may require extreme computational resources is not considered to be a major problem given the availability of fast, large memory, high storage personal computers.

2.2 The FDTD approach

The finite difference time domain method (FDTD) is a direct solution of Maxwell's time dependent equations. In order to fully appreciate the algorithm it is necessary to start from these classical equations which govern the propagation of electromagnetic waves [86]:

$$\nabla \times \mathbf{E} = -\frac{\partial \mathbf{B}}{\partial t}, \tag{2.1}$$

$$\nabla \times \mathbf{H} = \frac{\partial \mathbf{D}}{\partial t} + \mathbf{J}. \tag{2.2}$$

Where $\mathbf{E}$ is the electric field strength, $\mathbf{D}$ is the electric displacement, $\mathbf{H}$ is the magnetic field strength, $\mathbf{B}$ is the magnetic flux density and $\mathbf{J}$ is the current density. The electric field strength and current density are further related through Ohm's law which states that:

$$\mathbf{J} = \sigma \mathbf{E}, \tag{2.3}$$

where σ is the conductivity of the medium.

In a linear isotropic (LIS) medium the electric field and electric displacement can be related as:

$$\mathbf{D} = \epsilon_o \epsilon_r \mathbf{E} = \epsilon \mathbf{E}, \tag{2.4}$$

where ϵ_o is the permittivity of free space, ϵ_r is the relative permittivity of the medium and ϵ is the permittivity. Similarly the magnetic field and magnetic flux density are related as:

$$\mathbf{B} = \mu_o \mu r \mathbf{H} = \mu \mathbf{H}, \tag{2.5}$$

where μ_o is the permeability of free space, μ_r is the relative permeability of the medium and μ is the permeability.

Using equations 2.3, 2.4 and 2.5 Maxwell's curl equations can be rewritten as:

$$\nabla \times \mathbf{E} = -\mu \frac{\partial \mathbf{H}}{\partial t}, \tag{2.6}$$

$$\nabla \times \mathbf{H} = \epsilon \frac{\partial \mathbf{E}}{\partial t} + \sigma \mathbf{E}, \tag{2.7}$$

assuming μ and ϵ are not time dependent. In component form these equations (2.6 and 2.7) become:

$$\frac{\partial H_x}{\partial t} = \frac{1}{\mu}\left(\frac{\partial E_y}{\partial z} - \frac{\partial E_z}{\partial y}\right), \tag{2.8}$$

$$\frac{\partial H_y}{\partial t} = \frac{1}{\mu}\left(\frac{\partial E_z}{\partial x} - \frac{\partial E_x}{\partial z}\right), \tag{2.9}$$

$$\frac{\partial H_z}{\partial t} = \frac{1}{\mu}\left(\frac{\partial E_x}{\partial y} - \frac{\partial E_y}{\partial x}\right), \tag{2.10}$$

$$\frac{\partial E_x}{\partial t} = \frac{1}{\epsilon}\left(\frac{\partial H_z}{\partial y} - \frac{\partial H_y}{\partial z} - \sigma E_x\right), \tag{2.11}$$

$$\frac{\partial E_y}{\partial t} = \frac{1}{\epsilon}\left(\frac{\partial H_x}{\partial z} - \frac{\partial H_z}{\partial x} - \sigma E_y\right), \tag{2.12}$$

$$\frac{\partial E_z}{\partial t} = \frac{1}{\epsilon}\left(\frac{\partial H_y}{\partial x} - \frac{\partial H_x}{\partial y} - \sigma E_z\right). \tag{2.13}$$

2.2.1 The FDTD Algorithm

The basis of the Yee algorithm [87] is to transform the partial derivatives in space and time in equations 2.8 to 2.13 to their discrete centred finite difference forms. To implement these changes Taylor expansions are used to express each differential equation as an infinite sum of finite differences around a centre point. To do this the entire region to be modelled is divided into small cells on a Cartesian grid.

In Yee's original notation a space point of the rectangular three dimensional grid is denoted by:

$$(i, j, k) = (i\delta x, j\delta y, k\delta z). \tag{2.14}$$

Where i, j and k are integers, $\delta x, \delta y$ and δz are the unit cell spatial dimensions in the x,

y and z directions respectively. Yee denoted any function of space and time as:

$$F^n(i,j,k) = F(i\delta x, j\delta y, k\delta z, n\delta t). \tag{2.15}$$

where n is an integer and δt is the time step.

To second order accuracy the centred finite difference equations for the space (x) and time (t) partial derivatives are:

$$\frac{\partial F^n(i,j,k)}{\partial x} = \frac{F^n\left(i+\frac{1}{2},j,k\right) - F^n\left(i-\frac{1}{2},j,k\right)}{\delta x} + o(\delta x)^2 \tag{2.16}$$

$$\frac{\partial F^n(i,j,k)}{\partial t} = \frac{F^{n+\frac{1}{2}}(i,j,k) - F^{n-\frac{1}{2}}(i,j,k)}{\delta t} + o(\delta t)^2 \tag{2.17}$$

Equations for the y and z spatial directions can easily be obtained by considering equation 2.16. These equations show the centre differencing approximation at work, in which the value of interest is evaluated from the corresponding value at points half a step before and half a step after the point of interest. These steps are in space or time as appropriate.

The components of the electric and magnetic fields are evaluated at positions on the Yee cell as shown in Figure 2.1.

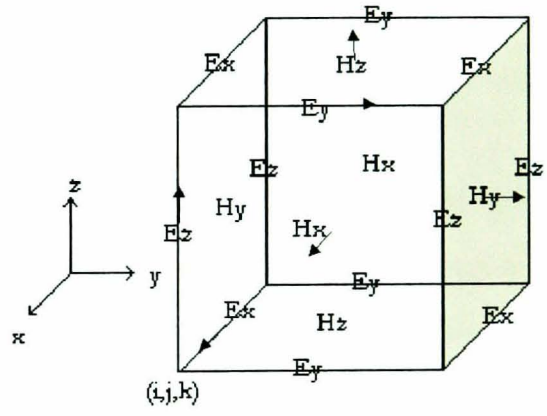

Figure 2.1: *The Yee Cell, electric fields are evaluated on the edge centres of the cell and the magnetic fields on the face centres.*

The electric fields are evaluated on the edge centres of the Yee cell and the magnetic fields on the face centres. The fields are offset by a half space step with each magnetic field component surrounded by electric field components and vice-versa. Values of electrical conductivity and permittivity are defined for each electric field lattice point and values of magnetic permeability and equivalent conductivity are defined for each magnetic field

lattice point [88]. Through the replication of this cell throughout the simulation region the continuous region is transformed into discrete sections.

Transforming equations 2.8 to 2.13 using the centre difference approximation (equations 2.16 and 2.17) yields the Yee algorithm. Equations 2.18 and 2.19 give the relevant discretised equations for the E_x and H_x components [89]. The remaining electric and magnetic components are similar.

$$E_x^{n+1}(i+\frac{1}{2},j,k) = \left[\frac{1-\frac{\sigma(i,j,k)\Delta t}{2\epsilon(i,j,k)}}{1+\frac{\sigma(i,j,k)\Delta t}{2\epsilon(i,j,k)}}\right] E_x^n(i+\frac{1}{2},j,k) + \frac{\frac{\Delta t}{\epsilon(i+\frac{1}{2},j,k)\Delta x}}{1+\frac{\sigma(i,j,k)\Delta t}{2\epsilon(i,j,k)}} \times$$

$$\left[H_z^{n+\frac{1}{2}}(i+\frac{1}{2},j+\frac{1}{2},k) - H_z^{n+\frac{1}{2}}(i+\frac{1}{2},j-\frac{1}{2},k) + H_z^{n+\frac{1}{2}}(i+\frac{1}{2},j,k-\frac{1}{2}) - H_z^{n+\frac{1}{2}}(i+\frac{1}{2},j,k+\frac{1}{2})\right] \tag{2.18}$$

$$H_x^{n+\frac{1}{2}}(i,j+\frac{1}{2},k+\frac{1}{2}) = H_x^{n-\frac{1}{2}}(i,j+\frac{1}{2},k+\frac{1}{2}) + \frac{\Delta t}{\mu(i,j+\frac{1}{2},k+\frac{1}{2})\Delta x} \times$$

$$\left[E_y^n(i,j+\frac{1}{2},k+1) - E_y^n(i,j+\frac{1}{2},k) + E_z^n(i,j,k+\frac{1}{2}) - E_z^n(i,j+1,k+\frac{1}{2})\right] \tag{2.19}$$

FDTD is a time stepping procedure in which the electric field values at a time t are used to calculate the magnetic field at time t+δt. These values of the magnetic field can then be used to find the electric field at time t+2δt. In this way the fields are propagated through the simulation space [61]. At each time step the field values are updated and the previous values lost so that no matrix inversion is needed. This results in a lower memory requirement than other numerical approaches . The maximum absolute value of the electric field components, $|E_x|, |E_y|, |E_z|$, found in the last time step of the simulation are generally taken as the magnitude of the phasor of the steady state field [67].

In this form these six equations can readily be implemented to computationally model electromagnetic fields in a variety of propagation problems. For more information on the FDTD algorithm the reader is referred to the many reference books available e.g. [90, 91, 92].

2.2.2 Accuracy and Stability

Taflove [67] was the first to consider the problems of accuracy and stability of the Yee algorithm and provide suitable criterion. It is necessary for the unit cell spatial distances δx, δy and δz to be much smaller than the wavelength (λ). In fact $\delta x, \delta y, \delta z \leq 0.1\lambda$ has been shown to give sufficient accuracy [89]. This then places a limit on the possible frequency that can be considered for a particular cell size.

To ensure stability within the simulation the grid size must be related to the time step δt through the relationship:

$$\nu_{max}\delta t \leq \left(\frac{1}{(\delta x)^2} + \frac{1}{(\delta y)^2} + \frac{1}{(\delta z)^2}\right)^{-\frac{1}{2}} \tag{2.20}$$

as proven by Taflove [67]. Where ν_{max} is the maximum wave phase velocity. This is necessary so that the plane wave source travels at most one cell length per time step. For a cubic lattice ($\delta x = \delta y = \delta z = \delta$) this equation is usually modified to [67]:

$$\delta t = \frac{0.5\delta}{c} \tag{2.21}$$

to give a greater margin of stability in the algorithm.

2.2.3 Perturbation methods

In the FDTD method the simulation is started through the application of some excitation to the system. The most popular excitation schemes are the continuous sinusoid, the Gaussian shaped pulse and the exponentially decaying sinusoid [43]. For continuous excitation the simulation ends when the fields reach a steady state. In the particular case of sinusoidal excitation, where the incident wave excitation varies sinusoidally the simulation ends when all fields show sinusoidal excitation [67]. For pulse excitation the simulation ends when the fields converge to zero. The use of a Fourier Transform to give results for a range of frequencies is common in the cases of pulse and exponentially decaying excitation [93]. Sinusoidal excitation is used when monochromatic analysis of a given situation is required. In this work the weighting functions are required at specific frequencies and so sinusoidal excitation is the most appropriate source method.

2.2.3.1 Sinusoidal excitation

The general form of the incident wave excitation for a continuous sinusoidal plane wave is:

$$E_{int} = A\sin(2\pi f \delta t\, n) = A\sin(\omega\, \delta t\, n) \tag{2.22}$$

where A is the amplitude, ω is the angular frequency, f is the frequency, δt is the time step size and n is the number of the iteration [67]. For all fields to exhibit this sinusoidal variation i.e. for the simulation to end requires time stepping for a time equal to several periods of oscillation of this incident wave [75]. It has been shown that the Q-factor of the structure or phenomenon being modelled is approximately equal to the number of periods of oscillation necessary to reach a steady state [88]. The introduction of a small isotropic conductivity within the simulation space (external to any scatterer) can result in a quicker convergence of the fields to the steady state behaviour [73].

2.2.4 Total / Scattered Fields

In the first instance the FDTD technique was primarily used for the investigation of scattering of electromagnetic fields from objects. By including a field source in the simulation space, however, it is possible to easily model the many types of radiating structures.

In the case of scattering bodies the FDTD technique is often employed to determine the scattered fields only. Alternatively in the total field approach, the total fields are often found only in a sub-domain of the simulation space which contains the scattering object, and the scattered fields are found elsewhere in the grid [94, 95]. In this method the incident wave is applied along one edge of the total field, and then is subtracted out the other end after propagating through the region containing the scatterer. This means that the only field components to reach the scattered field region are those which are reflected off the scatterer. In order to allow separation of the field values into total and scattered field components the media filling the simulation region must behave linearly. In that case:

$$E = E_{tot} = E_{scattered} + E_{incident}. \tag{2.23}$$

It has been proposed that the total field approach is better in that it results in less numerical dispersion and it accommodates non-linear media with greater ease [96]. Additionally the fields reaching the mesh truncation points are easier to absorb. In the case of structures which have shielding properties, the scattered fields can become very small. leading to numerical noise problems, so again the total field method is the most appropriate [75]. For linear non shielded cases, however, the scattered field only approach may be better [94]. In the case where it is the radiation and not scattering of fields that is being modelled, as is the case in this work, clearly only total fields are applicable [97]. Mathematically both the total and scattered field approaches should produce the same field values. This is, however, the idealised free space case and is rarely seen in practice [94].

2.2.5 Mesh Truncation and Boundary Techniques

A disadvantage of the FDTD method over some of the other computational techniques is that the computational domain contains not only the structure of interest but the structure and the volume surrounding it. This fact necessitates an absorbing boundary at the edges of the computational domain to absorb the outgoing electric and magnetic fields. Ideally for unbounded problems this outer boundary must not produce any reflections of the field quantities, whilst also being located close to the structure of interest in order to reduce computer storage requirements.

Absorbing boundary conditions (ABCs) fall into two camps: material ABCs and differential equation based (non-material) methods. Until the mid 1990's, when the perfectly matched layer was proposed by Berenger, non-material ABCs were by far the most common method of mesh truncation. These techniques involve factoring the wave equation and allowing only for the propagation of outgoing waves at the edges of the computational domain [94]. Of the non-material based ABCs one of the most popular is that of Mur [98].

In 1994 Berenger [99] proposed the perfectly matched layer (PML) as a material absorbing boundary condition. Although not the first attempt at a material ABC, e.g. Taflove [75],

this method has proven to be the best method of field truncation by far [100]. The basis of the PML technique is to split the electric and magnetic fields in the boundary region in two component fields. This has the benefit of allowing more accurate specification of the material properties of the region [77] and this leads to a boundary layer which will absorb waves of arbitrary direction of propagation and wavelength in a short distance.

Initially proposed in two dimensions the PML has since been extended to three dimensions by Berenger [101] and Katz *et al* [102] among others. Further extensions of this method allow it to be applied to many situations including anisotropic, lossy and non-linear media and to non-orthogonal and curvilinear based FDTD algorithms [103]. It has also been noted that with appropriate layer grading, the PML method produces reflections that are orders of magnitude smaller than those produced by the Mur technique [77].

The main limitation with the application of the PML in the simulation is the increase in computational requirements to implement the technique. This layer effectively surrounds the area of interest in several layers of absorbing material. To implement the PML requires an additional 4-10 cells at the edges of the simulation space in all dimensions. For an already large computational domain (e.g.100*100*100 cells) this represents a sizable increase (125,000 to 330, 000 cells). As a result of this in the presence of lossy dielectrics some researchers prefer the less computationally demanding Mur method [104].

To limit the size of the PML layer, its conductivity is taken to be large which results in a very small electric current relaxation time, much smaller than the time step of the general FDTD volume. To account for this the use of exponential and not centred difference time differencing has been proposed [101]. Petropoulos, [105], has shown however that the use of exponential time differencing provides no benefit over the standard centred time differencing and the fields in the PML must be calculated with a sufficiently small time step. An alternative ABC proposed by Petropoulos *et al* [106] for higher order FDTD schemes is shown to work as well as the Berenger PML with less computational cost.

An excellent review of the many material and non-material based absorbing boundary conditions and in particular the PML and its extensions can be found in the review of Shlager and Schneider [94, 95].

2.2.6 Errors in the algorithm

Several sources of error are present in the FDTD algorithm, in particular in the modelling of curved structures, from numerical dispersion and from numerical instability.

2.2.6.1 Numerical Dispersion

The use of the finite difference equations in the Maxwell curl equations leads to a dispersion of the simulated wave modes [88]. This is a result of the fact that (due to the central differencing approximations) waves of different frequencies propagate at slightly different speeds within the simulation than they would in free space [89]. Non physical results can occur as a consequence of this factor and so it is necessary to consider the presence of numerical dispersion in the FDTD algorithm. Analysis by Taflove and Umashankar [88] gives that the numerical dispersion can be described by:

$$\left(\frac{1}{c\delta t}\right)^2 \sin^2\left(\frac{\omega\delta t}{2}\right) = \frac{1}{(\delta x)^2}\sin^2\left(\frac{k_x\delta x}{2}\right) + \frac{1}{(\delta y)^2}sin^2\left(\frac{k_y\delta y}{2}\right) + \frac{1}{(\delta z)^2}\sin^2\left(\frac{k_z\delta z}{2}\right) \tag{2.24}$$

where k_x, k_y and k_z are the x,y and z components of the wavevector, k. For comparison, the analytical dispersion relation is given by:

$$\frac{w^2}{c^2} = k_x^2 + k_y^2 + k_z^2 \tag{2.25}$$

for a plane wave in a lossless medium.

In the limit that δx, δy, δz and δt $\rightarrow$ 0, the numerical dispersion relation reduces to the analytical relation [88]. Thus numerical dispersion can be reduced to a reasonable amount by sufficiently decreasing both the time step and unit cell size.

2.2.6.2 Numerical Instability

In order to model the electromagnetic fields accurately it is necessary to consider the effects of sharp changes in both the material and field properties. If this is not taken into account numerical instabilities would be introduced to the stimulation. The use of a sufficiently fine grid size, however, is adequate to combat these problems [82].

Great care must be taken in the modelling of dielectric boundaries in the FDTD technique to ensure that the results remain accurate and to prevent instabilities in the simulation [79]. In order to account for dielectric boundaries in the simulation space it is necessary to modify the basic FDTD algorithm. In the case where the mesh is uniform, it is enough to use the average of the dielectric values across the boundary for the boundary dielectric value. In the case of non uniform grid or a 2 dimensional change in permittivity this is not sufficient and more detailed modifications are necessary [107].

Nadobny *et al* [108] consider the case of a sharp discontinuity in material parameters of a one cell layer or bone equivalent (ϵ_r =5) surrounded by muscle equivalent (ϵ_r =30) in a spherical shell model. For this one dimensional change, comparisons with Bessel function expansions for the same model gives good agreement for each electric field component when the boundary between the media is parallel to one of the principal axes directions.

To model a dielectric boundary accurately it is likely that a greater number of nodes per wavelength, i.e. a smaller grid size, and a smaller time step need be implemented [79]. For reasons of computational efficiency the use of a non-uniform grid is preferred. Thus in regions of smooth field changes a less dense grid can be implemented.

2.2.6.3 Dealing with curved objects

As the general grid shape is orthogonal, straight line objects can be modelled with ease. Unfortunately when curved or sloped shapes are modelled this grid shape can lead to problems. Several techniques have been employed to attempt to solve this problem.

Initially the staircase method was employed. This involves using a fine grid size and replacing a curved line with two orthogonal components. The part of the curved line at 45 degrees to the horizontal is replaced by a horizontal and a vertical line. This solution, however, does require larger computational resources and may lead to spurious reflections at the corners [109]. Additionally non physical resonances may occur near to the inner corners as a result of this technique [89]. Albeit for many situations these problems are not too serious and this is an acceptable solution.

To reduce the computational time and memory requirements for the staircase method many attempts have been made to successfully combine coarse and fine grids. In these approaches the fine grid is only used in the curved regions as in [110] and [111]. Extensions to this idea are discussed in [112] and [113], along with a discussion of some of the problems encountered in its application.

Other techniques include the use of non-orthogonal grids to model curved boundaries. This technique also requires more computational resources but can give better convergence than the original FDTD technique [114]. A saving of computational resources can also be found for this method by combining orthogonal and non-orthogonal grids [115]. A similar idea to this is to reformulate the FDTD algorithm in curvilinear co-ordinates.

The third main approach to this problem is that of conformal mapping. This method allows the grid elements to have an arbitrary shape and can lead to savings in computer resources over orthogonal FDTD with finer grid sizes [109]. The contour path (CP) method [116] is a conformal technique that can be applied to model both curved boundaries and sharp edges and corners. This is a result of the fact that the CP algorithm reduces to the original FDTD algorithm when not in a region close to a curved boundary. The use of unstructured grids makes this method very suitable for complex geometries. A brief description of some other possible conformal techniques can be found in [116].

It is also possible by means of post processing of results obtained from a standard FDTD simulation to correct for the errors resulting from curved / sloped interfaces between different media [108]. This method is of particular interest for hyperthermia applications where the position and orientation of the various biological structures is of vital importance.

Finally a method proposed by Marrocco *et al* [117] allows the subdivision of the cell elements into 8 subvolumes without increasing the computational requirements. This dielectric subgrid resolution (DSR) method allows staircase modelling using a much larger basic grid size than previous techniques to achieve the same accuracy.

2.2.7 Sub-gridding

The solutions to the problem of modelling curved objects rely on a decrease in unit cell size. These finer grids can lead to computational storage problems. As previously discussed a solution to this is found in the combination of rough and course grids and the combination of orthogonal and non-orthogonal grids through subgridding the grid.

Of major importance to this technique is the coupling of the fine and course and the orthogonal and non-orthogonal grids. Away from these boundaries the normal finite difference equations are used. Many time and space interpolation schemes have been developed to advance the fields on the boundaries. Other techniques involve performing two runs of the simulation, the first for the entire coarse grid and the second for a reduced volume fine mesh.

To prevent non physical reflections in the field quantities upon crossing the fine to coarse boundary it is necessary to have a gradual change in cell size. Marrocco and Bardati [89] suggest an upper limit of a 20-40% change in spacing between adjacent cells along with the limit of:

$$\frac{\Delta_{max}}{\Delta_{min}} \leq 15 \tag{2.26}$$

between maximum and minimum grid sizes.

Another issue that must be dealt with is the need to model small regions of fine detail along with large uncomplicated areas. As using a grid fine enough for the detailed region over the entire region would be impractical, subgridding techniques need to be used. The methods previously described for curved surfaces, involving the combination of rough and fine grids, orthogonal and non-orthogonal grids and conformal methods can be applied in this situation.

Again the review paper of Shlager and Schneider [94, 95] provides a fairly exhaustive review of the various gridding methods considered since the invention of FDTD.

2.2.8 Computational Resources

In the FDTD method the computer memory and run time required are directly proportional to the size of the grid. The finer the grid size used the longer the run time and the more computational memory needed. This is a result of the aforementioned stability requirements which link the size of the time step to the grid size.

Several factors can lead to a decrease in the computational requirements. The use of symmetry in the simulation can lead to a significant reduction in the simulation size and thus in the computational requirements. Savings can also be found through the use of supercomputers and with parallel implementations of the algorithm. This is made possible due to the fact that the FDTD calculations are explicit and so can be performed in parallel [75]. If one processor is used the field vectors proceed one point at a time, if p processors are run concurrently then the field vectors proceed p points at a time [88]. For more detailed information on the implementation of Parallel Processing of the FDTD method the reader is referred to [118, 119].

2.2.8.1 Computational Time

The number of time steps needed for the simulation is dependent on the the time step, the unit cell dimensions, the frequency of the incident wave and on the number of periods of oscillation (T) necessary to reach a steady state [43]. Considering a cubic unit cell (of side δ) this is expressed as:

$$No.\,Time\,Steps = No.\,Periods\,Oscillation \times \frac{2c}{f\delta}, \tag{2.27}$$

as T=1/f. Thus lower frequencies take longer to compute even though they may require less periods of oscillation to reach a steady state [43]. In fact for the BEST [3] electromagnetic modeller the number of time steps to steady state is approximated as:

$$T(N) \cong 10\sqrt{3}Nc^{1/3} \tag{2.28}$$

where N is the simulation size.

2.2.8.2 Computational Storage

The amount of computer storage required for the simulation is dependent on N, the number of cells used, and on the number of arrays required to hold the data. Arrays are required to hold the values of E_x, E_y, E_z, H_x, H_y and H_z values at each cell. Additional arrays are required for $\sigma_x, \sigma_y, \sigma_z, \epsilon_x, \epsilon_y$ and ϵ_z if they are needed for the simulation. Depending on the programming and simulation arrays for just σ and ϵ may be sufficient. Arrays may also be needed to store the maximum absolute electric field components found in the final time step.

2.3 Applications of the FDTD method

The FDTD technique has been applied numerous times to the determination of the power deposition in lossy materials from a variety of radiating structures. One of the first examples of its use in this manner was by Taflove in 1975, [42]. He considered the absorption of electromagnetic radiation in models of the human eye at frequencies of 1.5GHz. The main problems with the numerical model were the effects of the staircase approximation of the eyeball and residual wave reflections at the absorbing boundary.

The use of FDTD in bioelectromagnetic problems was further considered by Sullivan *et al* [43] for several simplified cylindrical and spherical muscle / fat structures and then for the more complex case of a human torso irradiated at two frequencies (433MHz, 100MHz). Comparisons for the simple phantoms with analytical models showed excellent agreement with the FDTD predictions further establishing this technique for electromagnetic absorption applications.

The FDTD technique has since been used by Dimbylow for the calculation of the specific absorption rate in initially an anatomically realistic head model [76] and then for the case of a full body model [77]. A large literature has developed around the calculation of the SAR in the head, ear and body in the proximity of mobile telephone antennae structures, including [120, 121, 122, 123, 124, 125].

The FDTD method has also been applied to the determination of power deposition for specific antenna structures designed for hyperthermia treatments. Research on this subject includes the work by Cherry and Iskander [78], Pothecary and Railton [79], Samaras *et al* [80], Martens *et al* [81], Johnson *et al* [82] and recently Hirata *et al* [83].

In the above applications the FDTD method has been used to determine the power deposition patterns for either active applications (hyperthermia treatment) or for safety considerations in the presence of active radiating antennae. The FDTD technique has also been applied extensively in the determination of the power deposited for radiometric temperature sensing applications.

Wu and Neih [44] consider the patterns of power absorption for a TE_{01} waveguide probe in contact with a skin / muscle / fat phantom with an embedded tumour simulating region. Abe *et al* [45] consider the weighting functions obtained with a rectangular waveguide operating at 4 frequencies in a four layer biological phantom. Van Leeuwen *et al* [46] use the FDTD method to determine the weighting functions at the five operating frequencies of their multi-frequency antenna. These weighting functions are then applied in the temperature retrieval inversion process. Hand *et al* [26] and Maruyma *et al* [25] also use the FDTD approach to calculate the weighting functions as part of a temperature retrieval scheme.

The FDTD method continues to be amongst the most popular of the numerical methods applied to the problems of power deposition in biological and/ or lossy dielectrics.

2.4 Validations of FDTD modelling

As with any numerical technique it is necessary to ensure that the acquired results match those of experimental measurement and theoretical predictions. Since its invention the FDTD technique and in particular the programs implementing it have been validated by several means. The most popular of which are through direct comparisons with analytically obtained values for simple configurations [43, 75, 76, 88, 126], with experimentally obtained values [3, 79, 80, 81, 82, 85, 88, 126, 127, 128, 129, 130, 131] and with the results

of other numerical methods [88]. Comparisons with other numerical techniques, however, presents the necessity for the validation of this second technique. In some cases validations are performed by direct comparisons of simulated parameters with the complex impedance of antennae [3] and the reflection coefficient [85]. Taflove [88] found excellent agreement in comparisons of a range of scattering and absorbing bodies by all three means.

Dimbylow and Gandhi [76], and Mason *et al* [126] among others validate their use of FDTD modelling by means of comparison with a Mie series expansion. Both obtain excellent agreement for the SAR calculated in a dielectric sphere exposed to 1800MHz and 1GHz radiation respectively. Taflove [75] also considered the fields in a dielectric sphere phantom and obtained favourable comparisons between FDTD computed values and those of a Stratton series solution [132]. Both methods, Mie and Stratton expansions, involve the use of Bessel functions and are also employed by Sullivan *et al* [43] in a similar validation process.

Although comparisons by means of considering analytical solutions of simplified geometries provides a useful guide to the validity of a numerical technique it is also vital to consider more complex situations. To do this experimental methods that directly or indirectly determine the electric field values must be employed. Direct field measurement is generally performed by the use of an electric field (or equivalent) probe inside a phantom structure. Non-direct measurement can be obtained in the case of the SAR by non-invasive or sectional thermographic imaging of a phantom structure.

Making use of a thermographic camera it is possible to directly measure the specific absorption rate inside a phantom structure after exposure to a set radiation pattern. This is made possible as the SAR (W/kg) at a particular position is given by:

$$SAR = \frac{c\Delta T}{\Delta t} \tag{2.29}$$

where ΔT is the change in temperature, Δt is the exposure duration and c is the specific heat capacity of the phantom material(s).

Validations by this means have been performed by Samaras *et al.* [80] for a Lucite cone applicator for hyperthermia treatments, by Okano *et al.* [129] for SAR in a head model and by Mason *et al.* [126] in the case of a dielectric sphere. Excellent agreement is seen in

the comparisons of Okano *et al.* using this experimental approach. Reasonable agreement is obtained in the case of Samaras *et al* and Mason *et al.* Limitations of this validation method include large uncertainties when absolute SAR is required due to the problem of accurately determining the change in temperature in the presence of thermal diffusion effects and the cost of such an imaging system.

Alternatively relatively non perturbing electric field probes (dipole probes) are often employed to determine the near-field electric field inside various phantom materials and structures. Rine *et al* [131] and De Leeuw *et al.* [127] obtain good agreement between computed and measured relative SAR values making comparisons in this manner. Taylor *et al* [130], also obtain very close agreement between electric field values measured using an electric field probe and those obtained by FDTD modelling of a square RF coil with a saline phantom.

Camart *et al* [85] compare computed power deposition patterns with those measured using both an electric field probe and by measuring the increase in temperature in the phantom material. Good agreement is seen for the patterns of absorbed power deposition normalised by the maximum value in the volume. They further validate the FDTD method by making comparisons of the reflection coefficient with measured values and again obtain good agreement.

The non-resonant perturbation technique has also been applied to find the antenna near-field distribution [7, 79, 82, 133, 134]. In this method a small perturber is introduced into a phantom material and the measured resulting signal reflection is directly related to the SAR. Johnson *et al.* [82] measure the SAR using both a perturber and dipole probe and compare to FDTD values for various hyperthermia applicators and a saline phantom. Both dipole and probe measurements were in good agreement with the FDTD computed values.

In the case of biological tissues and foodstuffs any detectable thermal radiation is generated in the antenna near-field or near to far field regions [7]. In this near-field region the field direction (polarisation) can change rapidly with position which can give rise to large errors with both the modulated scatter and field probe sensing methods which are directionally sensitive [7, 131]. The non-resonant perturbation (NRP) technique, however, can

be employed to give absolute and polarisation independent measurements of field patterns close to an antenna aperture [133].

Further advantages of the NRP method are that it is reasonably simple to apply using relatively simple apparatus, compared with other possible techniques [133]. Additionally, the theory of this technique has been developed to allow its application to a wide range of situations including materials of consistency similar to biological tissue [7, 133]. In this situation high frequency power loss (both radiative and dissipative) in the material close to the perturber is significant. The encouraging results of Land [7, 133, 134] and Johnson *et al.* [82] also make it an appealing experimental method for validation purposes.

Validation of the FDTD modelling is performed here by comparisons with antenna return loss measurements (chapter 3), with the field forms of waveguide structures (chapter 3) and by employing the NRP technique (chapter 4). Earlier validations of BEST by Marrocco and Bardati have focused on comparisons with antenna impedance measurements [3].

2.5 The B.E.S.T. Modelling Tool

An early aim of the research work was to develop new software to run the FDTD simulations. Although initial work was successful, the unexpected availability of a well established program [3] from Bardati and Marrocco, Univerita Rome Tor Vergata, rendered this aim redundant. The Basic Electromagnetic Simulation Tool (BEST) uses the FDTD technique to compute electric and magnetic field propagation in a multitude of situations. The tool comprises a set of predefined shapes (e.g. sphere, circular cylinder, rectangular box, half sphere) which can be combined to model a desired structure. Details of the excitation source and excitation waveform type (e.g. sinusoidal, Gaussian) can also be specified.

Although the program performs all of the required basic functions and a good deal more some additional programming was required to achieve complete weighting function modelling. There are clearly some disadvantages to working with established software in

particular the inability to alter the base programming directly. This necessitates the need for additional post processing of results thus making the process less efficient. The advantages of using a complete finished program, most importantly the fact that it could be put to use immediately outweighed these problems.

The BEST program has since been incorporated into a full bioelectromagnetic program, VBLAB, linking it to the dielectric property models of Gabriel [135] and including fully specified models of infant and adult heads, and full body and head only rat models [136].

2.5.1 Implementation of B.E.S.T

In order to perform a simulation it is necessary for the user to make a script file which includes details of all the desired structures and their corresponding dielectric properties that make up the simulation. The script file also contains details of the excitation source and excitation waveform type and all output data formats required by the user.

Many options for viewing the results of the simulation are possible including one dimensional data or the change in each field component with time (probe data), two dimensional data on a chosen field component across a chosen plane (2D_OUT), and three dimensional data on either a field component or the specific absorption rate (3D_OUT). Data on the current and voltage at a particular location as a function of time can be found through the use of the I_Probe and V_Probe functions which compute Ampere and Faraday's laws respectively. For further details on the use of BEST the reader is referred to Marrocco *et al* [3] and the user manual [89].

2.5.1.1 BEST Field calculation

The instantaneous electric and magnetic field components are calculated and stored at the end of each period (T) of the simulation run. Additional programming allows data to be stored at a time of quarter of a period later. The amplitude of each of the fields can then be calculated as:

$$E(t) = E_o \sin(\omega t) \text{ and } E(t + T/4) = E_o \sin(\omega(t + T/4)) = E_o \cos(\omega t) \tag{2.30}$$

So that:

$$E^2(t) + E^2(t + T/4) = E_o^2(\cos^2(\omega t) + \sin^2(\omega t)) = E_o^2 \tag{2.31}$$

The specific absorption rate (SAR) can then be calculated directly from the electric field components as:

$$SAR = \frac{\sigma}{2}\left(E_{ox}^2 + E_{oy}^2 + E_{oz}^2\right). \tag{2.32}$$

This post processing of the results required an additional computational time of approximately 20 minutes.

2.5.1.2 Accuracy and Errors

An FDTD simulation with sinusoidal excitation ends when all fields achieve steady state variation. In the BEST modeller this is determined by computing the difference in the energy at the excitation frequency between two contiguous periods. The simulation ends when this error, displayed as a percentage, falls below a chosen threshold. The standard error in FDTD simulations is 5% [137], and so in all cases the simulations computed in this work use this limit.

2.5.1.3 Typical simulation sizes

On a personal workstation with 384MB of RAM using the BEST program it is possible to have a grid space of 150*150*150 cells (i.e. greater than one million cells). To fulfil accuracy requirements 10 cells are required per wavelength. This means that for a cubic grid the maximum simulated cube would have a side size of around 15 wavelengths. A simulation of this size takes approximately 8 hours to compute on a Pentium 3, 900MHz personal workstation. Storage space of 25 MB is required for each of the electric field arrays and a further 20 MB for the material parameter array and finally 30MB for the array of SAR values. Once the SAR has been computed the individual electric field and material arrays can be removed.

Chapter 3

Validation 1: Monopole radiator over ground plane; Waveguide field computation.

Modeling validation is performed by direct comparison with structures for which known field and return loss values are available. The forms of the validations used have been determined by the type of coupling systems used for the temperature measurement applications of interest. In general these take the form of dielectrically loaded waveguides with integral broadband coaxial transformers [2].

Validation is performed by three main means: comparison of the form and field impedances of waveguide electric and magnetic fields, investigation of the impedance - frequency behaviour of monopole antennas and experimental determination of the field forms of open waveguide antennas measured using the non-resonant perturbation method.Validation of the waveguide field forms and of the monopole radiator are considered in the present chapter. Validations by means of experimental field measurement are described in detail in the following chapter.

3.1 Experimental validation of monopole probe model

Of prime importance in the validation of computational modeling is investigation of the simulation field source. This source takes the form of a "monopole" radiator above a perfect electrical conductor (PEC) ground plane. It is essential to ensure that the behaviour of the monopole probe is as expected. To this end the variation of several key parameters were investigated: the length of probe to wavelength ratio (l/λ) and the length to probe radius ratio (l/a). Additionally the effect of enclosing the probe in plastic, adding a capacitive tip on the end of the probe and using the probe to source a TE_{01} mode waveguide were considered.

3.1.1 Experimental work to determine power reflection

In all cases a signal (s_1) was fed into the antenna test system giving a reflected signal (s_2) and the power reflection coefficient (s_1/s_2) measured over a frequency range (f_1 to f_2) using a microwave reflectometer system. The measured return loss in dBs could then easily be converted to voltage or power reflection coefficients and directly compared with simulation results. Two main antenna test systems were investigated, that of a probe antenna above a ground metal plate and of a probe coupling in a waveguide structure. (All experimental work in this section performed by D. Land [138].)

3.1.1.1 Probe above ground plate

In the first test case a length of 50Ω coaxial cable was connected to a metal monopole antenna above a metal plate. A layer of microwave absorbing material surrounded the antenna to prevent interference from items around the edge of the finite size ground plate and from the edge of the ground plate itself. This test set up is shown in Figure 3.1.

Experiments were performed with a bare probe of varying lengths and widths, with a probe sheathed in PTFE and with the covered probe with a capacitive top, Figure 3.2.

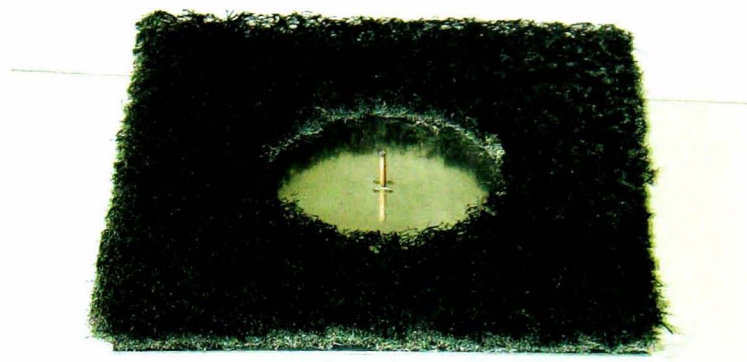

Figure 3.1: *Experimental probe setup featuring the monopole probe in the centre of a metal plate and surrounded by microwave absorbing material.*

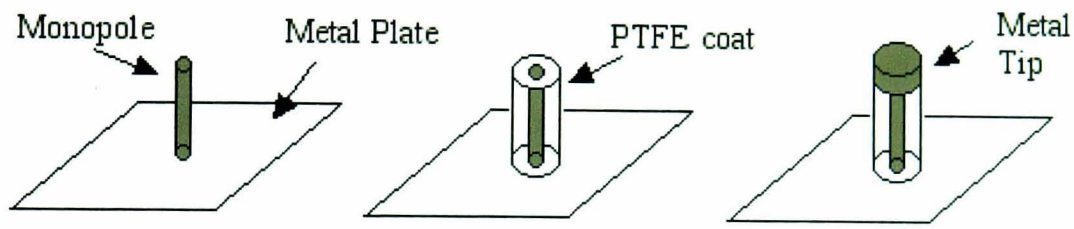

Figure 3.2: *Various experimental probe setups of a bare probe, probe sheathed in PTFE and the covered probe with a metal tip.*

3.1.1.2 Probe in Waveguide

In the second set of measurements the basic probe setup was used as the field source in a TE_{01} mode rectangular waveguide. The basic probe and a modified design, as shown in Figure 3.3, were considered. This modified design involved the inclusion of a brass cylinder, connected to the probe. The monopole and brass cylinder were then covered by a cylinder of PTFE. This PTFE coat extended from the base of the brass to the side of the waveguide and as a result also enclosed an air gap (OmniSpectra coaxial to waveguide transition 201841). In the simulation work the end of the transmitted wave was absorbed by several cells of perfectly matched layer. In the experimental work the waveguide was terminated with a well matched load.

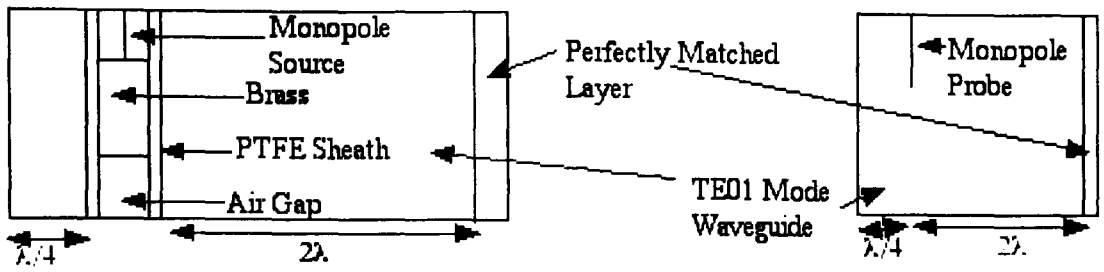

Figure 3.3: *Waveguide probe setups incorporating the bare probe as a the waveguide source. A modified design in which the probe is connected to a brass cylinder and surrounded by a PTFE coat is also considered.*

3.1.2 Simulation of antennae

The BEST electromagnetic modeling program was used to simulate the above antenna systems. In the first set of simulations a monopole source as shown in Figure 3.4 was connected to a ground plate of perfect electric conductor (PEC) material. The metal plate was simulated with a length of at least one wavelength.

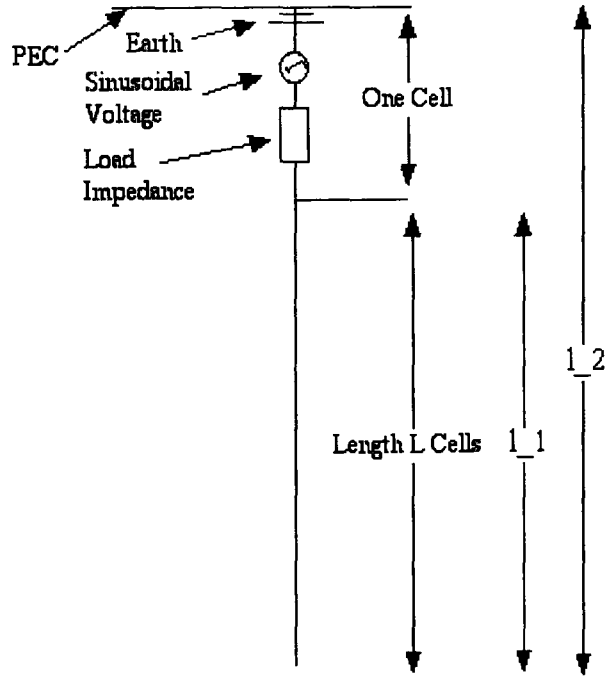

Figure 3.4: *Monopole probe as modelled in the simulation. The load cell of the monopole is that of a sinusoidally varying voltage with a series load resistor. The remaining cells are modelled as PEC of a given radius.*

The edges of the computational domain were modelled with a perfectly matched layer to mimic the experimental free space situation. The monopole probe is modelled as a source cell and a length of PEC. The source cell comprises a sinusoidal voltage generator and series load resistance (voltage and resistance set prior to simulation). The length and radius of the PEC component were varied to match experimental specifications.

For the waveguide transition simulations the probe system was modelled as in Figure 3.3, with the brass component assumed to be PEC. A limitation of the simulation software is the inability to handle real metal conductivity values. Such high conductivity parameters lead to severe instability in the simulation.

For both test systems the simulations were performed over a range of discrete frequencies values from 1.7GHz to 6.4GHz. Additional simulations were performed around the frequencies of rapid return loss variation.

3.1.2.1 Analysis of simulation data

The voltage variation across and the current in the generator cell were calculated at each time step of the simulation. Plots of the current and voltage against time step showed sinusoidally varying curves with the voltage leading the current by phase α. After a time the current and voltage have the forms:

$$I = I_o \sin(\omega t) \text{ and } V = V_o \sin(\omega t + \alpha), \tag{3.1}$$

where I_o and V_o are the amplitude of the current and voltage fields respectively and t is the time point of the simulation. Values of I_0, V_0 and α can be found directly from the current and voltage plots from which the impedance can be calculated as:

$$\mathbf{Z} = \frac{\mathbf{V}}{\mathbf{I}} = \frac{V_o}{I_o} e^{i\alpha} = R_R + iX_a, \tag{3.2}$$

where R_R is the radiation resistance and X_a is the reactance.

In order to compare directly with the experimental results the power reflection coefficient is calculated as:

$$Power\ Reflection = \frac{(R_g - R_R)^2 + X_a^2}{(R_g + R_R)^2 + X_a^2} \tag{3.3}$$

where R_g is the generator cell load which is set at 50Ω in the simulation to equal the experimental case.

3.1.3 Results for Power Reflection

Results for the various systems modelled are given in this section. Experiment and simulation results are compared on plots of power reflection against the length of monopole divided by the wavelength. Two different monopole lengths are used for the length / wavelength axis for the simulation results. The different lengths, l_1 and l_2 as shown on Figure 3.4, correspond to only the PEC rod and to the entire monopole length including the generator cell. In all simulations lengths l_1 and l_2 differ by one cell. The length in the experiment is that of solely the metal probe above ground. Simulations are performed with the metal rod of length equal to that of the experimental length.

3.1.3.1 Length to radius ratio varying simulations

Results for monopole length to radius ratio's (l/a) of 40 and 29.3 are shown in Figure 3.5. In both cases the results of the simulation match closely the experimental data when the length used is l_2 as defined above.

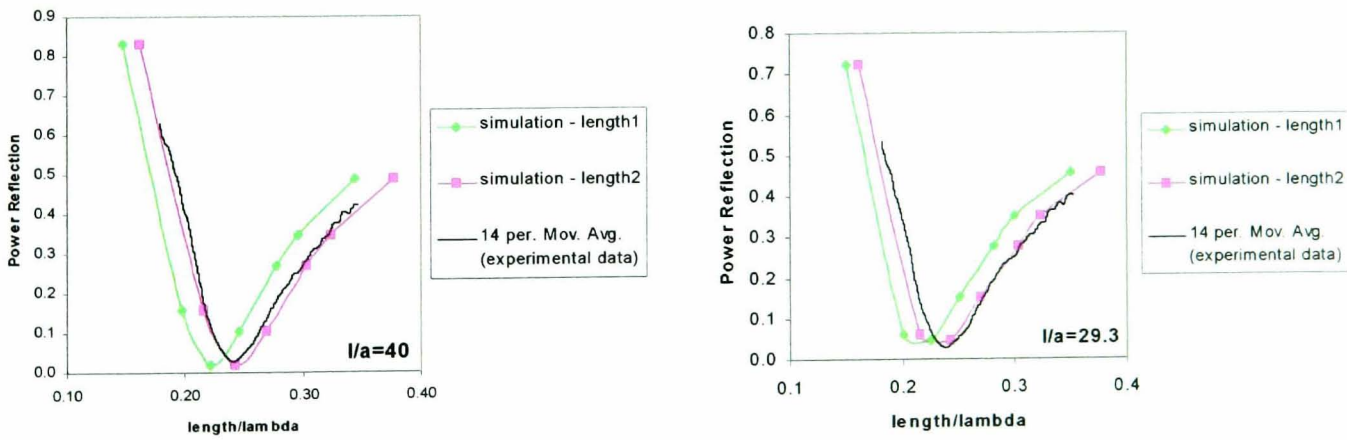

Figure 3.5: *Results for the power reflection of monopole antenna's with length to radius (l/a) ratio's of 40 and 29*

For a length to radius ratio of 13 the simulation results show the same shape as the experimental data but with a small offset, Figure 3.6. It would appear that at this length to radius ratio either the simulation begins to reach the limits of accuracy or the model is not as close a match to the experimental work as needed. In the experimental work a small ring of PTFE is placed around the monopole at the base plate connection. Inclusion of this ring in the simulation does not produce significantly different results (included on Figure 3.6).

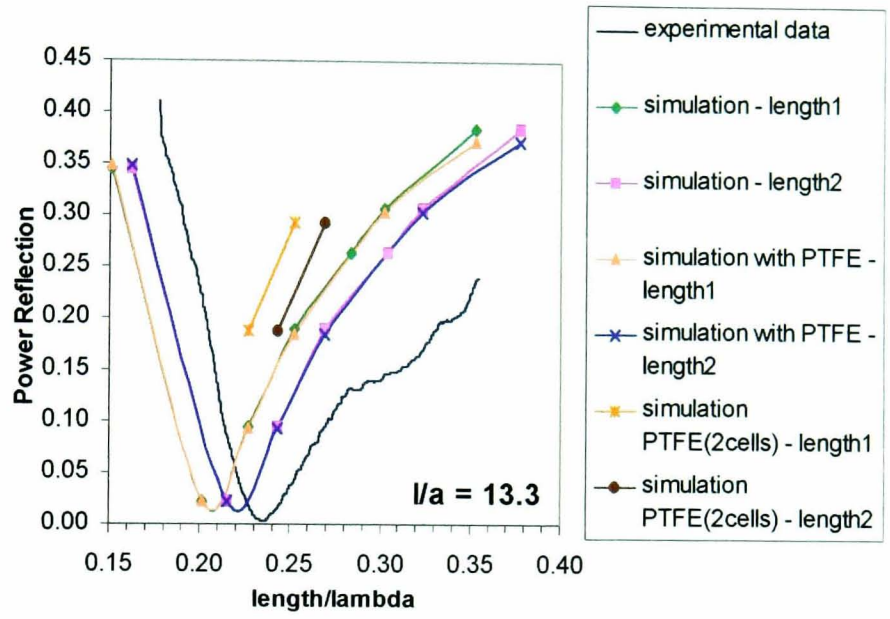

Figure 3.6: *Power reflection results for a monopole length to radius ratio of 13 showing the offset in experimental and simulation data. The limited effect of the additional ring of PTFE in the simulation can also be seen.*

In the experiment the monopole is not in direct contact with the ground plate. In the simulation the monopole must connect with the ground plate to avoid instability, thus exact matching of the experimental conditions is not achieved. In the simulation the PTFE ring is around the monopole above the plate as the plate is needed to ground the monopole. In the experiment this ring is embedded in the ground plate, resulting in a small difference in the probe to ground capacitance. Even with this small difference in simulated and experimental results the simulated model is considered to be a good match to the experimental data.

3.1.3.2 Modified monopole results

For the test system of a monopole probe, length to radius ratio 25.85, with a PTFE coating the experiment and simulated data match well, as shown in Figure 3.7.

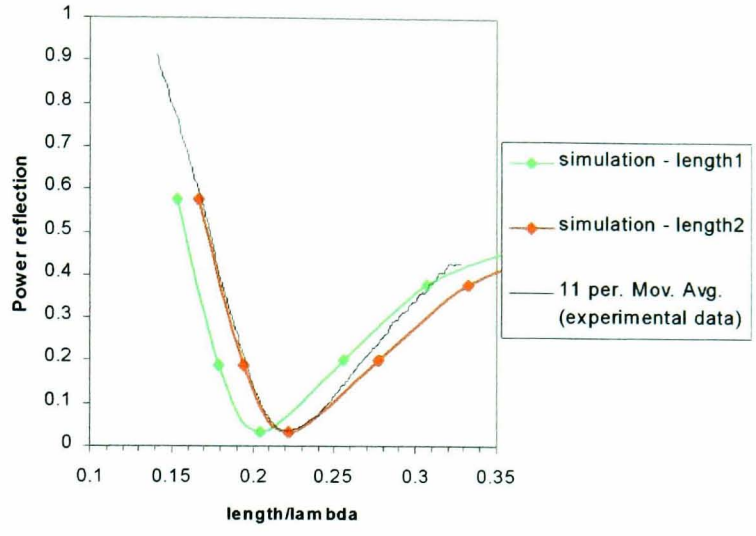

Figure 3.7: *Power reflection results for probe (l/a=25.85) with PTFE covering showing good agreement between simulation and experimental results.*

For the final test in this series a small metal tip is added to the probe just described (with PTFE coat and l/a=25.85). This adds a small capacitive loading to the probe which has been found experimentally to improve the matching, i.e. reduce the return loss, at the operating frequency of the probe. The physical length of this top is such that it falls at a half number of simulation cells. In order to compare accurately with experiment it was necessary to perform these simulations twice with the two top sizes. Again the results compare well with the best matching coming from the averaged values of two simulation runs, see Figure 3.8.

3.1.3.3 Probe sourcing TE_{01} mode waveguide

As previously mentioned for this test system two probe designs are considered. In each case the length to radius ratio for the probe is 26.3. In the case of the simple probe the simulated power reflection shows a similar broad band minimum pattern but is consider-

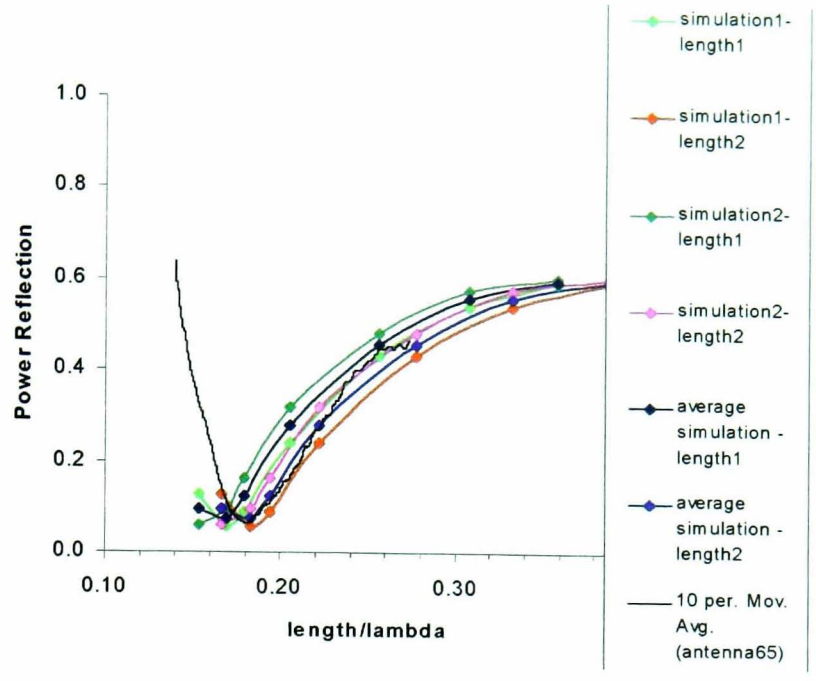

Figure 3.8: *Power reflection results for probe (l/a=25.85) with PTFE covering and metal tip. Best agreement is seen for the average of the two simulation runs.*

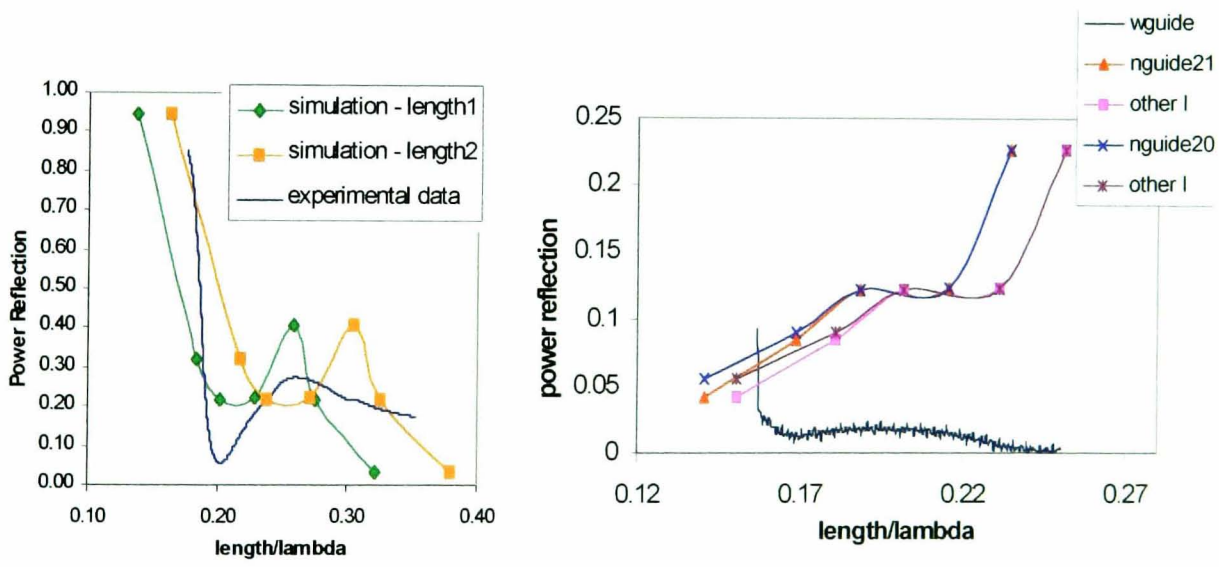

Figure 3.9: *Power reflection results for monopole exciting a waveguide structure in both simple and complex configurations.*

ably smaller in magnitude, see Figure 3.9. In the more complex probe case the patterns of results are relatively similar. In this case the best match occurs when length l_1 (see Figure 3.4) is used. These differences may be due to a number of factors: errors in calculation of V_o, I_o or α, or more likely limits to the simulation accuracy.

3.1.4 Calculation and comparison of impedance results

As part of the calculation of the power reflection of the ground plane monopole antennas the resistance and reactance of each antenna configuration has been computed. Direct comparisons of these quantities can be made with published work. In the first instance for a fixed monopole length to radius ratio (l/a) the complex impedance values over a range of frequencies are considered. This frequency variation is specified by the ratio of the antenna length to wavelength (l/λ). In the second case the monopole radius to wavelength ratio (a/λ) is fixed and the length of the monopole varies.

At zero frequency all impedance curves start at resistance equal to 0 and reactance equal to infinity [5]. As the frequency (length) increases the resistance and reactance increase, passing through the first resonance (zero reactance) at a length approximately equal to $\lambda/4$. As the frequency (length) increases further the resistance continues to increase while the reactance increases to a maximum and then decreases passing through zero at the second resonance where the monopole length is approximately equal to $\lambda/2$. The cycle continues through the third ($l \approx 3\lambda/4$) and fourth resonances ($l \approx \lambda$).

Comparisons are made for a fixed monopole length to radius ratio of 60 with those measured by Dorne and computed by Hallen [5] in Figure 3.10. The curves of Dorne and Hallen are considered to be in good agreement with each other given experimental difficulties. The simulated results compare favourably with these results over the frequency range considered. In Figure 3.11, the impedance curve for a fixed monopole radius to wavelength ratio of 0.0053 is compared to the computed values of King [6] for a ratio of 0.0064. Again very close agreement is seen between the simulated and published results.

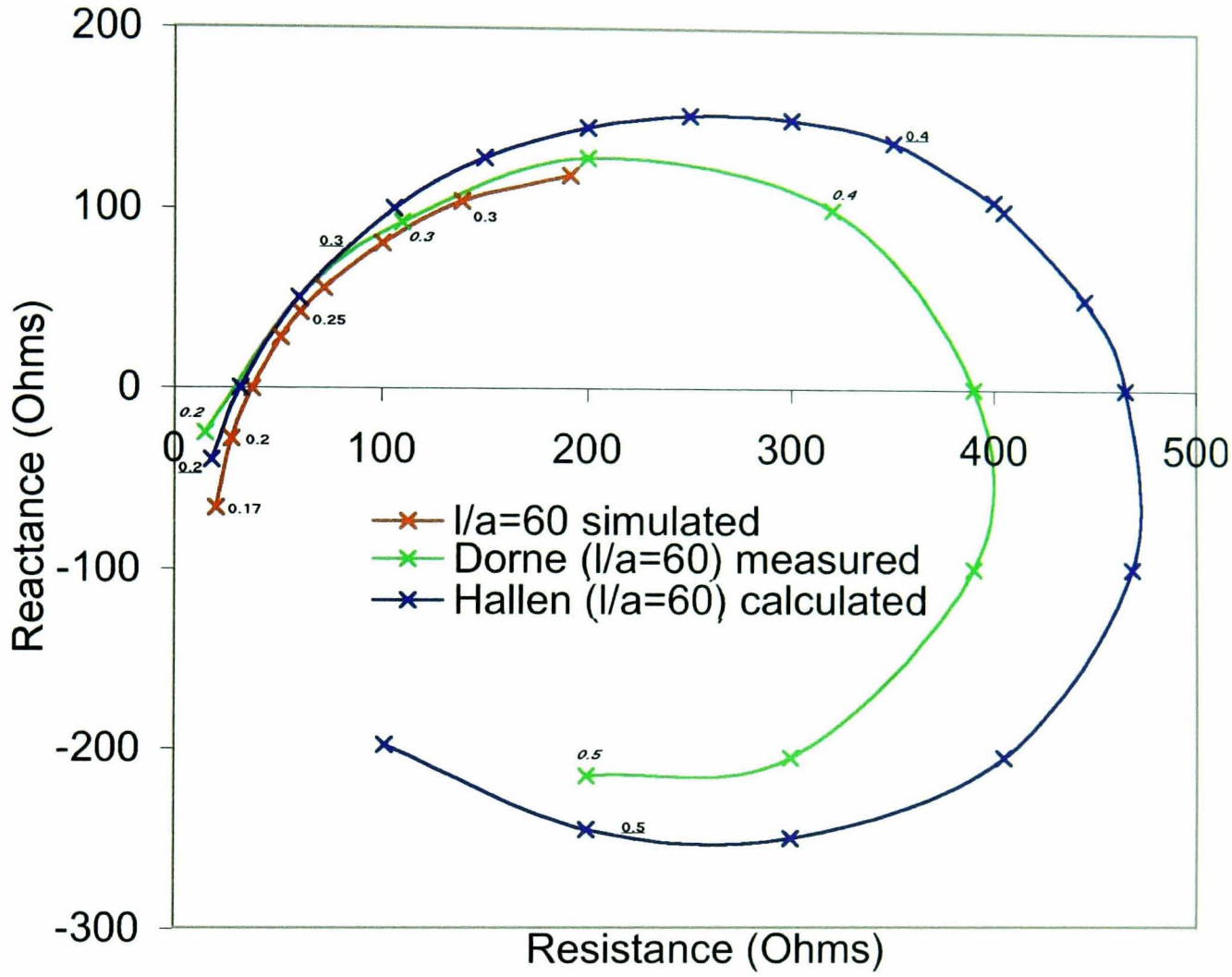

Figure 3.10: *Comparison of simulated impedance results with those measured by Dorne and computed by Hallen [5]. Length to wavelength ratio values are included on the plot in italic (Dorne), underlined (Hallen) and standard (simulated) text.*

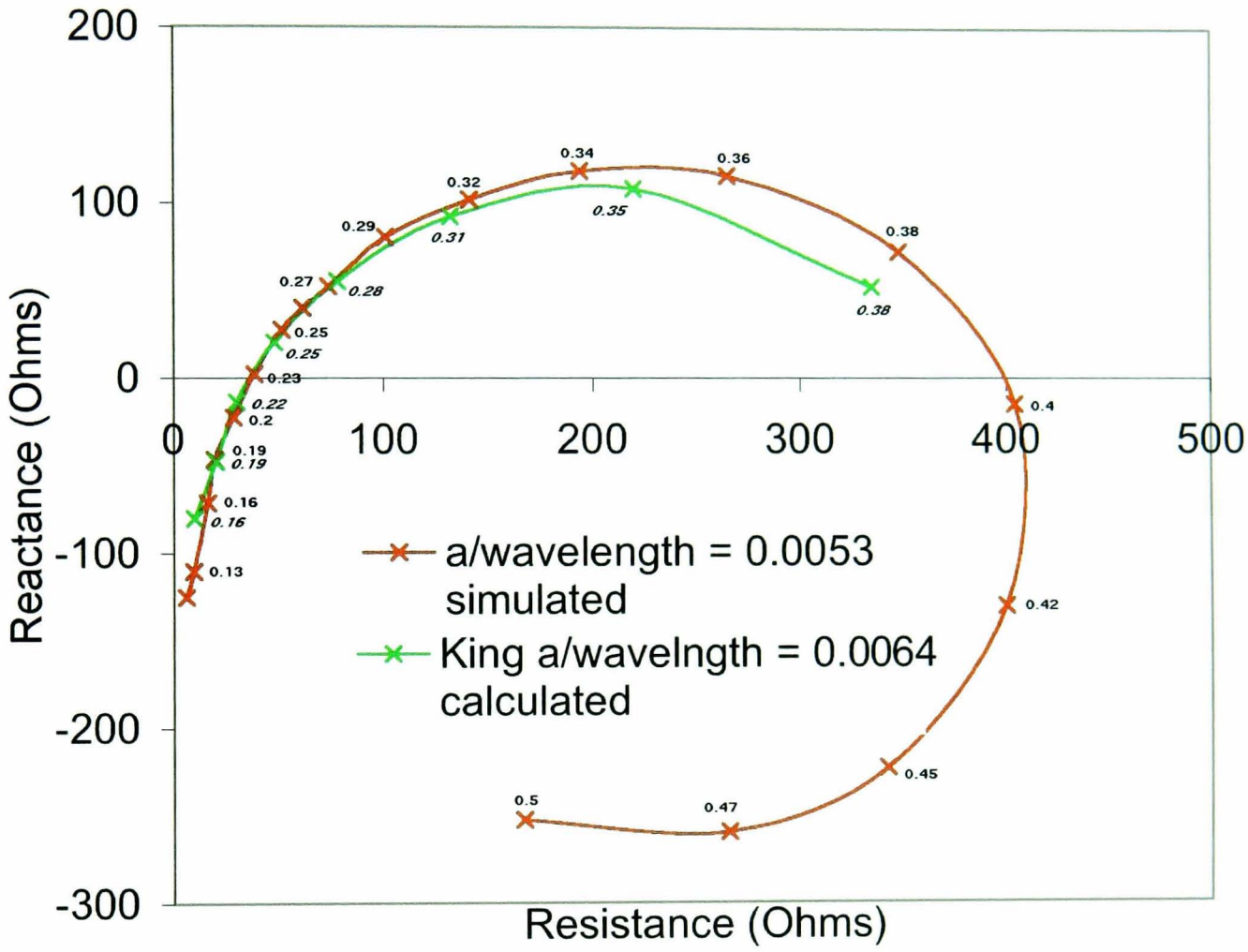

Figure 3.11: *Comparison of simulated impedance results with those computed by King [6]. Length to wavelength ratio values are included on the plot in italic (King) and standard (simulated) text.*

3.2 Validation of BEST field computation

The next important check of the modeling software is to ensure that the fields in a known size and excitation mode of a waveguide match theoretical predictions. It is also of interest to consider the power distribution in a waveguide structure to ensure the accuracy of the SAR calculation.

3.2.1 TE_{01} mode waveguide

The electric and magnetic field forms for a TE_{01} mode waveguide are well known and are given by Maxwell's equations as:

$$E_{x0} = -\frac{i\omega\mu B \sin(k_y y)}{k_y}, \qquad E_{yo} = 0, \qquad E_{zo} = 0 \tag{3.4}$$

$$H_{xo} = 0, \qquad H_{yo} = \frac{i\beta B sin(k_y y)}{k_y}, \qquad H_{zo} = B\cos(k_y y). \tag{3.5}$$

Where B is a constant, a and b are the x and y dimensions of the waveguide (z is the axis of propagation), k_y=π/a is the wave number, ω is the angular frequency, μ is the permeability and β is the phase constant. Additionally the electric and magnetic fields are related by:

$$E_x = -Z_{TE} H_y \tag{3.6}$$

where Z_{TE} is the transverse electric field guide impedance.

The power flow along the waveguide, from the Poynting Vector is:

$$Waveguide\ Power\ Flow = \frac{1}{2}\int_{a,b} -E_x H_y^* dx.dy \tag{3.7}$$

Making use of equation 3.6 and substituting for the wave number (k_y=π/a) and electric field amplitude E_{xo}:

$$Waveguide\ Power\ Flow = \frac{1}{2}\int_{a,b} \frac{E_{xo}^2 sin^2(\frac{\pi y}{a}))}{Z_{TE}} dx.dy \tag{3.8}$$

$$= \frac{E_{xo}^2 ab}{4Z_{TE}} \tag{3.9}$$

$$= -\frac{H_{yo}^2 ab Z_{TE}}{4}. \tag{3.10}$$

From a simulation of a rectangular waveguide (of cross section 72mm x 34mm) the power flow along the guide can be determined from the application of equations 3.6 and 3.10. The guide is modelled with source excitation of a simple monopole of length $\lambda_g/4$ and at a distance of $\lambda_g/4$ from the waveguide closed end. The open end of the waveguide ($\geq 2\lambda_g$ from the source) is modelled with 10 cells of perfectly matched layer to mimic free space. The generator cell has load impedance of 50Ω and input voltage of 1V.

The power along the waveguide is calculated from Equation 3.10 where H_{yo} is the magnetic field amplitude as determined by the simulation. The power flow along the guide was found to be 1.8mW. As a check of this value the power input to the guide at the monopole source is determined from the current and voltage probes. The input power was 1.97mW, larger than the power flow along the guide as expected. Using this value of power flow predictions as to the field variation of the non-zero field components can be determined. Comparisons of the non zero electric and magnetic field components, figures 3.12 and 3.13, show good agreement between simulation and experiment. The electric and magnetic fields are shown for positions of positive field variation along the guide.

The maximum relative error as seen in each non zero component and the maximum deviation from zero of the zero components along the guide is given in Table 3.1. For the non zero components the field values in a section of the waveguide approximately two wavelengths long were considered and the largest deviations from zero noted. The section was chosen at a distance of approximately 4λ from the source and 2λ from the PML. For the zero field components it was not possible to calculate a relative error. In this case the maximum value of these components (over the same region as before) was noted and is given in Table 3.1 as the maximum deviation from the expected zero value.

Finally it was also possible to determine from the magnitude of the E_x and H_y fields a value for the guide impedance Z_{TE}. This value can be compared to the simulation independent value:

$$Z_{TE} = Z_o \frac{\lambda_g}{\lambda_o}. \tag{3.11}$$

where Z_o is the free space impedance (377Ω), λ_o is the free space wavelength and λ_g is the guide wavelength.

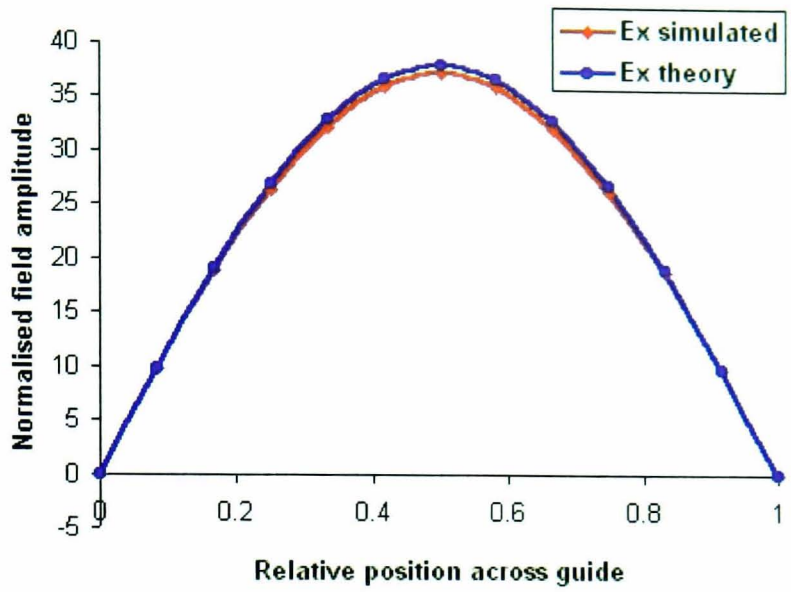

Figure 3.12: *Comparison of simulation results with theoretical predictions for the non-zero electric field components of a* TE_{01} *waveguide.*

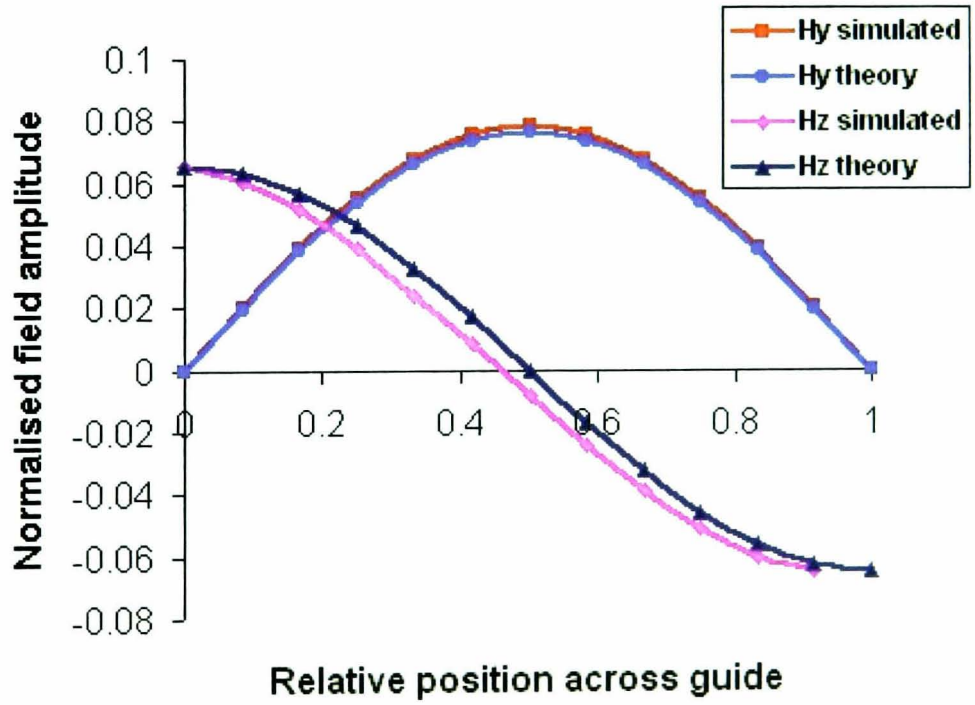

Figure 3.13: *Comparison of simulation results with theoretical predictions for the non-zero magnetic field components of a* TE_{01} *waveguide.*

Component amplitude	Maximum relative error	Max deviation from zero
E_{xo}	0.025	-
E_{yo}	-	0.74 (Vm^{-1})
E_{zo}	-	0.42 (Vm^{-1})
H_{xo}	-	5.3e-5 (Am^{-1})
H_{yo}	0.033	-
H_{zo}	1.0	-
H_{zo} (new length)	0.11	-
Z_{TE}	0.037	-

Table 3.1: *Relative error values for the non-zero field components and guide impedance, maximum deviation from zero for the zero field components.*

From Table 3.1 all components are very close to their theoretically predicted values except for H_z. Possible reasons for this are a simulation artifact which sets all field components to zero on the guide walls. This effectively shortens the guide dimension and in the case of the H_z component has a notable effect. Correcting the theoretical prediction for this shorted width leads a more accurate match as shown in Figure 3.14.

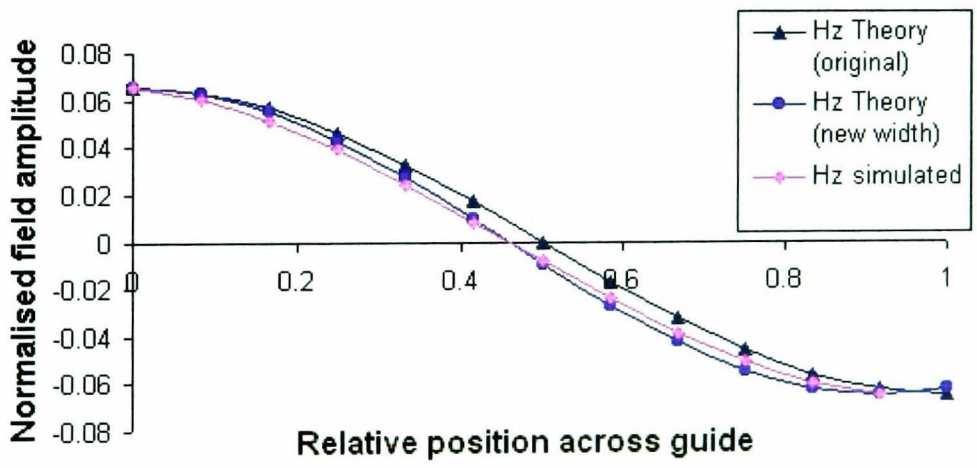

Figure 3.14: *Comparison of simulation result of the H_z magnetic field component of a TE_{01} waveguide with original and modified theoretical predictions.*

3.2.2 Power distribution in a TE_{01} mode waveguide

Two simulations were performed to determine the spatial location of all the power in the waveguide system. The first simulation was of a basic monopole probe, as in Figure 3.4. sourcing a TE_{01} mode waveguide with the power absorbed by a perfectly matched layer after a distance of greater than two wavelengths. In the second simulation the power is absorbed by a wedge of absorbing material, shown schematically in Figure 3.15. The power dissipated in the absorber can be found only in the second simulation.

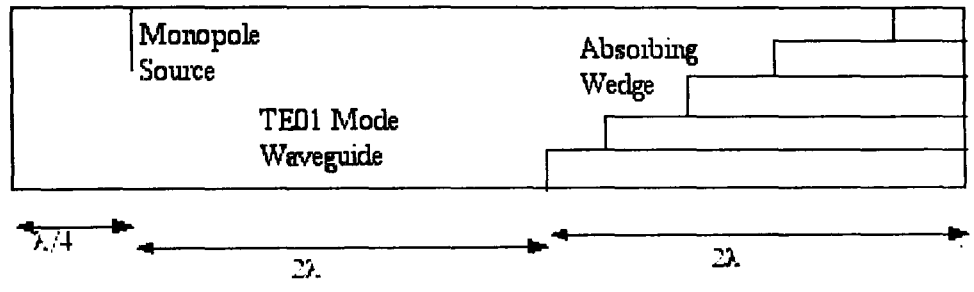

Figure 3.15: *TE_{01} mode waveguide terminated by wedge of absorbing material.*

The (average instantaneous) generated power can be found in a number of ways, two such methods are:

$$Power1 = \frac{\sum_i I_i V_i}{N} \qquad \text{and} \qquad Power2 = \frac{1}{2} V_o I_o \cos\alpha. \tag{3.12}$$

where N is the total number of data points recorded, I is the current in the generator cell and V is the voltage across the generator cell. A comparison of these methods for many different simulation test systems shows that the variation in values is extremely small, see figures 3.16, 3.17 and 3.18 for bare monopole, PTFE sheathed monopole and waveguide antenna configurations respectively. Method 1 is more simple to calculate and includes data from the initial transients in the current and voltage fields. Thus method 1 was chosen as the preferred method for this analysis.

The value of source power is taken as 100% of the total power and is found as:

$$Source\ Power = \frac{1}{2} V_g I_g \cos(\alpha) \tag{3.13}$$

where I_g is the current through the generator cell and V_g is the voltage across the source only.

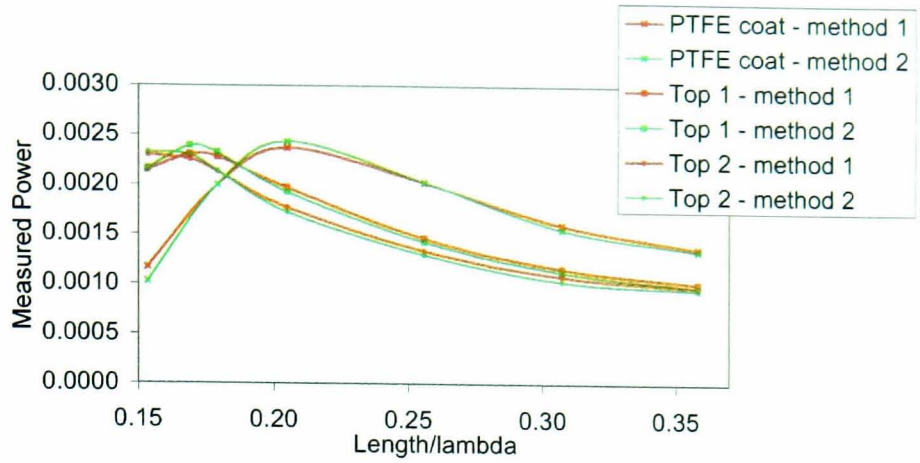

Figure 3.16: *Comparison of methods of computing the generated power for the modified monopole simulations.*

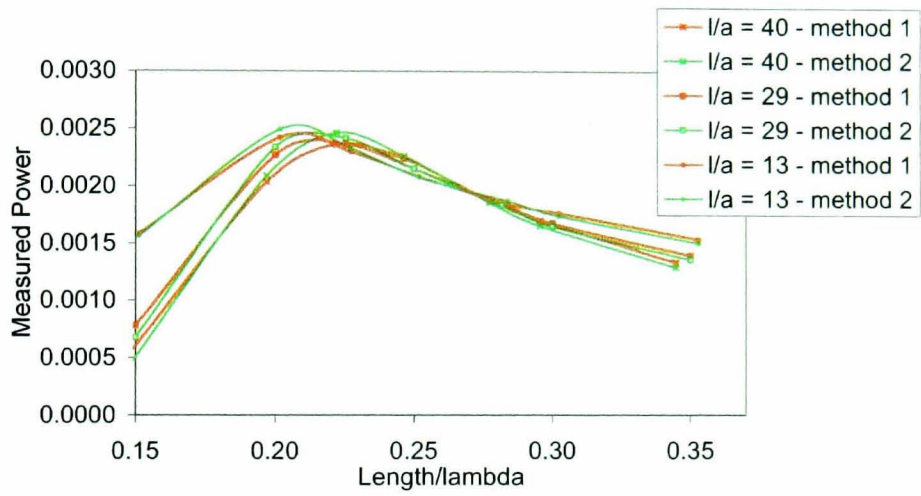

Figure 3.17: *Comparison of methods of computing the generated power for the simple monopole configurations.*

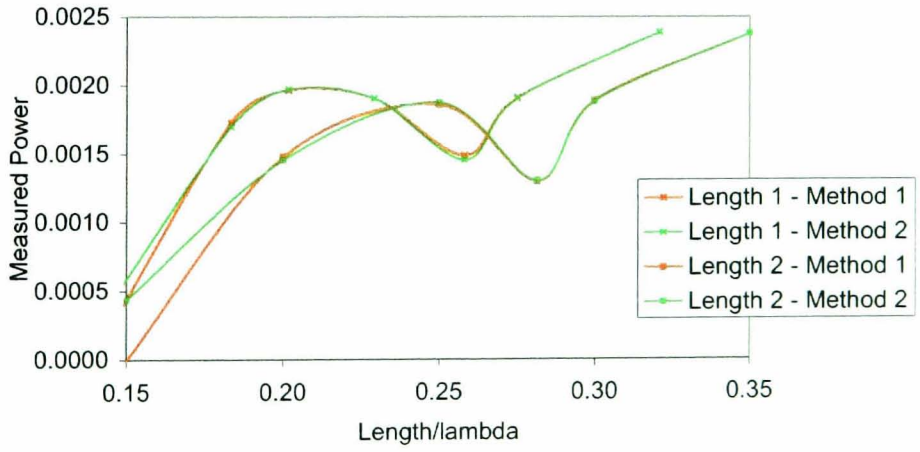

Figure 3.18: *Comparison of methods of computing the generated power for the waveguide simulations.*

As the voltage can only be measured across a complete cell of the simulation space it is not possible to measure V_g directly. It is possible, however, to simply consider the source power as equal to the sum of the generated power and the generator loss.

The amount of power dissipated in the load resistor (generally set to be 50 Ω) is calculated as:

$$Generator\ Loss = \frac{1}{2} I_g^2 R_g \tag{3.14}$$

The power flow along the waveguide is found using the Poynting Vector (Equation 3.10), as before. Finally the power absorbed in the absorbing wedge is calculated as:

$$Load\ Dissipation = \int_{volload} \frac{1}{2} \sigma E^2 dx.dy.dz \tag{3.15}$$

The distribution of power along the waveguide for both absorbing conditions is displayed in table 3.2. The smaller value of power along the guide for the wedge absorber as opposed to the PML can be accounted for by increased reflections at the guide end. For these simulations the power distribution can clearly be accurately localised and accounted for.

	PML absorber % Power	Wedge absorber % Power
Source power	100	100
Generator loss	31	31
Output power	69	69
Power along guide	69	66
Absorbed power		66

Table 3.2: *Power distribution along a TE_{01} mode waveguide terminated by a wedge absorber and using a 10 cell PML.*

3.3 Conclusions

Computational modeling of various configurations of monopole radiator above a ground plate have been successfully validated by means of comparison with return loss measurements. Further to this comparisons of simulations of this monopole probe sourcing a TE_{01} mode waveguide with experimental return loss values showed reasonable similarity. Additional validation of the monopole model was achieved through comparison of simulated impedance values with those of published literature. For both a fixed monopole length to radius ratio across a range of frequencies and for a fixed monopole radius to wavelength ratio over a range of monopole lengths the simulated values were in close agreement to the work of Dorne and Hallen [5] and King [6] respectively.

Investigation of the electromagnetic field forms in a TE_{01} mode waveguide showed good agreement for all field components with theoretical predictions. Additionally the simulation independent value of guide impedance again compared well with the expected value. Finally it has been shown that the distribution of power in the waveguide (input power, power flow along the guide and absorbed power) can be determined.

Chapter 4

Validation 2: TE_{11} mode cylindrical antenna coupled to simulation media

The coupled field zone directly in front of the antenna aperture provides the major contribution to the weighting function and it is essential that this near field region is modelled accurately. This is tested in the final and most indepth method of validation and involves the use of an experimental field sensing technique. This technique, non-resonant perturbation (NRP)[134], is used to determine the variation of the electric field in a variety of simulation materials when coupled to an actively excited waveguide. Direct comparisons with simulated results of the same material system are then made.

4.1 Non-resonant field perturbation theory

The basis of this technique, developed by Land [7] after Steele [139], is to find the change in the field reflection coefficient upon introduction of a perturber at a specific location in the antenna field of view. The Lorentz reciprocity theorem is applied to the measurement region in the presence and absence of a perturber as:

$$\int_s (\mathbf{E}_1 \times \mathbf{H}_2 - \mathbf{E}_2 \times \mathbf{H}_1).d\mathbf{S} = 0 \tag{4.1}$$

Where $\mathbf{E}_1$ and $\mathbf{H}_1$ exist in the absence of a perturber, $\mathbf{E}_2$ and $\mathbf{H}_2$ exist in the presence of a perturber, and $\mathbf{S}$ is a surface enclosing the entire region. The surface S is composed of three distinct surfaces, S_1 - the input port through which power enters the system and at which the reflection coefficient is measured, S_2 - the surface surrounding the remaining measurement region and S_3 a surface surrounding the perturbing object [7]. These three surfaces are shown in Figure 4.1. As $S=S_1+S_2+S_3$ equation 4.1 can be evaluated on each surface in turn and the results added linearly.

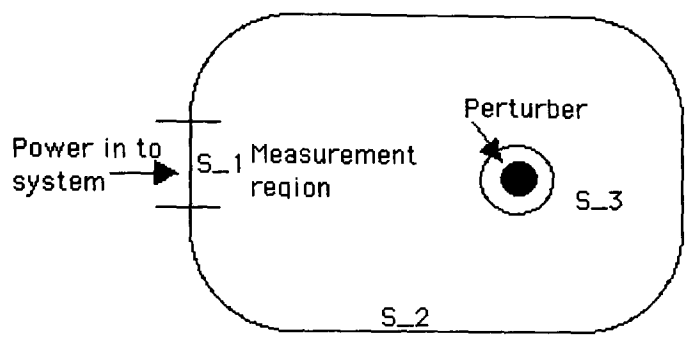

Figure 4.1: *The three surfaces of application of the Lorentz reciprocity theorem for the non resonant perturbation technique. Reproduced from [7].*

4.1.1 Surface S_1

The surface S_1 is generally defined to be normal to the axis of the guiding wave structure in which the fields of the waves entering and reflected from the region are well defined and of the same mode. For Γ_1 and Γ_2 being the field reflection coefficients in the presence and absence of a perturbing object the fields are given as [7]:

$$E_1 = (1+\Gamma_1)E_{1i} \qquad H_1 = (1-\Gamma_1)H_{1i} \tag{4.2}$$

$$E_2 = (1+\Gamma_2)E_{2i} \qquad H_2 = (1-\Gamma_2)H_{2i} \tag{4.3}$$

where i denotes the incident wave fields.

For harmonic waves the time averaged Poynting vector gives the input power through surface S_1 in the presence and absence of the perturber as:

$$W_{1i} = \int_{S_1} \frac{1}{2} E_{1i} H_{1i} dS \qquad W_{2i} = \int_{S_1} \frac{1}{2} E_{2i} H_{2i} dS. \tag{4.4}$$

The power input to the system is kept constant so that W_{1i}=W_{2i}. Noting that for constant impedance $E_{1i}/H_{1i} = Z = E_{2i}/H_{2i}$ and as surface S_1 is oppositely directed to the incident wave the contribution to the surface integral from surface S_1 is:

$$4(\Gamma_2 - \Gamma_1)W_{1i} = 4\Delta\Gamma W_{1i}. \tag{4.5}$$

4.1.2 Surface S_2

The surface S_2 is defined such that there is no contribution to the integral over this surface [7]. Open regions of the surface are assumed to be at a large distance from the measurement region so that the fields at surface S_2 are plane waves normal to the surface and thus contribute zero to the integral. For the case of absorbing or conducting parts of the surface it can be assumed that the waves will be attenuated rapidly with distance. Essentially if surface S_2 is stationary throughout the measurement process there can be no effect on the measured reflection coefficient [138].

4.1.3 Surface S_3

For the third surface, over the perturbing object, the surface integral is transformed to the volume integral over the volume (v) enclosed by the surface. Applying Maxwell's equations to harmonic fields of angular frequency ω gives the contribution to the surface integral as [134]:

$$[i\omega(\epsilon_p - \epsilon) - \sigma] \int_v (E_1 \cdot E_2)dv + i\omega(\mu_p - \mu) \int_v (H_1 \cdot H_2)dv + \int_v (E_1 \cdot J_p)dv \tag{4.6}$$

where μ, ϵ and σ are the permittivity, permeability and conductivity of the medium external to the perturber, μ_p and ϵ_p are the permittivity and permeability of the perturber and J_p is the current density in the perturber.

For a general perturber, interaction occurs with both the electric and magnetic fields. In the particular case of a dielectric perturber interaction will occur with only the electric field. For the case of SAR measurements and validation of power deposition patterns,

only the electric field need be determined as detailed by Land [133]. For this reason only the electric field terms will be considered further so that the contribution to the integral to be considered is:

$$[i\omega(\epsilon_p - \epsilon) - \sigma] \int_v (E_1 \cdot E_2) dv \tag{4.7}$$

assuming the perturber to have negligible loss.

4.1.4 Complete surface integral

The Lorentz reciprocity theorem (equation 4.1) then gives:

$$[i\omega(\epsilon_p - \epsilon) - \sigma] \int_v (E_1 \cdot E_2) dv + 4\Delta\Gamma W_i = 0 \tag{4.8}$$

So that the change in reflection coefficient is given by:

$$\Delta\Gamma = -\frac{1}{4W_i}[i\omega(\epsilon_p - \epsilon) - \sigma] \int_v (E_1 \cdot E_2) dv. \tag{4.9}$$

It is further assumed that the dimensions of the perturber are small compared with the wavelength of the fields in the measurement region so that the fields (E_1 and H_1) can be taken as constant over the perturber volume. For a spherical perturber of radius a, application of this quasi-static approximation gives [133]:

$$E_2 = \frac{3\epsilon'}{\epsilon_p + 2\epsilon'} E_1. \tag{4.10}$$

where ϵ' is the real part of the permittivity of the external medium and ϵ_p is the perturber permittivity. The quasi-static approximation is to consider the lowest order wave to be TEM so that the distribution of the fields in the transverse plane is similar to those for static fields [28]. The reflection coefficient is then directly related to the square of the electric field as:

$$\Delta\Gamma = \frac{\pi a^3 \epsilon'}{(\epsilon_p + 2\epsilon')}[i\omega(\epsilon' - \epsilon'_p) + (\omega\epsilon + \sigma'')]\frac{E_1^2}{W_i} \tag{4.11}$$

where the perturber is assumed to have negligible loss.

This reflection coefficient has both real (giving field amplitude information) and imaginary (giving field phase information) components as the presence of the perturber changes both the energy stored and the power dissipated in the volume occupied by the perturber [7].

A change in the relative permittivity value represents a change in the stored energy and a change in the loss factor or conductivity represents a change in the dissipated power.

4.1.5 Weighting function measurement

The specific absorption rate (SAR) which is equivalent to the weighting function, as discussed in chapter 1, is given by:

$$SAR = \frac{1}{2}(\omega\epsilon'' + \sigma)\frac{E_1^2}{W_i} = \frac{1}{2}(\omega\epsilon_e'')\frac{E_1^2}{W_i}. \tag{4.12}$$

where ϵ_e'' is an effective loss containing all material loss contributions.

The magnitude of the reflection coefficient can then by related directly to the SAR as:

$$|\Delta\Gamma| = \frac{\pi a^3 \epsilon'}{(\epsilon_p + 2\epsilon')}[\omega^2(\epsilon' - \epsilon_P)^2 + \omega^2\epsilon_e''^2]^{\frac{1}{2}}\frac{E_1^2}{W_i} \tag{4.13}$$

i.e.

$$SAR = \frac{2 + \frac{\epsilon_p}{\epsilon'}}{\left[1 + \left(\frac{\epsilon' - \epsilon_p}{\epsilon_e''}\right)\right]^{\frac{1}{2}}}\frac{|\Delta\Gamma|}{2\pi a^3} \tag{4.14}$$

Thus by measuring the field refection coefficient in response to a small spherical dielectric perturber it is possible to directly determine the pattern of power dissipation in a phantom material.

4.2 NRP - Experimental technique

The NRP experimental set-up consists of a microwave source at approximately 3.2GHz (can be varied) which enters the system as shown in Figure 4.2. At the Magic-T device the signal divides with half going to the measurement end and half to the calibration end. On route to the measurement end the signal passes through a four screw tuner.

The signal is then transmitted through the antenna to the phantom material. After interaction with the phantom region the reflected signal passes back through the waveguide

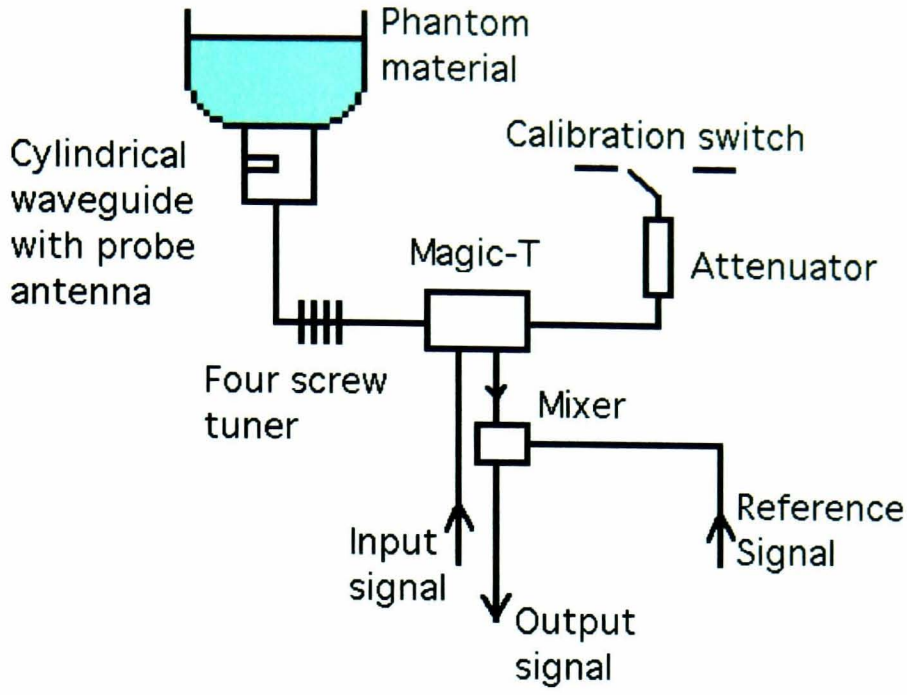

Figure 4.2: *Schematic of the experimental layout of the NRP experiment.*

and 4-screw tuner to the Magic-T and then to a hetrodyne mixer. The four screw tuner is used to cancel out any reflection effect seen without the perturber present (i.e. set Γ_1 to zero). Using four screws ($\lambda/8$ apart) allows matching of the reflection magnitude at any phase (0-360°). In the presence of a pertubing object the remaining reflected signal is mixed with a reference signal of 3.200003GHz to allow linear amplification of the signal at 3kHz. The change in reflection coefficient magnitude and phase of this reflected signal are then sent to the appropriate meters and on to the computer for analysis.

At the calibration arm end is a switch between a 100% matched load and 100% reflection condition. Prior to reaching this switch the signal must pass through an attenuator of known attenuation. In the matched load position there is no reflection and this is the position used for taking measurements. With Γ_1 set to zero (using the 4-screw tuner) and the perturber out of the measurement volume when this switch is set to the short circuit position a known reflection coefficient is displayed. This allows calibration of the measured reflection coefficients.

The apparatus of the non-resonant perturbation experiment is shown in figures 4.3 and 4.4. Figure 4.3 shows the signal generators, waveguide components, magic-T, meters and the phantom apparatus. A more detailed view of the test structure is seen in Figure 4.4.

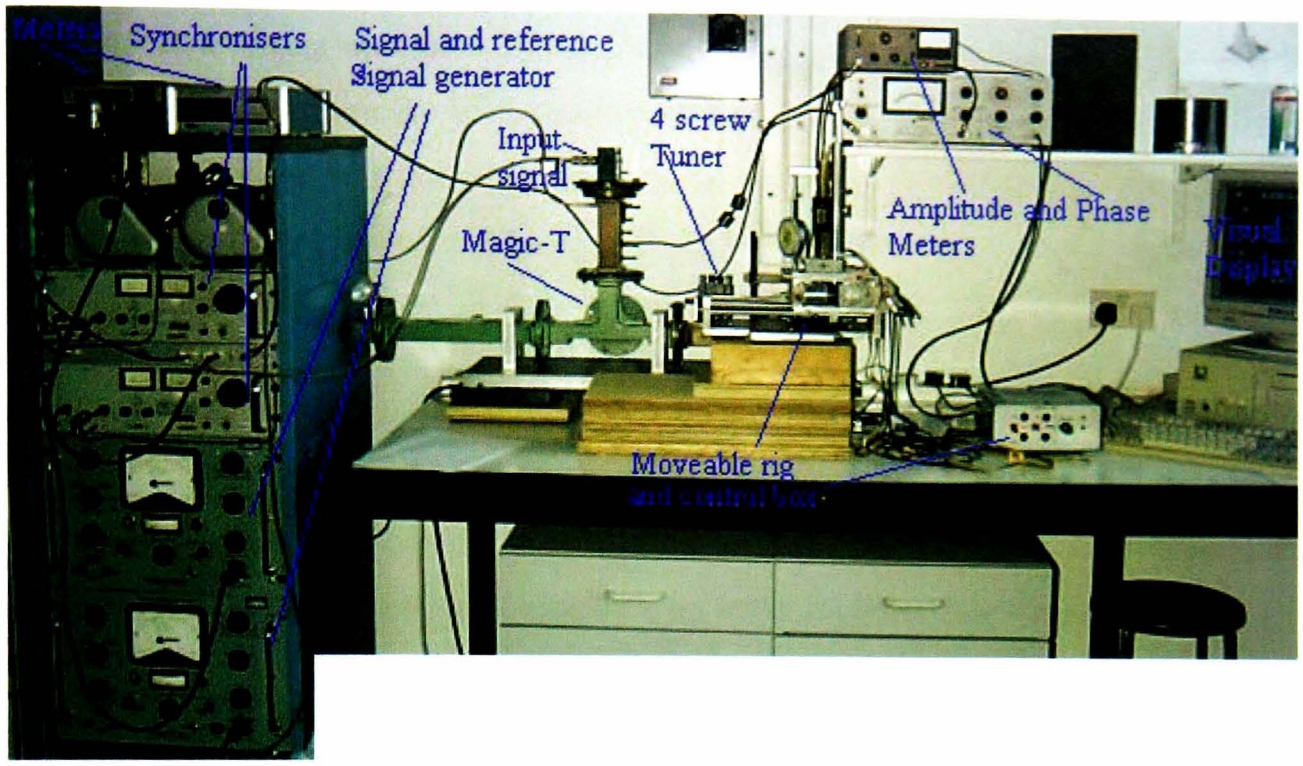

Figure 4.3: *Photograph of NRP test apparatus, featuring signal generators, waveguide structures and components, appropriate meters and the test structure.*

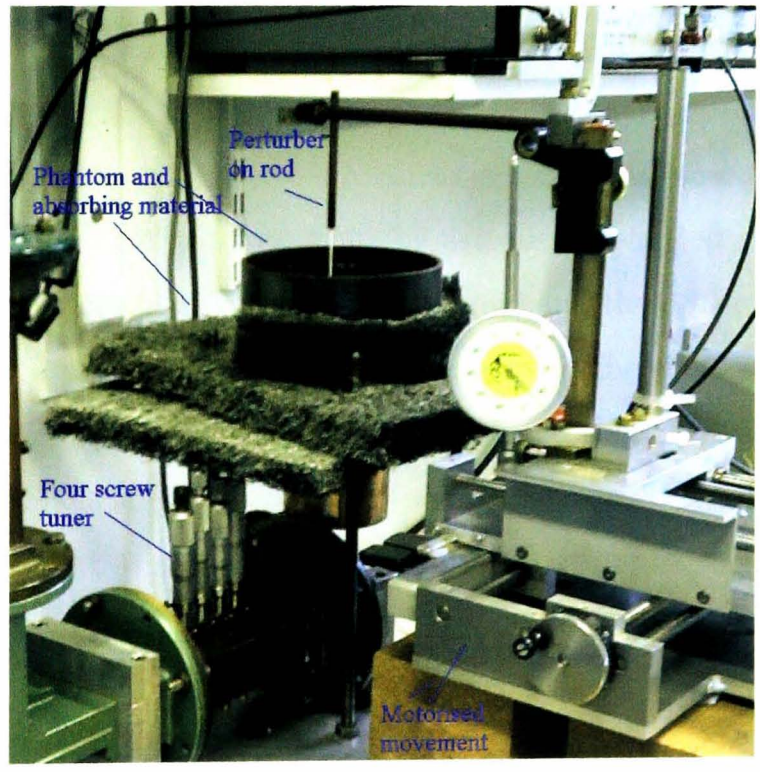

Figure 4.4: *Photograph of the test system comprising primarily of a cylindrical antenna, phantom material and glass bulb perturber.*

The test structure is composed primarily of a cylindrical container partially filled with a lossy solution sitting upon a cylindrical metal TE_{11} mode waveguide which houses the probe antenna (located on the left hand side wall within the waveguide). Additionally the waveguide is attached to a flat metal plate upon which the container sits. This container has walls composed of Tufnol (2mm thick) and a very thin base made of Mylar film ($\leq$ 1mm thick). In some cases the container is surrounded by microwave absorbent material.

A small air filled glass sphere located at the end of a blown glass rod is used as the perturbing object or perturber. The top of the rod connects to a motor system allowing movement of the sphere in any direction within the phantom. The glass sides of the sphere and the base of the container are considered to be to thin too affect the reading.

4.2.1 Perturber dimensions

As stated in section 4.1.4 it is necessary for the diameter of the perturber to be small compared to the signal wavelength in the material. In a sucrose solution the signal wavelength is ~15mm reducing to ~10mm for deionized water. Ideally a sphere of 1-2mm would be used. Practically, however, this diameter poses problems. As the antenna is housed in an empty (air filled $\epsilon_r' = 1$) waveguide and the fields propagate to the phantom material ($\epsilon_r' = 35$) there is a large reflection of the signal. This means that the signal that can couple to the material is small so that the measured reflected signal is small. Thus the larger the bulb used the larger the reflected signal and the easier it is to measure. An additional consideration when a small perturber is used is the effect of the presence of the glass rod in the measurement volume. If too large a perturber is used, however, the phase of the electric field will change over the surface of the sphere. Experiments were initially performed using a sphere of diameter 9mm and latterly a sphere of diameter 3mm was used.

4.2.2 Presence of dielectric layers

In order to ensure that the simulation accurately models layered structures experiments were performed using the basic model with dielectric layers as shown in Figure 4.5. Three sizes of layer were considered, 1.5mm, 3.5mm and 6.5 mm. Results are only presented for the larger two heights as it proved to be very difficult to obtain repeatable results with the smaller layer present. This was as a result of extreme difficulty in obtaining a stable zero initial reflection coefficient (Γ_1).

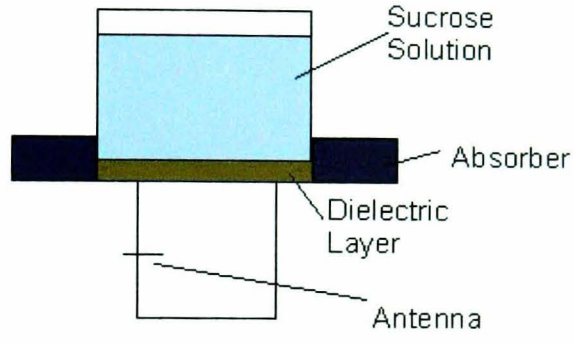

Figure 4.5: *Schematic showing the inclusion of dielectric layers in the nrp test system.*

4.3 NRP Experimental results and analysis

In this section the results for the various experimental test systems are given after a discussion of the necessary procedures for data post processing.

4.3.1 Interpretation of experimental results

The raw data results from the experimental work require post processing to ensure ease of comparison between experimental data sets, as well as between experimental and computed results. In particular it is vitally important to ensure that the position corresponding to coordinate (x,y,z) is identical for all sets of results.

4.3.1.1 Matching of position - x, y coordinates

Figure 4.6 details the position of the probe antenna in both the simulated model and the experiment. The probe in the experiment is at an angle of approximately 30° from that in the simulated model. Rather than have a less accurate simulation model of the apparatus by using an approximation to the probe antenna it was deemed more appropriate to rotate the experimental structure by this angle. Thus as shown in Figure 4.6 the probe was positioned directly along the x-axis making the modelling as simple as possible. In order to compare the results, however, it was necessary to rotate either the experimental or simulated data to match. As the experimental data sets contained a considerably smaller number of values they were chosen to be rotated to match the simulation results.

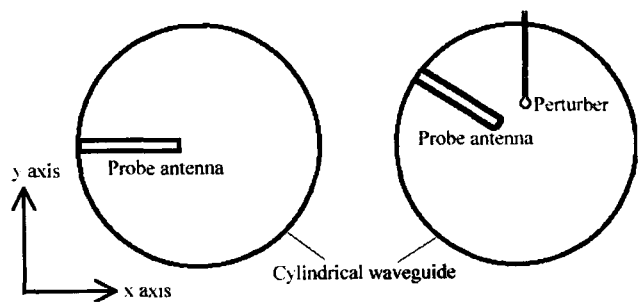

Figure 4.6: *Schematic of antenna probe position in simulation and experimental work respectively.*

The rotation of the experimental data to match the simulation data format is performed by applying the rotation matrix:

$$\begin{bmatrix} \cos\theta & -\sin\theta \\ \sin\theta & \cos\theta \end{bmatrix} \tag{4.15}$$

to the initial data to obtain the new values where θ is the rotation angle. In addition to a rotation of the experimental data for an exact match of experiment and computation it is necessary to perform a translation in the y-axis. Although this translation is included in the post-processing of the data, it should not affect the result due to the symmetry of the test system.

4.3.1.2 Matching of position - z coordinate

In order to compare experiment and simulation directly it was necessary to be certain of the height of the centre of the perturber from the antenna. In the experiment the base of the container is made from a very thin Mylar layer. Under the weight of the phantom material this layer dips into the lower cup forming a curved surface. In the case of the idealised simulation this curvature is not taken into account. Figure 4.7 gives an indication of the scale of this effect.

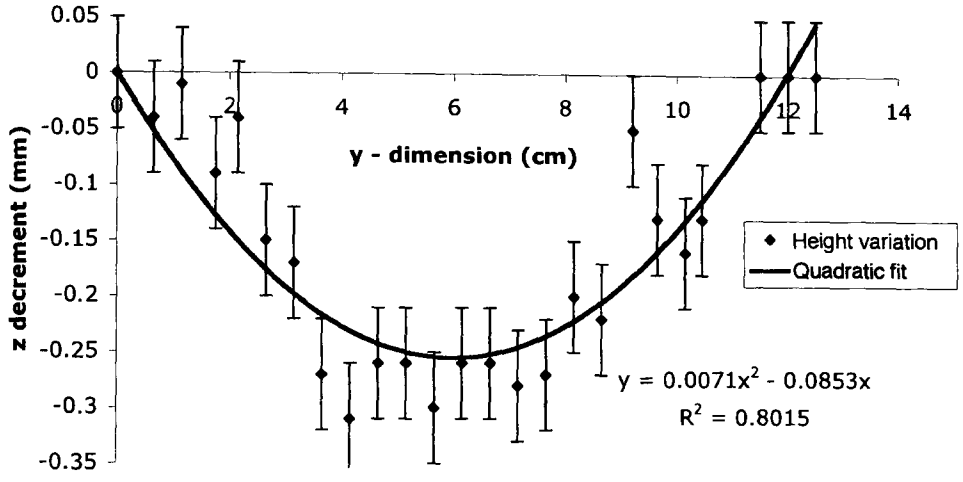

Figure 4.7: *Plot showing the effect of a dip in the base of the phantom container base. Around the centre of the test system this effect is roughly constant at 2.5mm.*

To account for this dip, the height noted in each experiment is the height of the bulb above the metal plate. The dip in the base of the phantom container is such that its value around the centre point is reasonably constant over several centimetres. Thus the height chosen for comparison is that of the height of the perturber centre above the metal plate plus 2.5mm to account for this effect. The presence of dielectric layers removes any effect of height variation.

4.3.1.3 Interpolation of data

The raw data format is that of data obtained at a given x and z position over a range of y position values, this then repeats at a series of x positions. One data set then consists of a number of' 'rows of data corresponding to this experimental procedure. Due to the limits of both time available and computational response time it would be difficult to obtain a value for the power normalised weighting function at every point within the phantom material.

As the most suitable means for comparison of the experimental data sets, both with each other and with the simulation data, is through graphic illustration it is necessary to interpolate the data available to produce a full result matrix. This interpolation is performed using a cubic spline interpolation in the commercially available program EasyPlot [140]. The interpolation is performed to give a matrix of approximate size 150*150 cells, with each cell corresponding to 1mm in the x and y dimensions. Graphical representations of the experimental data, as shown in the following section, can then be produced using MatLab [141].

4.3.1.4 Calibration of experimental data

Finally as the raw experimental data is that of the reflection coefficient it is necessary firstly to calibrate using a known reflection coefficient and then to obtain from this calibrated reflection coefficient the power normalised weighting function as given by equation 4.14. Thus to obtain the weighting function it is necessary to determine a multiplication factor (F) as given by:

$$F = \frac{\left(2 + \frac{\epsilon'_{pt}}{\epsilon'_{ph}}\right)}{\left(1 + \left(\frac{\epsilon'_{ph} - \epsilon'_{pt}}{\epsilon''_{ph}}\right)^2\right)^{\frac{1}{2}}} \times \left(\frac{\Gamma}{2\pi a^3}\right) \tag{4.16}$$

where $\epsilon'_{pt}, \epsilon'_{ph}, \epsilon''_{ph}$ are the dielectric constants and loss factors of the perturber and phantom respectively, Γ is the calibrated reflection coefficient and a is the radius of the perturbing sphere.

4.3.2 Errors present in experiment

Several sources of error are present in the non-resonant perturbation experiment. In particular these errors contribute to an error in the above multiplication factor. Standard error propagation techniques are used to determine the total error in this factor from each constituent variable. The overall error value varies slightly depending on the calibration factor of each particular experiment. This variation, however, is only a fraction of a percent. To the nearest percentage, overall errors are given in table 4.1 for the sucrose and water phantoms. Additionally a breakdown of the individual contribution to the total error of each variable is given for a particular water phantom experiment.

Clearly the major constituent of this error is in the measurement of the radius of the perturbing object. As this error is roughly 0.1mm the required degree of accuracy of this component is apparent.

Material	Percentage error (100*dF/F)	Material	Component	Percentage contribution
Water	27	Water	a	73
Sucrose	22	Water	ϵ'_{pt}	0
		Water	ϵ'_{pt}	0
		Water	ϵ'_{ph}	0
		Water	ϵ''_{pt}	25.5
		Water	Γ_f	1.5
		Water	Total (=dF)	100

Table 4.1: *Percentage error present in the calculation of the multiplication factor (F) for the NRP experimental procedure for the water and sucrose phantom materials. Also given is a breakdown of the contribution to the total error in the multiplication factor of the errors in each variable for a specific water error calculation.*

4.3.3 Experimental Results

In this section the results of the non-resonant perturbation experiments are displayed for both the water and sucrose phantoms, for the small and large perturber situations and with and without the presence of dielectric layers. The z positions of each data set are given as the height of the centre of the perturbing object above the base of the phantom structure.

4.3.3.1 Water phantom

Figures 4.8 and 4.9 illustrate an example of the normalised power absorption patterns detected at varying z positions within the water phantom material. Results are displayed for heights of 10mm in Figure 4.8 and at 11.5 and 14 mm in Figure 4.9. In addition to a graphical comparison of the data it is possible to consider the maximum value in the pattern. This value, obtained from the non-interpolated data, gives a potential method for amplitude comparison.

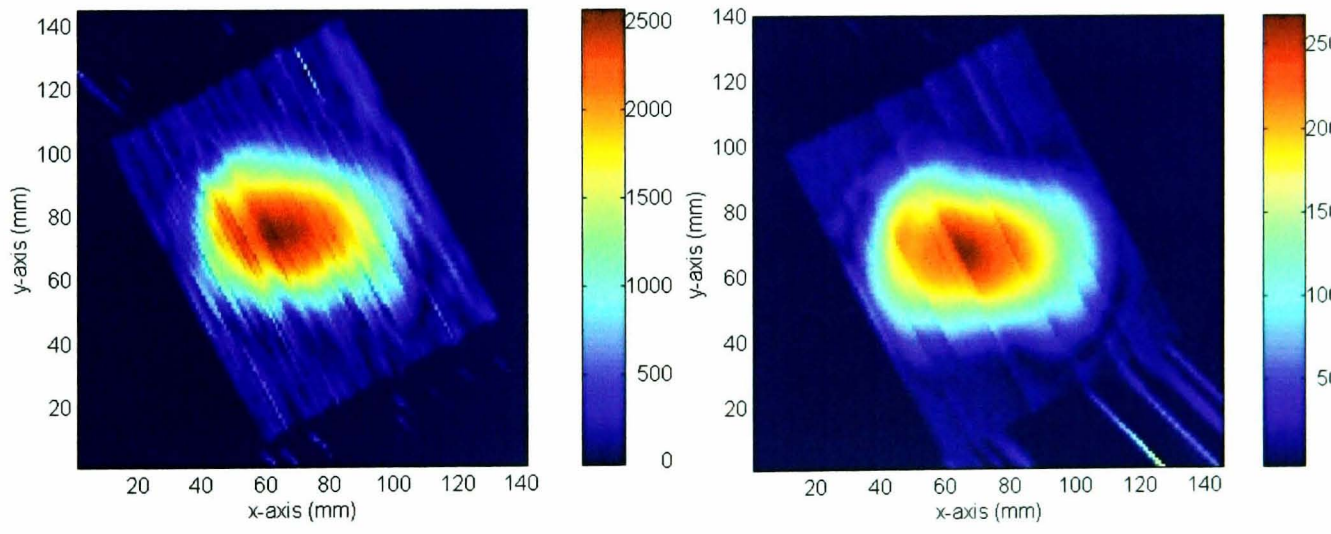

Figure 4.8: *Results for water phantom with the larger perturber at total height from the phantom base of 10mm, with maximum amplitude values of 2549 and 2656 respectively.*

It is clear that for all data sets the overall shape of the image is consistent, and as the height from the phantom base increases the amplitude falls.

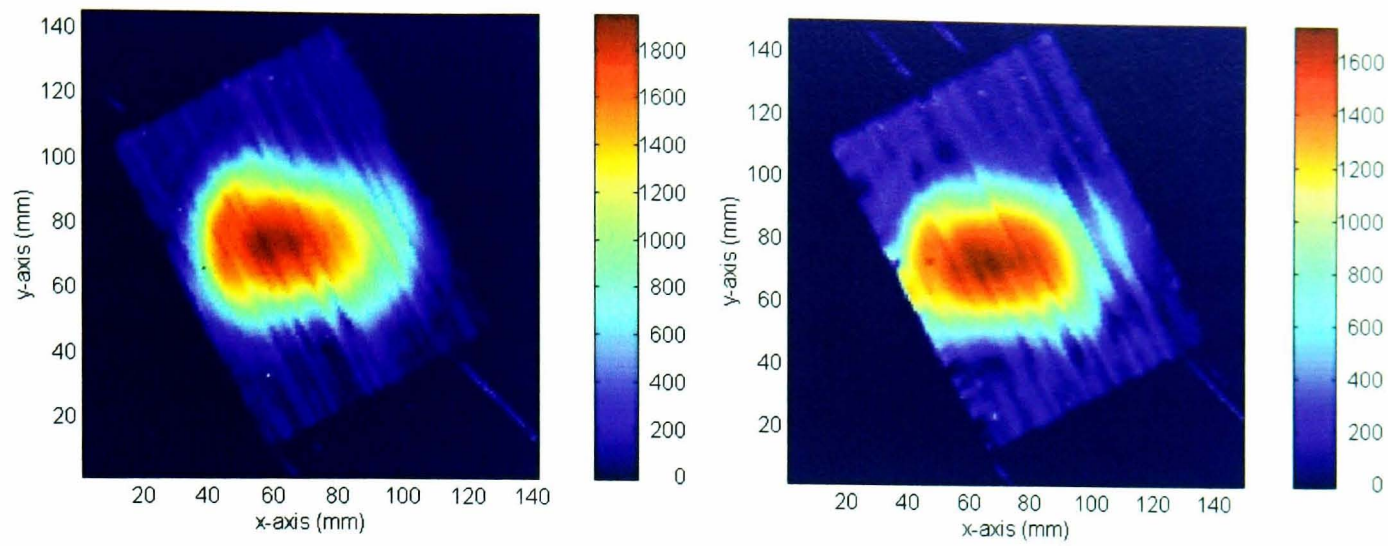

Figure 4.9: *Results for water phantom with the larger perturber at total heights from the phantom base of 11.5 and 14mm, with maximum amplitude values of 1932 and 1717 respectively.*

4.3.3.2 Water phantom with medium layer

With the incorporation of a dielectric layer of height 3.5mm to the water phantom as before the maximum amplitude is again seen to fall with increasing distance from the phantom base. Heights from phantom base (including the layer) of 9, 10.5 and 13mm are shown in Figure 4.10, with corresponding maximum amplitude values of 3870, 3017 and 1894.

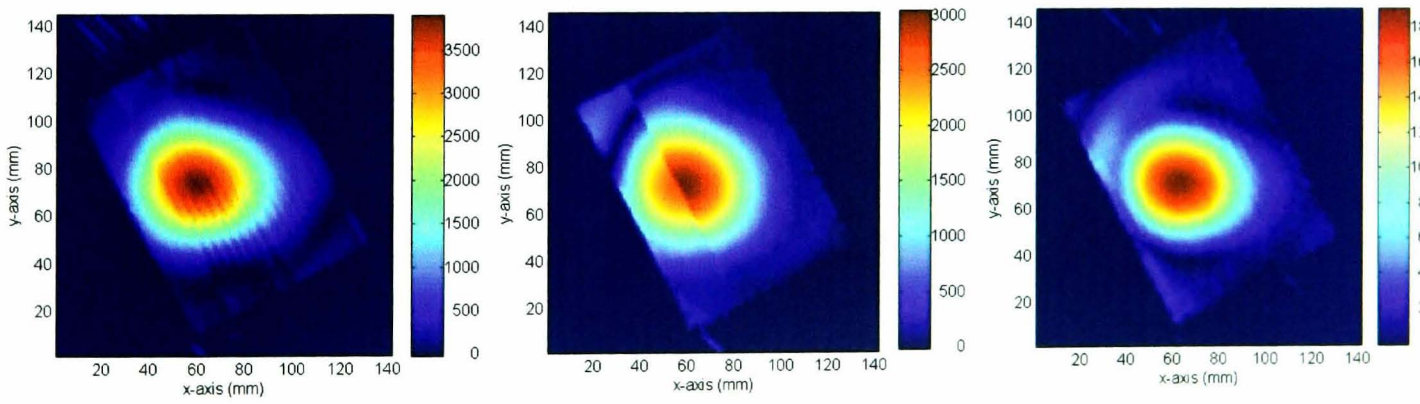

Figure 4.10: *Results for water phantom above the 3.5mm dielectric layer at total heights from the phantom base of 9, 10.5 and 13mm with maximum amplitude values of 3870, 3017 and 1894 respectively.*

4.3.3.3 Effect of layer in water phantom

Comparison of the results seen at roughly equivalent z positions with and without the 3.5mm dielectric layer present highlights a sharpening of the power absorption pattern. This can be attributed to two possible effects. Firstly the presence of the dielectric layer eliminates the curved base seen in the non-layered results. This will serve to sharpen the peak in the results. Secondly the signal transmitted through the layer will be a modified form from that without the layer.

Comparisons are made with and without a layer present at heights of 10/10.5 mm, (Figure 4.11) and 13/13.5 mm (Figure 4.12). In both cases the maximum amplitude value seen with the layer present is greater than without the layer at the same height. This is as expected and can be attributed to the fact that the layer presents a much lower conductivity than the water. So that at the same height the signal that has passed through only water will have attenuated by a greater amount than that which has passed though the layer and then water. This variation in maximum amplitude value is not as considerable as expected, however.

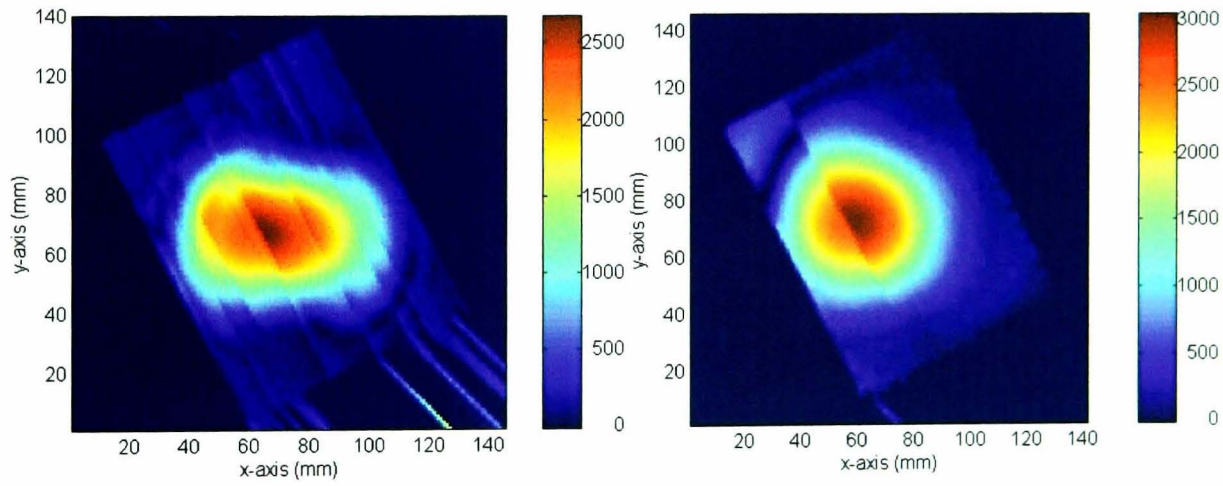

Figure 4.11: *Results for water phantom alone and above the 3.5mm dielectric layer at total heights from the phantom base of 10 and 10.5 mm respectively. Maximum amplitude values of 2656 and 3017.*

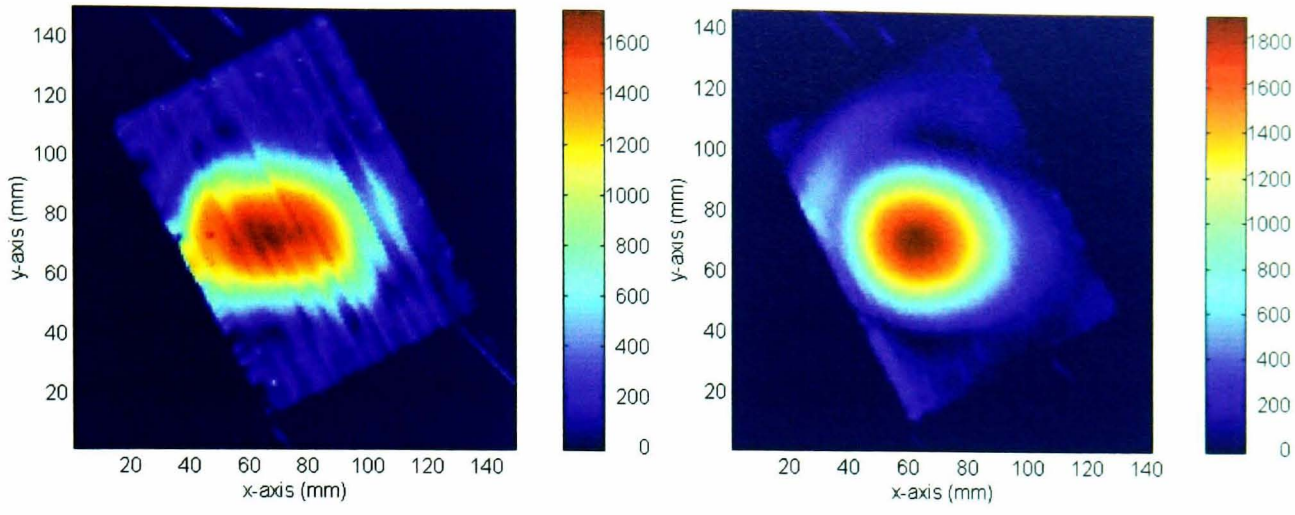

Figure 4.12: *Results for water phantom alone and above the 3.5mm dielectric layer at total heights from the phantom base of 13 and 13.5 mm respectively. Maximum amplitude values of 1717 and 1894.*

This affect on the pattern is also seen in the case of a larger dielectric layer (6.5mm). In Figure 4.13, results are shown for the water phantom and a large layer at a height of 13.5mm. This result is compared to that of water without the layer present at a height of 13mm. Again the maximum amplitude for the test run with the layer present (2846) is greater than for the equivalent height without (1717). The amplitude for the larger layer is also larger than that for the equivalent height with the medium layer.

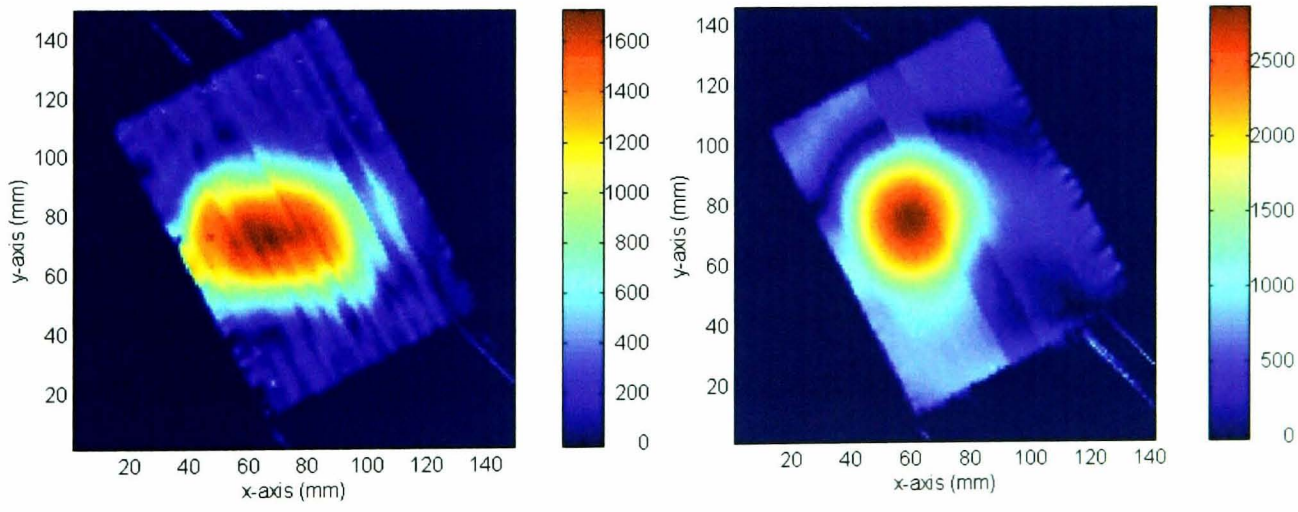

Figure 4.13: *Results for water phantom alone and above the 6.5mm dielectric layer at total heights from the phantom base of 13 and 13.5 mm respectively. Maximum amplitude values of 1717 and 2846.*

4.3.3.4 Sucrose phantom results

In the case of the sucrose phantom a similar power absorption pattern is obtained. The results for a 33% (by mass) sucrose solution are shown in Figure 4.14 at a height of 7.5mm and with maximum amplitude of 2547. This amplitude is comparable in magnitude to those of the water phantom at heights of 3mm more (~10mm). This is to be expected as the sucrose solution has a notably larger conductivity than the water solution, (Table 4.2), and hence higher absorption of the signal will occur.

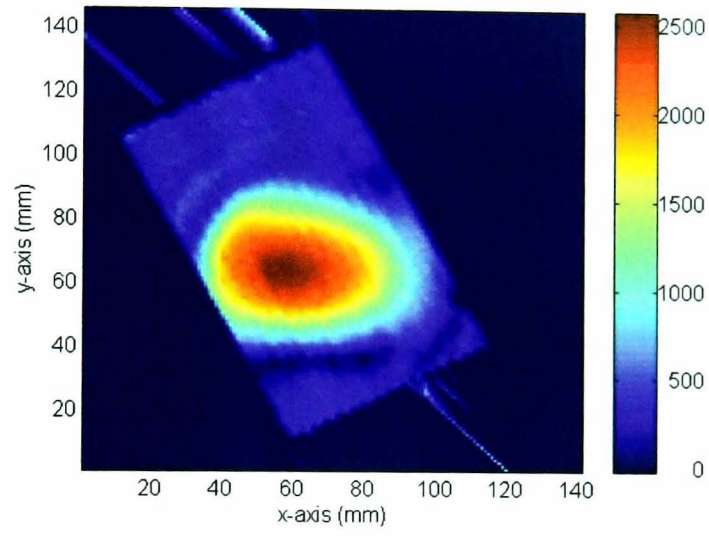

Figure 4.14: *Results for sucrose phantom at total height from the phantom base of 7.5 mm with a maximum amplitude of 2547.*

4.3.3.5 Effect of perturber diameter on result

Although the results obtained with the larger diameter perturber are accurate in terms of graphical representation the magnitude of the power absorption is very small in comparison to the simulation work. Many approaches were considered to determine the reason for this mis-match and the size of the perturbing object proved to be a major contributing factor. As previously mentioned in Section 4.1.4, the size of the perturber must be small compared to the wavelength for the quasi-static approximation in the theoretical derivation to hold.

Use of a small perturber, however, has the effect of a great loss in accuracy of the pattern. For the small perturber experiments it is still possible to consider both the graphical representation and the maximum amplitude value for comparisons, although more care must be taken when drawing conclusions from this data.

Figures 4.15, 4.16 and 4.17 compare the results for a water phantom alone, water phantom with 3.5mm layer and the water phantom with 6.5mm layer for both the small and large bulb perturber. Results are displayed for approximately equivalent heights above the phantom base in all three figures. The effect on the magnitude of the power absorption is clearly apparent as is the decline in pictorial clarity.

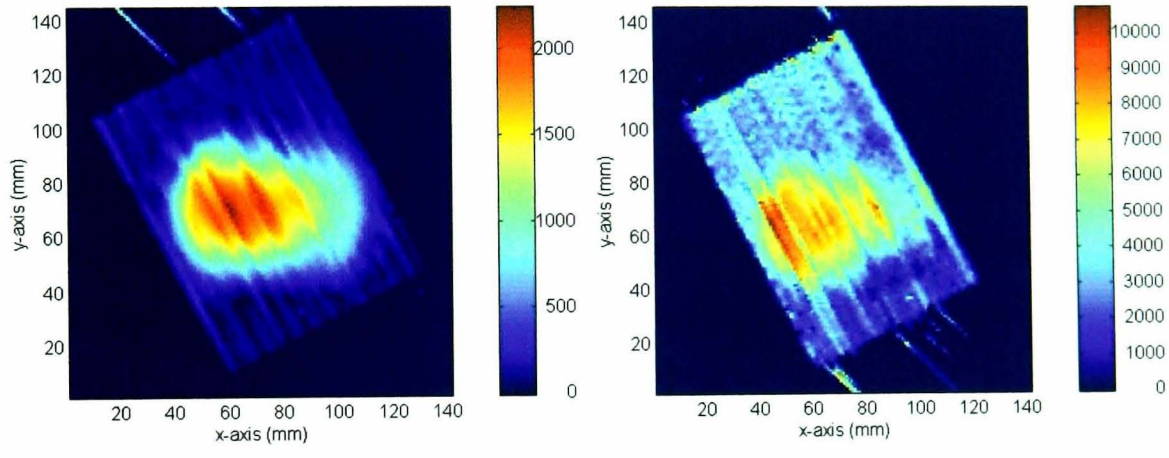

Figure 4.15: *Results for the water phantom measured using the small and large perturber at a heights of 14 and 14.5 mm respectively.*

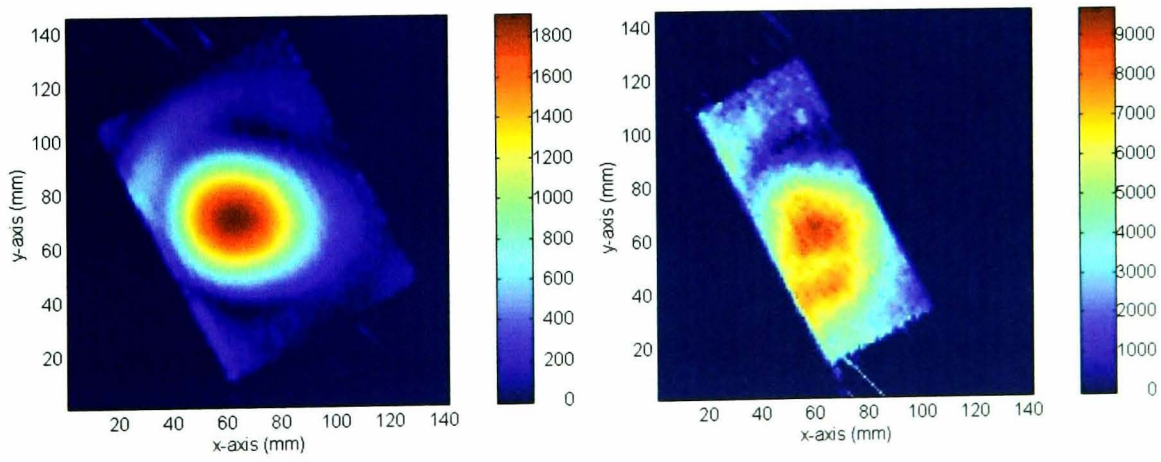

Figure 4.16: *Results for the water phantom above the 3.5mm dielectric layer measured using the small and large perturber at a heights of 13.5 and 13 mm respectively.*

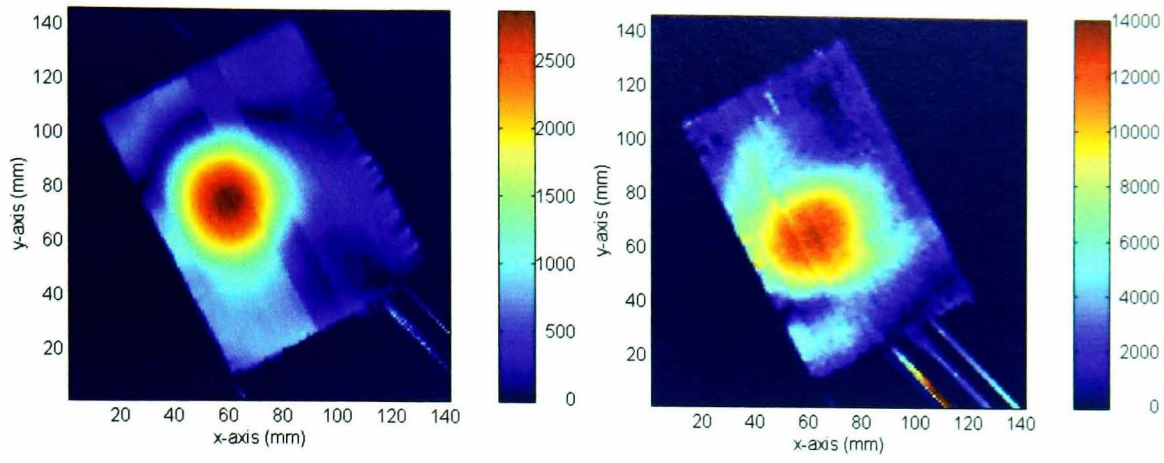

Figure 4.17: *Results for the water phantom above the 6.5mm dielectric layer measured using the small and large perturber at a heights of 13 and 12.5 respectively.*

4.3.3.6 Water phantom results with small perturber

The pattern of declining maximum amplitude is still apparent with the small perturber as shown in Figures 4.18, 4.19 and 4.20 for both the test structure of only water, water with the 3.5mm layer and water with the 6.5mm layer. It is also possible to detect the apparent sharpening of the maximum in the presence of the layers. The resolution of the image is clearly at its best for the conditions where the largest signal is present.

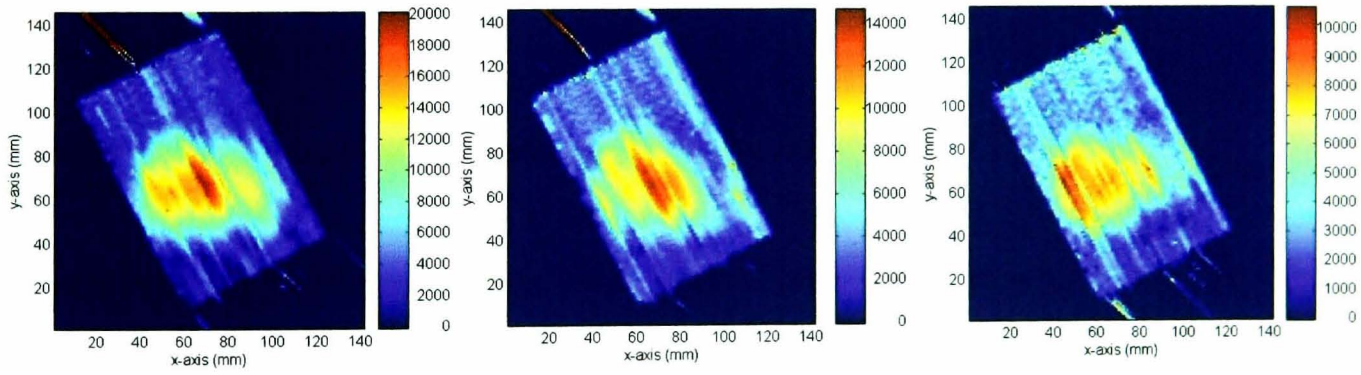

Figure 4.18: *Results for water phantom at total heights from the phantom base of 6.5, 10.5 and 14.5 mm respectively using the small perturber. Maximum amplitude values as measured are 19970, 14590 and 10644.*

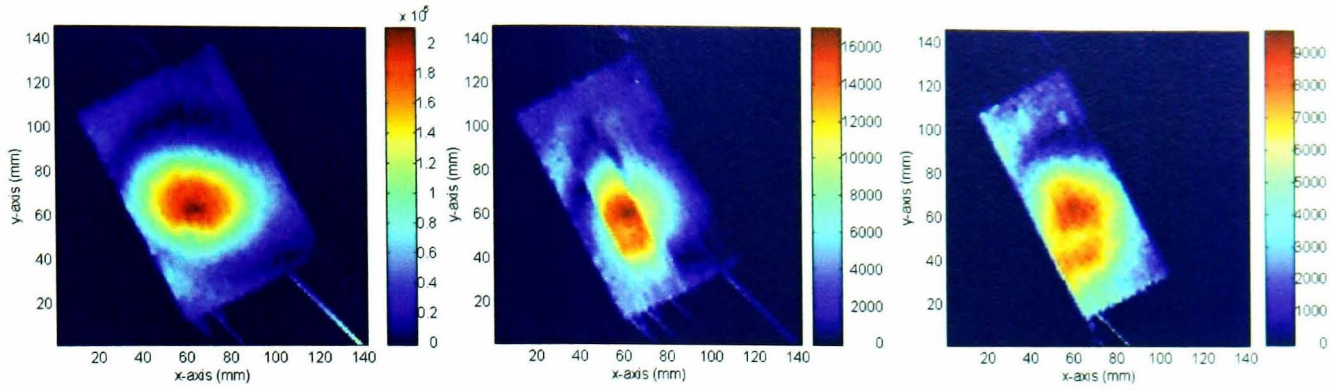

Figure 4.19: *Results for water phantom above the 3.5mm dielectric layer at total heights from the phantom base of 6, 9 and 13 mm respectively using the small perturber. Maximum amplitude values as measured are 20892, 16870 and 9607.*

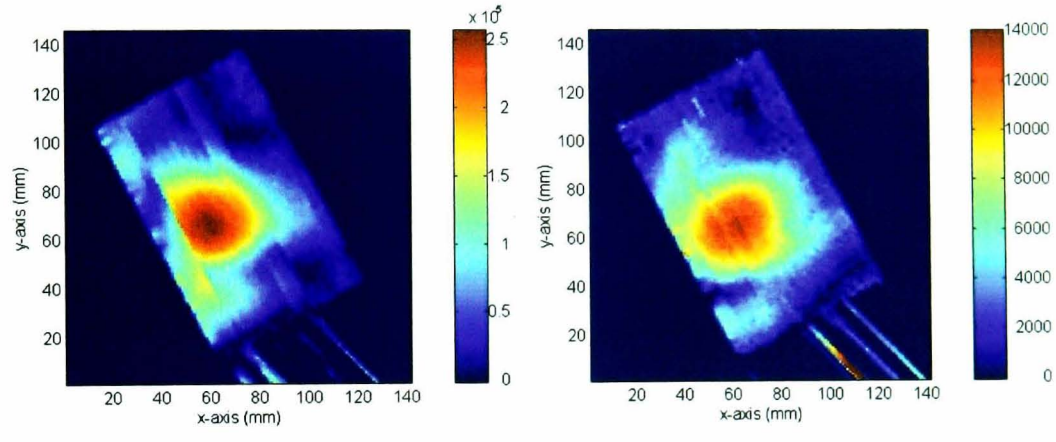

Figure 4.20: *Results for water phantom above the 6.5mm dielectric layer at total heights from the phantom base of 8.5 and 12.5 mm respectively. Maximum amplitude values as measured are 25463 and 13907.*

4.3.3.7 Sucrose phantom with small perturber

This is repeated for the sucrose phantom, with a decline of amplitude with position from the base and more accurate patterns for the test systems corresponding to areas of higher signal. Results for the sucrose phantom only and the sucrose phantom above the 3.5mm dielectric layer are shown in figure 4.21 and 4.22 respectively.

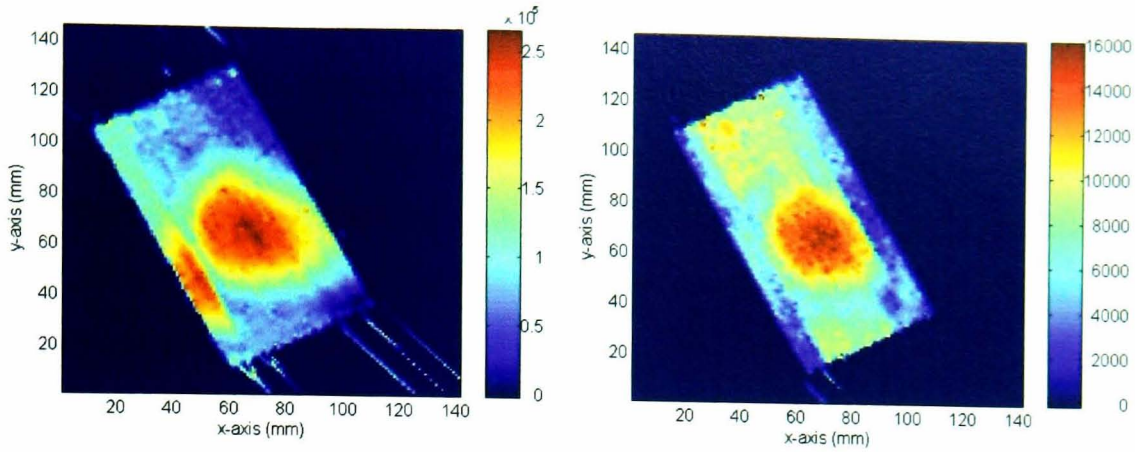

Figure 4.21: *Results for sucrose phantom at total heights from the phantom base of 6.5 and 10.5 mm respectively measured with the small perturber. Maximum amplitude values as measured are 26242 and 15979.*

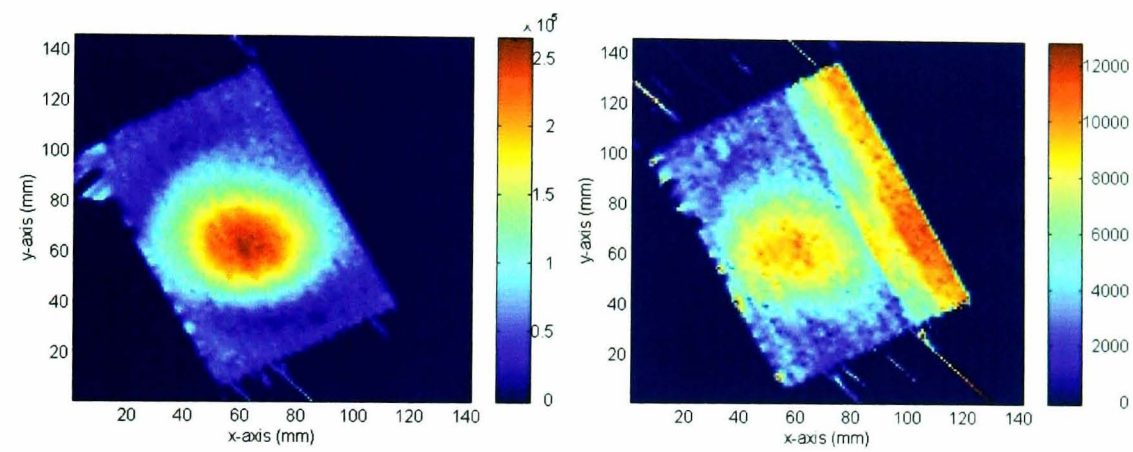

Figure 4.22: *Results for sucrose phantom above the 3.5mm dielectric layer at total heights from the phantom base of 8.5 and 12.5 mm respectively measured with the small perturber. Maximum amplitude values as measured are 26240 and 12702.*

4.3.3.8 Effect of layers with small perturber

In the measurements made with the small perturber the effect of the layers on the maximum amplitude of the results is not as expected. Comparing the results in Figures 4.18 and 4.19 for the water phantom and with / without layer situations it can be seen that there is no notable increase in the maximum amplitude values as when the layer is present for the same height from phantom base. In fact in some cases in the presence of the dielectric layer the amplitude is smaller than without this layer present. This effect is also apparent in the sucrose phantom case.

A possible reason for this decreased amplitude in the presence of these dielectric layers involves the presence of a secondary reflection. It is possible that the size of the layers is such that a radial field is excited out of the layer. This signal could then reflect from the various experimental apparatus around the test system and give a skewed reflection coefficient. The result measured by the perturber is the sum of these effects, hence the interference type pattern.

A series of readings performed with the sucrose phantom and 3.5mm layer at various x and y positions to establish the nature of this effect is seen in Figure 4.23. It can be seen that the variation in reflection with height above the phantom base is not as expected, i.e. it does not follow an exponential decay curve. When using a larger perturber this effect is minimised as a result of averaging over the bulb surface, also shown in Figure 4.23.

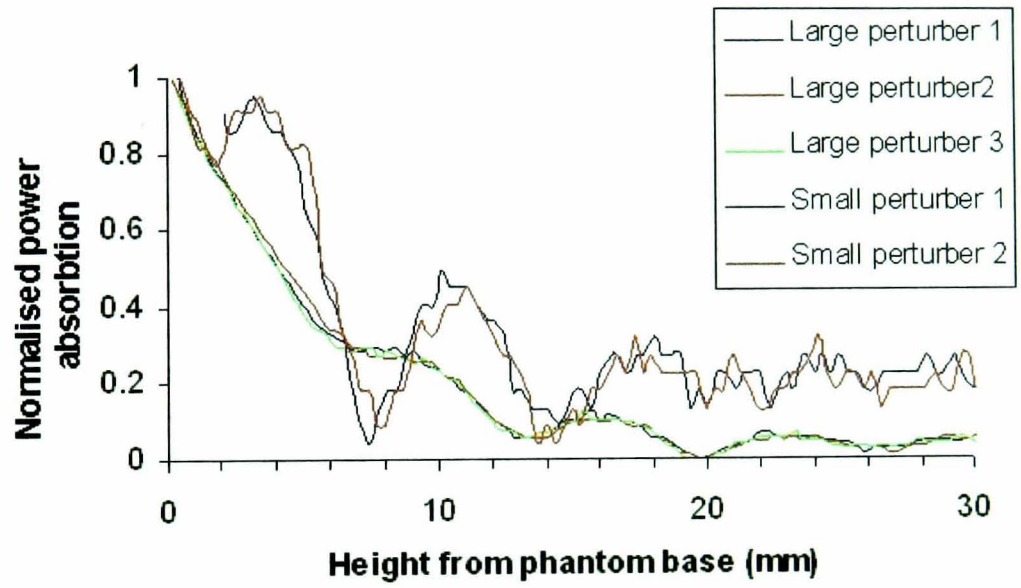

Figure 4.23: *Test system results with 3.5mm dielectric layer highlighting the secondary reflections problem.*

With the presence of absorber around the layer, this effect is minimised, Figure 4.24, however this field leakage will still occur. Hence the magnitude of the reflected signal will be smaller than expected in all cases. Attempts to model this situation, involving the inclusion of small PEC layer at one side of layer and secondly including a PEC rod above the phantom have proved unsuccessful. As a result maximum amplitude comparisons between experiment and simulation in these cases are not possible.

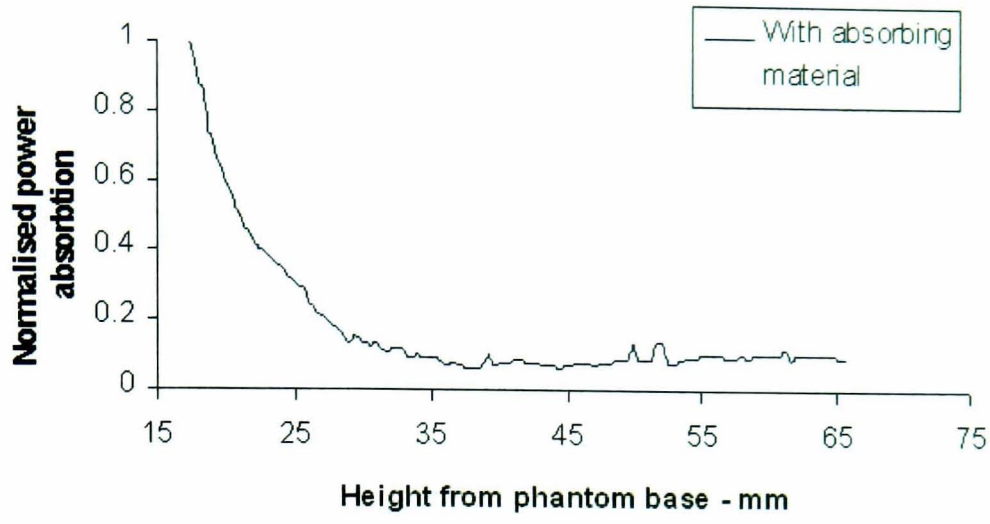

Figure 4.24: *Test system with absorbing material resulting in the expected exponential decay curve.*

4.4 Non-resonant perturbation - simulation model

The apparatus of the non-resonant perturbation experiment, as shown in the Figure 4.25, formed the simulated region. The main items are a cylindrical container partially filled with a lossy solution sitting upon a cylindrical metal waveguide which houses the probe antenna. Additionally the waveguide is connected to a flat metal plate upon which the beaker sits surrounded by microwave absorbent material.

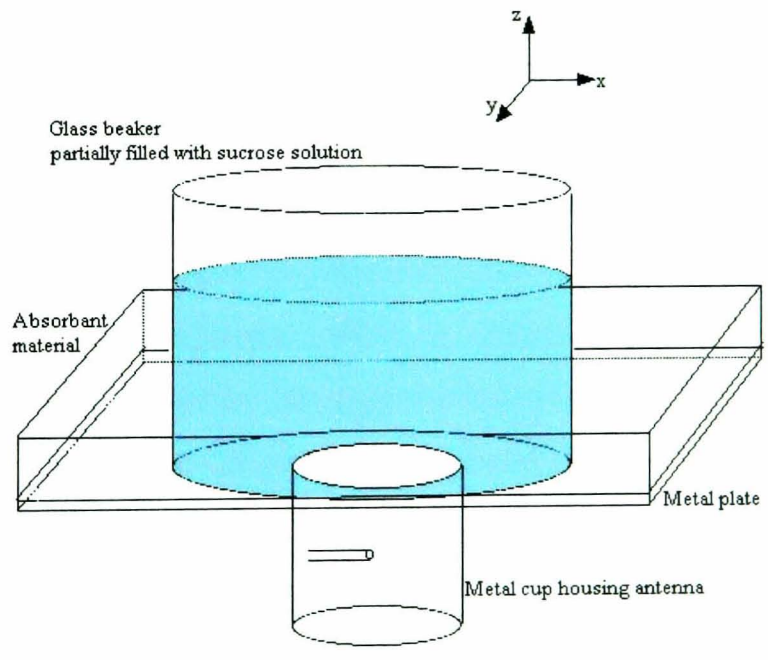

Figure 4.25: *Apparatus modelled for simulation of NRP experimental work.*

The probe within the metal cup, as shown in the Figure 4.26, is modelled as a circular cylinder of plastic PTFE with a cylindrical metal rod in the centre. At the tip of probe is a short cylinder of metal. An x directed monopole of length one cell is located at the end of the probe next to the waveguide side. This is the source of the excitation and has a voltage generator amplitude of 1V and a load resistance of 50Ω.

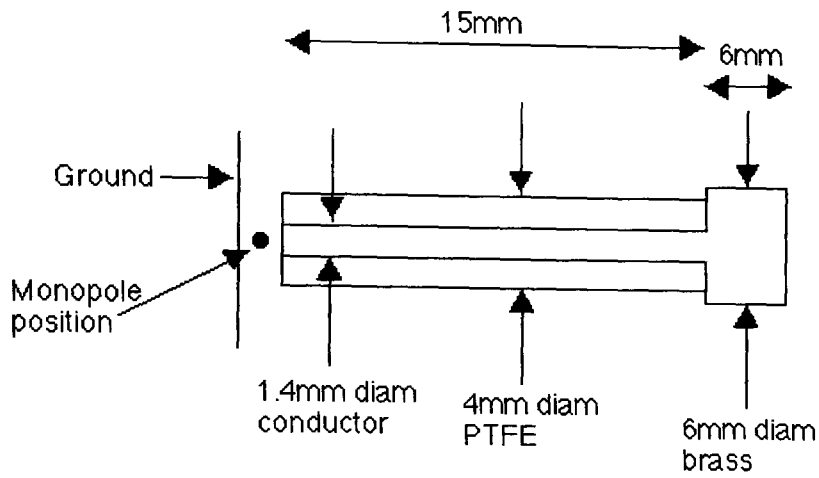

Figure 4.26: *Model of probe antenna as used in the NRP experimental work.*

4.4.1 Phantom materials and their properties

The phantom materials used in the experiment are those with dielectric properties close to those of the higher water content body tissues and food stuffs. In particular experiments were performed on de-ionised water and sucrose solutions. The dielectric properties of the water solutions were found using the Cole-Cole approximation, as detailed in section 1.4.1. For the sucrose solutions the properties were determined from experimental measurements using the cavity resonance technique [40] at a temperature of 20°C. Any variation in temperature of the solution during the experimental process is assumed to be negligible as care is taken to ensure that the phantom materials equilibrate to room temperature. Further to this investigation of the variation of the water dielectric properties around room temperature (20°C), Figure 4.27, shows only minor variation with temperature. Values for each liquid used in the simulation work are shown in Table 4.2 along with those values approximated for the Tufnol components [142].

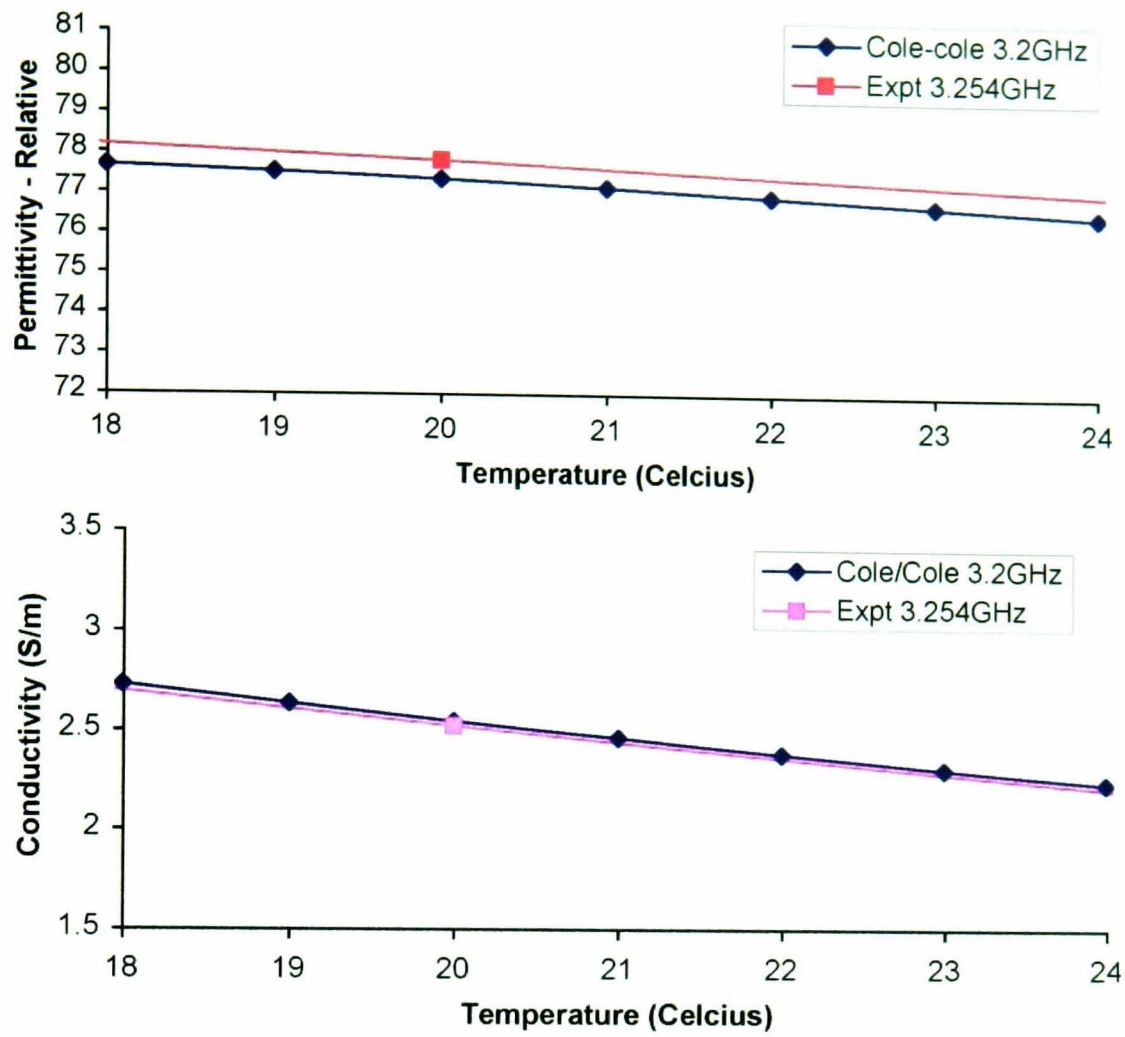

Figure 4.27: *Variation in dielectric properties with temperature of water solution around temperature. Experimental data from Hasted [8].*

Component	Dielectric constant	Conductivity (Sm^{-1})
Water	77.34	2.54
Sucrose (33% by mass)	55	3.7
Tufnol - 1	3	0.0053

Table 4.2: *Dielectric parameters of the solutions and Tufnol components of the test system.*

4.4.2 Simulation results and analysis

In order to compare the simulation work directly with the experimental results it is necessary to ensure that the value calculated for the SAR is the same in both cases. From the experimental work a value for:

$$SAR_E = \frac{1}{2}\frac{\sigma(r)E(r)^2}{W_i} \tag{4.17}$$

where W_i is the input power to the experiment, can be found for a given point in the phantom material.

From the simulation work a value for:

$$SAR_S = \frac{1}{2}\frac{\sigma(r)E(r)^2}{W_s} \tag{4.18}$$

where W_s is the input power to the simulation, can be found for a given position in the simulation space. For accurate comparisons it is essential to ensure that the normalisation of SAR by input power is the same in both cases and that the results to be compared correspond to the same physical position within the test structure.

4.4.2.1 Normalisation of simulation weighting function by input power

In the experimentally determined SAR results the normalisation by the input power is inherent in the calculation. For the simulated results several possible approaches to determining the input power to the simulation have been considered, both by calculation of the input power and of the total dissipated power. Although expected to be identical it is found that these values differ, by at most 10%, see Table 4.3. The input power is used for normalisation as it is the most closely related to the power normalisation of the experiment.

4.4.2.2 Effect of dielectric layers in simulation

Results shown in Figure 4.28 show the effect of layering on the simulated weighting function. The simulated data shows that as the layer thickness increases the weighting function maximum at a specific height above the antenna increases as expected from theory.

Simulation Model	Input power (mW)	Total absorbed power (mW)
Water (no layer)	2.06	1.95
Water (medium layer -1)	2.43	2.45
Water (medium layer - 2)	2.45	2.60
Water (large layer -1)	2.48	2.74
Water (large layer - 2)	2.46	2.70
Sucrose (no layer)	2.22	2.18
Sucrose (medium layer -1)	2.44	2.70
Sucrose (medium layer - 2)	2.48	2.80

Table 4.3: *Comparison of normalisation methods for the simulation models of the nrp experiments.*

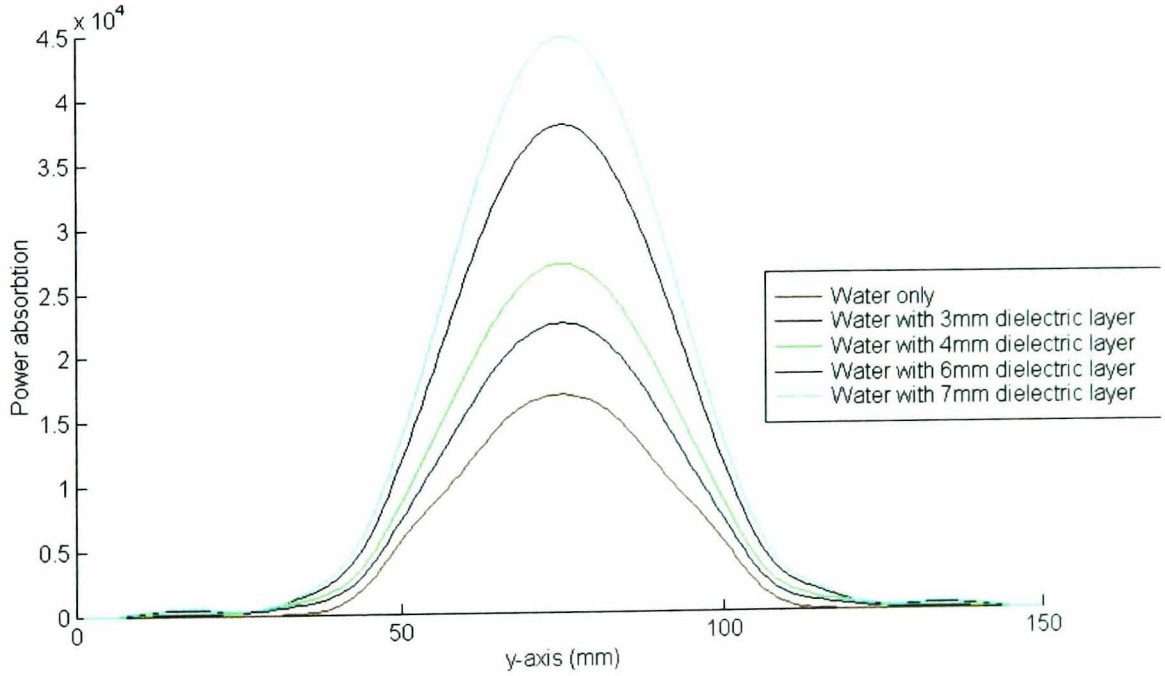

Figure 4.28: *Effect on the magnitude of the weighting function of the presence of dielectric layers in the simulated model.*

4.5 Comparison of experimental and simulated results

As a first method of determining a match between the experimental and simulated results comparisons are made of the normalised (each data set to maximum value 1) graphical representations seen for each test structure. Secondly a rough comparison of the numerical match is made through comparisons of the maximum amplitude value. In the case of the experiments made with the large perturber this second comparison is of little use as the data sets on average disagree by a factor of 5.

4.5.1 Water phantom results

Figure 4.29 shows the normalised results of the water phantom as measured and simulated at a height of 10mm. Although the experimental data sets show the obvious effects of the interpolation scheme at the outer areas of the pattern the match is reasonable. In particular the maximum values are observable in approximately the same area and the maximum / minimum / maximum (left to right in picture) is apparent in both. Additionally the elongated minimal region at higher x values is also apparent.

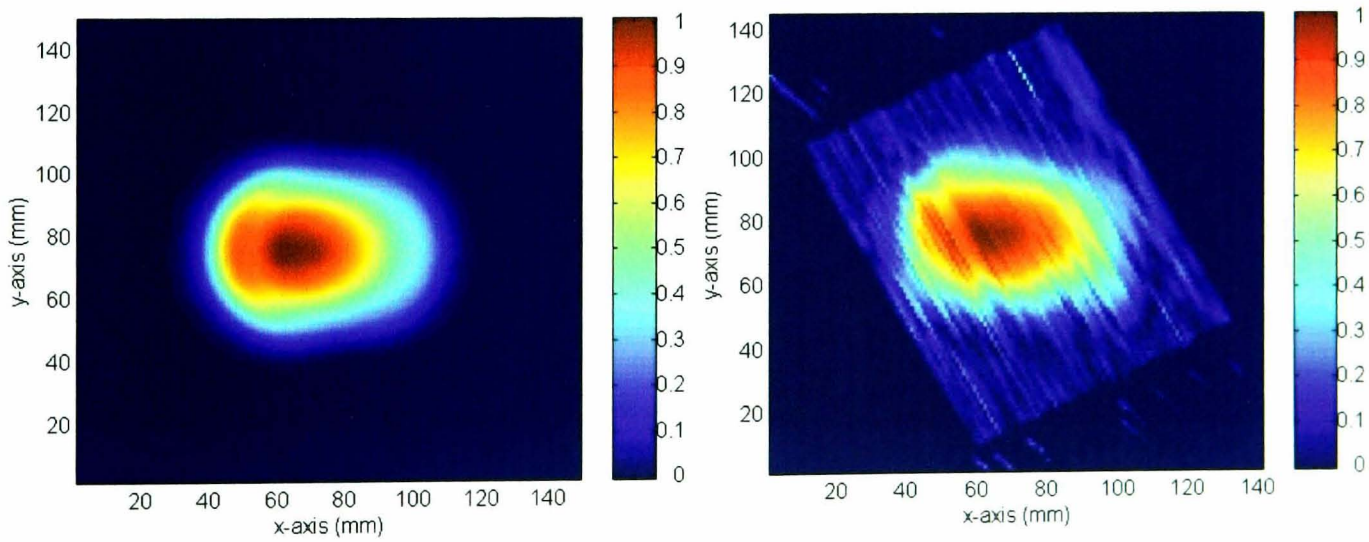

Figure 4.29: *Comparison of normalised simulated and experimental results at a height from phantom base of 10mm.*

This matching is also seen in Figure 4.30 which shows the comparison of results at a height of 11.5mm. Again the major features of the pattern are apparent in both data sets.

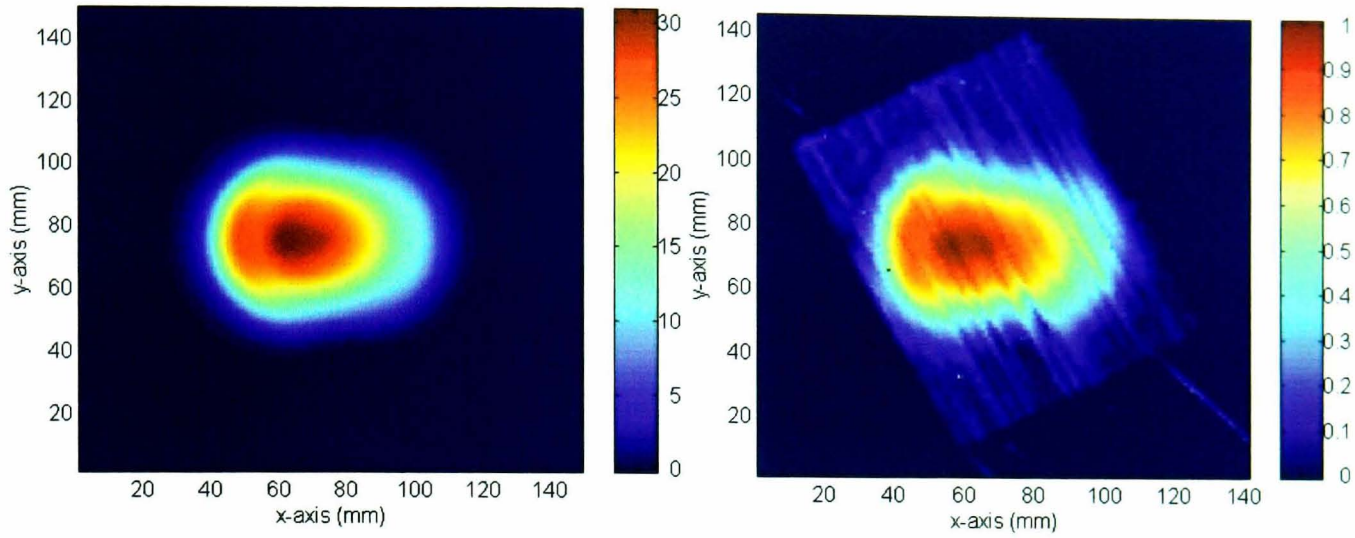

Figure 4.30: *Comparison of normalised simulated and experimental results at a height from phantom base of 11.5mm.*

As the height from the phantom base increases the accuracy of the experimental data sets diminishes. Although the basic shape of the pattern is seen to match in Figure 4.31, measured at a height of 13mm, some of the more specific details are missing.

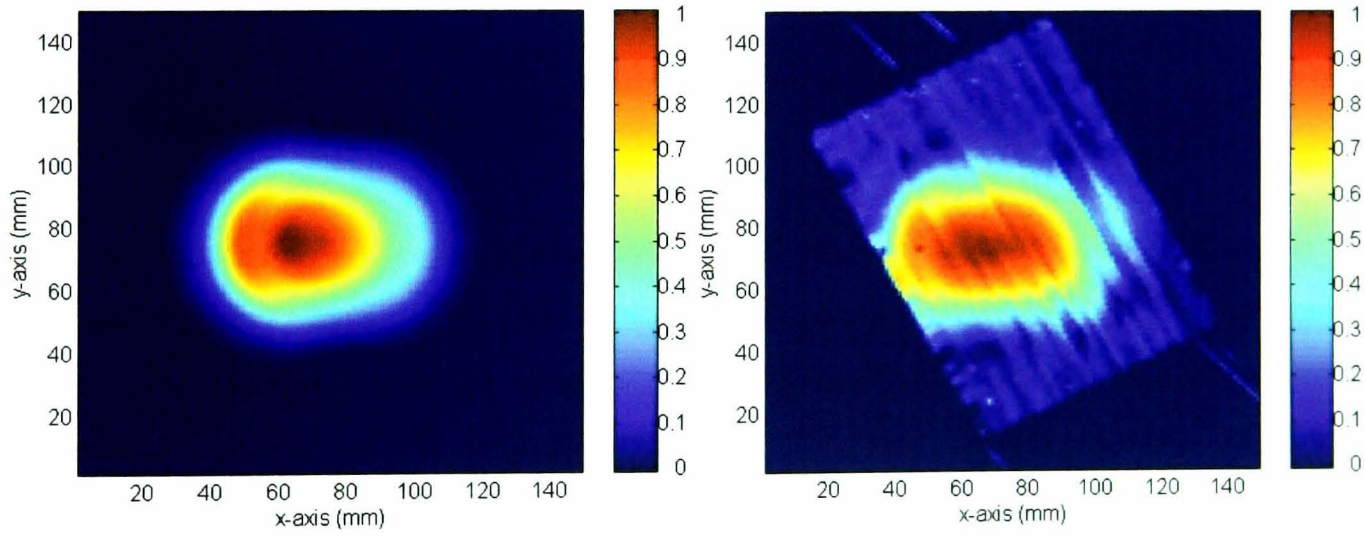

Figure 4.31: *Comparison of normalised simulated and experimental results at a height from phantom base of 13mm.*

4.5.2 Sucrose phantom results

In the case of the sucrose only phantom as measured at a height of 7mm the match between experiment and simulation is evident, Figure 4.32. With the exception of a less well defined maxima, most likely a result of the dipped base in the experiment, the patters are very close. The improved nature of this match occurs as a result of the larger reflection seen for sucrose as opposed to water and at the lower height.

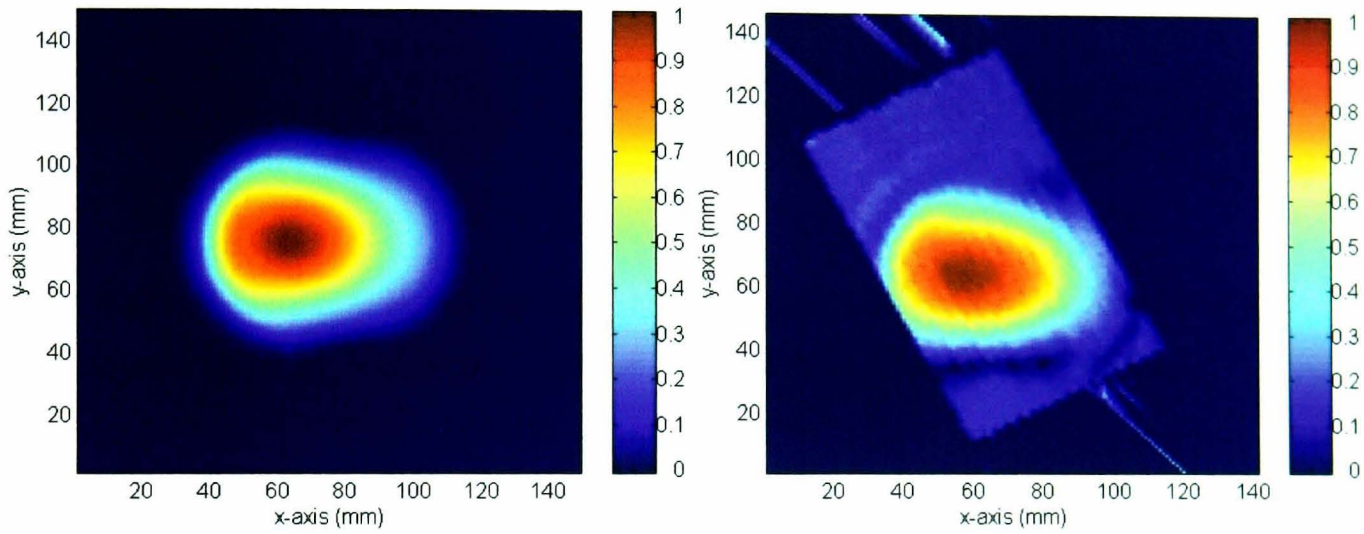

Figure 4.32: *Comparison of normalised simulated and experimental results for sucrose at a height from phantom base of 7mm.*

4.5.3 Water phantom with layers

In the case of the layered test structures the match between data sets is also observable. In the case of the water phantom with a 3.5mm dielectric layer, Figure 4.33, the data sets are very close to an exact match. Due to the inclusion of the layer in this test system the maxima is as sharp as the simulated data set. In a repeat of this experimental test system the extremely close match is repeated, Figure 4.34.

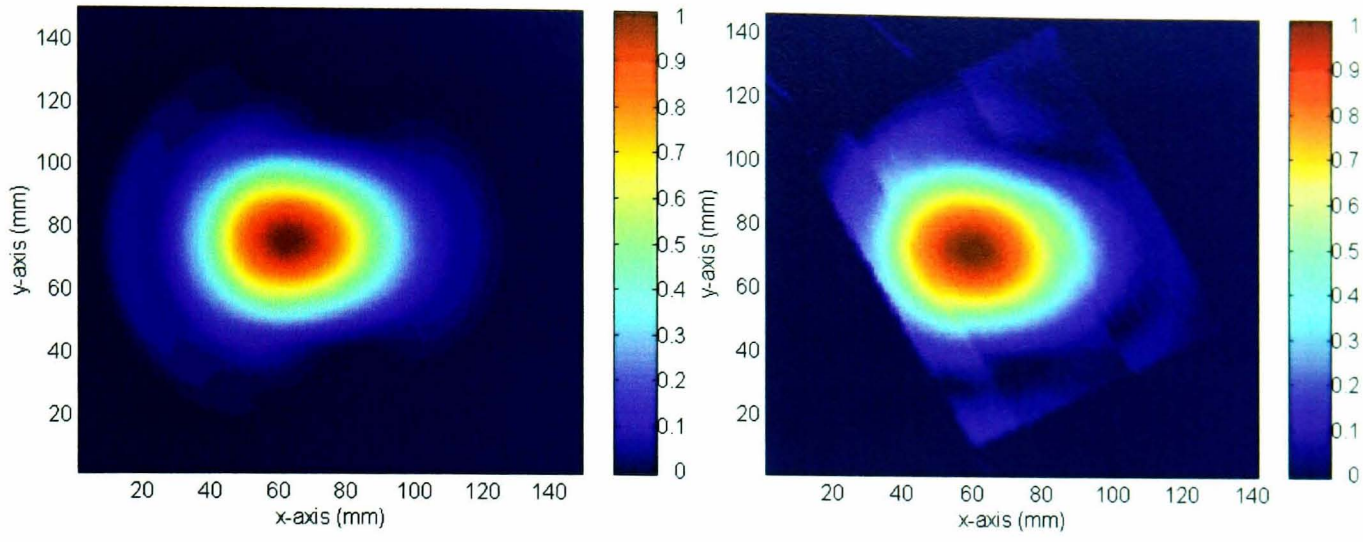

Figure 4.33: *Comparison of normalised simulated and experimental results for a water phantom with the 3.5mm dielectric layer at a height from phantom base of 9mm.*

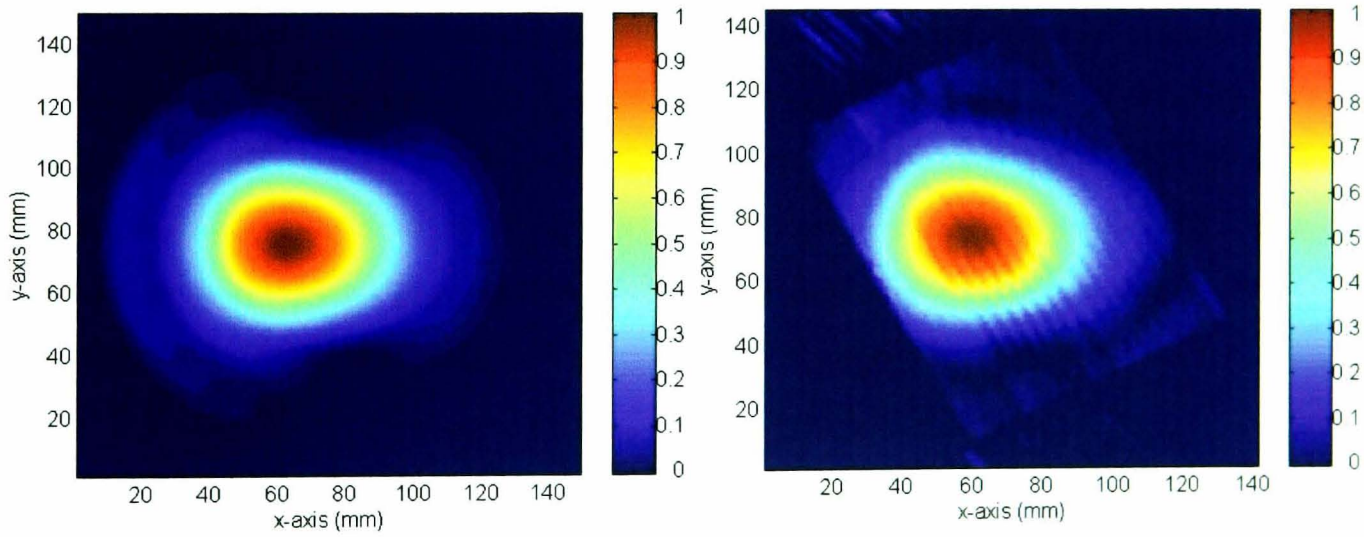

Figure 4.34: *Comparison of normalised simulated and experimental results for a water phantom with the 3.5mm dielectric layer at a height from phantom base of 9mm.*

In the test system including a larger dielectric layer of 6.5mm the results again match reasonably well, Figure 4.35. Although the experimental data shows more of a spread than the simulated data, the similarly in the power absorption pattern is still apparent.

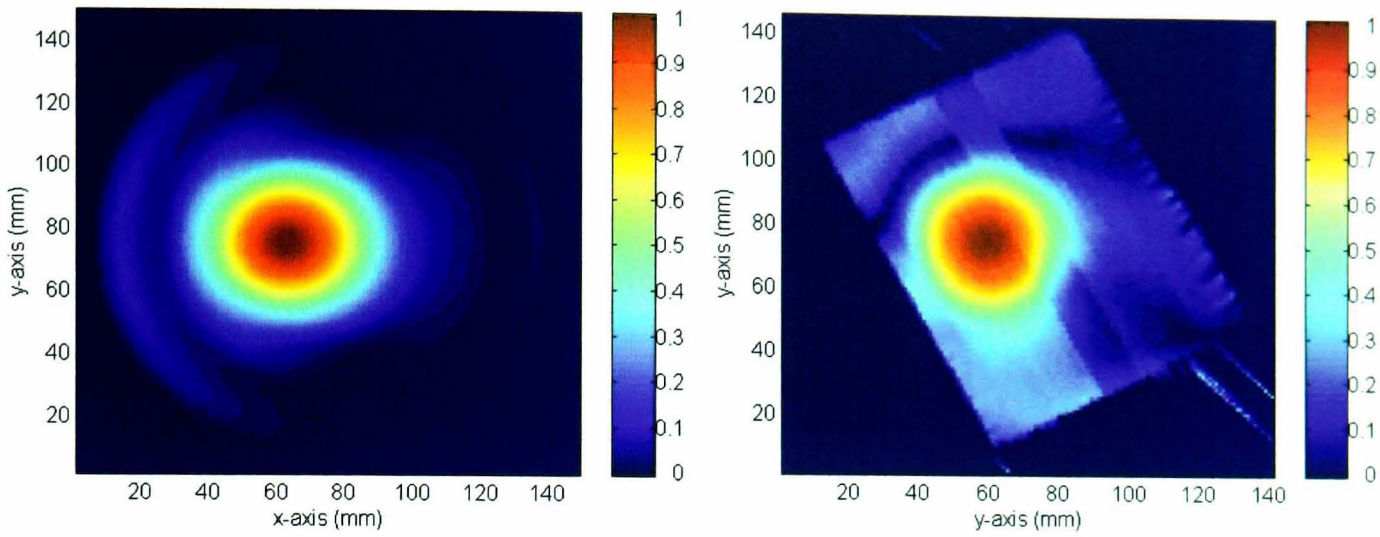

Figure 4.35: *Comparison of normalised simulated and experimental results for a water phantom with the 6.5mm dielectric layer at a height from phantom base of 13mm.*

4.5.4 Comparisons using smaller perturber data

In the case of the smaller perturbing object although the pattern obtained in most cases gives the same basic outline as the simulated result comparisons of this nature are not straightforward. Two clear exceptions to this are as detailed in Figures 4.36 and 4.37. These figures correspond to a test structure of a 3.5 mm dielectric layer measured at 6mm with a water and sucrose phantom respectively. Although the match is clearly not as good as in the larger perturber cases the agreement is reasonable.

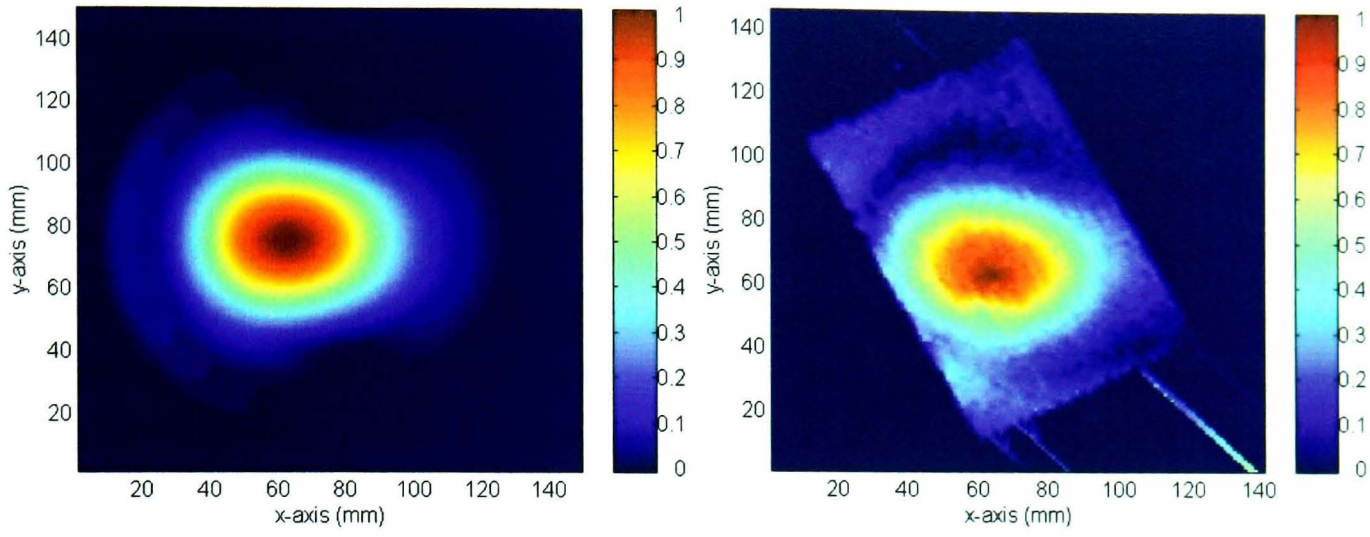

Figure 4.36: *Comparison of normalised simulated and experimental results for a water phantom with the 3.5mm dielectric layer at a height from phantom base of 6mm.*

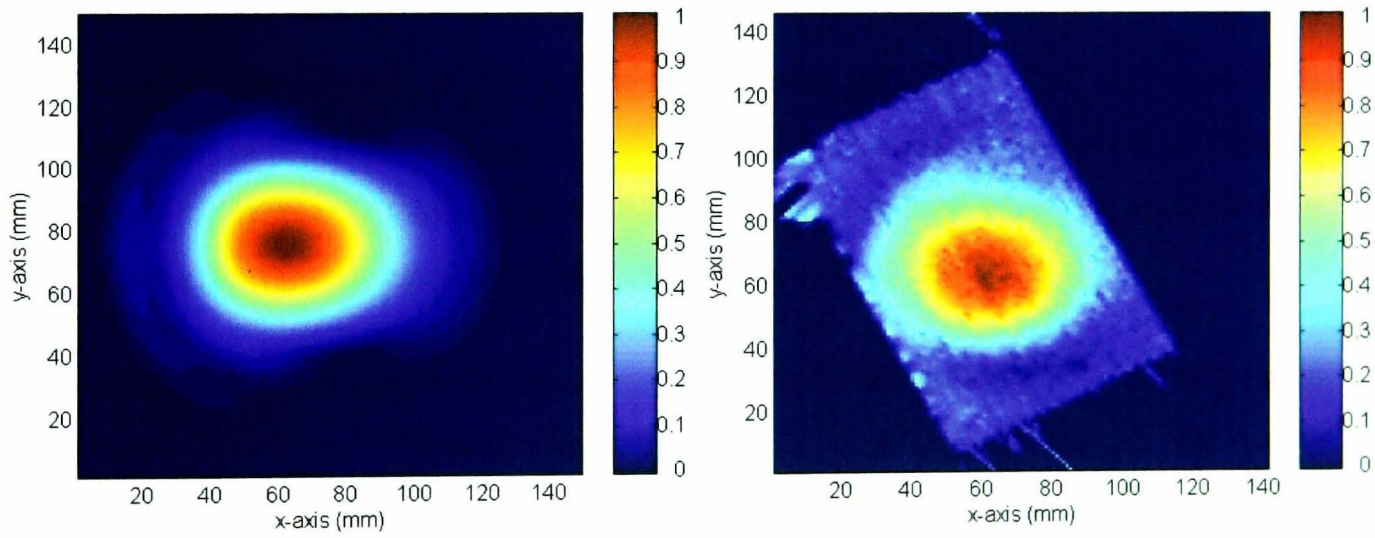

Figure 4.37: *Comparison of normalised simulated and experimental results for a sucrose phantom with the 3.5mm dielectric layer at a height from phantom base of 6mm.*

4.5.5 Effect of layers

For both experiment and simulated methods the effect on the weighting function pattern is similar. With the addition of a layer the patterns are seen to become more symmetrical and less oval in shape. As previously mentioned in the simulation the power absorption at a given height is much larger in the presence of a dielectric layer. This is not the case in the experimental work. This unexpected effect is attributed to the loss of signal radially out through the dielectric layer and is not seen in the simulated work. Several simulations on this problem have been considered and the effect has not been replicated. This discrepany may indicate a limitation of the simulation technique as it does not repeat this experimental finding. As a result of this problem comparisons of test systems with a layer present are restricted to those of relative SAR values.

4.5.6 One-dimensional weighting function comparisons

A further means of comparison is to compare the weighting function curve over the entire depth of the phantom structure. The simulation results allow for simple calculation of this curve. With the experimental work data is obtained at a limited number of heights above the phantom base. In order to compare these results with the simulated ones each set of maximum values and height positions is plotted and fitted with an exponential decay curve. In most cases there are only 2 ot 3 data points with which to make this fit, however as only a general approximation is desired this is sufficient. An exponential fit is chosen as this is the form expected of the attenuation curve.

The experimental fitted values are then compared to the simulated results and to a plane wave attenuation curve. Figures 4.38 and 4.39 give these comparisons for the water phantom alone and for the water phantom with the 3.5mm dielectric layer respectively. In both cases the simulation curve matches the experimental to a reasonable degree, particularly in the 3.5mm dielectric layer case. In order for non-accurate amplitude values not to hamper the comparison relative SAR is plotted in all cases.

In the case of the sucrose phantom less experiments were performed giving a much less

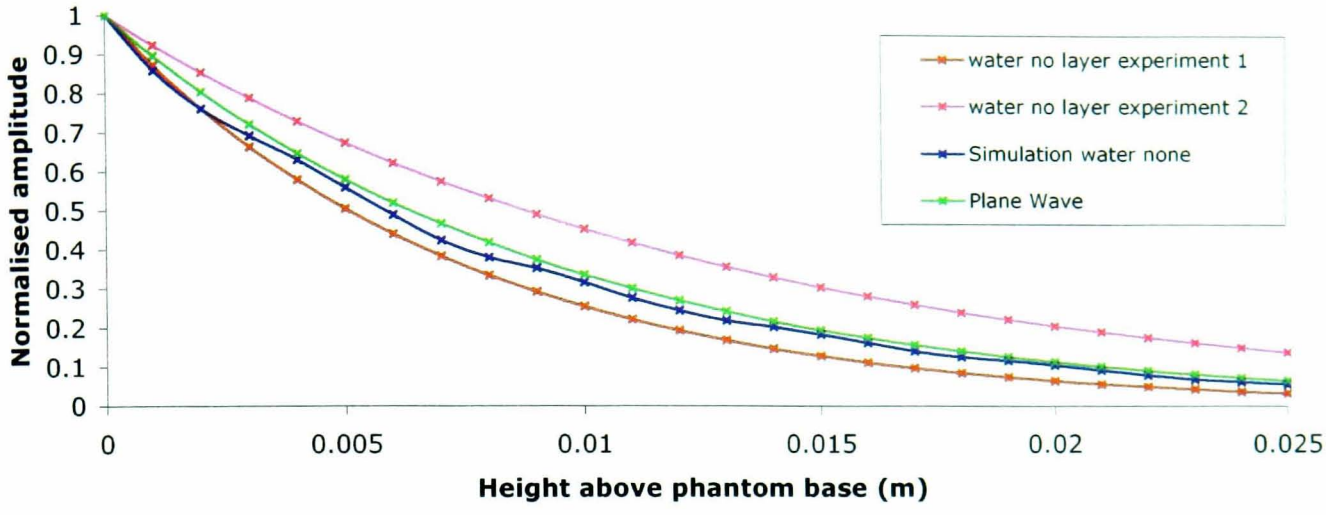

Figure 4.38: *Comparison of the exponential experimental curves and simulation data for the test system of water only.*

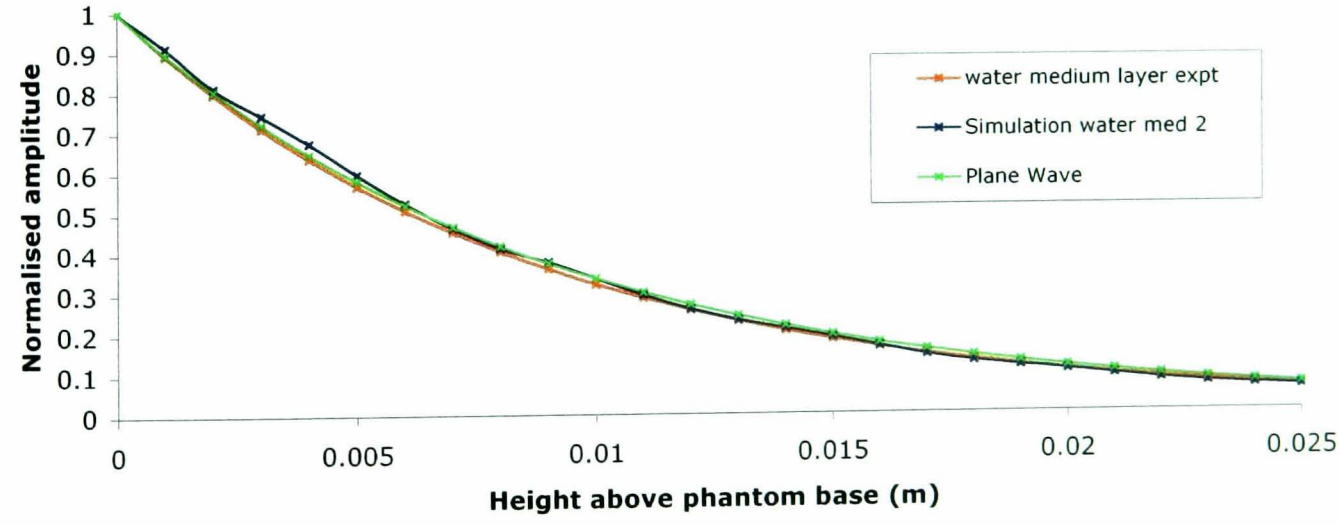

Figure 4.39: *Comparison of the exponential experimental curves and simulation data for the test system of water with the 3.5mm dielectric layer.*

accurate fit as shown in Figures 4.40 and 4.41. It is clear in both cases, sucrose alone and sucrose with 3.5mm dielectric layer, that the experimental decay is less rapid than the simulated. A less accurate fit is expected for the sucrose phantom, however, as a result of the higher attenuation of signal.

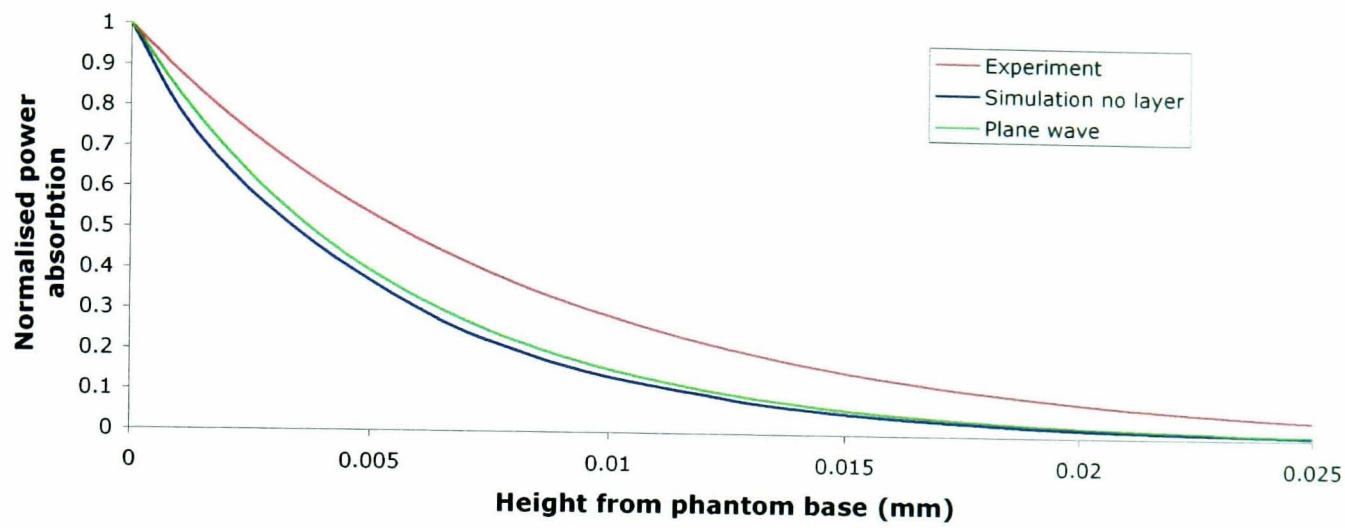

Figure 4.40: *Comparison of the exponential experimental curves and simulation data for the test system of sucrose only.*

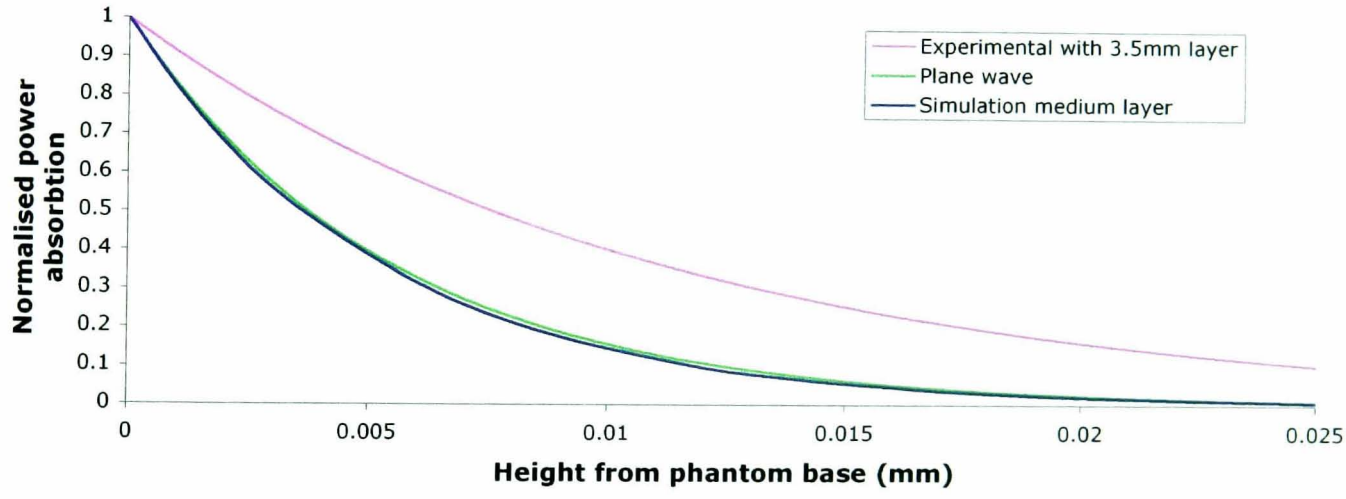

Figure 4.41: *Comparison of the exponential experimental curves and simulation data for the test system of sucrose with the 3.5mm dielectric layer.*

To ensure that the simulated results for the sucrose phantom are behaving as expected several runs of the experiment were performed for the sucrose phantom with different perturbing objects. Although this allows determination of a reasonable plot of weighting function variation with height above phantom base, which can be compared to the simulated data, it is not possible to use this as a means of amplitude comparison.

Figure 4.42 shows the experimental and simulated relative SAR data for the sucrose phantom above the 6.5mm dielectric layer. In this case a reasonable match is seen for the one-dimensional plot.

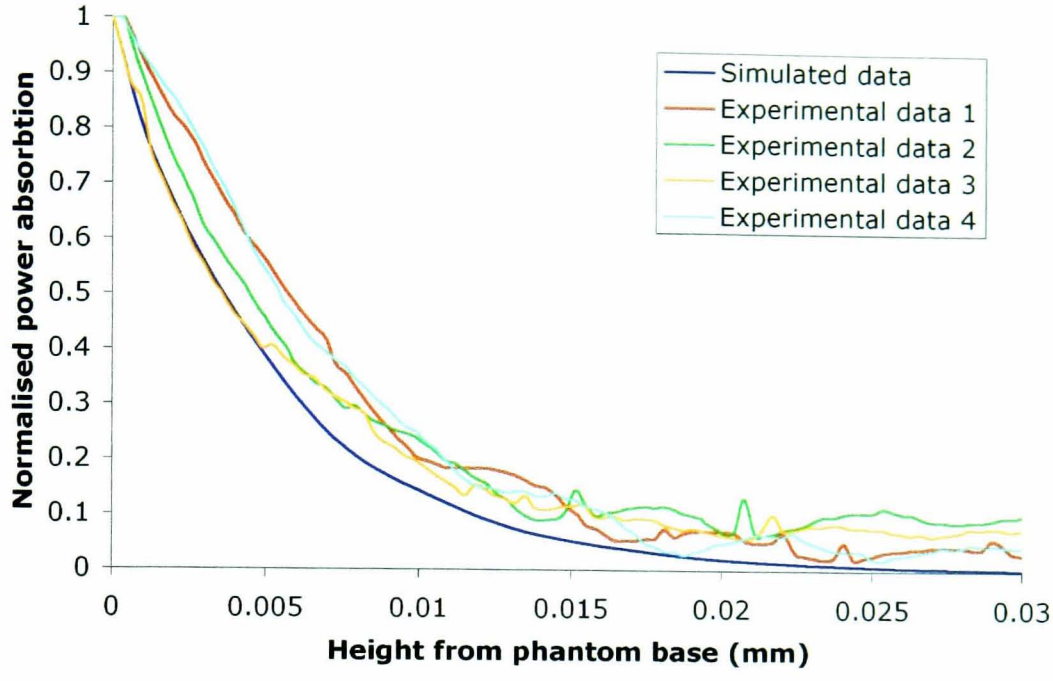

Figure 4.42: *Comparison of the exponential experimental curves and simulation data for the test system of sucrose with the 6.5mm dielectric layer.*

4.5.6.1 Error in position of z comparison

Fitting an exponential of the form $\exp(\alpha z)$ to the simulation data at a given x and y position as z varies allows determination of a value for the attenuation coefficient α. Error analysis on this fitted equation gives a measure of the effect of an error in the z co-ordinate used for the experiment / simulation comparisons. The errors introduced by an uncertainty of 2mm in the height from the phantom base for a range of water and sucrose test systems are 36% and 45% of the maximum value respectively. The larger value for the sucrose phantom is a result of the more rapid attenuation (hence larger α) in that case.

4.5.7 Maximum amplitude comparisons

As a final means of comparison the maximum amplitude values as seen for the water and sucrose phantom materials in both the experiment and simulation are displayed in Table 4.4. In all cases reasonably good agreement is seen, with the greatest relative error (relative to the experimental result) of 0.38. With the errors as described for the experimental measurements and any height mismatch combined to give an overall error this is a reasonable agreement. Comparisons are only made for the test systems in which there is no dielectric layer present.

Phantom material	Height (mm)	Experimental value	Simulation value	Relative error	Combined error
Water	6.5	24648	27500	0.116	0.36
Water	6.5	19970	27500	0.377	0.36
Water	10.5	14290	17900	0.252	0.36
Water	10.5	14590	17900	0.227	0.36
Water	14.5	13781	11300	0.180	0.36
Water	14.5	10644	11300	0.062	0.36
Sucrose	6.5	26242	31400	0.197	0.45
Sucrose	10	15979	14250	0.108	0.45

Table 4.4: *Comparison of maximum values for the experiments and simulation models of the NRP test systems by means of relative error. Also given is the total error present in the experiment and simulated results.*

4.6 Conclusions

Validation of the computational modelling of the near field of a TE_{11} mode cylindrical antenna coupled to various simulation materials, with and without the presence of dielectric layers, has been achieved. In the first instance the experimentally determined patterns of power dissipation in the x-y plane compare well with simulated results. Further to this, comparisons of the maximum amplitude of the absorbed power at a given z position from simulated and experimentally determined values agree to within experimental errors. Limitations in the computational modelling have been determined in terms of the inability of the model to reproduce the effects on the amplitude seen in the presence of dielectric layers.

As a result of this validation it can be assumed that the results of the computational models are accurate to within the stated error of 5% for the case of simple unilayer materials. Any additional discrepancy in the weighting function computation in these instances can be attributed to errors in the values used for the dielectric properties of the materials modelled.

Further to the validations in this and the proceeding chapter it is now possible to apply this modelling tool to the specific areas on interest in the determination of weigting function behaviour and other applications of microwave radiometry.

Chapter 5

Dual-frequency medical / close contact antenna for multi-frequency temperature measurement

For microwave radiometric temperature sensing a suitable "guiding" structure must couple to the viewed volume. In most cases this structure is a waveguide antenna filled with a low loss dielectric [10, 24, 48, 58] providing a broadband low power-loss structure. The presence of the dielectric loading serves to reduce the impedance mismatch between the antenna and viewed material and also to reduce the size of the waveguide [38]. Mono-mode circular [10] and rectangular waveguides with [45] and without [24, 48, 58] a flange have been considered. Multiprobe antennae consisting of arrays of rectangular waveguides have been used for correlation radiometry [11]. For the case of multi-frequency radiometry, systems with more than one waveguide [143] and systems of one cross-polarised waveguide with several receivers [25] have been introduced.

Transition from the waveguide to the coaxial feed to the radiometer receiver is achieved by means of an electric field probe placed quarter of a wavelength from the closed end of the waveguide. This probe transition can provide adequate matching over the radiometer power bandwidth and low insertion power loss with modest capacitive loading [138].

In order to measure microwave temperatures at two frequencies with a close contact

antenna it is necessary to design such an antenna under the constraints of several limiting factors. Of primary importance to the operation of the antenna is that the level of power reflection of each probe antenna within the guiding structure is kept as small as possible. The second consideration is that of any practical limitations in manufacturing the antenna. Finally it is also important to consider the power loss in the antenna with the aim of minimising any correction to the microwave temperature to account for this loss. Once designed and built the antenna can be tested on a range of phantom materials. Comparisons of the microwave temperature, generated by particular temperature profiles in known source materials, as measured by the antenna can then be compared with computed values.

5.1 Design of dual-frequency antenna

Once an initial guiding structure is chosen it is necessary to position two probe antennae within the guide, one operating centred at 1.35GHz and the other at 3.2GHz. To minimise cross-coupling between the two measurement probes they are positioned at 90° to each other. The process of determining the best possible position of the probe antenna is performed primarily using the BEST simulation program confirmed by return loss measurements.

A waveguide with circular cross section loaded with dielectric powder ($\epsilon_r' = 11$) propagating TE modes forms the basic structure. By using a waveguide of this nature propagating primarily the TE_{11} mode the relatively small change in field form from within the guide to the load material results in a low power reflection at the antenna aperture / phantom load interface [144].

In order to have TE_{11} mode propagation at both frequencies the antenna structure is oversized for operation at 3.2GHz and undersized for operation at 1.35GHz. The higher frequency field is therefore composed of the TE_{11} and some higher order modes. At 1.35GHz the waveguide length is approximately half a wavelength, resulting in a lower frequency field composed of the TE_{11} mode with some contribution from evanescent modes set up by the probe. With a smaller waveguide of this nature practical considerations of

antenna size and weight were met.

5.1.1 Probe positioning

Theoretically to have maximum power transfer from antenna to waveguide structure and then this structure to the phantom material the location of the probe antenna within the waveguide should be at a distance of approximately:

$$\lambda_g/4 \tag{5.1}$$

from the waveguide closed end, where λ_g is the guide wavelength. Practically because of finite probe diameter and associated fringing fields this exact distance may not be the best position for minimum power reflection. It is necessary therefore to simulate several configurations with small changes to the distance used based around this value. Additionally from similar considerations the length of the monopole used in the simulation should be approximately equal to a quarter of the guide wavelength. Again, for the same reasons as above, in practice this may not be exact hence the length of the monopole used is varied in several sets of simulations.

5.1.2 Form of results

Further to the forms of validation considered in chapter 3 the power reflection (equation 3.3), is plotted against the ratio of the length of the monopole and the simulation wavelength. In order to obtain a range of data points on the latter axis it is necessary to vary either the frequency (and thus wavelength) or the monopole length. In most cases the power reflection curve is given for a specific monopole length and at a range of frequencies.

From section 3.1.3, it can be noted that the best matching of simulation to experiment in the results of power reflection occurred when the length of the probe antenna was taken to be the length of the metal rod and the monopole source cell. For this reason the length of the monopole is stated as the entire length, metal rod and source cell in all results. Current and voltage information are obtained directly from the modelling software and

can be processed as in section 3.1.2.1 to obtain a value for the power reflection seen in each simulation.

5.1.3 Phantom materials

The completed dual frequency radiometer will be used for measurements on a variety of materials with dielectric properties that vary from pure water to high protein content mixtures. Simulations were performed with a phantom composed of 25% protein mixed with saline solution (see section 6.1 for details of the calculation of the permittivity and conductivity of such a mixture). In the first instance the conductivity and permittivity were assumed constant over the frequency ranges - taking the value as calculated at the centre frequency (1.35GHz and 3.2GHz). In the next set of simulations the values used were specific to each simulation frequency. In addition to this a third model incorporating a free space (air) phantom is included. (This final model is considered for the purposes of checking the modelling and not for signal generation purposes.) The dielectric properties of the phantom materials are given in tables 5.1 and 5.2 for 1.35GHz and 3.2GHz respectively.

Frequency (GHz)	Relative Permittivity	Conductivity (Sm^{-1})
1.3	54.21	1.26
1.35	54.18	1.2
1.4	54.16	1.3
1.5	54.10	1.35
1.6	54.05	1.40
1.8	53.92	1.52

Table 5.1: *Relative permittivity and conductivity for 25% protein/saline mixture in the frequency range 1.3 to 1.8GHz.*

Frequency (GHz)	Relative Permittivity	Conductivity (Sm^{-1})
3.0	52.88	2.47
3.2	52.66	2.67
3.3	52.55	2.77
3.4	52.43	2.88
3.5	52.31	2.99
3.6	52.19	3.10
3.8	51.93	3.33
4.0	51.67	3.57

Table 5.2: *Relative permittivity and conductivity for 25% protein/saline mixture in the frequency range 3.0 to 4.0GHz.*

5.1.4 Probe antenna for 1.35GHz operation

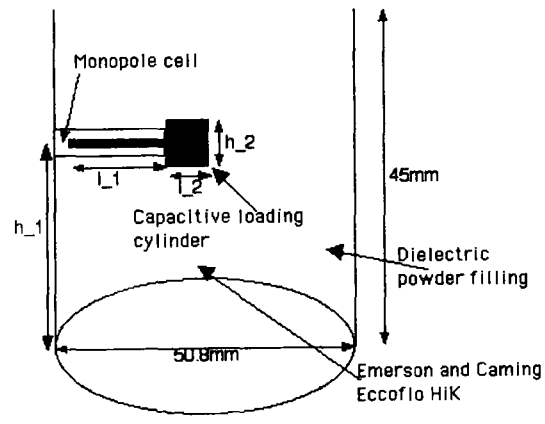

Figure 5.1: *Schematic of the form and position of the 1.35GHz probe antenna.*

Figure 5.1 shows a schematic diagram of the waveguide antenna and probe intended for 1.35GHz operation. Marked on the figure are the various parameters which are varied in the simulations. In an attempt to lower the frequency at which minimum power reflection occurred a "capacitive loading" tip of perfectly conducting metal was added to the end of the monopole rod. In addition to the height above base plate, h_1 and length of the rod, l_1, the length and width of the tip, h_2 and l_2 respectively, were varied. Finally the probe was sheathed in PTFE, and both the position and length of this dielectric coating were also considered.

5.1.4.1 Frequency independent protein / saline phantom loading material

In the case of the 25 % protein / saline mixture phantom the power reflection curves are considered over a frequency range of 1.3 - 1.8GHz, Figure 5.2. Each configuration is simulated at the specific frequencies of: 1.3, 1.35, 1.4, 1.5, 1.6 and 1.8GHz and an associated value of power reflection determined.

In the first instance the height of the probe from the base of the waveguide was set to be 26mm and the length of the monopole rod and metal tip investigated. Figure 5.2 gives the results of these simulations and clearly shows that a minimum pattern is obtained. The minimum position, however, in all cases corresponds to a frequency of 1.6GHz. Moreover the value of the power reflection, corresponding to the 1.35GHz frequency, is greater than 40 % for all configurations considered.

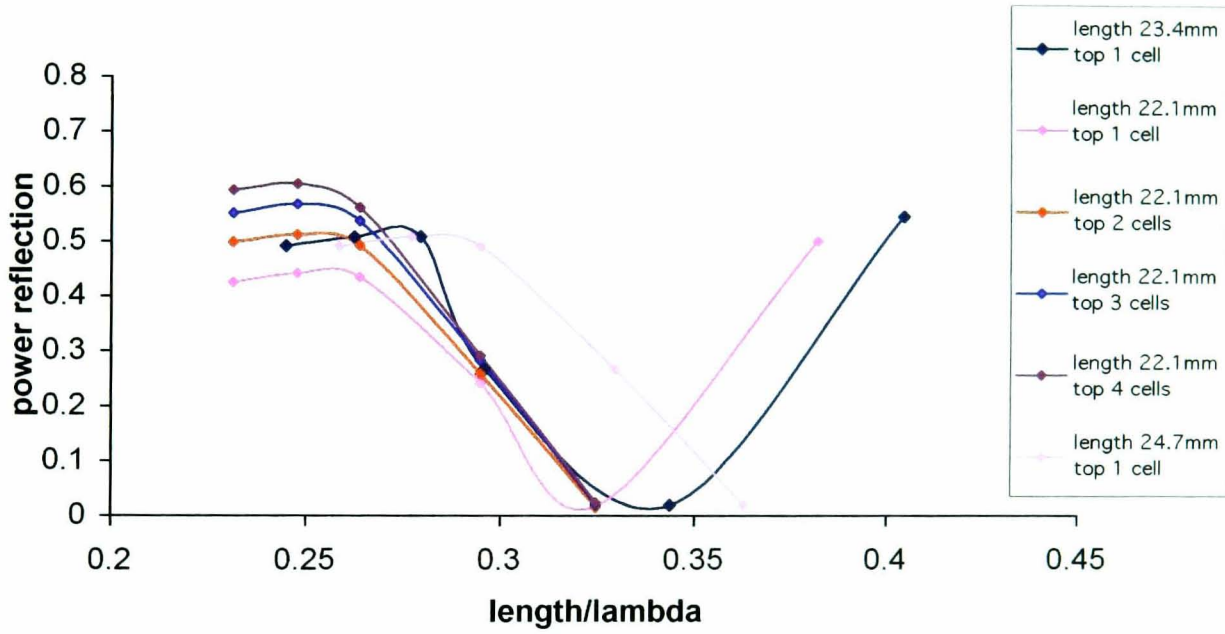

Figure 5.2: *Power reflection curves with frequency independent protein / saline phantom mixture. Variations in monopole length and top size considered are shown. In all cases the data points correspond to the simulation frequency (1.3, 1.35, 1.4, 1.5, 1.6 and 1.8GHz).*

Increasing the length of the monopole has no notable effect on the size of the minimum. Increasing the length of the top serves to increase the power reflection in this case. As no improvement could be found using varying lengths with this phantom type, a phantom configuration in which the parameters were frequency dependent, was considered.

5.1.4.2 Frequency dependent protein / saline phantom mixture.

The sets of simulations performed with the frequency dependent phantom material properties considered the effect of both variations in the length of the monopole rod and in the height of this rod above the end of the waveguide.

Figure 5.3 illustrates the effect of changing the length of the monopole and as before the minima pattern is obtained but with the minimal point at frequencies greater than or equal to 1.5GHz. In all cases the monopole was fixed at a height of 26mm from the waveguide base. Reduction in the length of the monopole again does not have a marked effect on the position of the power reflection minimum. Again the addition of a top serves to increase the power reflection magnitudes seen.

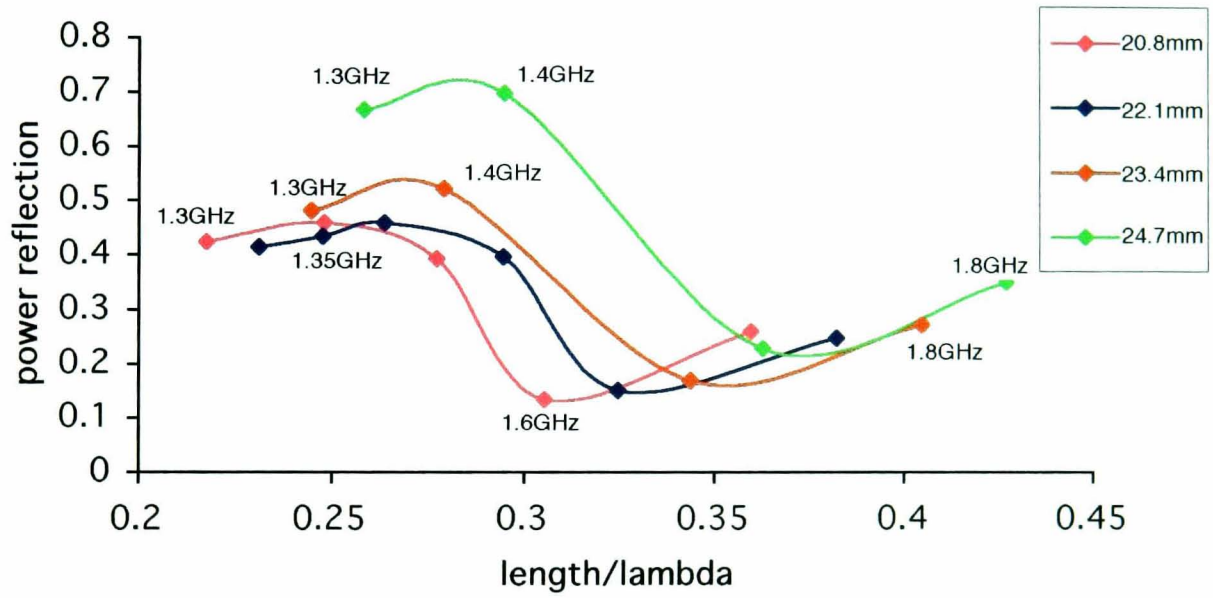

Figure 5.3: *Power reflection curves with frequency dependent protein / saline phantom mixture. Variations in monopole length and top size considered are shown. In all cases the data points correspond to the simulation frequency used. Data points correspond to simulation frequency, varying from 1.3 to 1.8GHz.*

It can be seen from Figure 5.4 that an increase in the position of the monopole above the base of the waveguide leads to a lower valued minimum. The minimum, however, still occurs at frequencies higher than desired. In all cases the length of the monopole was fixed at 22.1mm with a top of length 1.3mm. Again for this phantom extending the length of the top has little effect on the power reflection curves.

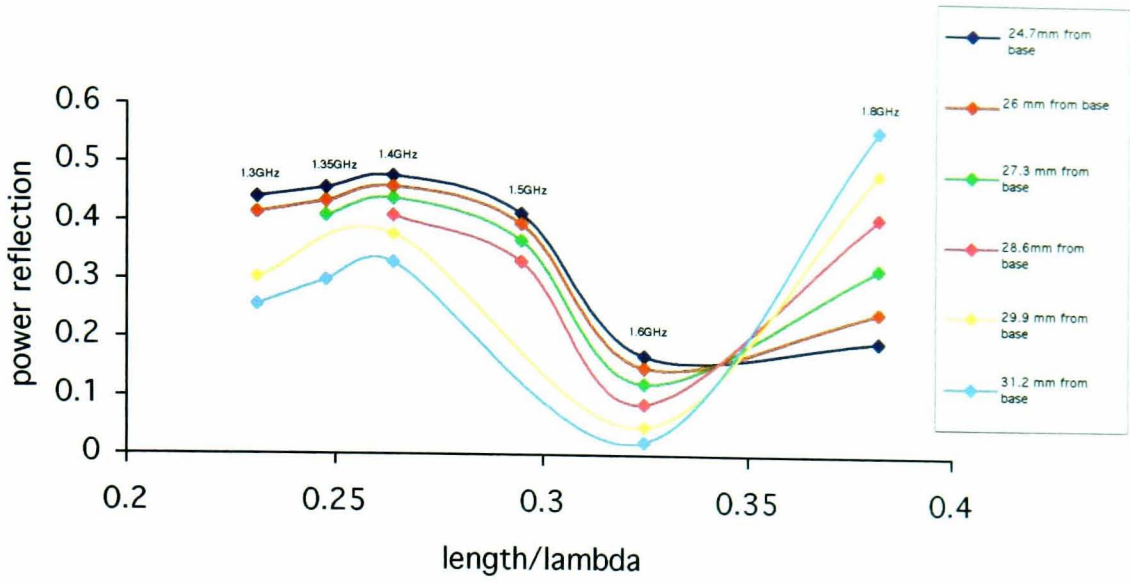

Figure 5.4: *Power reflection curves centred around 1.35GHz with frequency dependent protein / saline phantom mixture. Variations in distance between the monopole rod and the waveguide base are considered. In all cases the data points correspond to the simulation frequency used (1.3, 1.35, 1.4, 1.5, 1.6 and 1.8GHz).*

5.1.4.3 Improved monopole model

From the results of the previous sections (5.1.4.1 and 5.1.4.2) it is clear that there is a fundamental problem with the design of the antenna which makes operation at 1.35GHz difficult. The physically simplest factor to change is that of the radius of the monopole. In all configurations considered to far the radius of the monopole and associated rod was set at 0.65mm. Radii of 1.5 and 2mm were then considered.

For a monopole of radius 2mm it is necessary for the cell size of the simulation to be set to 4mm. For this case the power reflection curves show the desired minima pattern with minimum position at 1.4GHz as shown in Figure 5.5.

The cell size required to model such an antenna is such that the required accuracy over the range of test phantoms materials will be inadequate. As a result a compromise of using a model monopole radius of 1.5 mm (cell size 3mm) is required. In this case there is still a well defined minimum in the power reflection curve, although it is of a slightly larger magnitude. Figure 5.6 shows the changes in the pattern of power reflection as the

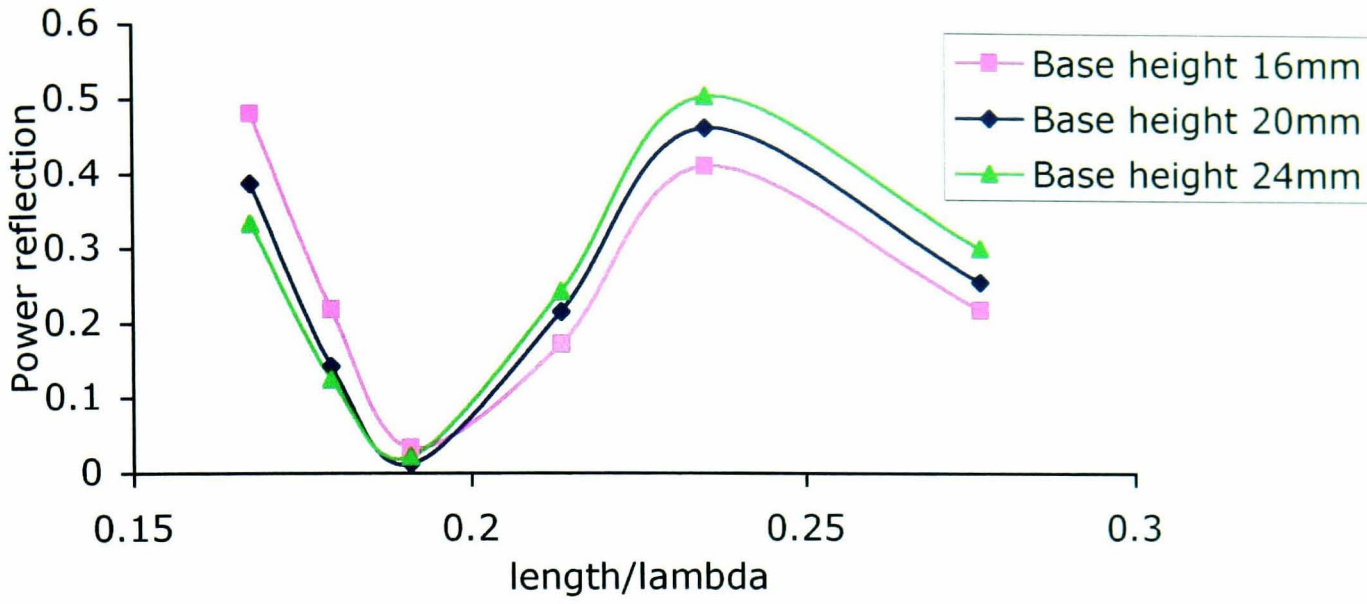

Figure 5.5: *Power reflection curves with frequency dependent protein / saline phantom mixture. Variations in distance between the monopole rod and the waveguide base are considered for a monopole of diameter 4mm. In all cases the data points correspond to the simulation frequency used (1.3, 1.35, 1.4, 1.5, 1.6 and 1.8GHz).*

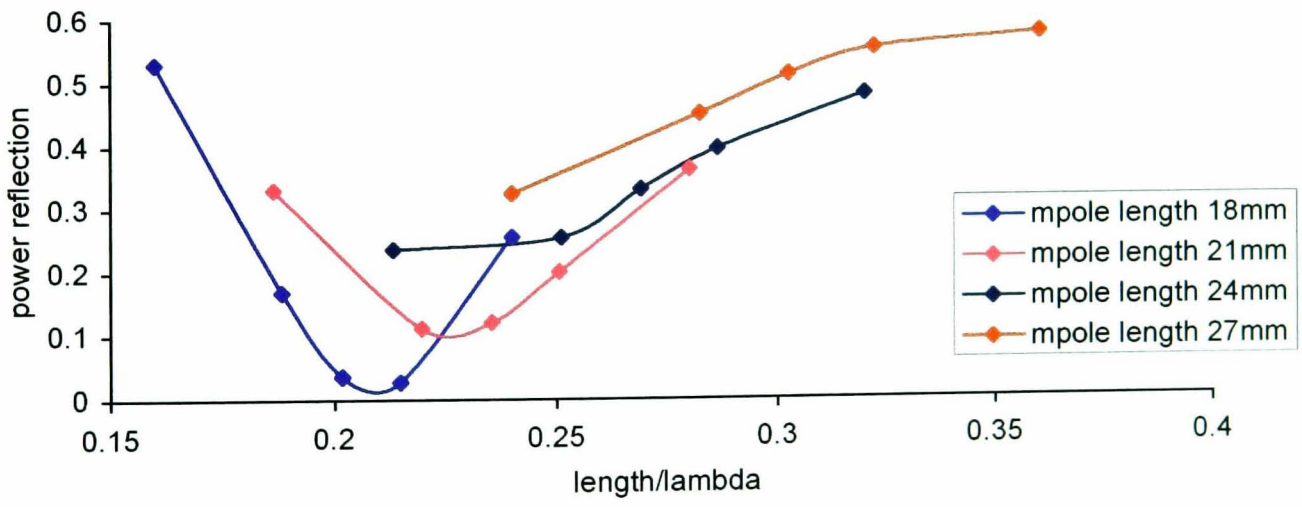

Figure 5.6: *Power reflection curves with frequency dependent protein / saline phantom mixture. Variations in the length of the monopole rod are considered for a monopole of diameter 3mm. In all cases the data points correspond to the simulation frequency used (1.2, 1.3, 1.35, 1.4 and 1.5GHz).*

length of the monopole increases from 18 to 27mm at a fixed distance from the base of the waveguide. For these simulations no top was attached to the monopole and the PTFE coat was limited to two cells, one surrounding the generator cell and the other covering the first cell of the metal rod.

For this configuration there is clearly a useful minimum in power reflection at 1.35GHz. Variations in the height above waveguide end of the monopole around this value (24mm) do not produce significantly different values. Although the result for a monopole length of 18mm represents the lower power reflection, the length of 21mm is chosen. The reason for this choice is that the curve is shallower and gives a better value over the entire operating bandwidth.

5.1.4.4 Optimal 1.35GHz probe configuration

The configuration chosen for 1.35GHz operation, based on the modelling, is such that the: entire monopole length = 21mm; height of monopole above waveguide base = 24mm; monopole radius = 1.5mm; and PTFE coat = 2 cells. As a final check of the suitability of this configuration a range of sample phantom materials from 0-80 % protein in saline were investigated. The dielectric parameters used are those determined in Section 6.1. Figure 5.7 details the result of these investigations.

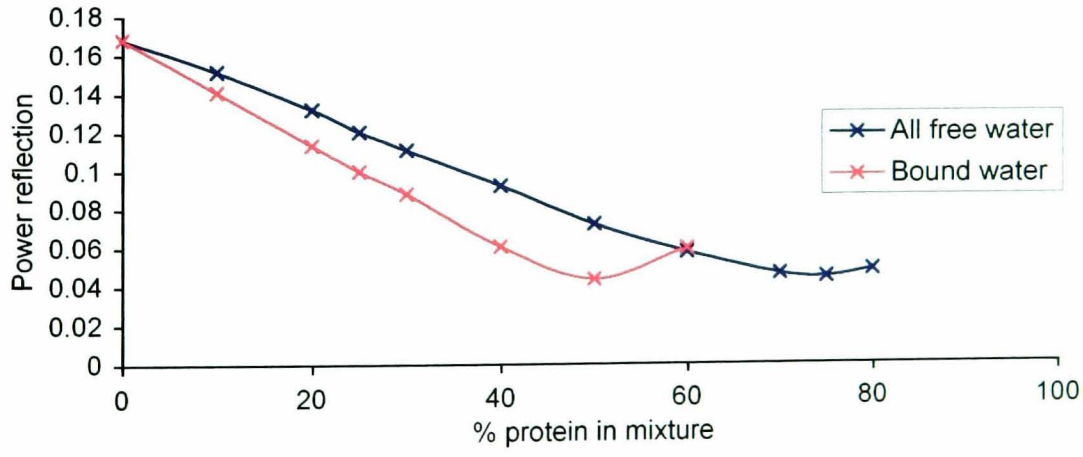

Figure 5.7: *Power reflection over a range of phantom materials ranging from pure saline to 80% protein in a protein saline mixture for 1.35GHz antenna.*

It can be seen that in all cases the power reflection is below 20%. This is acceptable and so the configuration is considered suitable.

5.1.5 Probe antenna for 3.2GHz operation

This process must then be repeated to determine the most suitable probe configuration for operation at 3.2GHz. A schematic of the 3.2GHz monopole probe is given in figure 5.8 Marked on the figure are the various parameters which are varied in the simulations. In addition to the height above base plate, h_3, and length of the antenna, l_4, the length of coating of PTFE around the monopole, l_3 was also investigated. In the first instance the radius of the monopole was set at 0.65mm.

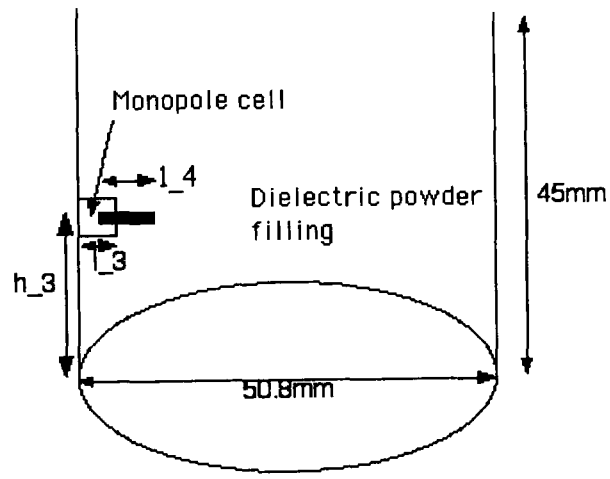

Figure 5.8: *Schematic of the form and position of the 3.2GHz probe antenna.*

5.1.5.1 Frequency independent protein / saline phantom mixture.

For the initial phantom of a protein / saline mixture with frequency independent parameters the power reflection curves for several lengths are shown in Figure 5.9. As the monopole length increases the power reflection at 3.2GHz falls to give a reasonable value. For the smaller monopole lengths the power reflection corresponding to 3.2GHz is above 20%.

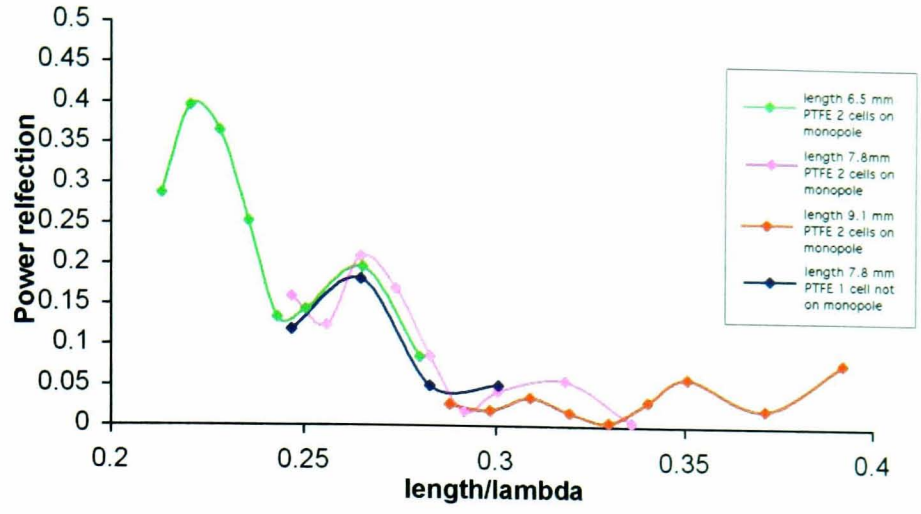

Figure 5.9: *Power reflection curves with frequency independent protein / saline phantom mixture. Variations in monopole length and ptfe covering are shown. The data points correspond to the simulation frequency (3.0, 3.1, 3.2, 3.3, 3.4, 3.5, 3.6, 3.8 and 4.0GHz or the subset 3.0, 3.2, 3.4 and 3.6GHz.*

5.1.5.2 Frequency dependent protein / saline phantom mixture.

In the case where the phantom materials are specific to the frequency of interest the results are more promising. As can be seen in Figure 5.10 increasing the length of the monopole again gives smaller power reflection. In particular for the configuration with a monopole length of 9.1mm gives an extremely low value of power reflection at 3.2GHz of 0.0005. For completeness Figure 5.11 shows the effect on the power reflection of a change in PTFE coating of the monopole. Only minor changes to the power reflection curves are seen as a result.

5.1.5.3 Free space phantom

In the case of the air phantom large variations in the power reflection curve are seen, Figure 5.12. Again for a monopole of length 9.1mm there is a reasonable minimum in power reflection corresponding to the frequency of 3.2GHz. For the other lengths the power reflection at 3.2GHz is quite large as a result of a mis-match reflection at the antenna aperture, a dielectric to air transition. The sensitivity to frequency of the phase of this reflection at the monopole will give rise to this varying power reflection.

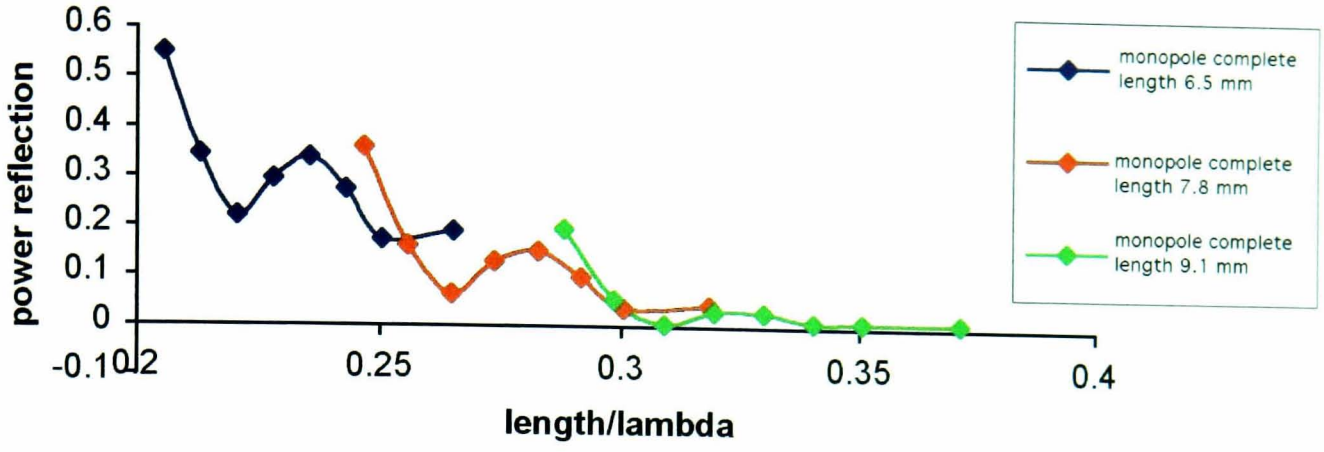

Figure 5.10: *Power reflection curves with frequency dependent protein / saline phantom mixture. Variations in monopole length and ptfe covering are shown. In all cases the data points correspond to the simulation frequency (3.0, 3.1, 3.2, 3.3, 3.4, 3.5, 3.6 and 3.8GHz).*

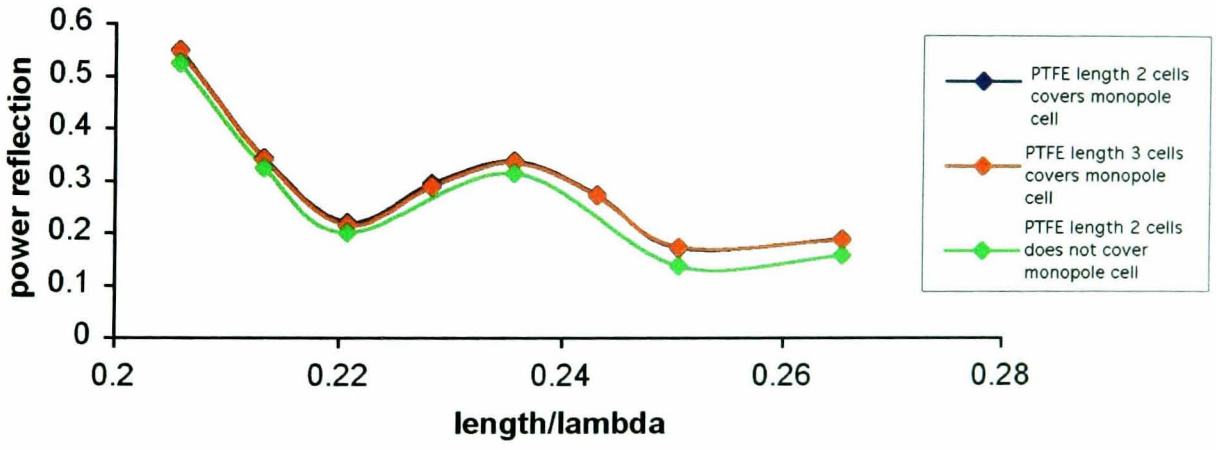

Figure 5.11: *Power reflection curves with a frequency dependent protein / saline phantom mixture. Variations in PTFE covering, as detailed on plot, for a monopole of length 7.8 mm and at a height of 6.5mm. Data points correspond to the simulation frequency (3.0, 3.1, 3.2, 3.3, 3.4, 3.5, 3.6 and 3.8GHz).*

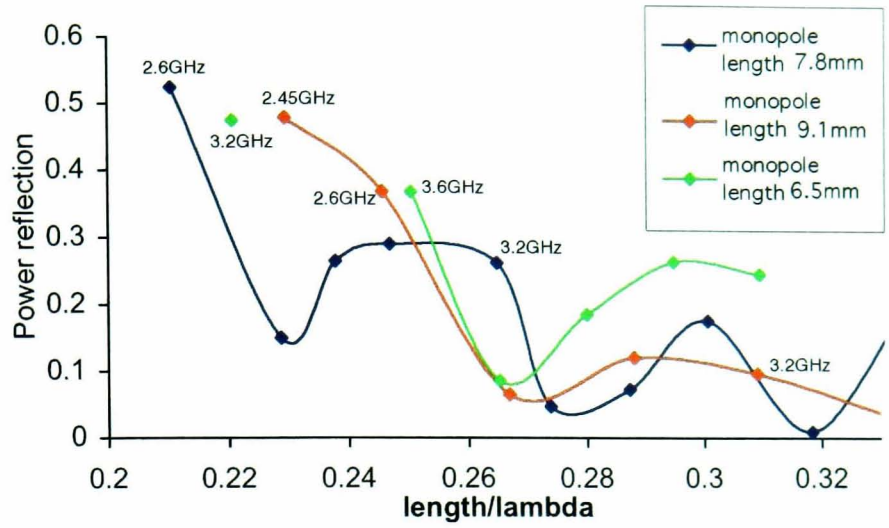

Figure 5.12: *Power reflection curves centred around 3.2GHz with free space phantom. Variations in monopole length are shown. Data points correspond to a range of simulation frequencies (varying from 2.45GHz to 4.4GHz).*

For all simulations of the 3.2GHz monopole considered so far the monopole has been at a height of 6.5mm from the waveguide closed end. There is little effect of variations in this height as shown in Figure 5.13.

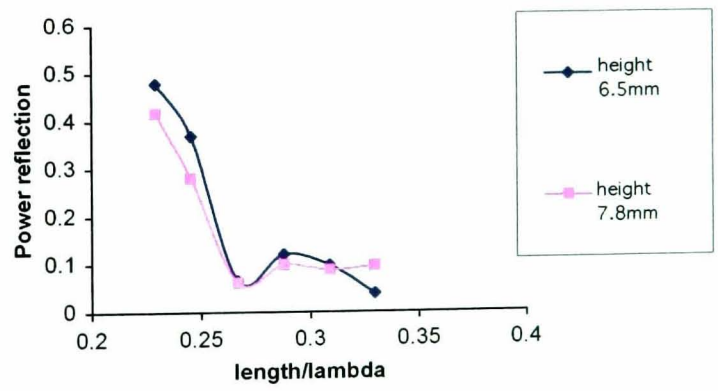

Figure 5.13: *Power reflection curves with free space phantom. Variations in the height of the monopole above the waveguide base. The data points correspond to the simulation frequency (2.45, 2.6, 2.8, 3.0, 3.2 and 3.4GHz).*

5.1.5.4 Optimal 3.2GHz probe configuration

The configuration chosen for 3.2 GHz operation is such that the: entire monopole length = 9.1mm; height of monopole above waveguide base = 6.5mm; monopole radius = 0.65mm; and PTFE coat = 2cells. The power reflection values obtained with this antenna configuration with a frequency dependent mixture is shown in Figure 5.14 and can be seen to be very small at the operating frequency of 3.2GHz.

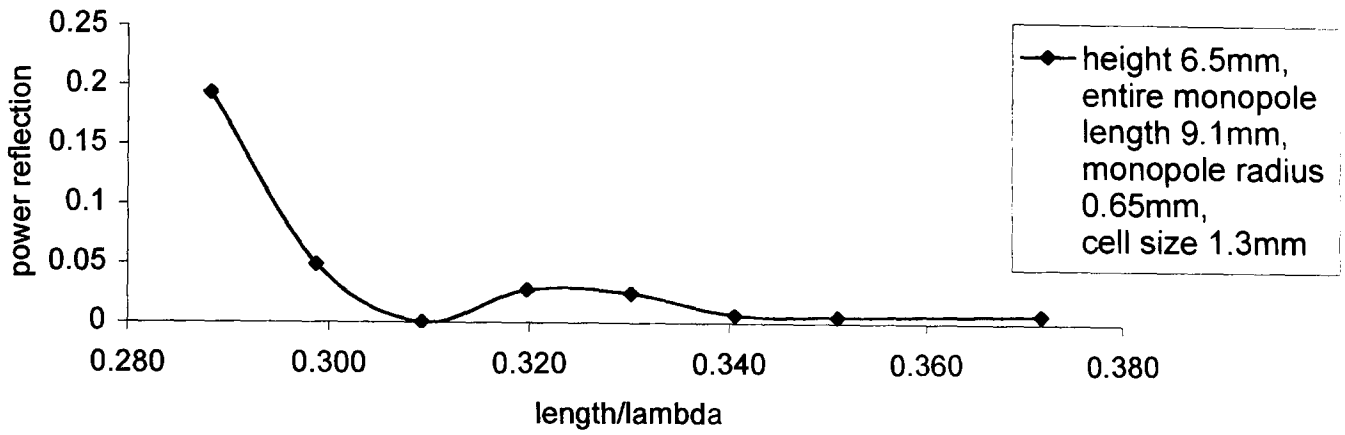

Figure 5.14: *The power reflection curve seen for the optimal probe configuration with a frequency dependent saline / protein mixture. The data points correspond to the simulation frequency used (3.0, 3.1, 3.2, 3.3, 3.4, 3.5, 3.6 and 3.8GHz)*

Again as a final check of the suitability of this configuration a range of sample phantom materials from 0-80 % protein in saline were investigated. The dielectric parameters used are those determined in Section 6.1. Figure 5.15 details the result of these investigations and it can be seen that in all cases the power reflection is below 0.25%. This is extremely small and so the configuration is considered suitable.

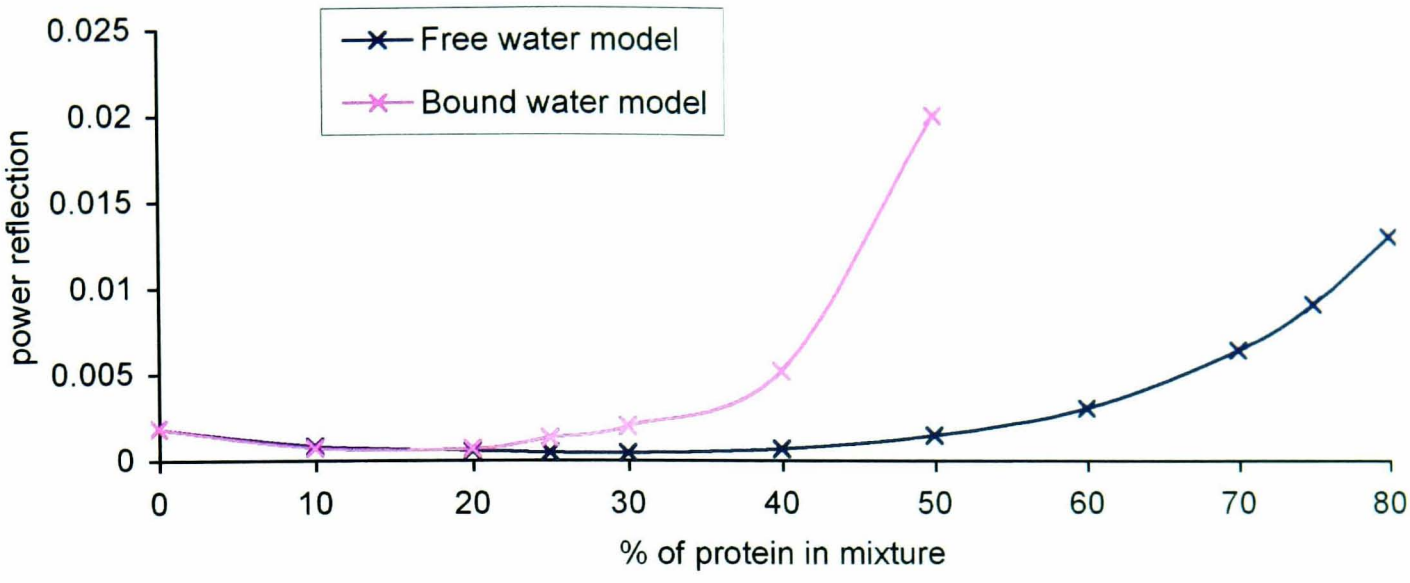

Figure 5.15: *Power reflection over a range of phantom materials ranging from pure saline to 80% protein in a protein saline mixture for 3.2GHz antenna.*

5.1.6 Complete dual frequency antenna configuration

The completed dual frequency antenna incorporates both probe antenna, as shown in Figure 5.16, and can be operated at 1.35 and 3.2GHz. Experimental return loss measurements (performed by D. Land [138]) confirmed the modelled predictions.

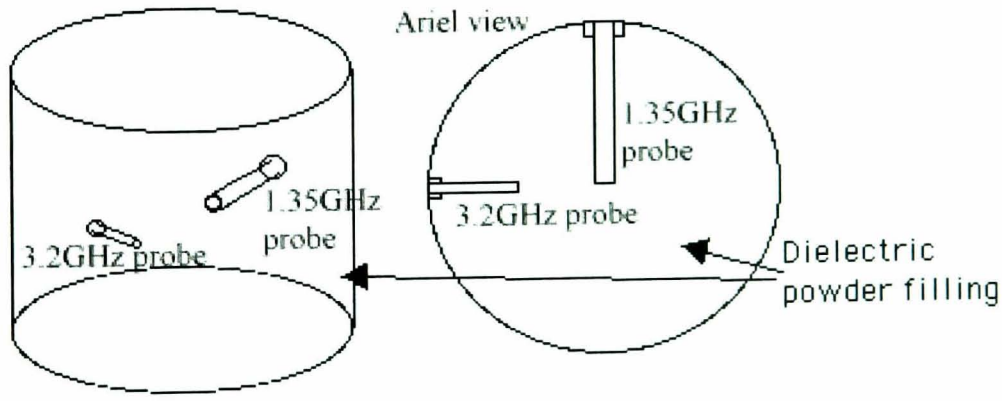

Figure 5.16: *Schematic of completed waveguide antenna operating at two frequencies, probe antenna positioning is shown.*

5.2 Experimental work with dual frequency antenna

Once constructed the dual frequency antenna is first tested and then used to provide data to be used in temperature reconstruction investigations. It is possible using this antenna to measure the microwave temperature at two frequencies for known temperature distributions. The accuracy of the different temperature profile retrieval methods discussed in chapter 7 can then be considered.

Unfortunately as a result of the amount of radiation emitted from the large number of computer systems in the vicinity of the experimental laboratory it is necessary to shield the antenna. This shielding, primarily required for operation at 1.35GHz (as computer processor speeds are getting very close to this value), is provided by a microwave oven cavity. This form of cavity is designed to ensure minimal radiation transfer into or out of the closed cavity structure.

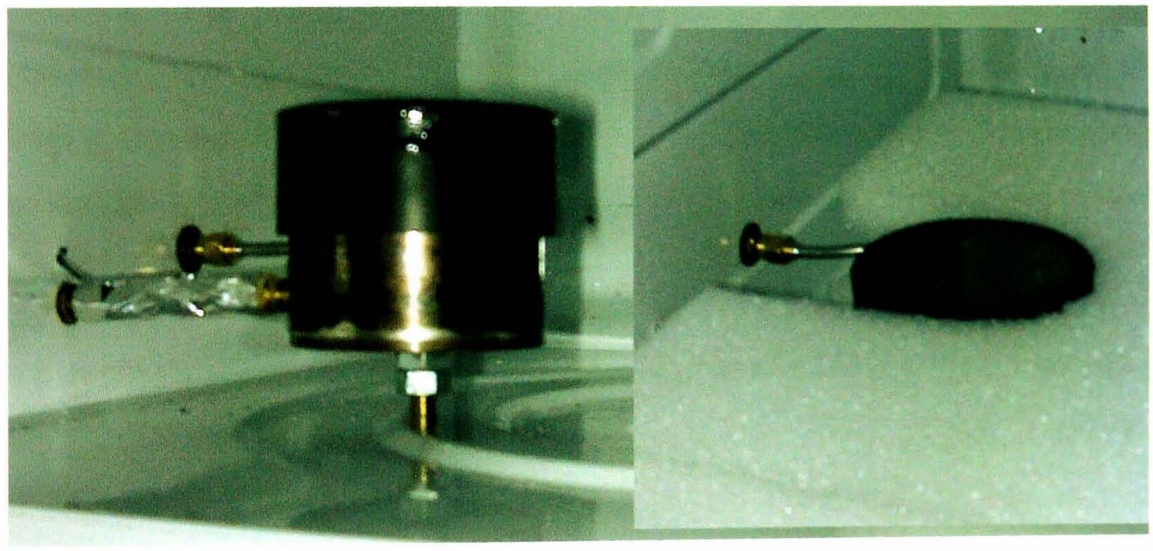

Figure 5.17: *The completed dual frequency antenna housed inside a microwave oven cavity. Inset picture shows the supporting material surrounding the antenna.*

Figure 5.17 shows the dual frequency antenna positioned inside the cavity with outputs to the radiometer from each frequency probe. Inset in this picture is the antenna surrounded by material to provide mechanical support. The presence of this material allows simple positioning of a phantom structure at the antenna aperture.

The antenna / radiometer system is calibrated daily with a water mixture of known uniform temperature, measured using a platinum resistance thermometer accurate to 0.1°C. This daily check was necessary to account for small changes in calibration parameters resulting from differences in ambient temperatures from day to day. The use of a uniform temperature solution requires that the microwave temperature reading obtained at each measurement frequency should be equal and should match the actual temperature of the liquid. As the microwave signal measured comes from what is inherently a noise source the raw data is smoothed to give a more accurate reading. Operation at 1.35GHz suffers from more interference as a result of the use of a narrower bandwidth and higher loss components increasing the noise temperature of the system.

5.2.1 Potato phantom with linear temperature gradient

In the first instance an attempt is made to produce a quasi-linear temperature profile in a given material. The phantom material in which this gradient is to be set up is chosen to be a mashed potato mixture. The reasons for this choice of material includes the ease with which a repeated sample can be produced, the semisolid nature of the completed phantom and finally the similarity of the potato dielectric properties to those of biological materials and many other foodstuffs.

The mashed potato phantom was produced from a commercially available instant potato mix [145]. The completed mixture is composed of water (~80% by mass), sodium chloride (~0.2%), and various other solids (carbohydrates, fibre, protein and fat). Section 6.1.3 details the determination of the dielectric properties of the mashed potato at the frequencies of 1.35GHz and 3.2GHz over the temperature range of 0-50°C.

5.2.1.1 Experimental phantom apparatus

The apparatus used to produce a linear temperature gradient comprises an infra red heat lamp above the potato phantom and a source kept as close to 0°C as possible below the phantom, see Figure 5.18. The mashed potato mixture is encased in various hollow

polystyrene boxes with cling-film acting as base and lid. The cling-film is used primarily to prevent the mashed potato drying out, i.e. to keep the water content of the mixture stable. Further to this it enables ease of movement of the phantom between heating apparatus and the measuring antenna. The thickness of the cling film is such that it has a negligible effect on the microwave temperature reading.

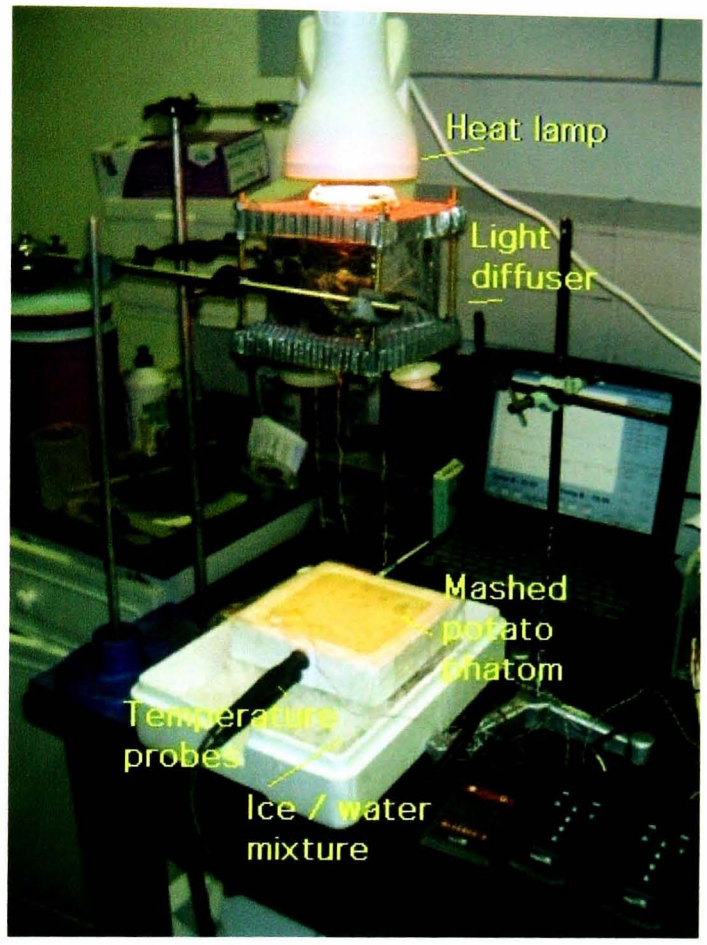

Figure 5.18: *Apparatus used to produce linear temperature gradient in potato mixture. Includes an infra red heat source, a light diffuser, the mashed potato phantom with temperature probes and an ice/water mixture at 0° C.*

The base of the potato phantom is keep cold by using a continually monitored ice/water mixture which will remain at or very close to 0°C. A heat sink is attached to the base of a metal plate which is positioned inside the ice / water solution. The potato mould is then placed on top of this plate. At a distance of approximately 20cm above the phantom mould are a heat lamp and light diffuser. The temperature profile in the potato is measured through the strategic positioning of thermocouple probes near the centre of the phantom at varying heights. Over time a quasi-linear gradient across the potato mixture will be set up using this apparatus, shown in Figure 5.18.

Each thermocouple probe and meter are calibrated to within an error of 0.1°C using the platinum resistance thermometer. A temperature probe attached to the metal base plate is calibrated to give an indication of the temperature of the base of the potato mixture. The error in the latter temperature is larger than for the other probes ($\sim$ 0.5°C), however the contribution to the overall microwave signal is smallest from this position so this larger error is acceptable. Although this method is acceptable when determining the base temperature prior to microwave measurement it does not allow further base temperature determination. For this reason a probe is soldered to a small copper plate (1cm$\times$1cm) and this plate placed in contact with the potato. A second temperature plate, coated with reflective paint, is used to determine the top surface temperature. The mashed potato phantom had dimensions of approximately 135mm x 135mm x 40mm and required 1 to 2 hours heating to produce a linear temperature profile.

One of the main sources of error in the accurate determination of the linear profile produced is in the exact knowledge of the position of the temperature probes. To ensure that the probes enter the polystyrene outer layer of the phantom at right angles to the side a perspex holder is employed. Small holes, approximately every one centimetre, in a perspex block ensure that each probe is positioned at a known height in the phantom and that each probe is straight. Small variations from this expected height are determined upon completion of the experiment when the probes are removed.

5.2.1.2 Heat diffuser

The difficulty in this arrangement lies in ensuring uniform heating across the surface of the potato phantom. To achieve the desired uniformity it is necessary to design and build apparatus to diffuse the heat source. This diffuser, show in Figure 5.19 comprises two layers of aluminium honeycomb material of thickness 1.5 cm, separated by a distance of approximately 8 cm. In order to refocus the light between the layers there is a surrounding of aluminium foil. On top of the higher aluminium layer is a small glass cylinder covered in aluminium foil. This top is required to remove the distinct "hot-spot" produced by the heat lamp. In addition the heat lamp and diffuser are covered with aluminium foil to prevent any leakage of heat and light to the surrounding area. This configuration has

been designed and shown to produce uniform heating by Chen [146].

Figure 5.19: *Apparatus used to diffuse the light from the heat lamp to give uniform heating of the phantom material.*

The nature of the heat production means that accurate determination of uniformity of heating is difficult. With the light source removed the surface of the potato cools rapidly. Thus determination of uniform heating of the surface is difficult as the surface temperature changes rapidly with time. The overall result is unreliable even with rapid successive probing at varying locations. As a result the method of determining if the heat pattern is uniform has been reduced to a simple determination "by eye". It is possible with all other light sources extinguished to determine to a reasonable degree of accuracy if the pattern of heat produced by the lamp on a piece of white paper is uniform. A sample heat pattern is shown in Figure 5.20. Unfortunately, as a result of limitations in photographic resolution, this image is not a very accurate representation of the heating pattern as can be determined by the human eye. From this image it is clear that although uniform heating can be produced over part of the surface of the potato less heating will occur around the edges of the phantom. For this experiment this uniformity is acceptable as it is necessary that the temperature is fairly uniform solely across an area the size of the antenna aperture. A modified configuration, shown in Figure 5.21, in which the metal plate, potato phantom and ice mixture and placed inside a large polystyrene box is also used. This latter alteration serves to further focus the heat source onto the potato mould.

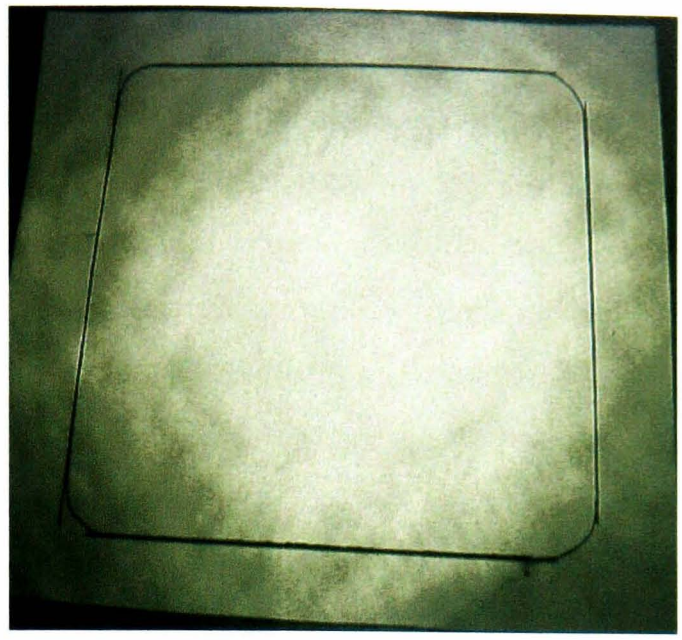

Figure 5.20: *Pattern of light from the heat lamp. In order to ensure that the contrast between hotter (lighter) and cooler (darker) areas is apparent in this image a greyscale colour map is employed.*

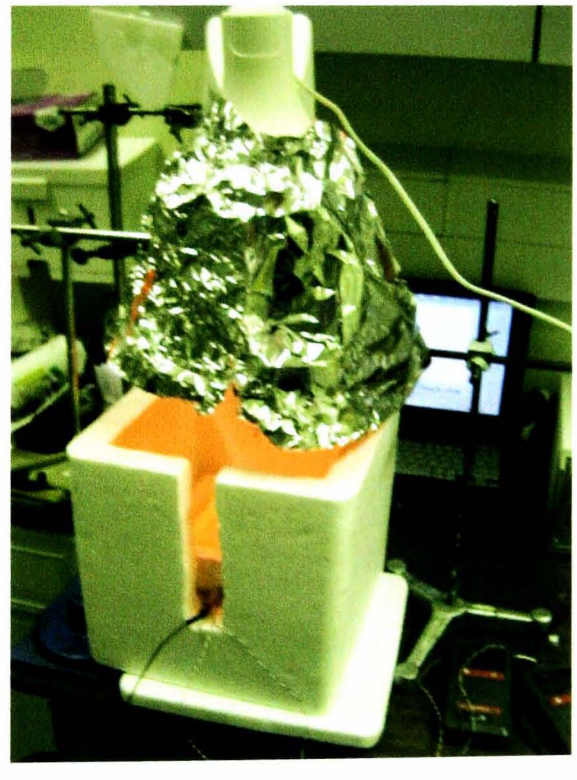

Figure 5.21: *Modified apparatus with the mashed potato phantom with temperature probes and the ice/water mixture are encased in a large polystyrene box.*

5.2.1.3 Radiometer reading

Once a suitable linear profile has been established in the potato mixture, on average taking 1-2 hours of slow heating, the probes are removed and the potato phantom transferred to the antenna for measurement. The removal of the probes and repositioning of phantom require approximately 30 seconds. Each microwave temperature reading then requires a further 20 seconds each, 5 seconds to reach a steady value and 15 seconds to provide a reasonable average temperature. Unfortunately due to time constraints it was not possible to ensure that the system would work at 1.35GHz and 3.2GHz simultaneously. The reason being interference caused by the circuitry of one antenna on the other. Thus a switch between the two frequencies was employed.

The effect of this time delay firstly between heating and measuring and secondly between the microwave readings must be considered for accurate comparisons. A maximum and minimum best estimate of the gradient and intercept can be determined from readings taken directly before the heat source is removed and directly after the microwave readings are taken. It is necessary to remove the probes during readings firstly to remove any effect on the measured microwave temperature and secondly to ensure that the door of the cavity could be closed. It was possible, however, to leave the surface probes in place.

Clearly over the time that the microwave reading is performed there will also be a change in the thermal gradient in the phantom. By allowing the phantom to cool once positioned inside the cavity over several minutes the profile stabilises, minimising these effects.

5.2.2 Linear gradient results

To give a feel for the nature of the linearity produced by this method sample linear profiles are shown in Figure 5.22 along with a best fit line through the data. As errors are present both in the position of the probe (x-axis) and in the measured temperature (y-axis) it is necessary to fit the data to a straight line given the errors in both co-ordinates. This data fitting is performed using the *fitexy* function from Press *et al* [147].

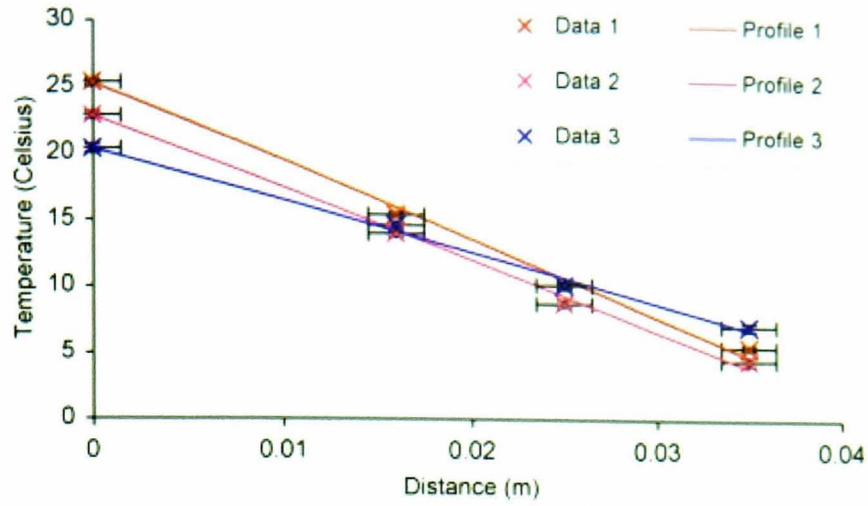

Figure 5.22: *Sample linear profiles set up in the mashed potato material.*

This curve fitting produces values for the gradient and intercept of the line with associated errors. An indication of the goodness of the fit is also given in terms of a chi-squared value (with 1 corresponding to a perfect fit). Curves which have a chi-squared of 0.4 or less are disregarded. Table 5.3 gives the parameters of the fit (gradient, intercept) with associated errors and the chi-squared value for each of the measured profiles.

5.2.2.1 Computational model

Comparison of the measured microwave readings can be made with the computationally expected values. By simulating the potato phantom and dual frequency antenna the one dimensional weighting function can be determined. This weighting function along with the best fit values of gradient and intercept for each profile will give a microwave temperature as:

$$T_{mw1/2} = \int w(z)T(z)dz = \int w(z) * (mz + c)dz \tag{5.2}$$

$$= m \int w(z)zdz + c \int w(z)dz \tag{5.3}$$

$$= mW_{1/2} + c \tag{5.4}$$

where m is the linear profile gradient, c is the intercept and the subscripts 1 and 2 represent the frequencies of 1.35 and 3.2GHz respectively.

Profile	m	δm	c	δc	χ^2	Profile	m	δm	c	δc	χ^2
1A	-7.43	0.80	26.56	0.62	0.84	9A	-6.66	0.68	28.92	0.51	0.68
1B	-6.15	0.67	24.2	0.58	0.88	9B	-5.74	0.60	23.59	0.49	0.46
2A	-5.83	0.56	25.23	0.58	0.91	10A	-5.72	0.60	23.39	0.49	0.47
2B	-5.58	0.54	23.43	0.57	0.9	10B	-4.42	0.47	22.44	0.45	0.63
3A	-5.37	0.52	22.73	0.56	0.93	11A	-4.43	0.47	22.34	0.45	0.62
3B	-4.78	0.47	22.06	0.55	0.94	11B	-3.89	0.42	21.54	0.43	0.64
4A	-4.74	0.47	21.75	0.55	0.91	12A	-3.91	0.42	21.34	0.43	0.68
4B	-4.30	0.43	21.17	0.54	0.93	12B	-3.50	0.38	20.73	0.42	0.71
5A	-4.23	0.42	20.66	0.54	0.88	13A	-3.64	0.44	20.53	0.43	0.72
5B	-3.83	0.39	20.26	0.53	0.9	13B	-3.04	0.38	19.55	0.41	0.68
6A	-4.18	0.51	19.79	0.52	0.55	14A	-2.88	0.32	17.03	0.51	0.96
6B	-3.92	0.48	19.51	0.51	0.52	14B	-2.74	0.31	16.60	0.51	0.82
7A	-3.36	0.43	18.8	0.5	0.62	15A	-4.25	0.52	21.49	0.44	0.83
7B	-2.98	0.39	18.21	0.49	0.63	15B	-3.92	0.48	20.32	0.43	0.73
8A	-3.01	0.39	18.12	0.49	0.62						
8B	-2.72	0.37	17.64	0.49	0.84						

Table 5.3: *Linear profiles obtained with values for the gradient ($^\circ C/cm$) and intercept ($^\circ C$) with associated errors and χ^2 value for each fit.*

The mashed potato phantom is modelled to incorporate layers of different temperature to roughly mirror the dielectric form of the actual potato mixture. As each profile covers a range of temperature variations a range of simulations (12) each with six to seven layers of different temperatures are performed and the most representative applied for the calculation of the microwave temperatures. At 3.2GHz these layers are 5Δ=6.5mm wide and at 1.35GHz 2Δ=6mm wide.

5.2.2.2 Comparison of results

The calculated microwave temperatures for the temperature profiles determined before ($Tcalc_1$) and after ($Tcalc_2$) the actual microwave reading are displayed in Table 5.4 for 3.2GHz measurements and in Table 5.5 for 1.35GHz measurements along with the actual readings. The error in measured microwave temperature is taken to be 0.4°C at 3.2GHz and 0.5°C at 1.35GHz, slightly higher than the error of the radiometer (0.3°C) to account for the fact that the temperature profile changes over the measurement time. The error in the probe position is taken as 2mm and in each temperature probe reading as 0.4°C. The error in the computed temperature is calculated from the errors in the gradient, intercept and weighting function (taken as 5%) using standard error analysis on equation 5.4.

Profile	Tmw2 (°C)	$Tcalc_1$ (°C)	$Tcalc_2$ (°C)
1	23.71 ± 0.40	22.98 ± 0.73	21.24 ± 0.66
2	22.96 ± 0.40	22.46 ± 0.64	20.77 ± 0.62
3	20.60 ± 0.40	20.10 ± 0.62	19.71 ± 0.60
4	20.11 ± 0.40	19.43 ± 0.60	19.06 ± 0.58
5	19.83 ± 0.40	18.60 ± 0.58	18.40 ± 0.56
6	17.52 ± 0.40	17.68 ± 0.58	17.53 ± 0.57
7	16.74 ± 0.40	17.10 ± 0.54	16.70 ± 0.53
8	15.91 ± 0.40	16.60 ± 0.53	16.27 ± 0.52
9	21.36 ± 0.40	**25.71** ± 0.61	20.73 ± 0.58
10	19.85 ± 0.40	20.53 ± 0.58	20.27 ± 0.51
11	18.61 ± 0.40	20.16 ± 0.51	19.63 ± 0.48
12	18.21 ± 0.40	19.42 ± 0.48	19.01 ± 0.46
13	19.24 ± 0.40	18.67 ± 0.49	17.99 ± 0.45
14	15.32 ± 0.40	15.61 ± 0.53	15.24 ± 0.53
15	19.22 ± 0.40	19.41 ± 0.51	18.39 ± 0.49

Table 5.4: *Computed and measured microwave temperature readings at 3.2GHz for the linear profiles listed in Table 5.3. One outlier point highlighted.*

At 3.2GHz for thirteen (of the fifteen) profiles the computed and measured temperature profiles agree within the stated error ranges. A plot of measured against computed microwave temperature, Figure 5.23, displays a clear trend towards agreement. The effect of the delay in measurement and a possible underestimation of the weighting function are also apparent. Given the inaccuracies in the experimental technique, however, this constitutes reasonable agreement.

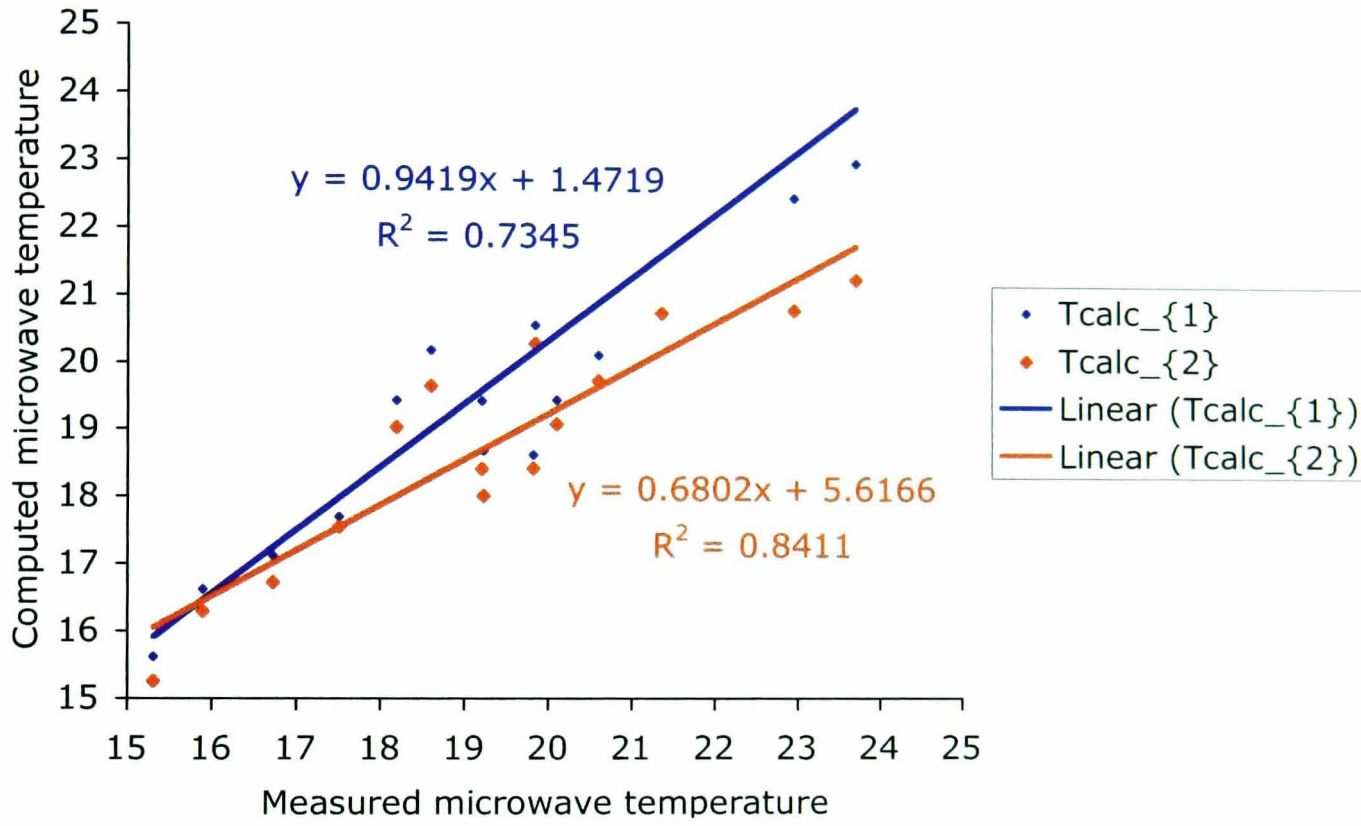

Figure 5.23: *Comparison of computed and measured microwave temperatures for a linear temperature profile measured at 3.2GHz.*

At 1.35GHz the match between measured and computed microwave temperatures is not as good as the higher frequency case, see Table 5.5. For over half of the profiles considered the computed and measured temperatures agree within the stated errors. There may be several reasons why the computed and measured temperatures are not in close agreement. Firstly the depth of the potato mould (4cm to 4.6cm) is such that the weighting function at 1.35GHz has not attenuated sufficiently to ensure that the entire contribution to the measured signal comes from the potato mixture. Further to this to ensure an accurate representation of the changing dielectric parameters with temperature (and hence dis-

Profile	Tmw1 (°C)	$Tcalc_1$ (°C)	$Tcalc_2$ (°C)
1	18.57 ± 0.5	17.28 ± 1.17	16.52 ± 1.02
2	18.34 ± 0.5	17.59 ± 0.93	16.11 ± 0.90
3	17.26 ± 0.5	15.54 ± 0.89	15.66 ± 0.84
4	17.10 ± 0.5	15.41 ± 0.83	15.42 ± 0.79
5	16.67 ± 0.5	14.91 ± 0.79	15.05 ± 0.75
6	13.94 ± 0.5	14.37 ± 0.84	14.41 ± 0.81
7	13.84 ± 0.5	14.43 ± 0.75	14.33 ± 0.71
8	13.92 ± 0.5	14.20 ± 0.71	14.10 ± 0.69
9	16.09 ± 0.5	20.60 ± 1.00	16.22 ± 0.92
10	15.36 ± 0.5	16.04 ± 0.92	16.83 ± 0.75
11	15.11 ± 0.5	16.72 ± 0.75	16.61 ± 0.68
12	14.90 ± 0.5	16.38 ± 0.69	16.29 ± 0.64
13	17.30 ± 0.5	15.75 ± 0.72	15.56 ± 0.64
14	13.54 ± 0.5	13.17 ± 0.67	12.92 ± 0.66
15	16.69 ± 0.5	16.10 ± 0.79	15.34 ± 0.75

Table 5.5: *Computed microwave temperature readings compared with measured microwave temperatures at 1.35GHz for the linear profiles listed in Table 5.3. One outlier point highlighted.*

tance) the simulation model includes many layers of potato corresponding to different temperatures. As a large cell size is used for the 1.35GHz model (Δ=3mm) the depth of each potato layer corresponds to only two simulation cells. This small number of cells per layer is approaching the limits of accurate determination of the weighing function (see discussion in section 6.2.3). By using a sub-grid with smaller cell size over the potato part of the simulation space inaccuracies in the weighting function as a result of this would be reduced. Finally the greater inaccuracies in the loss factor model for the mashed potato at 1.35GHz at the lower temperatures (insignificant at 3.2GHz) will contribute to errors in the computed weighting function.

5.2.3 Potato phantom with quadratic temperature gradient

A modified configuration is required to produce a quadratic temperature profile within the potato phantom. In this case the potato phantom moulds remained as in the linear profile case. For this profile, however, the mashed potato phantom is suspended between two sets of equivalent heat lamps and diffusers, shown in Figure 5.24.

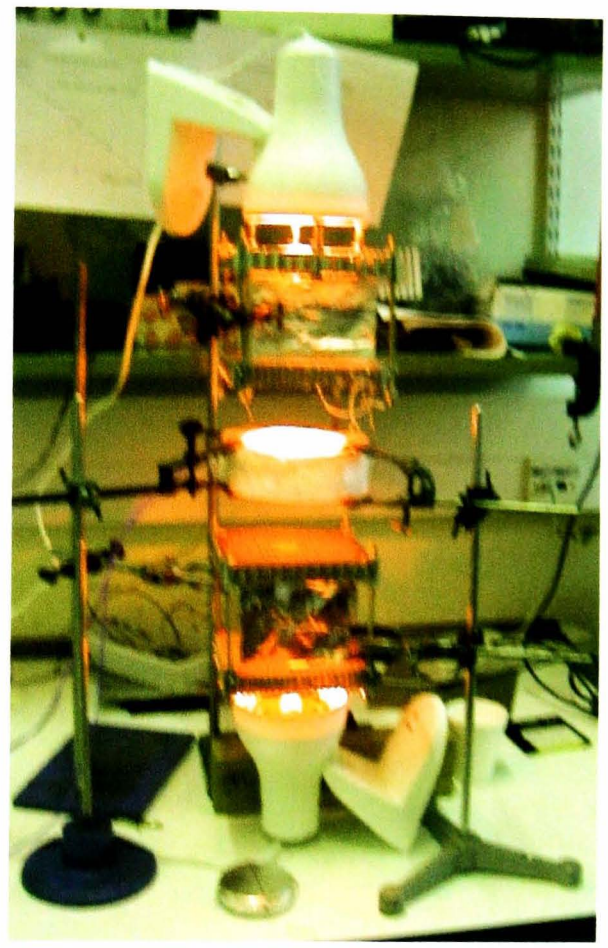

Figure 5.24: *Apparatus used to produce a quadratic temperature gradient in potato mixture. Includes two infra red heat lamps, two light diffusers and the mashed potato phantom with temperature probes.*

The device to remove the heat lamp "hot spot" is removed as with this device in place the heating of the potato is so slow that a quadratic profile is virtually impossible to achieve. Again through the use of probes at positions within the phantom, and making use of the two surface contact plates it is possible to ensure that the desired profile is produced.

5.2.4 Quadratic profile results

Unlike the linear profile case it is far from simple to fit a quadratic curve given errors in both co-ordinates. As a result the curves are fitted using a least squares method with only the error in thermocouple reading taken into consideration. Again those profiles which are too far off the desired quadratic shape are removed. Sample quadratic profiles are shown in Figure 5.25 along with the fitted curves. Table 5.6 gives the coefficients of the quasi-quadratic temperature profiles along with the correlation (r^2) value for each profile.

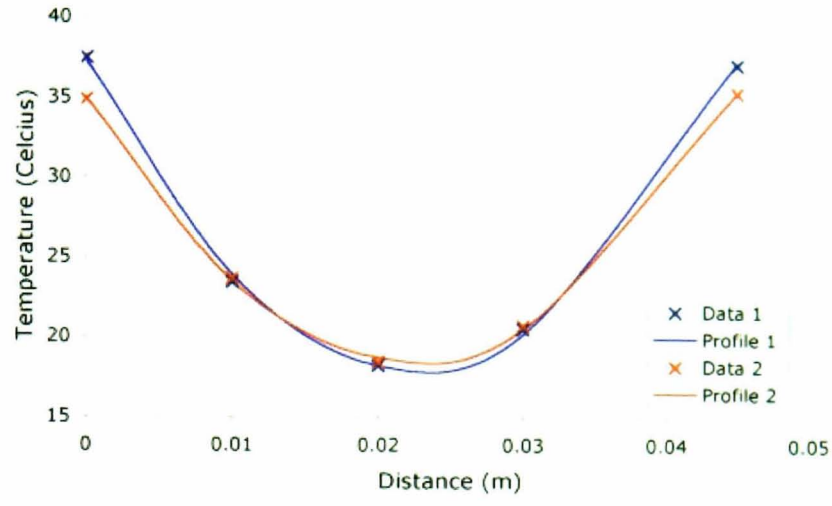

Figure 5.25: *Sample quadratic profiles set up in the mashed potato phantom material.*

5.2.4.1 Computational model

Comparison of the measured microwave reading can be made with the computationally expected values as before. The one dimensional weighting function along with the best fit values of the quadratic for each profile will give a microwave temperature as:

$$T_{mw1/2} = \int w(z)T(z)dz = \int w(z) * (az^2 + bz + c)dz \quad (5.5)$$

$$= a\int w(z)z^2dz + b\int w(z)zdz + c\int w(z)dz \quad (5.6)$$

$$= aW_{1_A/2_A} + bW_{1_B/2_B} + c \quad (5.7)$$

where a, b and c are the parameters of the quadratic profile and the subscripts 1 and 2 again represent the frequencies of 1.35 and 3.2GHz.

The simulated model of the experimental configuration again considered the potato mixture as being composed of several layers of mashed potato each at different temperatures (with the associated dielectric properties). At 3.2GHz six or seven layers, each 6.5mm wide as before, are employed. At 1.35GHz layers of 6mm wide again are used. Five simulations covering different temperature ranges are considered for comparisons.

Profile	a	δa	b	δb	c	δc	r^2
1A	29814	262	-1324	48	24.9	0.5	0.988
1B	20742	262	-938	48	22.5	0.5	0.981
2A	28458	262	-1256	48	27.4	0.5	0.993
2B	23306	262	-1098	48	27.2	0.5	0.995
3A	18398	262	-843	48	24.6	0.5	0.988
3B	14306	262	-660	48	23.5	0.5	0.965
4A	12117	262	-545	48	22.4	0.5	0.962
4B	8161	262	-368	48	21.3	0.5	0.902
5A	35646	260	-1527	49	38.0	0.5	0.999
5B	21879	260	-993	49	34.3	0.5	0.990
6A	20426	260	-915	49	33.6	0.5	0.983
6B	14348	260	-659	49	31.9	0.5	0.955

Table 5.6: *Quasi-quadratic temperature profile parameters in* $^\circ C/m$.

5.2.4.2 Comparison of results

Tables 5.7 and 5.8 give the measured and computed microwave temperatures at 3.2GHz and 1.35GHz respectively. At both frequencies the match between measured and computed temperatures is within the stated errors for over half of the profiles considered.

Profile	Tmw2 (°C)	$Tcalc_1$	$Tcalc_2$
1	19.8 ± 0.4	18.9 ± 0.6	18.2 ± 0.6
2	21.2 ± 0.4	21.5 ± 0.6	22.1 ± 0.6
3	19.1 ± 0.4	20.8 ± 0.6	20.5 ± 0.6
4	19.4 ± 0.4	20.0 ± 0.6	19.6 ± 0.6
5	31.3 ± 0.4	30.5 ± 0.6	29.3 ± 0.6
6	27.5 ± 0.4	29.0 ± 0.6	28.6 ± 0.6

Table 5.7: *Comparisons of measured and computed microwave temperatures at 3.2GHz for quasi-quadratic temperature gradients.*

Profile	Tmw1 (°C)	$Tcalc_1$	$Tcalc_2$
1	17.5 ± 0.5	16.0 ± 0.9	16.0 ± 0.9
2	18.2 ± 0.5	18.9 ± 0.9	19.3 ± 0.9
3	17.2 ± 0.5	18.7 ± 0.9	18.9 ± 0.9
4	18.3 ± 0.5	18.7 ± 0.9	18.8 ± 0.9
5	27.3 ± 0.5	27.9 ± 0.9	27.2 ± 0.9
6	26.1 ± 0.5	27.2 ± 0.9	27.2 ± 0.9

Table 5.8: *Comparisons of measured and computed microwave temperatures at 1.35GHz for quasi-quadratic temperature gradients.*

In addition to the errors discussed for the linear profile case, several additional errors are present in the quadratic case. As the potato heats it becomes less solid and as the mould is suspended for heating this causes the potato to drop and change position. The uniformity of heating on each of the exposed surfaces is also less uniform in this case due to the removal of part of the heat diffuser. Finally as the potato cools the quadratic temperature profile is quickly lost removing the possibility of repeated measurement with a more stable profile. As before the match is better at the higher frequency.

5.2.5 Conclusions

The dual frequency antenna has been applied to measure the microwave temperature at 1.35GHz and 3.2GHz for a mashed potato phantom material. Methods for producing both linear and quasi-quadratic temperature profiles in the mashed potato have been established. Comparisons of the measured microwave temperatures with those computed from the parameters of the temperature profile fit have been made. In both the linear and quadratic profile conditions a reasonable agreement between computed and measured temperature values is seen. This serves to provide further validation of the computational modelling of the weighting function using the dielectric modelling developed (Section 6.1.3).

Several improvements to the experimental procedure and configuration would improve this match. In particular the use of a greater volume (i.e. greater depth) of potato in the mould should significantly improve the measurements at 1.35GHz, however this benefit is offset by the greater difficulty in producing the desired temperature profiles in such a phantom. Technical improvements to the 1.35GHz radiometer would reduce some the calibration uncertainties and reduce the measurement time. Simultaneous temperature measurement at both frequencies would further remove some of the uncertainties as a result of the long measurement time. Finally by working in a low electromagnetic noise environment, thus removing the need for antenna shielding, the microwave measurement could be made simultaneously with the thermocouple temperature profile readings further improving accuracy. In terms of the quasi-quadratic temperature profiles, a more stable profile is desirable. Slow heating of a frozen potato mould may provide a means of obtaining this and would have the advantage of allowing a more uniform surface heating.

Chapter 6

Behaviour of the weighting function

Investigation of the variation in the form of the weighting function with changes in key parameters is essential for accurate interpretation of microwave temperature measurements. By making use of BEST computational modelling it is possible to determine the effect on the weighting function of variations in frequency, dielectric layering and material dielectric properties.

The possible range of material dielectric properties that can be considered is huge. To cover a wide range of materials of interest to both biological and industrial applications a particular subset of phantom materials is considered for this work. In particular generic mixtures of saline with varying protein concentrations are considered along with the specific example of a mashed potato type material.

Comparisons are made and conclusions drawn on the effect of the variations in dielectric properties of the phantom materials on the computed weighting functions through the: variation in protein concentration in generic phantom type, inclusion of bound water in the phantom material model, effect of temperature variation and the effect of the measurement frequency. The limitations of the computational modelling are investigated through consideration of the effects of dielectric layering and finite verses infinite model bounds.

6.1 Calculation of the dielectric parameters of the phantom materials.

For a complete investigation of the weighting function it is necessary to have a workable model of the dielectric behaviour for each of the material types to be considered. This model must be able to provide the dielectric properties of the phantom materials over a range of temperatures and frequencies. To achieve such a model for a mixture material (mashed potato and generic saline / protein) it is necessary to apply a mixture equation along with experimentally determined information about the constituent parts of the mixture.

6.1.1 Mixture equations

Many different forms of mixture equation exist for a wide range of specific configurations. A thorough investigation of many mixture equations and their applicability to the modelling of biological materials has been performed by Gorton [40]. For this work the simplest mixture equation, the Maxwell mixture equation is used [86]. As only a sample range of dielectric properties are required it is not necessary to use a more complex equation. Further to this Gorton [40] states that the Maxwell equation is suitable to model biological materials for low volume fractions. The Maxwell equation states that for a small volume of material of type 1 $(\epsilon_1', \epsilon_1'')$ suspended in material of type 2 $(\epsilon_2', \epsilon_2'')$:

$$\epsilon'_{mix} = \epsilon'_2 \left(\frac{(\epsilon'_1 + 2\epsilon'_2) + 2v_1(\epsilon'_1 - \epsilon'_2)}{(\epsilon'_1 + 2\epsilon'_2) - v_1(\epsilon'_1 - \epsilon'_2)} \right) \tag{6.1}$$

$$\epsilon''_{mix} = \epsilon''_2 \left(\frac{(\epsilon''_1 + 2\epsilon''_2) + 2v_1(\epsilon''_1 - \epsilon''_2)}{(\epsilon''_1 + 2\epsilon''_2) - v_1(\epsilon''_1 - \epsilon''_2)} \right) \tag{6.2}$$

where v_1 is the volume fraction of the suspended component.

6.1.2 Generic protein / saline mixture

The first mixture considered is that of free water with dissolved salts (henceforth referred to as saline solution) and protein. Protein dielectric properties have been considered by many researchers including Grant and Keefe [148], Schwan [149] and Smith and Foster [150]. In all cases the value of relative permittivity and conductivity used for the protein component are $\epsilon_r' = 2.5$ and $\sigma = 0.2$ Sm^{-1} as measured by Campbell [151].

The concentration of salt in the saline considered is that of 0.9% salt by mass. This concentration is equivalent to the concentration of salt seen in physiological saline. The Cole-Cole relations [52], which adequately model the complex permittivity of water, can be used as a basis for determining the saline permittivity values. The effect of the salt contribution on the real part of the complex permittivity is small. In the case of the loss factor the presence of salt requires the addition of an ionic term in the Cole-Cole equation, [152]. The Cole-Cole equations used to model saline are:

$$\epsilon' = \frac{\epsilon_s - \epsilon_m}{1 + (f/f_r)^2} + \epsilon_m \tag{6.3}$$

$$\epsilon'' = \left(\frac{f}{f_r}\right) \frac{\epsilon_s - \epsilon_m}{1 + (f/f_r)^2} + \frac{\sigma}{2\pi f \epsilon_o} \tag{6.4}$$

where ϵ_s is the static permittivity, ϵ_m is the millimetre permittivity, f_r is the resonance frequency in GHz, f is the measurement frequency in GHz and σ is the sodium chloride ionic conductivity.

Many authors have considered the most appropriate form for each term in equations 6.3 and 6.4. Two sets of equations are considered in this work; a set based on empirical measurements from Land [138] and those compiled from literature as set forth by Gorton [40]. These equations, referred to as equation set 1 and equation set 2 respectively, are:

Equation Set 1

$$\epsilon_s = 87.2 - 0.353T \tag{6.5}$$

$$\epsilon_m = 4.5 \tag{6.6}$$

$$f_r = 6.1 + 0.511T \tag{6.7}$$

$$\sigma = 1.44(1 + 0.22(T - 20)) \tag{6.8}$$

Equation Set 2

$$\epsilon_s = 87.74 - 0.4008T + 9.398x10^{-4}T^2 \tag{6.9}$$

$$\epsilon_m = 4.3 \tag{6.10}$$

$$f_r = 7.99 + 0.375T + 0.00205T^2 \tag{6.11}$$

$$\sigma = 0.806 + 0.0317T \tag{6.12}$$

where T is the temperature in degrees Celsius.

6.1.2.1 Bound Water Model

In the second model the parameters are again calculated using mixture equations, however, in this case the water is considered to be present in both bound and free forms. The inclusion of bound water in the model results in a more accurate representation of the real life situation. Previous work on the subject of the binding of water to protein has given an estimate of 0.4g of water bound per 1g of protein present [40]. This estimate agrees well with the findings of Grant and Keefe [148] who estimate a range of 0.25-0.6 g/g. This estimate is used to calculate the amount of free and bound water present in the mixture. Values for the permittivity and conductivity of bound water, a rough estimate at best, are taken as $\epsilon' = 12$ and $\epsilon'' = 22$ from [40]. This is a notably smaller dielectric constant than for free water emphasising the fact that water when bound has lost nearly all ability to polarise with an applied field.

Two methods are employed to find parameters for the bound mixture. Firstly, method one, the mixture equations are applied twice. In this first instance bound water is treated as being a small fraction in protein. Relative permittivity and loss factor values can then be determined for this mix. The bound saline / protein mix is then considered as a small fraction mixed in saline and the mixture equations suitably applied. In the second method the permittivity of the bound water is assumed to be that of the protein, giving a larger percentage of protein equivalent material in the mix. The mixture equation is then applied as before with this altered volume fraction.

6.1.2.2 Saline / Protein complex permittivity values

Tables 6.1 and 6.2 detail the complex permittivity values for the generic protein / saline phantom at varying protein concentrations and at the frequencies of 1.35GHz and 3.2GHz. In the tables [**1**] and [**2**] represent the simple phantom with equation sets 1 and 2 respectively, [**3**] and [**4**] represent the bound phantom with parameters determined using methods 1 and 2 respectively. This information is also displayed graphically in figures 6.1 and 6.2 for ease of interpretation.

As expected in both the 1.35GHz and 3.2GHz frequency ranges the results are similar for equations 1 and 2 and for methods 1 and 2. In the case of the bound model this is encouraging as both methods used are an estimate as to how to model the behaviour of the bound water. The bound model conductivity values are notably smaller than that of the simple model. There is some suggestion that the relaxation frequency of bound water occurs in the range of 100-800MHz [148, 149, 150, 152]. This would suggest that the loss of bound water at GHz frequencies is minimal and certainly much less than that for the free water case. The reduction in relative permittivity for the bound case is also as expected to account for the reduction in the high permittivity free water and its replacement by lower permittivity bound water. (The reader is referred to Hasted [8] for a full account of water and biological tissue as dielectrics.)

It can be seen that the values of relative permittivity are very similar for the frequencies of 3.2GHz and 1.35GHz. At frequencies below 10GHz the relative permittivity is fairly constant and close to the "static" or "low - frequency" permittivity [8, 148]. At these frequencies dipoles in the material are able to follow the variations in the applied field and the permittivity is constant at its maximum value [152]. The marked difference in the effective conductivity at the two frequencies is also as expected. At the relaxation frequency the loss factor achieves its maximum value, and for water based materials at room temperature this occurs near 30GHz. The low frequency tail of this effect results in a falling off to zero of the loss with decreasing frequency so that the loss at 3GHz is larger than that at 1GHz.

Volume	Permittivity				Conductivity (Sm^{-1})			
fraction	ϵ' **[1]**	ϵ' **[2]**	ϵ' **[3]**	ϵ' **[4]**	σ **[1]**	σ **[2]**	σ **[3]**	σ **[4]**
0.10	66.79	66.74	62.32	61.80	3.42	3.43	3.17	3.16
0.20	57.17	57.13	49.34	48.50	2.91	2.91	2.48	2.45
0.25	52.66	52.63	43.48	42.50	2.67	2.68	2.16	2.13
0.30	48.34	48.31	38.00	36.90	2.44	2.45	1.87	1.84
0.40	40.22	40.20	28.00	26.70	2.01	2.02	1.34	1.30
0.50	32.72	32.70	19.11	17.70	1.62	1.62	0.87	0.83
0.60	25.78	25.77	11.15	9.70	1.25	1.26	0.45	0.41
0.70	19.34	19.33	4.01	2.50	0.92	0.92	0.08	0.08
0.75	16.29	16.28	3.72	2.50	0.76	0.76	0.04	0.04
0.80	13.34	13.33	-	-	0.60	0.60	-	-

Table 6.1: *Dielectric properties (relative permittivity and conductivity) calculated at 3.2GHz using:**[1]** - simple model, equations 1; **[2]** - simple model, equations 2; **[3]** - bound model, method 1; **[4]** - bound model, method 2.*

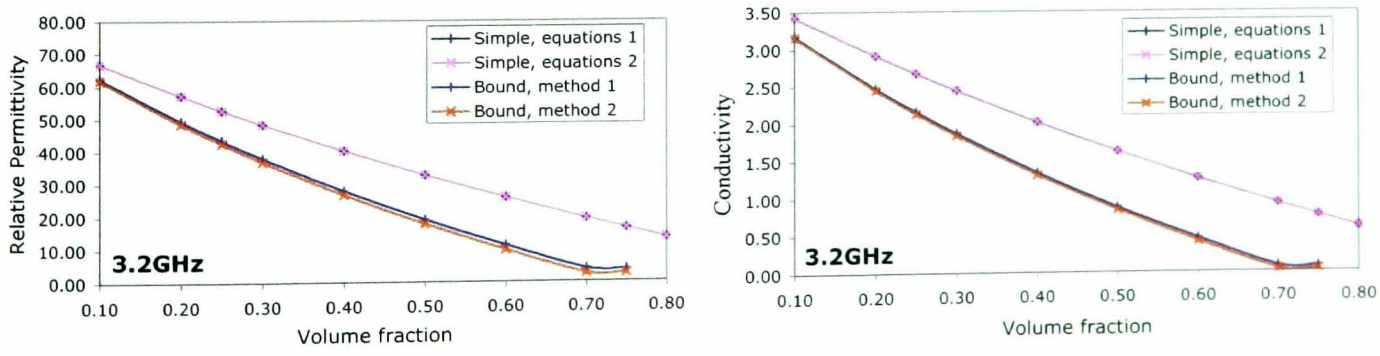

Figure 6.1: *Variation of dielectric properties, relative permittivity (right) and conductivity (left), of a protein saline mixture with varying protein contribution at 3.2GHz.*

Volume	Permittivity				Conductivity (Sm^{-1})			
fraction	ϵ' **[1]**	ϵ' **[2]**	ϵ' **[3]**	ϵ' **[4]**	σ **[1]**	σ **[2]**	σ **[3]**	σ **[4]**
0.10	68.75	68.72	64.10	63.60	1.64	1.64	1.52	1.51
0.20	58.83	58.80	50.70	49.90	1.39	1.39	1.18	1.17
0.25	54.13	54.16	44.70	43.70	1.28	1.28	1.03	1.02
0.30	49.73	49.71	39.00	38.00	1.17	1.17	0.89	0.88
0.40	41.36	41.34	28.70	27.50	0.96	0.96	0.64	0.62
0.50	33.64	33.62	19.60	18.20	0.77	0.77	0.41	0.40
0.60	26.49	26.47	11.40	9.90	0.60	0.60	0.21	0.19
0.70	19.85	19.84	4.00	2.50	0.44	0.44	0.03	0.02
0.75	16.70	16.69	3.70	2.50	0.36	0.36	0.03	0.02
0.80	13.67	13.66	-	-	0.29	0.29	-	-

Table 6.2: *Dielectric properties (relative permittivity and conductivity) calculated at 1.35GHz using:**[1]** - simple model, equations 1; **[2]** - simple model, equations 2; **[3]** - bound model, method 1; **[4]** - bound model, method 2.*

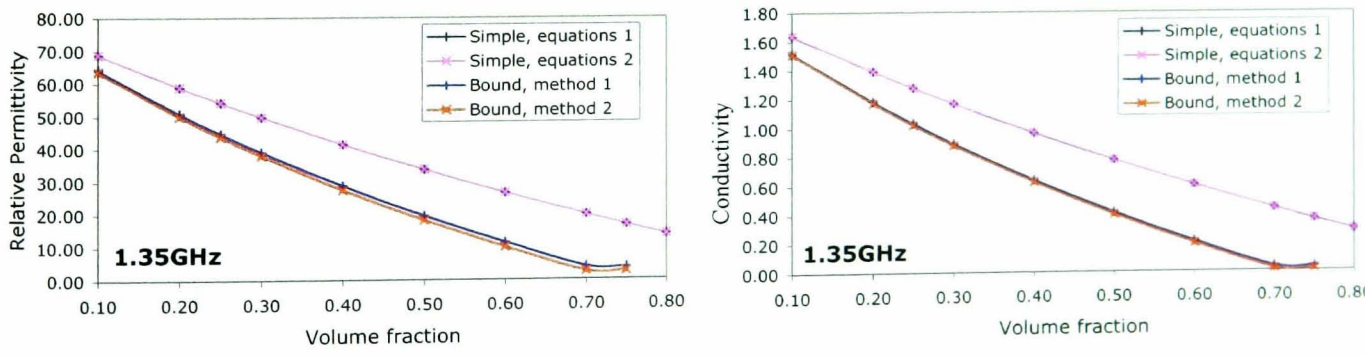

Figure 6.2: *Variation of dielectric properties, relative permittivity (right) and conductivity (left), of a protein saline mixture with varying protein contribution at 1.35GHz.*

6.1.2.3 Variation in permittivity with temperature

Temperature variation in the simple phantom model can be investigated through the temperature dependence of equations 6.9, 6.11 and 6.12. In this way it is possible to study the effect on the dielectric properties and thus weighting function over temperature ranges from 10 to 50°C. Figure 6.3 details the change in dielectric constant and conductivity with increasing temperature. As the temperature increases the dielectric constant at both 1.35GHz and 3.2GHz slowly diminishes. The conductivity at 1.35GHz increases with increasing temperature while the conductivity at 3.2GHz decreases with increasing temperature.

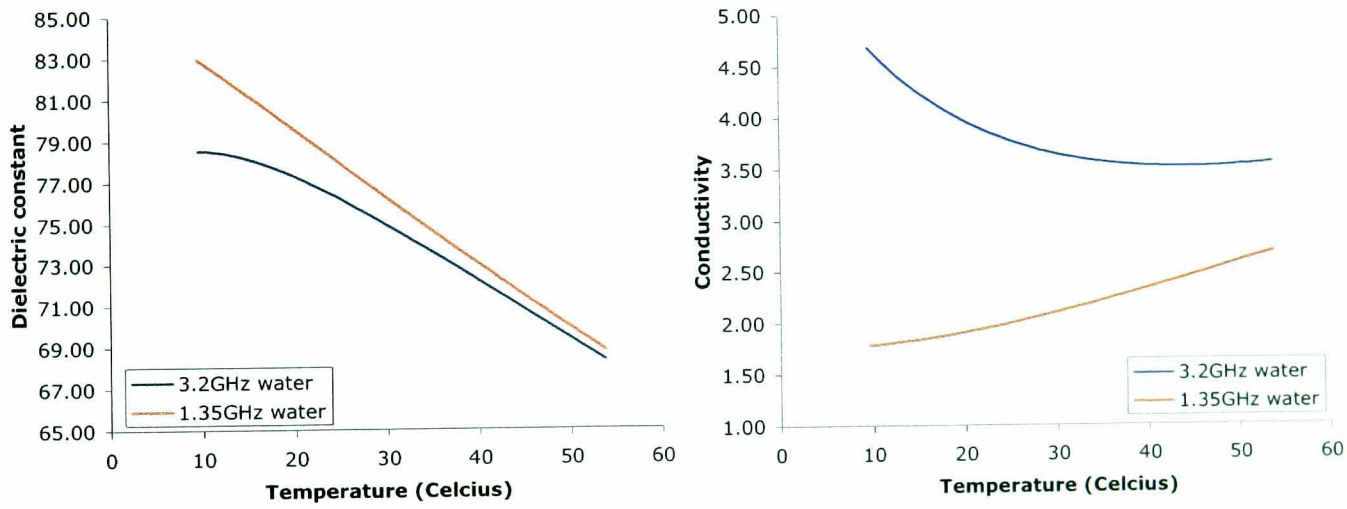

Figure 6.3: *Variation of dielectric properties, relative permittivity (right) and conductivity (left), of a pure 0.9% saline mixture with temperature at 1.35GHz and 3.2GHz.*

6.1.3 Mashed potato model

Information regarding the variation of the permittivity and conductivity of the mashed potato over a range of temperatures (0-50°C) at the frequencies of 1.35GHz and 3.2GHz was also required. As the mashed potato mixture is used extensively for the experimental investigation of the dual frequency antenna (section 5.2) and temperature retrieval processes (section 7.2) an accurate model of the behaviour of the complex permittivity of the potato mix is essential.

Although the determination of potato dielectric properties have been considered by several authors, Roebuck and Goldblith [153] and Burfoot *et al* [154] in particular, there is little information on suitably accurate predictive models for both dielectric constant and loss. For this reason a resonant cavity perturbation technique [155] was used to determine the complex permittivity of the mashed potato mixture at 3.18GHz over the appropriate temperature range. Additional measurements at 1GHz at one specific temperature (22.4°C) were performed using the terminated coaxial line method as a cavity was not available at this frequency. (The techniques and equipment were essentially those of Gorton [40].)

Further to this, measurements were made of solutions of water, saline, sucrose, and a starch / water mixture at 3.2GHz over the same temperature range, again using the cavity perturbation technique. These solutions are considered to enable determination of the the key elements of the dielectric interactions in the mashed potato. Making use of these measurements and the previously published data a basic model of the complex permittivity of the mixture is proposed for 3.2GHz. This model is then extended to allow prediction of the permittivity to be expected at 1.35GHz. (All experimental measurements were made by D. Land [138].)

6.1.3.1 Mashed potato composition

The mashed potato mixture considered was prepared from a commercially available instant potato mixture. The major components of this mixture are listed in Table 6.3 as given on the product packaging [145]. The mass of the dielectrically dominant constituents, namely water and sodium chloride, were also determined directly.

The percentage of water in the mixture was determined by measuring the mass of a range of samples of mashed potato prior to and after aeration. It was assumed that given a suitable length of time all free water in the mixture would evaporate leaving the remaining constituents. Repeated measurements of samples from several batches of mashed potato give the mean result stated in Table 6.3. Each sample was left for over 24 hours to allow any water present to evaporate. The measured water content is in agreement with stated value.

Component	* by mass per 100g	+ by mass per 100g
Water	80.3	80 ± 2
Fibre	0.2	-
Protein	1.2	-
Sodium Chloride	0.3	0.2
Carbohydrate	14.1	-
Sugars	0.3	-

Table 6.3: *Composition of the mashed potato mixture. * - by mass, as listed on product packaging. + - by mass, determined experimentally.*

The sodium chloride content was determined at a Northern Foods Plc. laboratory by ashing a sample (burning so that all that remains are the various salts and minerals present) and then titrating against a particular reagent [1].

The mass of the remaining constituents is then taken to be the remainder of the 100g minus the water and salt parts. This constitutes less than 2% of the total mixture and it is assume that in dielectric terms each of these remaining constituents behave in a manner similar to the carbohydrate component. As a result the mixture is assumed to have three key dielectric parts: water, sodium chloride and carbohydrate. The dielectric behaviour of each of these constituent parts is itself fairly well known. Interactions between carbohydrate and water and carbohydrate and saline are more difficult to predict.

6.1.3.2 Model of dielectric constant at 3.2GHz

The real part of the complex permittivity of the mashed potato is by far the simpler to understand and so is considered first. The dominant contribution to the dielectric constant of the mixture will come from the relaxation of polar water molecules. The presence of the small amount of sodium chloride will serve to reduce the water dielectric constant value by a small fraction. This drop is accounted for by the fact that the the

[1]Thanks to R. Seaby, Northern Foods.

presence of the salt will displace some water molecules and the salt will bind some water molecules causing a reduction in polarisation of the water. In this mixture, however, the level of sodium chloride is such that any effect of this nature is insignificant.

The presence of the carbohydrate (starch) component in the mixture serves to reduce the dielectric constant through the displacement of some of the water molecules with non-polarisable starch molecules and the binding of the water molecules which reduces the ability of these water molecules to align with the applied field.

To ensure that in terms of dielectric constant the interaction of water and starch is negligible, comparisons between experimentally measured and theoretically predicted values are made. The complex permittivity of pure starch / water mixtures, made from Cornflower [156] and water, are determined over a range of temperatures using the cavity perturbation technique. The results of these measurements, along with the appropriate Maxwell mixture equation model curves for the real part of the permittivity, are displayed in Figure 6.4.

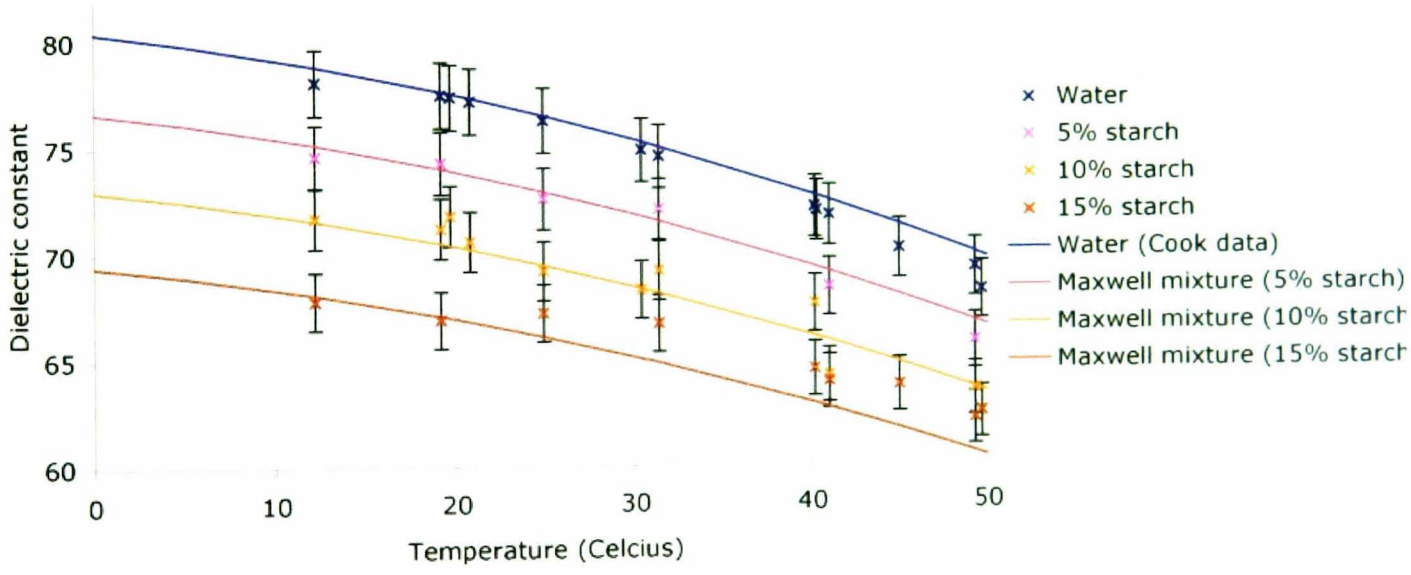

Figure 6.4: *Comparison of the modelled carbohydrate / water mixture dielectric constant using Maxwell's mixture equation and experimental data points.*

The dielectric constant values used for water, the aqueous component of the mixture, are those of Cook's [157] experimental data over the temperature range of 0 - 50°C. For this model the suspended component, carbohydrate, has dielectric constant 2.5 [153]. Finally the volume fraction of carbohydrate in the mixture is determined from the mass fraction

and the density of carbohydrate ($\sim$ 1.5 x10^3 kg m^{-3}). This density is taken to be similar to that of glucose, sucrose, fructose, lactose and similar carbohydrates [158].

Clearly the modelled curve fits the experimental data given a 2% error in each data point and assuming a 2% error in the curve (not plotted for ease of inspection). Thus it can be concluded that the water and carbohydrate can be taken to be non-interacting at this level of accuracy. It is then acceptable to use the Maxwell mixture equation to model the dielectric constant of the mashed potato mixture.

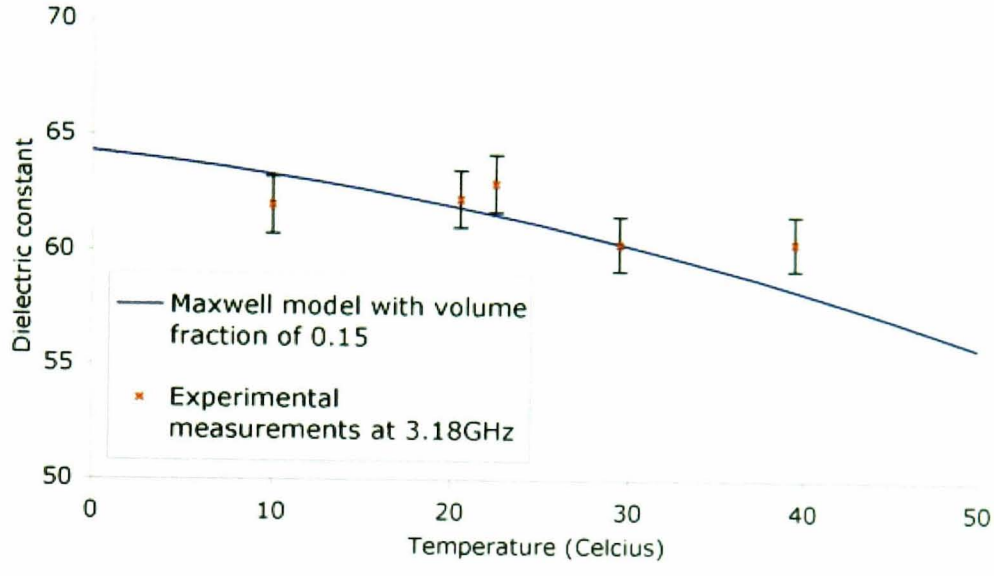

Figure 6.5: *Comparison of the modelled mashed potato dielectric constant using Maxwell's mixture equation and experimental data points.*

Figure 6.5 shows the Maxwell mixture equation model and the experimentally measured potato data over the entire temperature range. The volume fraction used for the mashed potato model is 0.15, this is equivalent to a carbohydrate concentration of 22.5% by mass. This concentration is approximately 2.5% greater than experimentally determined. Possible reasons for this increase are density differences from the value used and the loss of some free water as bound water. In fact Cornillion [159] states that starch binds water as 26% of its mass, although the exact amount of interaction will vary depending on the type of starch. It is apparent from this figure that the real part of the permittivity of the mashed potato mixture can be accurately modelled at 3.2GHz using this method. This agrees with research by Brown and George [160] which has shown Maxwell modelling to be appropriate for mashed potato mixtures.

6.1.3.3 Dielectric constant model at 1.35GHz

As the method of using Maxwell's mixture equation is appropriate at 3.2GHz it can be assumed that the same method would yield reasonable results at lower frequencies (1-1.35GHz). This assumption is viable as any water - carbohydrate interaction has been shown to have a negligible effect on the dielectric constant. At these frequencies, however, there is little data available in the literature for comparisons with modelled predictions. Burfoot *et al.* [154] give a range of measurements over the temperature range of 0-100°C at 0.9GHz but his sample is of a significantly different water content. In fact only the data of Roebuck and Goldblith [153] and Land [138] can be considered i.e. effectively two data points both near room temperature. Additionally in the case of the measurements of Roebuck and Goldblith the dielectric constant quoted for 100% water is approximately 3 parts less than the now accepted value. As a result an error of approximately 5% must be considered with his data.

Figure 6.6 details this data along with the Maxwell mixture model. The dielectric constant used for the carbohydrate fraction is equal to the value used at 3.2GHz as indicated by the measurements of Roebuck and Goldblith [153]. The water dielectric properties are calculated using the Cole-Cole approximation as detailed in section 6.1.2. The best match to the experimental data of Land is for a volume fraction of 0.167, corresponding to a mass fraction of 0.25. Again this is greater than expected from experimental water content mixtures.

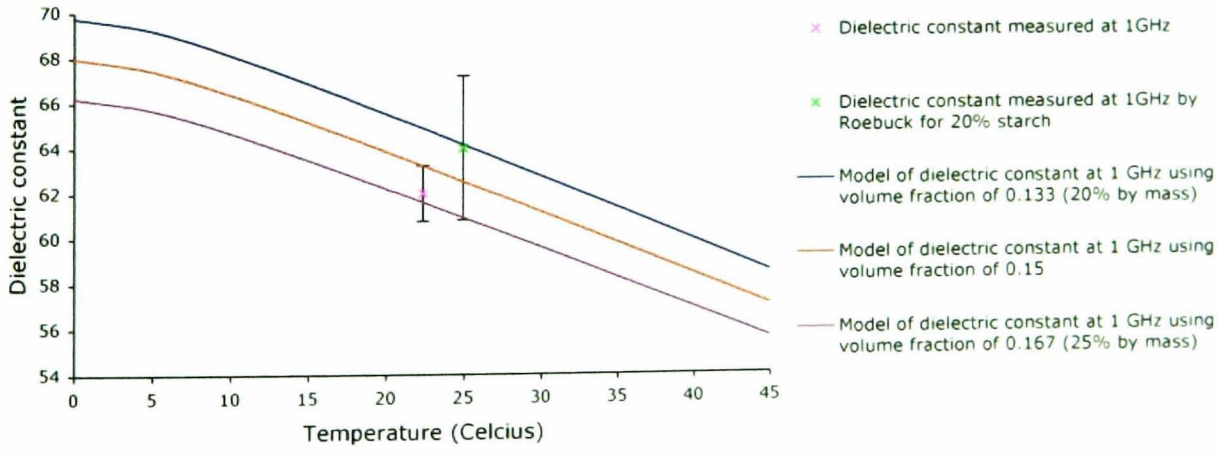

Figure 6.6: *Comparison of the modelled mashed potato dielectric constant using Maxwell's mixture equation and literature at 1GHz.*

This difference may be due to an increased effect of the change of free water to bound water. It is also possible that the value used for the dielectric constant of carbohydrate, 2.5, is offset from the actual value at 1GHz, although an effect of this nature would be small. Given these uncertainties the model is as good as can be made with the information available at present.

6.1.3.4 Model of loss factor at 3.2GHz

Modelling the loss factor of the potato mixture at 3.2GHz proved to be more complicated than determining the behaviour of the dielectric constant. Initial attempts to model this loss using a Maxwell mixture equation of saline and carbohydrate as before were unsuccessful. At all temperatures the modelled values fell well below the data of Land and Roebuck and Goldblith. Considering a simple starch/water mixture as before and comparing the results with Maxwell mixture modelling demonstrates the problem (see Figure 6.7).

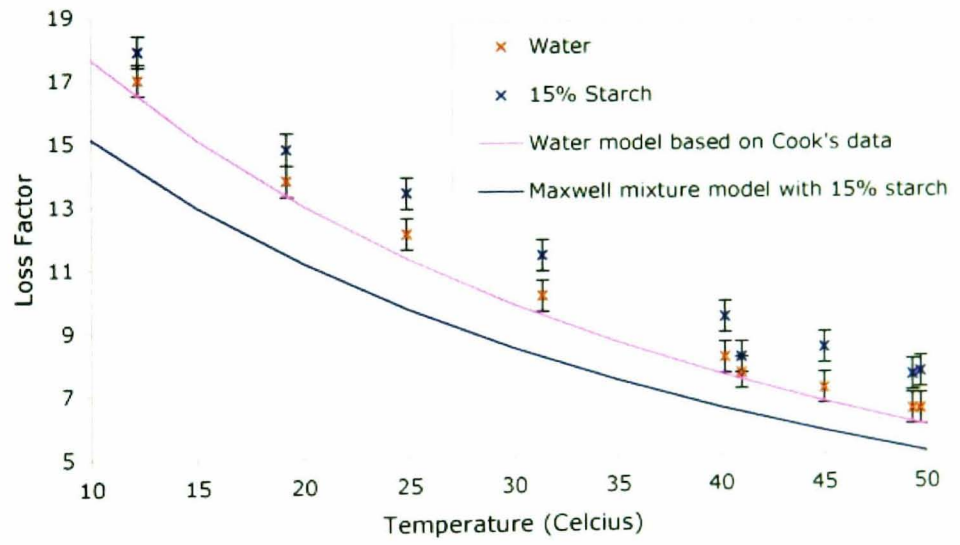

Figure 6.7: *Modelled and measured loss factors for water and a 15% water carbohydrate mixture at 3.18GHz.*

A symbiotic relationship between the starch and water can be seen as the loss factor of the mixture is greater than that of the water alone. This effect has also been noted by Roebuck and Goldblith [153] and as a result of these interacting constituents it was concluded that the Maxwell equation was not appropriate for this situation. The form of

this interaction serves to increase the overall loss, most likely a result of the presence of the bound water in the mixture. The relaxation curve of the bound water is such that the resonance will occur at a lower frequency than for free water and the curve itself will have a larger spread [40, 148, 149]. The resonance frequency of the bound water is likely to lie between 1 and 5 GHz [40] and so this effect will be seen for both frequency cases. It can also be seen in Figure 6.7 that the experimentally determined loss factor values for water closely match the fit to Cook's data which provides a good check on the measurement technique.

To understand the nature of any interaction it was necessary to determine the interaction of water and starch and then of saline and starch. The latter effect is described by Bircan and Barringer [161] and at a concentration of 0.2% salt the loss factor of the mixture differs from that of a water / starch mixture of the same proportion by less than 1 unit. The starch / water interaction, however, is a little more complicated.

Bircan and Barringer [161], found that as the concentration of the starch in the starch/water mixture changes over 0 to 25% by mass the loss factor remains fairly constant at the pure water value. Measurements by Land, however, suggest a small but definite effect from this interaction; this has also been seen by Roebuck and Goldblith [153]. Figure 6.8 details the difference in loss factor from a pure water sample seen for a 20% by mass starch water mixture at several temperatures. These measurements were made using the resonant cavity method as before on samples produced from corn starch and water.

Measurements at temperatures below 12°C were not possible and so an extrapolated value of this interaction is used for these temperatures. The size of the interaction at these temperatures is very small ($\approx \pm 0.5$F/m) so that this is an acceptable approach.

Investigation of this interaction as the concentration of starch in the starch water mixture varies is shown in Figure 6.9 at 12.2°C, 19.2°C and 24.9°C. Over the concentrations of interest in this work (18-22 % starch) the change in value of this interaction is small, ± 0.1, so that the interaction for 20% starch is used in the model.

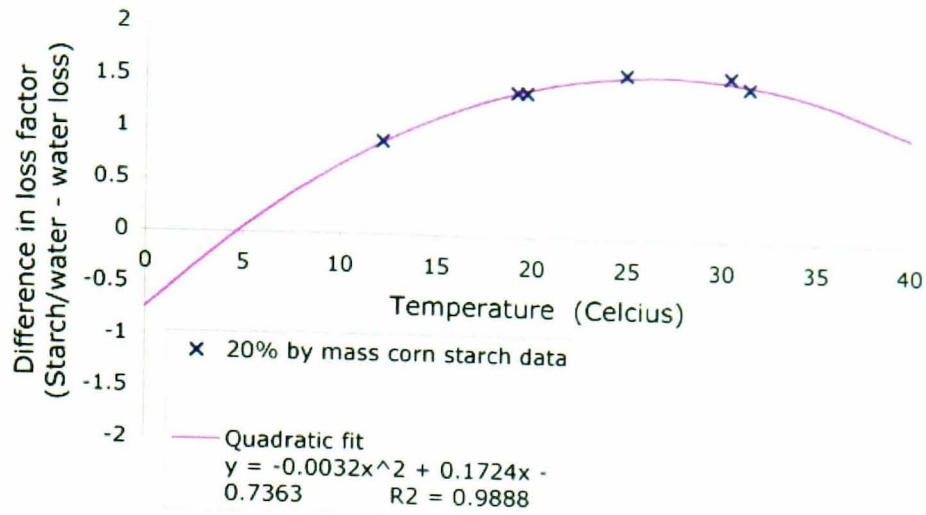

Figure 6.8: *Difference in Loss factor of pure water and 20% water - starch mixture measured at 3.18GHz and at varying temperatures.*

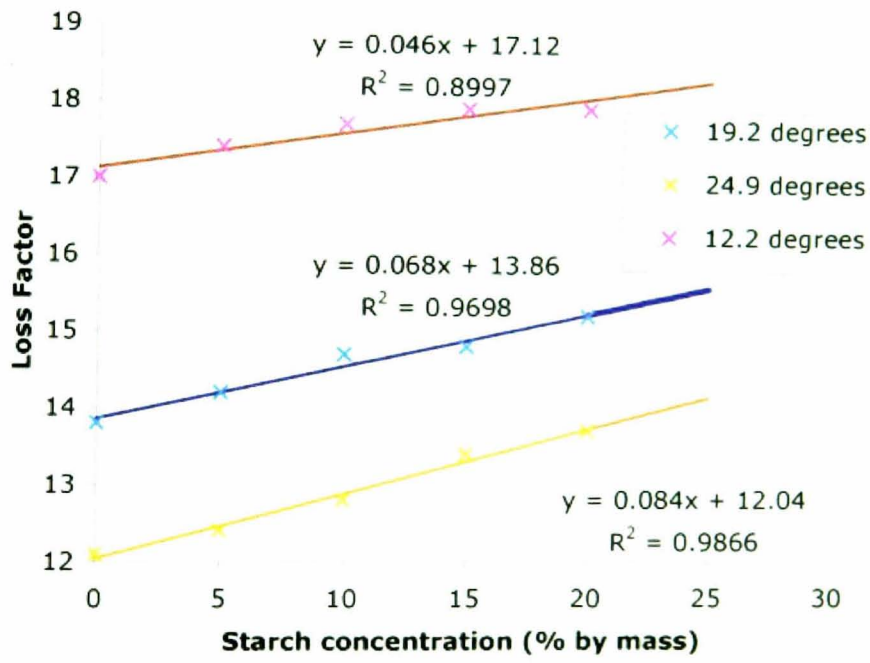

Figure 6.9: *Effect of changes in concentration of starch water solution on the measured loss factor at three different temperatures.*

The loss factor of the mashed potato can now be considered as resulting from three terms: the loss factor value of a pure water solution, the small contribution of the saline loss and the contribution arising from the starch / water interaction:

$$\text{total loss} = \text{water loss} + 0.25\% \text{ sodium chloride loss} + \text{starch / water interaction} \tag{6.13}$$

0.25% saline is considered as there is 0.2g of sodium chloride in approximately 80g of water. The results of this model are plotted in Figure 6.10 along with the experimentally determined mashed potato values. The water loss is determined from Cook's experimental data and the sodium chloride loss from equation 6.8 linearly extrapolated for a 0.25% solution. The loss factor model is clearly a very good match to the experimental data at this frequency.

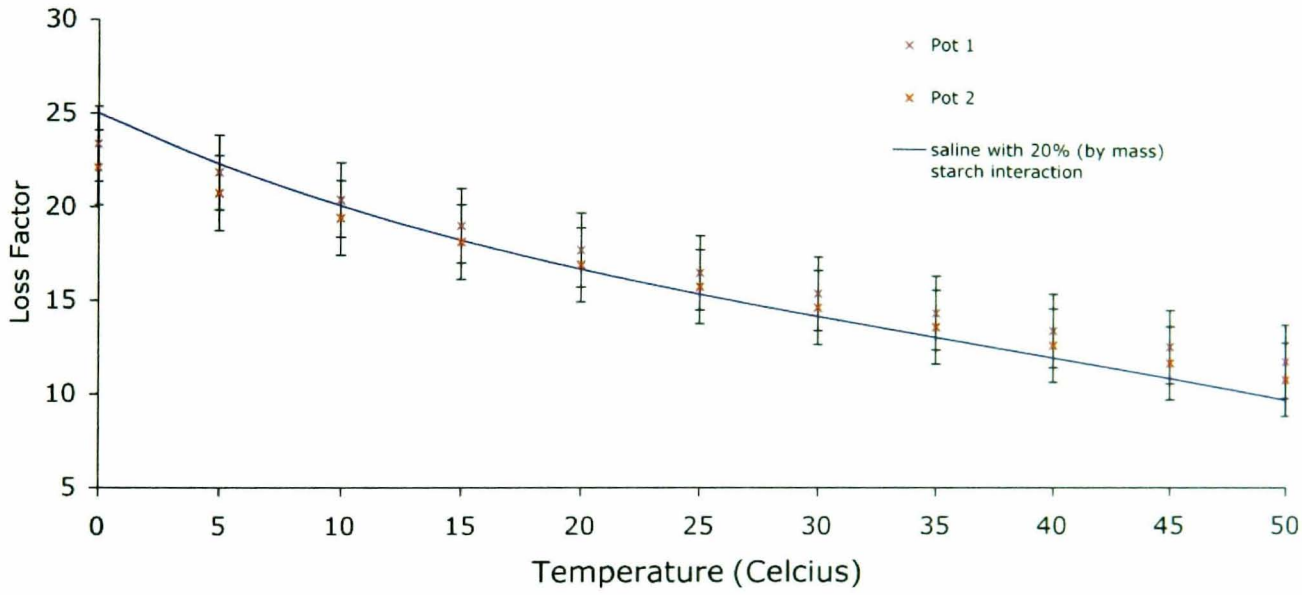

Figure 6.10: *Comparison of the modelled mashed potato loss factor and experimental data points.*

Variations in the water content of the mixture and relative volume fraction of the starch component will primarily affect the results in terms of variations in the saline loss to be added. The effect from the water-starch interaction will be trivial compared to this effect. With each sample of potato produced one would assume some variation in exact water content and hence saline concentration. It has been shown by Bircan and Barringer [161] that as the salt content increases to over 1% a sizeable salt starch interaction also contributes. For the samples of mashed potato considered here, however, the saline

concentration is unlikely to rise above 0.5%. In the majority of samples a carbohydrate concentration of 20% is obtained and hence the values for this concentration are used.

6.1.3.5 Loss factor model at 1.35GHz

Again, as an apparently appropriate method of modelling the loss factor at 3.2GHz has been demonstrated it is hoped that a similar approach will work at 1.35GHz. As previously mentioned it has been much more difficult to experimentally obtain a wide range of data values at this frequency, however, in this case some data is available from the literature.

In addition to the one measurement from Land, Burfoot *et al.* [154] provide a range of loss factor values at 0.9GHz. Although the mashed potato used by Burfoot *et al.* has a much higher water content than desired this does not have a great effect on the loss factor values as previously discussed. The problem with the data of Burfoot *et al.* is that no actual salt content is stated, it can merely be assumed that there is salt present and that it is not more than 0.4% by mass of the complete mixture. It is hoped, however, that as Burfoot's measurements are made on a mashed potato mixture with no added salt that their sodium content will be similar to ours. No data can be taken for direct comparison with the potato model from Roebuck and Goldblith as their measurements do not involve any sodium chloride content. It is possible, however, to use Roebuck and Goldblith's data in determining the carbohydrate water interaction.

Due to the lack of information available to model the starch water interaction at this lower frequency the same form of interaction as is seen at 3.2GHz is employed. Thus the interaction is taken to have the quadratic form as before with a modified maximum value. This value is determined by considering the modelled value for pure water and 20% carbohydrate and comparing with Roebuck's value. A small correction term is then included so that these values match. The interaction is thus modelled as:

$$\text{Interaction Term} = -0.0032T^2 + 0.1724T - 0.3363 \qquad (F/m) \qquad (6.14)$$

where T is the Temperature.

The loss factor of the mashed potato is then modelled as in equation 6.13 and yields the curves shown in Figure 6.11. At 1GHz the modelled curve comes close to the data point of Land. At 0.9GHz the curve is close to all measurements of Burfoot *et al.* given an error of 5% to account for any salt content variation and an error of 2% in modelled data. It is also worthwhile noting that as the water content of the mashed potato mixture of Burfoot is greater than that considered here, it is likely that the water starch interaction term has overestimated the interaction in this case. Taken into account this would lower the modelled curve at higher temperatures providing a better fit.

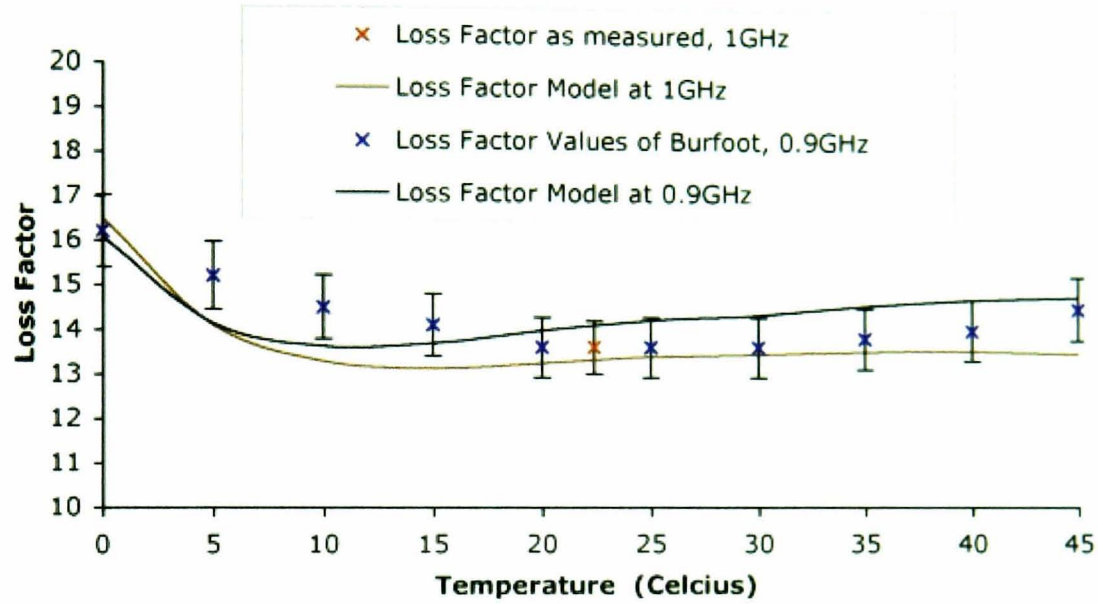

Figure 6.11: *Comparison of the modelled mashed potato loss factor and experimental data points around 1GHz.*

Although the interaction between the carbohydrate and water has not been fully accounted for, this model is reasonable, and at the higher temperatures (which are more relevant to this work) seems to be a good fit. Consequently this model will be considered acceptable for the mashed potato loss factor at 1.35GHz.

6.1.3.6 Mashed potato complex permittivity values

Figures 6.12 and 6.13 show the final form of the complex permittivity of the mashed potato mixture modelling at the frequencies of 1.35GHz and 3.2GHz over the temperature range of 0 to 50 °C. For each model a best fit polynomial is quoted with associated correlation

(r^2) value. These equations are stated below, where T is the temperature in degrees Celsius, f_1 corresponds to the frequency of 1.35GHz and f_2 corresponds to the frequency of 3.2GHz.

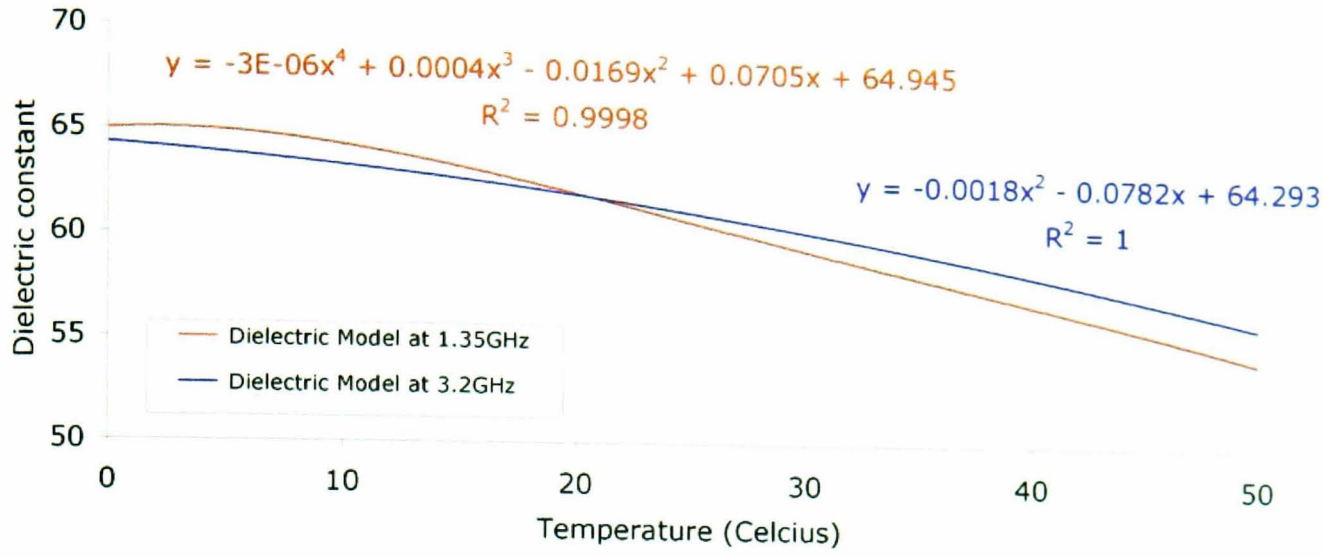

Figure 6.12: *Model of the dielectric constant of the mashed potato mixture at 1.35GHz and 3.2GHz.*

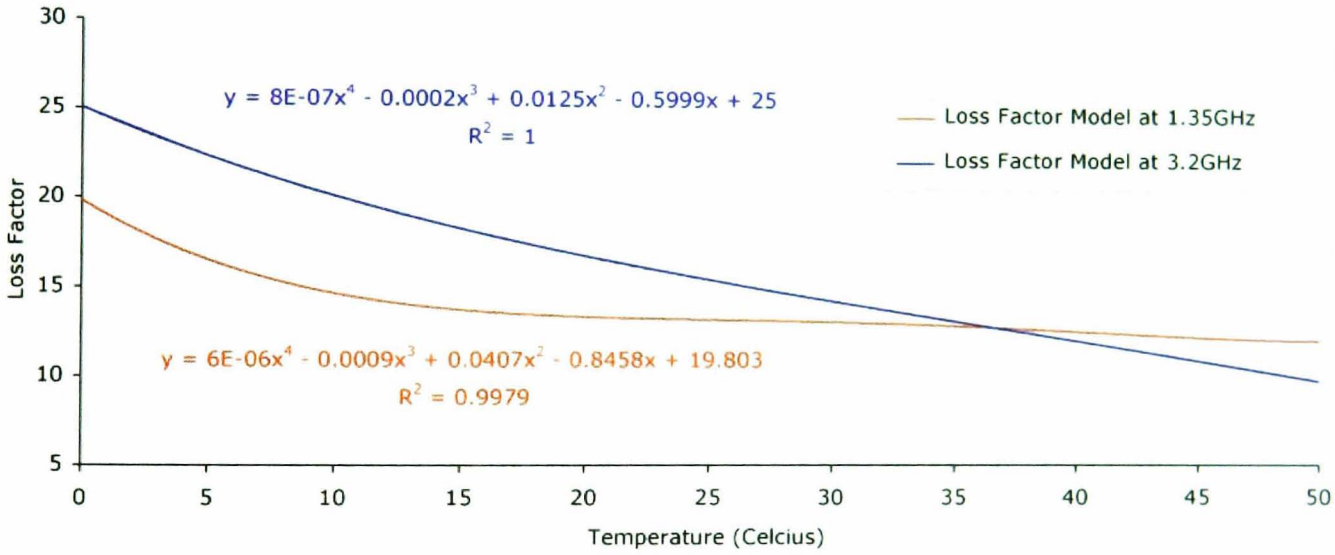

Figure 6.13: *Model of the loss factor of the mashed potato mixture at 1.35GHz and 3.2GHz.*

$$f_1 \quad \epsilon_r' = -3x10^{-6}T^4 + 0.0004T^3 - 0.017T^2 + 0.0705T + 64.95 \quad r^2 = 0.9998 \tag{6.15}$$

$$f_2 \quad \epsilon_r' = -0.0018T^2 - 0.0782T + 64.29 \quad r^2 = 1 \tag{6.16}$$

$$f_1 \quad \epsilon_r'' = 6x10^{-6}T^4 - 0.0009T^3 + 0.0407T^2 - 0.8458T + 19.8 \quad r^2 = 0.998 \tag{6.17}$$

$$f_2 \quad \epsilon_r'' = 8x10^{-7}T^4 - 0.0002T^3 + 0.0125T^2 - 0.5999T + 25 \quad r^2 = 1. \tag{6.18}$$

6.1.3.7 Conclusions of the mashed potato modelling

A model of the dielectric properties of mashed potato has been developed to allow evaluation of the variation in the permittivity and conductivity over a range of temperatures at two frequencies. Any interaction between starch and water has been shown to be negligible for the dielectric constant. As a result the dielectric constant at 3.2GHz has been accurately modelled using the Maxwell mixture equation. Results compare favourably to the results of Roebuck and Goldblith [153] and Bengtsson and Risman [162] and to experimental measurements over the temperature range of 0°C to 50°C. Further to this Maxwell modelling has been applied to determine the dielectric constant at 1.35GHz and again the results compare reasonably with the limited published data [154] and experiment.

The loss factor of the mashed potato mixture has been considered in some detail at 3.2GHz. It has been suggested that the symbiotic effect of adding starch to water serves to keep the loss factor of the mixture constant at the pure water value for starch concentrations of 0 to 25% [161]. In fact measurements made here suggests a small increase in loss factor as a result of addition of starch. This interaction has been modelled based on experimentally obtained data. It has been possible by considering this interaction to model the loss factor of the mashed potato at 3.2GHz and 1.35GHz by considering the pure water value and including a correction for the salt present and for the interaction of the starch and water. The results of this model provide values of the loss factor which compare favourably at both frequencies with the results of Roebuck and Goldblith [153] and Land at 3.2GHz and those of Burfoot *et al.*[154] and Land at 1.35GHz over a reasonably large temperature range (0-50 °C).

6.2 Weighting function comparisons

The weighting functions computed for the two phantom types; saline protein mixture and mashed potato, are considered in order to draw conclusions on the effect of changes in the dielectric properties and on the limits of the computational modelling. The phantom materials are excited by a dual-frequency antenna (see chapter 5 for the design specifics of this antenna) operating at 1.35GHz and 3.2GHz with a phantom of "infinite" extent of each of the proposed materials. Variations in this phantom model occur for consideration of the effects of dielectric layering and the effects of the finite bounds of the simulation space. Further details of these changes are given at relevant sections in the text. Simulations were performed with a cell size of 3mm at 1.35GHz and of 1.3mm at 3.2GHz. The phantom material covered an area of 426 mm x 426 mm x 237 mm at 1.35GHz and 185 mm x 185 mm x 104 mm at 3.2GHz.

6.2.1 Methods of comparison

Comparisons of the weighting functions are performed by considering the one dimensional weighting function, its relation to an equivalent plane wave and finally the contribution of the computed weighting function to temperature retrieval relations.

6.2.1.1 One-Dimensional Weighting Functions

For each simulation type the weighting function is determined at each position in a three dimensional phantom. To ease comparisons between each different simulation this three dimensional weighting function can be reduced to a one dimensional weighting function as:

$$w(z) = \int_x \int_y w(x, y, z) dx dy. \tag{6.19}$$

This one dimensional weighting function can be normalised in two ways:

$$\int w(z) dz = 1 \tag{6.20}$$

$$max(w(z)) = 1 \tag{6.21}$$

In order to compare weighting functions found from different simulations with each other, the usual normalisation method (equation 6.20) is employed. For a particular simulation configuration it can be of interest to compare the shape of the calculated weighting function to that of a plane wave. In this instance it is useful to re-scale both curves to the same scale (equation 6.21).

6.2.1.2 Plane Wave comparisons

For a plane wave (varying as $e^{-2\alpha z}$) the attenuation coefficient (α) for each phantom material is calculated from the dielectric properties as:

$$\alpha = \omega \sqrt{\frac{\mu\epsilon}{2}\left[\sqrt{\left(\frac{\epsilon''}{\epsilon'}\right)+1}-1\right]} \tag{6.22}$$

Plots of plane wave attenuation can then be compared directly with the computed weighting function results. It can be of interest to compute the equivalent attenuation coefficient of the weighting function by fitting an exponential to the computed curve.

Additionally, comparison of the the area under the attenuation curve from 1 to 1/e can be compared to the simulated result for each material. This area gives a useful measure of the dominant contribution to the microwave signal. For a plane wave this area is found by performing the integration and is given by:

$$\frac{1}{2\alpha}\left(1-\frac{1}{e}\right) \tag{6.23}$$

To determine the corresponding area for the simulation result it is necessary either to use numerical integration over the range of interest or to use the equivalent attenuation value. Numerical integration in this instance is not appropriate as the number of data points from the simulation available in the intensity range of 1 to 1/e is approximately 5 and without extrapolation of the computed curve to obtain a value at 1/e inaccuracies occur. For this reason the simulated area is computed using equation 6.23 with the best fit attenuation coefficient.

6.2.1.3 Temperature profiles

The microwave radiometry system measures the *microwave temperature* of the source material. Measuring this at two frequencies will give two temperatures. These temperatures are related to the actual temperature distribution in the material as:

$$T_{mw1/2}(z) = \int_0^\infty w(f_{1/2}, z)T(z)dz \tag{6.24}$$

where 1 and 2 represent the two frequencies of measurement. Using the BEST modeller it is possible to determine the weighting functions $w(f_1, z)$ and $w(f_2, z)$. It then remains to invert these equations to give an estimate of T(z). The simplest approach to this problem is to assume a known form of the temperature distribution. The simplest case is that of a linear temperature variation over the distance where w(r) is significant. Given this temperature form equation 6.24 reduces as:

$$T_{mw1/2} = \int_0^\infty w(f_{1/2}, z)(m.z + c)dz \tag{6.25}$$

So that

$$\frac{T_{mw1/2} - c}{m} = \int_0^\infty w(f_{1/2}, z).z.dz = W_{1/2} \tag{6.26}$$

Thus through simulation and experimental measurement an estimate of this gradient is possible as:

$$m = \frac{(T_{mw1} - T_{mw2})}{\left(\int_0^\infty w(f_1, z).z.dz - \int_0^\infty w(f_2, z).z.dz\right)}. \tag{6.27}$$

For each type of material considered the values of the integrals W_1, W_2 are computed and the effect of how variations in dielectric properties affects these values is considered. In terms of a plane wave equivalent these integrals reduce to the value $1/2\alpha_{1/2}$.

For a quadratic temperature profile the analysis is similar and the integrals of interest to be computed are $W_{1/2}$ as above and:

$$W_{1q/2q} = \int_0^\infty w(f_{1/2}, z).z^2.dz \tag{6.28}$$

which has the plane wave equivalent value of $1/2\alpha_{1/2}^2$.

Finally the case of an exponentially decaying temperature profile can be considered. This profile is of interest for medical applications as it forms part of the temperature profile

used to model the thermal distribution in the baby head [25] and has been shown to be an appropriate simple model for general body thermal modelling [27]. An exponential decay from a central (or arterial temperature T_c) to a surface temperature (T_s) of the form:

$$T(z) = T_c - (T_c - T_s)e^{-qz} \tag{6.29}$$

where q is either unknown or can be determined as:

$$q = \sqrt{\frac{w_b C_b}{K}} \tag{6.30}$$

where w_b is the blood perfusion, C_b is the blood specific heat capacity and K is the tissue thermal conductivity [27] is considered.

Substitution of this profile into equation 6.24 yields:

$$T_{mw1/2} = T_c - (T_c - T_s) \int_0^\infty w(f_{1/2}, z)e^{-qz}dz. \tag{6.31}$$

If the value of q is known the integral can be numerically determined and the resulting system of equations solved for the surface and central temperatures. If the weighting function is assumed to have an effective plane wave attenuation (α_e) then the integration can be performed to give:

$$T_{mw1/2} = T_c - \frac{(T_c - T_s)}{(1 + q/2\alpha_{1e/2e})}. \tag{6.32}$$

6.2.2 Variation of dielectric properties

The first set of materials to be modelled are the saline / protein mixture with varying protein contents from 0 to 80%. Initially with the saline modelled as being composed of entirely free water and latterly the effect of water binding to the protein is considered. All numerical integration is performed using the trapezoidal rule [163].

Figures 6.15, 6.16, 6.17 and 6.18 display the one dimensional weighting functions at 1.35GHz and 3.2GHz for the free water models and at 1.35GHz and 3.2GHz for the free and bound water models respectively. Considering each plot in turn it is clear that as the percentage of protein in the mixture increases the attenuation of the weighting function is less rapid and the contribution of the area directly beneath the antenna aperture diminishes. This corresponds in all cases to a marked decrease in conductivity of the

phantom mixture. In conjunction with this a decrease in the dielectric constant is also taking place.

Comparing figures 6.15 and 6.16 for the free water model at 1.35GHz and 3.2GHz the differences in the attenuation of the weighting function are apparent (note the different depth axis scales). At the higher frequency the attenuation is much more rapid leading to a microwave temperature reading that is more surface region dominant. Considering tables 6.1 and 6.2 it is clear that the values of the dielectric constant across the frequencies are approximately equal for all protein concentrations. Thus the decrease in conductivity at the lower frequency results in these differences. This is also the case for the free and bound water models, see figures 6.17 and 6.18. Considering the effect of the bound water in the phantom materials the decrease in conductivity this results in a similar slower attenuation and larger contribution from greater distance at both frequencies.

The conductivity of the free water phantom for a protein concentration of 50% at 3.2GHz is very similar to that of the conductivity of the free water phantom for 10% protein at 1.35GHz. The high frequency dielectric constant is approximately half that of the low frequency phantom. Comparing the one dimensional weighting function for these two configurations it is clear (Figure 6.14) that even with the same conductivity the lower frequency curve has a slower attenuation. The decreased dielectric constant of the higher frequency phantom would account for this difference.

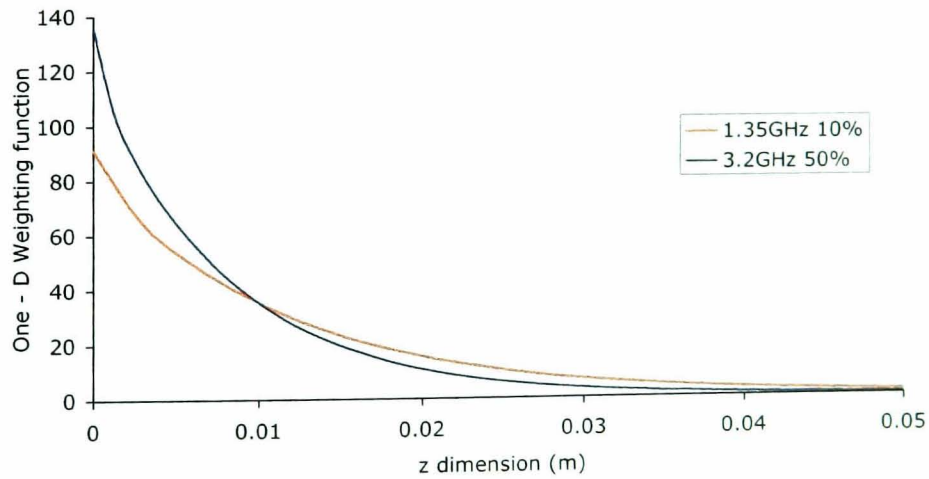

Figure 6.14: *One dimensional weighting function computed at 3.2GHz for 50% protein concentration and at 1.35GHz for 10% protein concentration.*

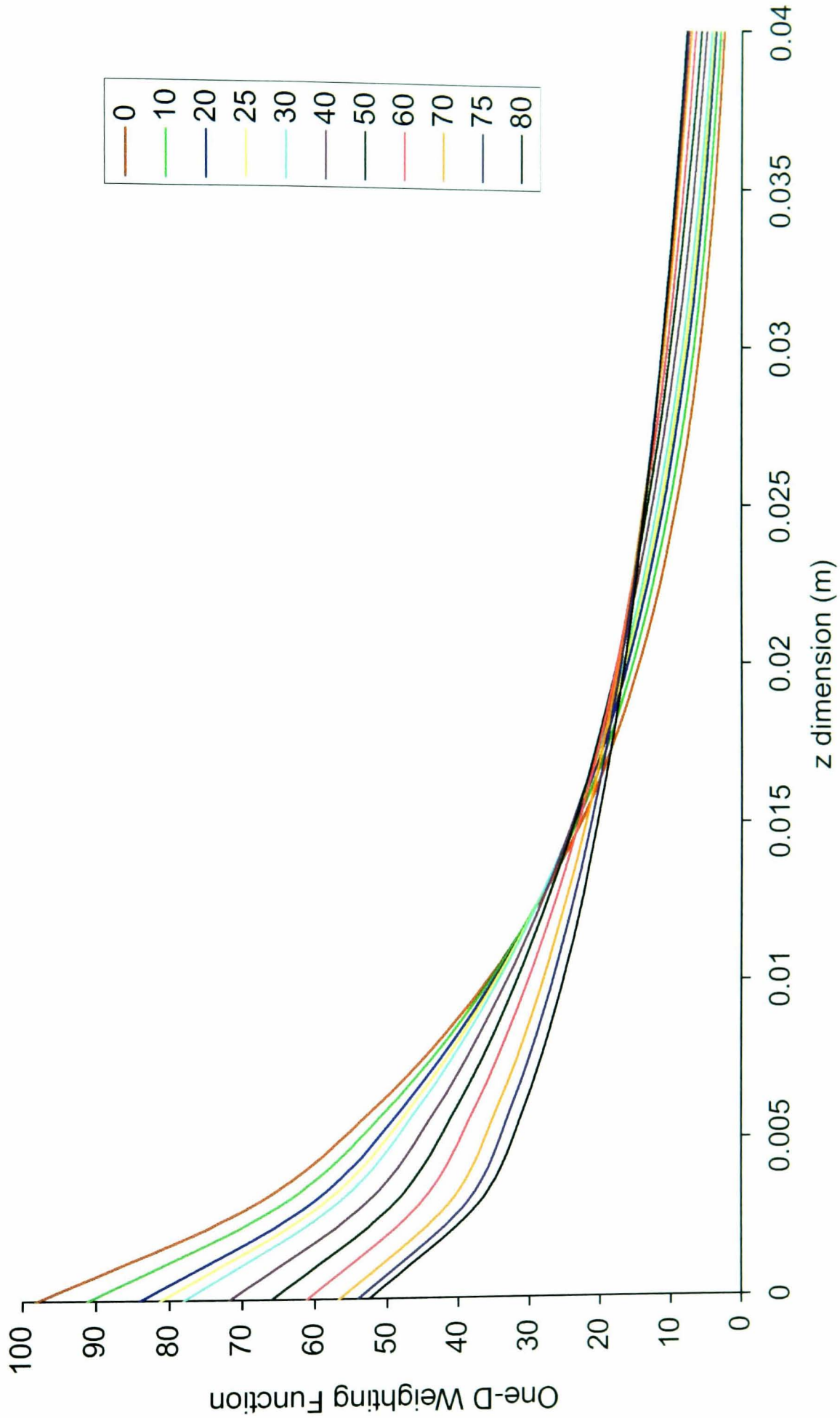

Figure 6.15: *One dimensional weighting function computed at 1.35GHz for varying protein concentrations 0-80% with free water model.*

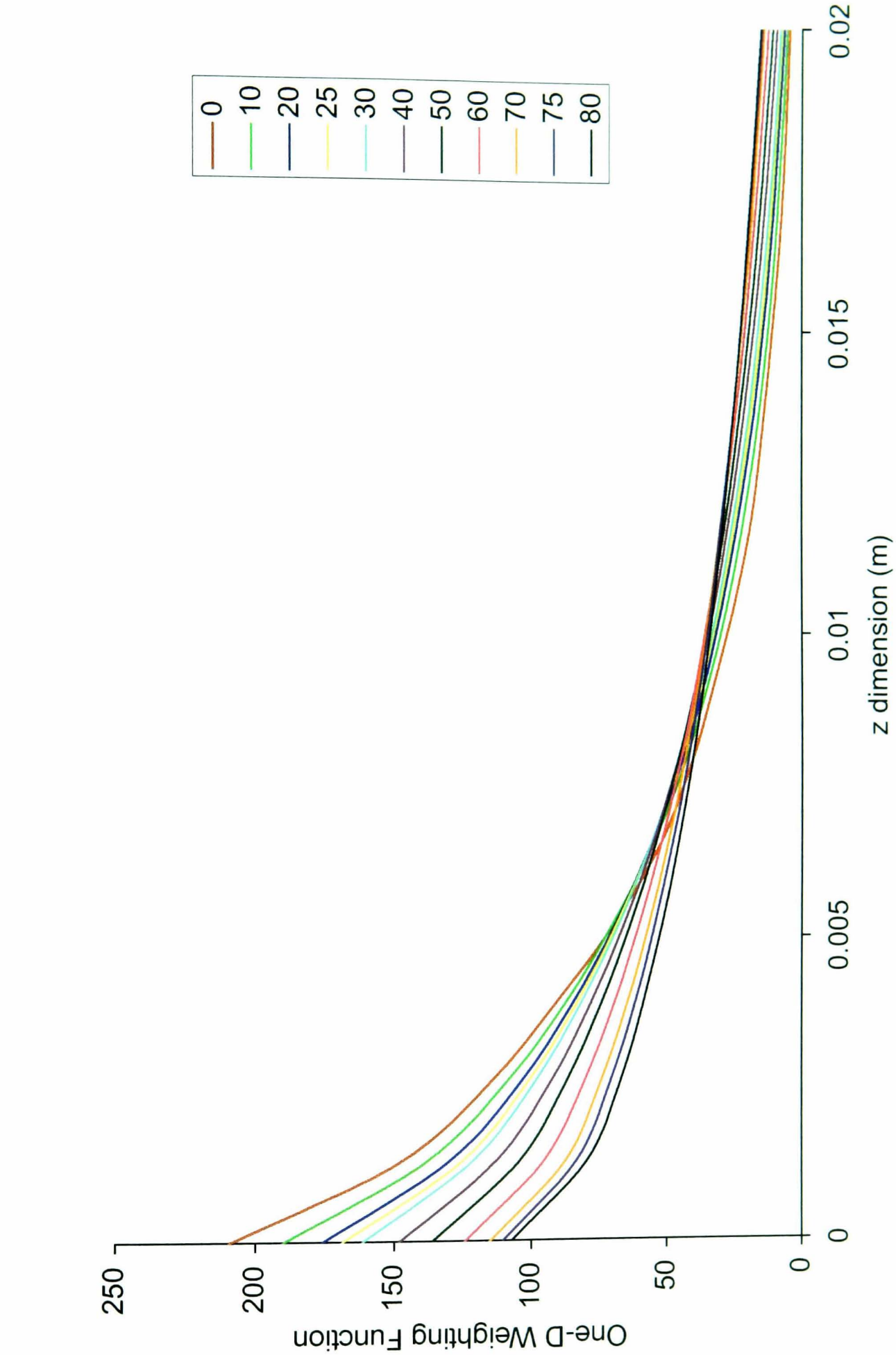

Figure 6.16: *One dimensional weighting function computed at 3.2GHz for varying protein concentrations 0-80% with free water model*

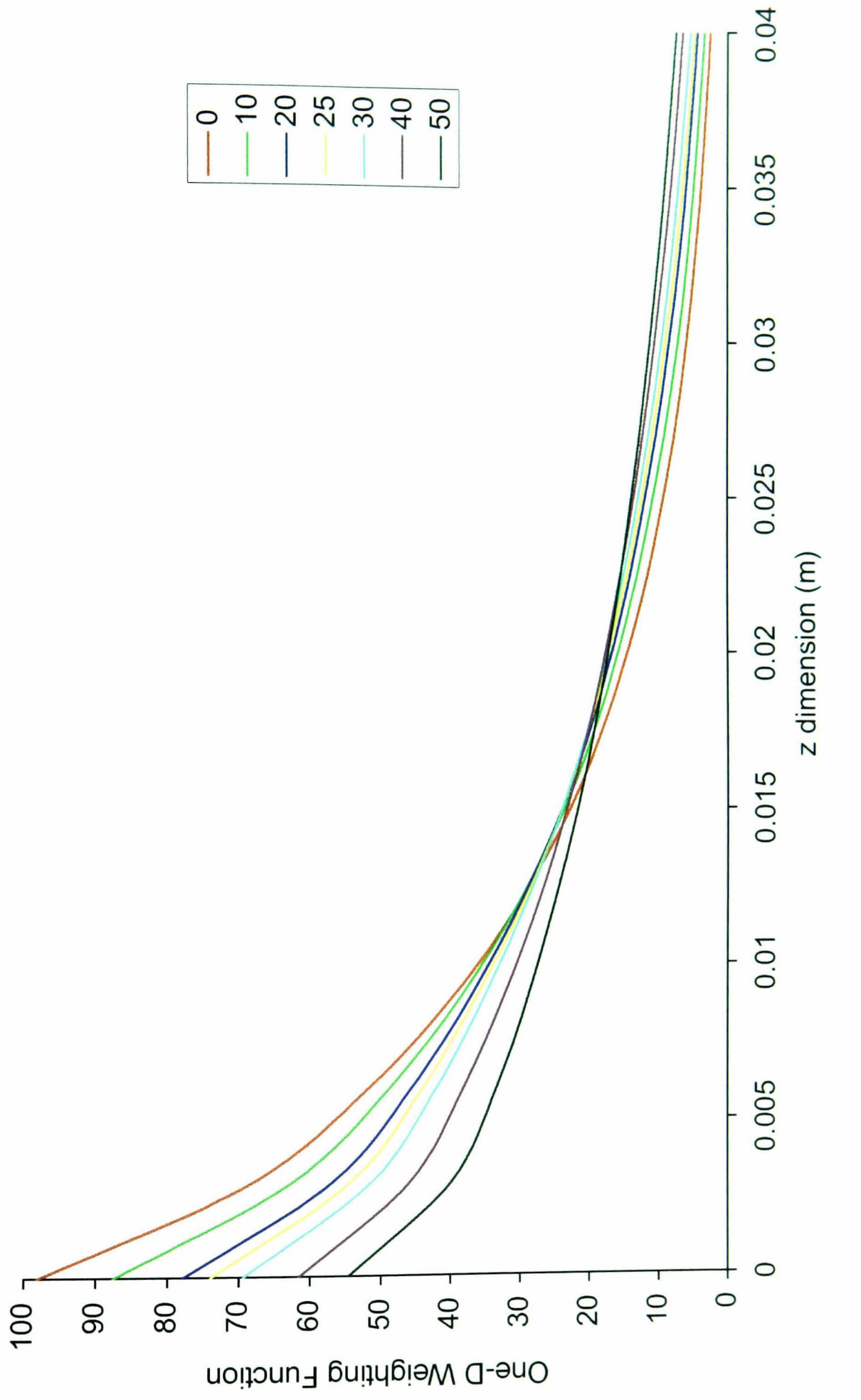

Figure 6.17: *One dimensional weighting function computed at 1.35GHz for varying protein concentrations 0-80% with free and bound water model.*

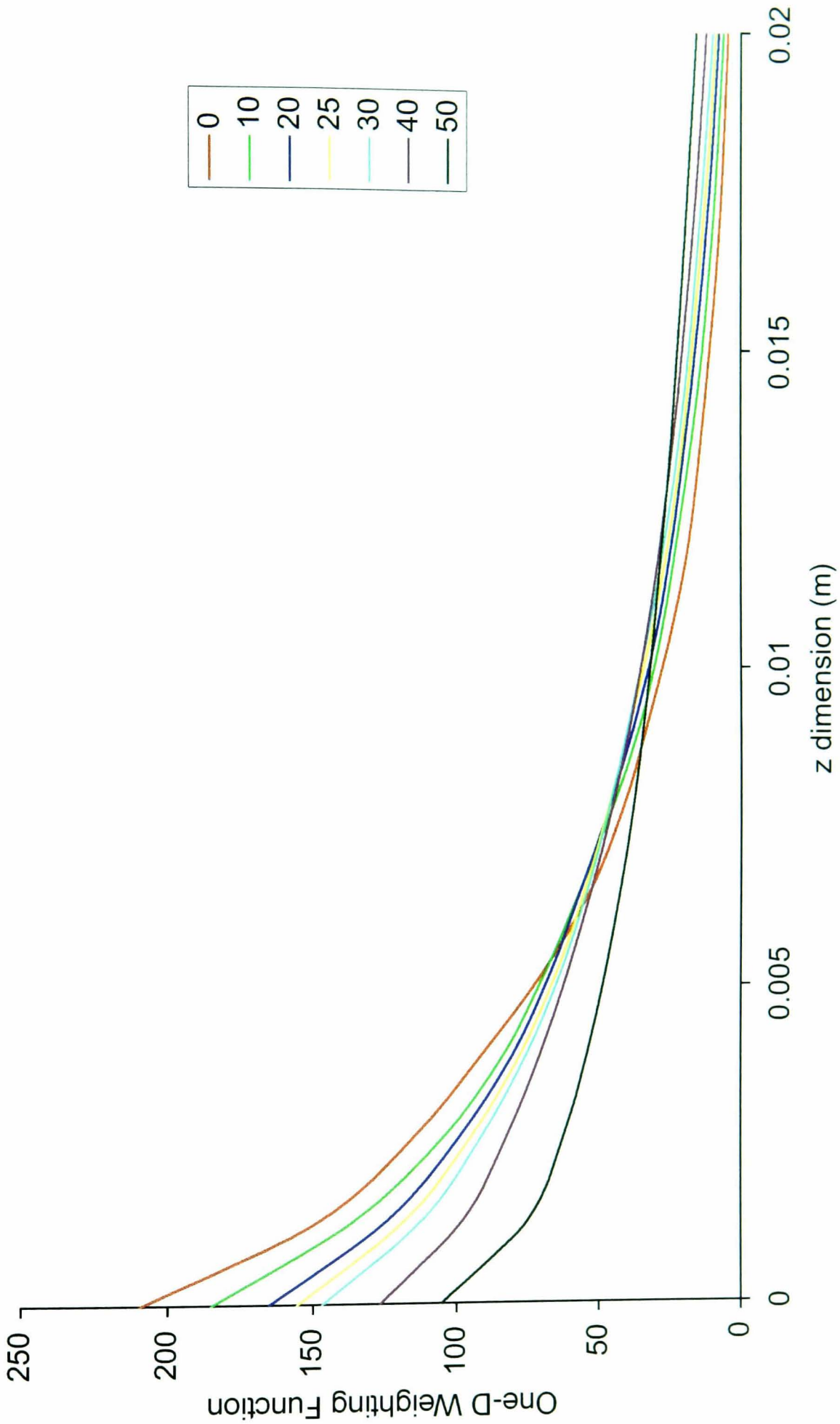

Figure 6.18: *One dimensional weighting function computed at 3.2GHz for varying protein concentrations 0-80% with free and bound water model.*

6.2.2.1 Temperature variation

Turning to the mashed potato phantom it is possible to investigate the effect of changes in the dielectric properties as a result of variation in temperature of the phantom. Simulations are performed with phantoms simulating mashed potato at 10°C, 20°C, 30°C and 40°C at 3.2GHz. Table 6.4 gives the dielectric properties of the mashed potato at these temperatures.

Temperature	Dielectric Constant	Conductivity (S/m)
10	63.11	3.62
20	61.78	3.04
30	60.10	2.57
40	58.07	2.21

Table 6.4: *Mashed potato dielectric property values for varying temperature at 3.2GHz.*

Figure 6.19 details the one dimensional weighting function at each temperature. The increase in temperature serves to reduce the conductivity of the mashed potato and as such results in a slower attenuation of the weighting function with increasing temperature.

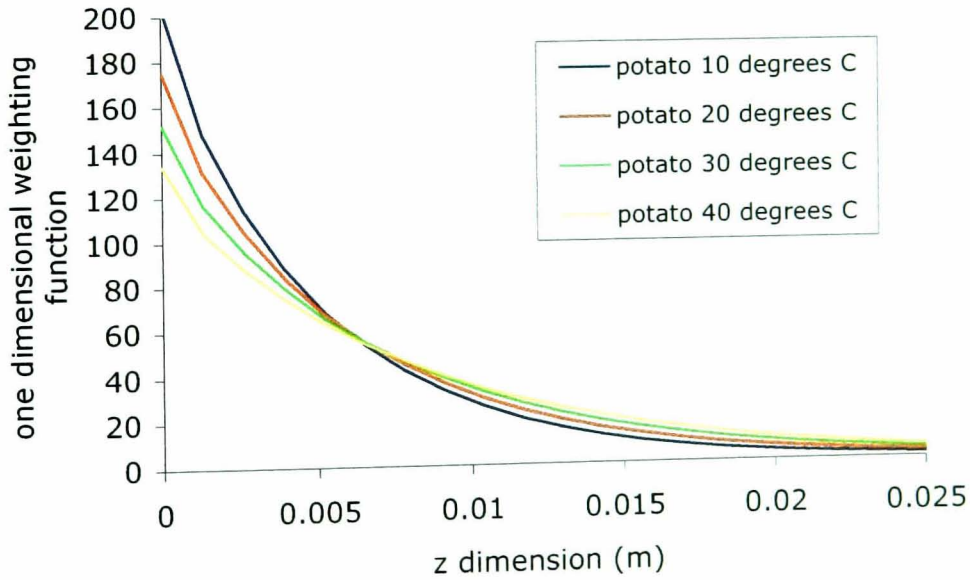

Figure 6.19: *One dimensional weighting function computed for varying temperatures of . mashed potato at 3.2GHz.*

6.2.2.2 Plane wave comparisons

As described in section 6.2.1.2 it is possible to compare the computed weighting functions to the equivalent plane wave response in a number of ways. At both frequencies for all phantom types the attenuation seen for the weighting function is as expected more rapid than that for the plane wave.

By fitting an exponential to the computed weighting functions the attenuation coefficient can be directly compared across all phantom configurations with the associated plane wave values, see tables 6.5 and 6.6 for the 1.35GHz and 3.2GHz results respectively. The fits were performed using the *fmins* function in MatLab [141] to fit a straight line to the log of the computed weighting function over the first 21 data points (corresponding to depths of 6.3cm and 2.7cm for 1.35GHz and 3.2GHz respectively). See Figure 6.20 for plots of the weighting function and plane wave equivalent fit for the 10% protein free water model at 1.35GHz and 3.2GHz. Correlations for all data sets were good ($r^2 \geq 0.998$) and the root mean square difference in all cases was small. A notable decrease in correlation and increase in error occurred for free model phantoms with greater than 50% protein. In the bound water model case the correlations fell at concentrations of around 40% protein, reflecting the change in dielectric properties for those models.

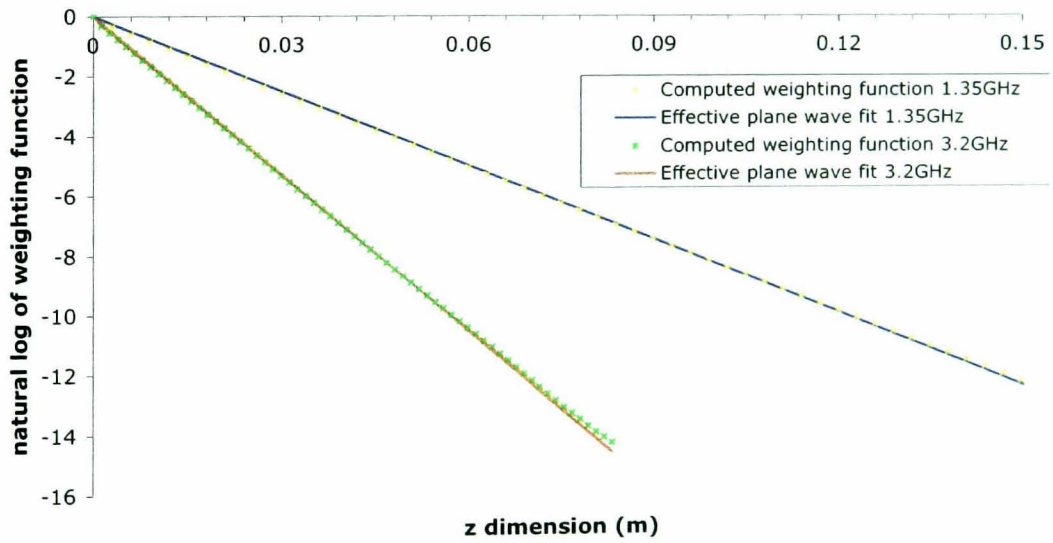

Figure 6.20: *Comparison of the natural logarithm of the one dimensional weighting function with effective attenuation plane wave curve for 10% protein saline mixture with free water model at 1.35GHz and 3.2GHz.*

% Protein	Free model simulated	Plane wave	Bound model simulated	Plane wave
0	45.3	39.8	-	-
10	41.8	36.8	40.1	35.3
20	38.3	33.8	35.2	30.9
25	36.9	32.3	33.1	28.8
30	35.3	30.9	30.8	26.6
40	32.0	27.9	26.4	22.2
50	29.0	24.8		-
60	26.1	21.7	-	-
70	23.3	18.3	-	-
75	21.6	16.4	-	-
80	20.2	14.5	-	-

Table 6.5: *Plane wave and effective attenuation coefficient (m^{-1}) at 1.35GHz for varying protein concentrations 0-80%.*

As observed in the earlier comparisons the computed values of effective attenuation coefficient for the weighting functions fall with increasing protein concentration at both frequencies. Over the range of 0 to 50% protein concentration in the free water models at both frequencies the attenuation coefficient for the plane wave is consistently approximately 12% less than that computed for the weighting function.

At larger protein concentrations the difference increases probably as a result of the lower correlation between the weighting function and plane wave, a result of a greater contribution of the near field effect. Considering the attenuation across frequencies the α values at 1.35GHz are approximately half those at 3.2GHz reflecting the factor 2 relationship between their conductivities. The effective attenuation coefficient computed for the bound water phantom is consistent with the pattern observed in the free water case.

Calculation of the area from intensity 1 to 1/e of the plane wave curve and the corresponding values determined from the weighting functions can then be computed using these values for the attenuation coefficient. For concentrations of 0 to 50% protein the

% Protein	Free model simulated	Plane wave	Bound model simulated	Plane wave
0	95.7	84.4	-	-
10	88.3	78.1	84.0	74.9
20	81.1	71.8	74.5	65.7
25	77.5	68.7	69.7	61.1
30	74.1	65.6	65.2	56.6
40	67.4	59.3	55.6	47.2
50	61.1	52.9	-	-
60	54.6	46.1	-	-
70	48.9	38.9	-	-
75	46.1	35	-	-
80	43.3	30.8	-	-

Table 6.6: *Plane wave and effective attenuation coefficient (m^{-1}) at 3.2GHz for varying protein concentrations 0-80%.*

plane wave area will differ consistently from that of the weighting function and be greater by approximately 12%.

6.2.2.3 Conclusions

The behaviour of the weighting function in one dimension is dependent primarily on the conductivity of the phantom material under consideration. Accurate knowledge of the conductivity is therefore essential for adequate representation of the weighting function. Further to this the effect of water binding should be considered as the presence of bound water in the phantom material leads to a significant difference in the attenuation of the weighting function.

The fit to an equivalent plane wave is applicable primarily in the case where the phantom is single layered only. For more complex phantom materials it is unlikely that a plane wave will adequately represent the weighting function. It is clear, however, that the assumption that the weighting function follow plane wave behaviour (with attenuation

coefficient as equation 6.22) will produce significant inaccuracies even with the high water content phantoms. Assuming a plane wave attenuation of 12% more than equation 6.22 provides a useful approximation for the weighting functions of this antenna (valid for ϵ_r= 35 to 70 and σ= 1 to 1.6 S/m at 1.35GHz and ϵ_r= 35 to 65 and σ = 1.6 to 3.4 S/m at 3.2GHz).

6.2.3 Dielectric layering

Turning to the more realistic cases of body tissues and foodstuffs, the modelling of dielectric layers is of primary importance both for simulating multi-layered materials and also to consider the effect of temperature variation with depth within a single layered material. The nature of FDTD modelling allows the independent specification of dielectric properties at each cell in the simulation space. As a result the modelling of dielectric layers within a phantom material is relatively straightforward. The finite extent of each cell, however, requires that the variation of dielectric properties be discrete as opposed to continually varying as in reality.

6.2.3.1 Multi-layered materials

The effect on the weighting function of the introduction of dielectric layers is considered at 1.35GHz using the free water phantom model at protein concentrations of 10, 20, 25 and 30 percent protein. Simulations are performed with four layers of equal size (10Δ=30mm, 5Δ=15mm and 3Δ=9mm). Plots of the one dimensional weighting function for the latter two layer sizes are shown in figure's 6.21 and 6.22. In this case the variation of dielectric properties from each layer to the next is sharp. Results are also displayed for simulations with averaged values used at the interface of the layers.

In this case the variation of the dielectric properties from one layer to the next constitutes a gradual increase (or decrease) with no abrupt changes. As a result the effect of layer changes on the one dimensional weighting function is small, especially for the larger layer sizes. In fact for the presence of a layer at depths of 30mm and more had little effect

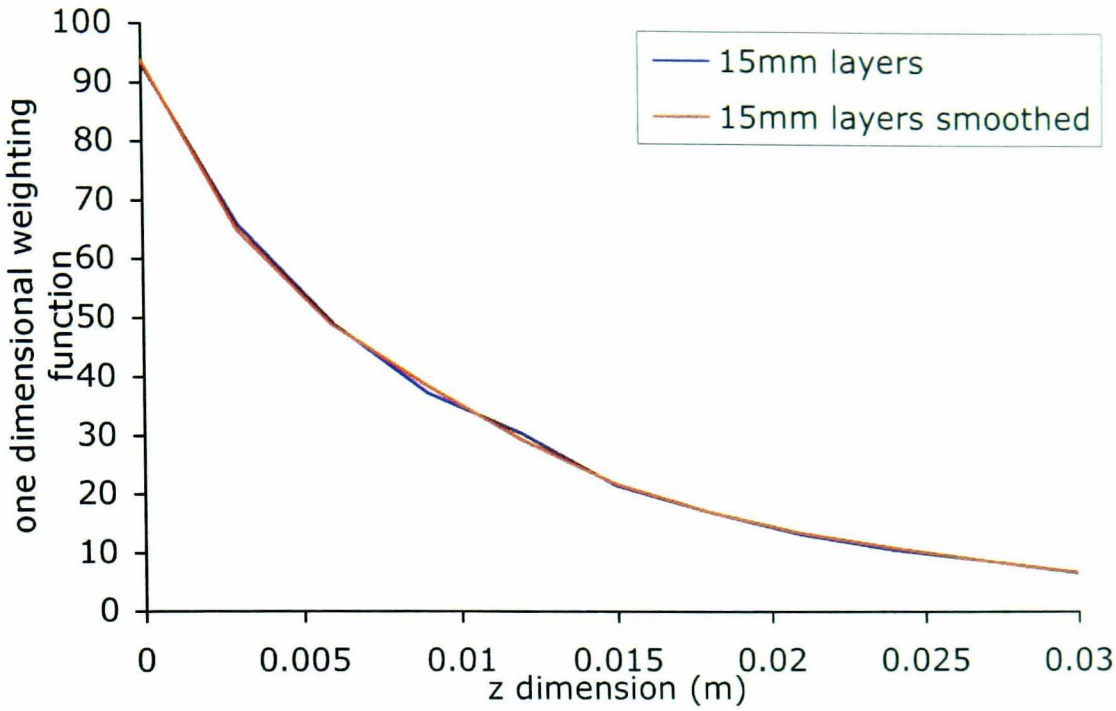

Figure 6.21: *One dimensional weighting function computed at 1.35GHz for a multi-layer phantom with 15mm deep layers. Phantom composition: 10% protein: 20%protein: 30%protein: 40%protein*

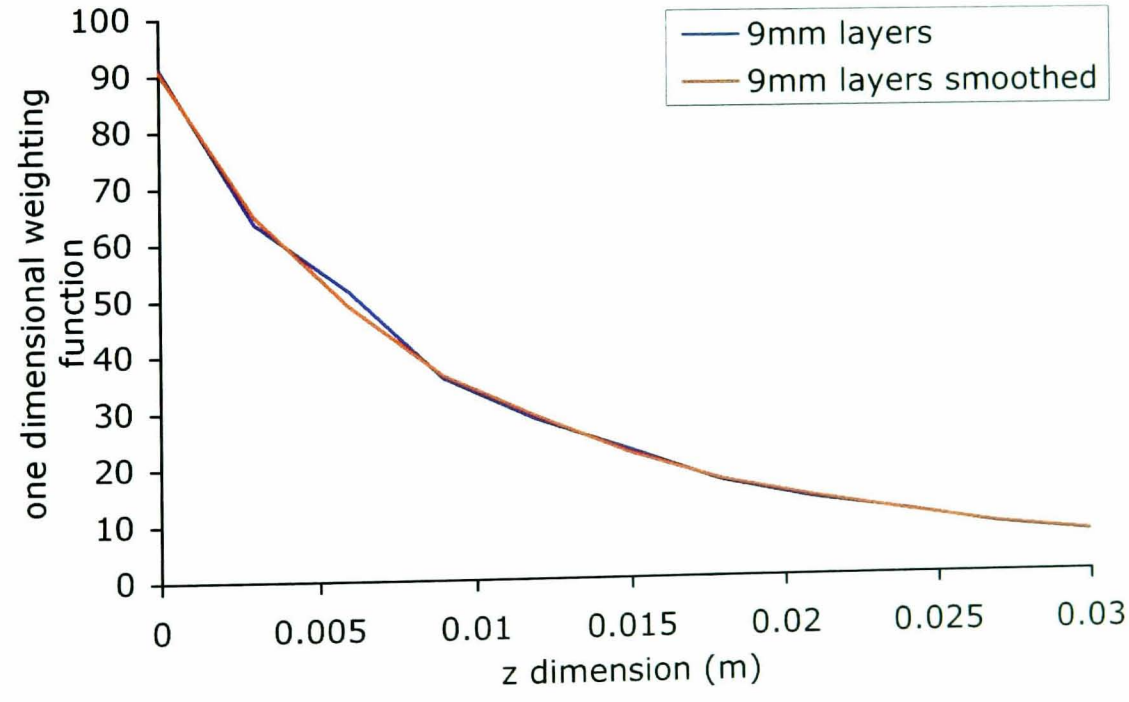

Figure 6.22: *One dimensional weighting function computed at 1.35GHz for a multi-layer phantom with 9mm deep layers. Phantom composition: 10% protein: 20%protein: 30%protein: 40%protein.*

on the weighting function. For the smaller layer sizes of 15mm and 9mm the presence of the layer results in small artifacts in the resulting weighting function. The inclusion of intermediate layers, with averaged dielectric values, serves to reduces this effect and once again produce a smoothly varying weighting function.

Investigation of dielectric layering in which the dielectric properties of each layer varies markedly from the adjacent layers is performed by considering a three layer phantom (composed of 10%, 50% and 10% protein concentration layers) with and without intermediate layers. Figures 6.23, 6.24 and 6.25 give the one dimensional weighting function for these simulations for layers of 30mm, 15mm and 9mm respectively.

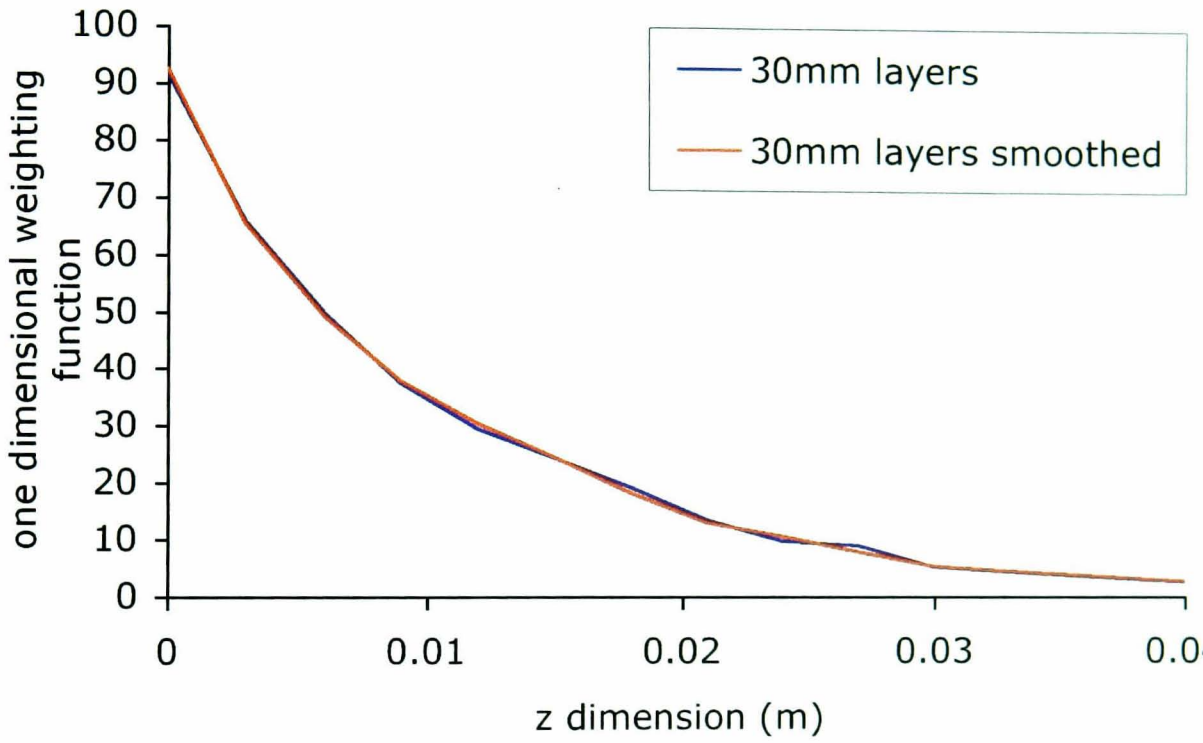

Figure 6.23: *One dimensional weighting function computed at 1.35GHz for a multi-layer phantom with 30mm deep layers. Phantom composition: 10% protein:50%protein:10%protein.*

For dielectric layers of this form the adverse effects on the weighting function are more apparent. For all layer sizes considered the computed weighting function suffers from inaccuracies near the layer boundaries, the effect increasing as the size of the layer reduces. Through the use of intermediate layers of averaged dielectric property values, however, this effect can be greatly diminished.

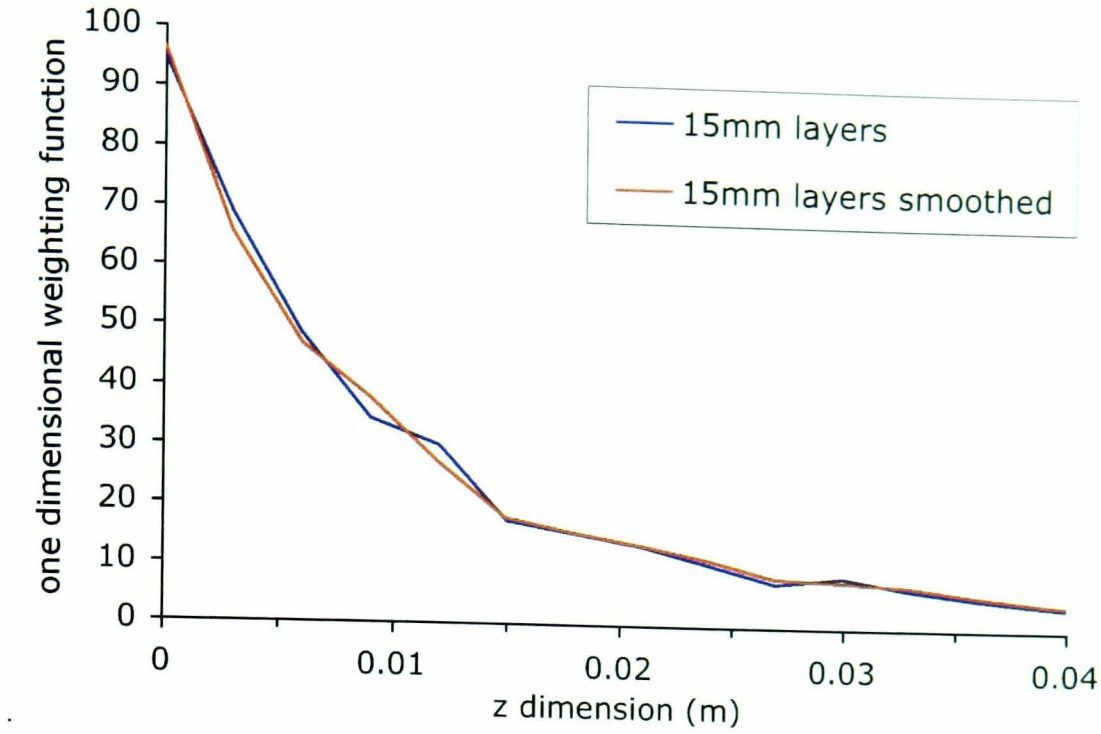

Figure 6.24: *One dimensional weighting function computed at 1.35GHz for a multi-layer phantom with 15mm deep layers. Phantom composition: 10% protein:50%protein:10%protein.*

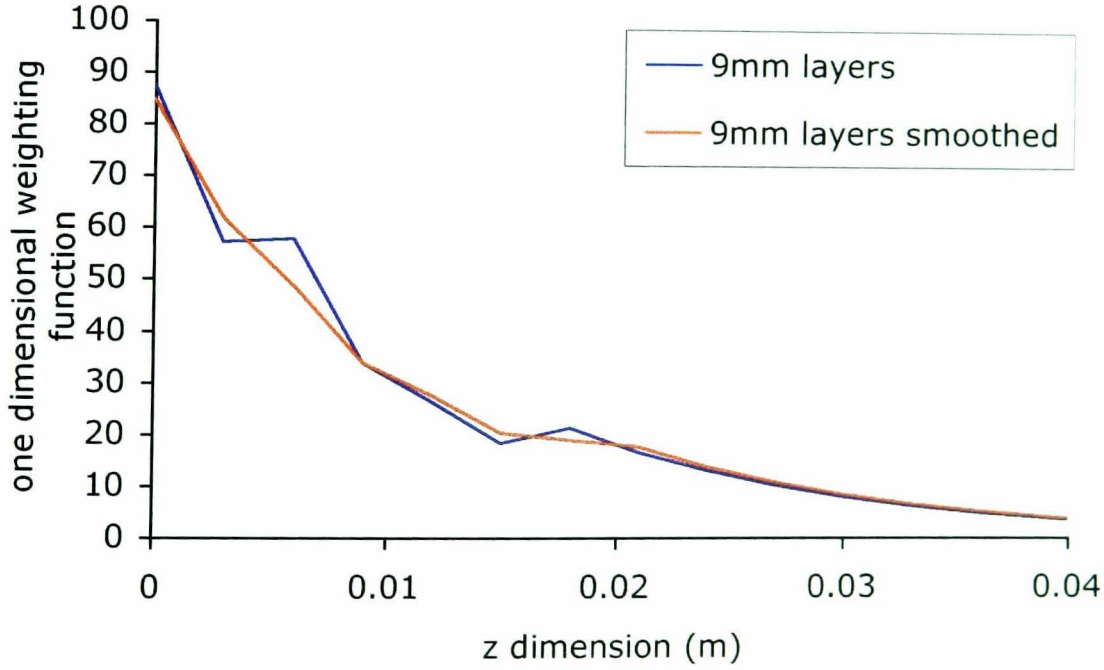

Figure 6.25: *One dimensional weighting function computed at 1.35GHz for a multi-layer phantom with 9mm deep layers. Phantom composition: 10% protein:50%protein:10%protein.*

6.2.3.2 Temperature gradients

The modelling of temperature gradients within the mashed potato phantom material. discussed in chapter 5, is identical to that of modelling of dielectric layers in a multi layered material. In this instance sharp discontinuities in dielectric properties are not a problem as the dielectric properties vary continuously, either increasing or decreasing, as the temperature in the material changes.

6.2.3.3 Conclusions

Complex phantom materials composed of several layers of different dielectric properties can be modelled with relative ease. The use of intermediate layers of averaged dielectric property values results in a marked reduction in the instabilities seen for the cases of small dielectric layers and sharp discontinuities in the material parameters. Such layers would be required in cases where the first layer boundary occurs at depths where the weighting function is less than 90% attenuated.

6.2.4 Effect of finite verses infinite phantom materials

An important limitation of using the FDTD modelling technique is the computational demands of each simulation performed. Reducing the size of the computational domain can result in dramatic reduction of the time and hard drive space required for each simulation. This option is investigated by considering the effect on the weighting function of reducing the z dimension of the simulation space by successive amounts.

Simulations were performed at 1.35GHz for a 25% protein free water model mixture with z dimensions of 57mm, 117mm, 177mm and 237mm. Figure 6.26 shows the one dimensional weighting functions for these four phantom dimensions. For the largest three models the effect of the reduced z dimension size is minimal, a result of the fact that the weighting function is close to zero by 60mm. For the shortest z dimension simulation the attenuation of the weighting function suffers from a greater instability. A best fit to this weighting

function does, however, produce an attenuation coefficient very close to that of the larger z dimension simulations. If the exact form of the weighting function is to be used in a further calculation then it would be inappropriate to shorten the z dimension by more than 60mm for these phantom materials. Similarly at 3.2GHz, Figure 6.27, a limit of z dimension of around 41mm should be imposed.

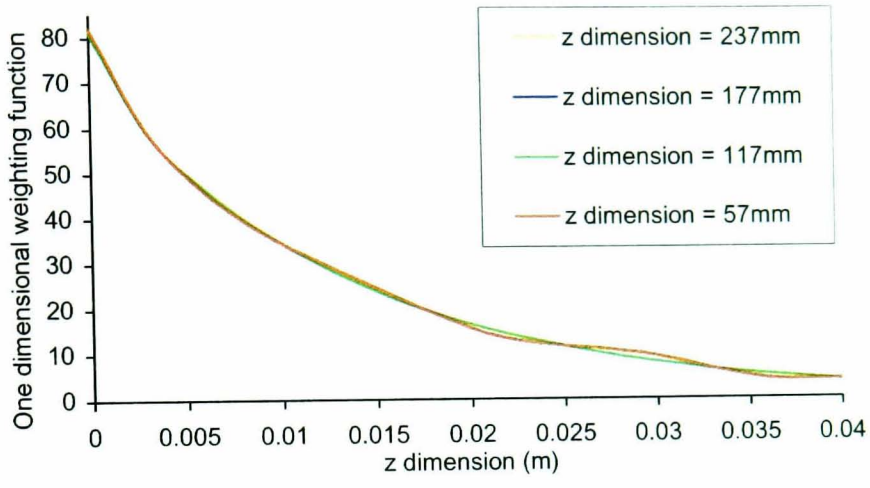

Figure 6.26: *Effect of reduction of the z dimension of the simulation space on the computed one dimensional weighting function.*

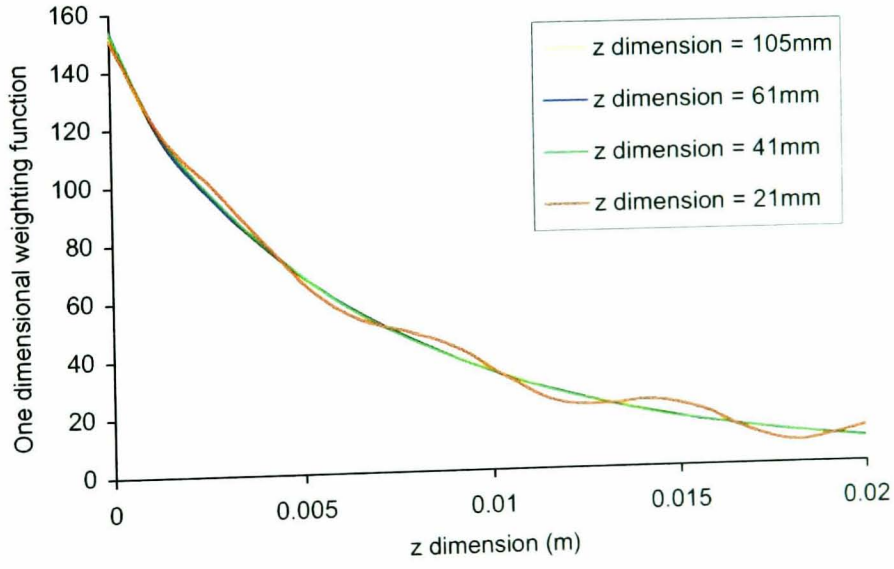

Figure 6.27: *Effect of reduction of the z dimension of the simulation space on the computed one dimensional weighting function.*

6.2.5 Implications for temperature retrieval

For retrieval of temperature profiles, it is essential that the weighting function be known as accurately as possible. It is clear that changes in the dielectric properties of the phantom materials as a result of water binding and temperature variation can have a significant effect on the computed weighting function. As a result these variations must be taken into account when determining the weighting functions. Through suitable layering the variation in dielectric properties as a result of a temperature gradient can be considered.

For the case of single layered materials the use of an effective attenuation coefficient can not only reduce the further computations required (equations 6.27 and 6.28) but allow evaluation of parameters not possible with direct use of the numerical weighting function. In particular for the example of an exponentially decaying temperature profile, (Equation 6.31), using an effective attenuation allows determination of the central and surface temperatures from measurements made at only two frequencies.

To ensure that this approximation of using an effective attenuation coefficient is valid the integral computations are performed numerically from the one dimensional weighting function (labelled wf) and directly from the effective attenuation coefficient (labelled α_e). Tables 6.7 and 6.8 display these computations for the integrals relevant to linear and quadratic temperature profiles for the 1.35GHz and 3.2GHz free water phantoms only. It is clear that in all cases the values computed from the plane wave fit are in close agreement with those of the computed weighting function.

In the more realistic situations of multi-layered materials the use of one effective attenuation coefficient is not suitable. In this case, however, it may be possible to split the integral, computing α_e for each layer and performing the integration independently over each layer. The overall integral being simply the linear sum of the computed integral from each layer. This is made possible as a result of the direct dependence of the relative contribution to the temperature signal on the conductivity.

The retrieval of temperature profiles is discussed in greater detail in the following chapter with further discussion of the effects of computation on the weighting function on the reconstructed temperature distribution.

% Protein	1.35GHz wf	1.35GHz α_e	3.2GHz wf	3.2GHz α_e
0	1.074e-02	1.103e-02	5.078e-03	5.224e-03
10	1.168e-02	1.196e-02	5.579e-03	5.66E-03
20	1.277e-02	1.304e-02	6.083e-03	6.16E-03
25	1.329e-02	1.355e-02	6.378e-03	6.45E-03
30	1.393e-02	1.418e-02	6.681e-03	6.75E-03
40	1.540e-02	1.561e-02	7.368e-03	7.42E-03
50	1.713e-02	1.722e-02	8.164e-03	8.18E-03
60	1.913e-02	1.914e-02	9.203e-03	9.16E-03
70	2.189e-02	2.150e-02	1.041e-02	1.02E-02
75	2.398e-02	2.317e-02	1.122e-02	1.09E-02
80	2.614e-02	2.471e-02	1.226e-02	1.15E-02

Table 6.7: *Computation of $W_{1/2}$ using the computed weighting function (wf) and the effective attenuation coefficient (α_e) at 1.35GHz and 3.2GHz.*

% Protein	1.35GHz wf	1.35GHz α_e	3.2GHz wf	3.2GHz α_e
0	2.394e-04	2.432e-04	5.360e-05	5.457e-05
10	2.829e-04	2.860e-04	6.384e-05	6.415e-05
20	3.379e-04	3.402e-04	7.586e-05	7.594e-05
25	3.659e-04	3.672e-04	8.328e-05	8.316e-05
30	4.020e-04	4.023e-04	9.139e-05	9.109e-05
40	4.916e-04	4.873e-04	1.112e-04	1.101e-04
50	6.102e-04	5.934e-04	1.368e-04	1.339e-04
60	7.672e-04	7.329e-04	1.746e-04	1.678e-04
70	1.017e-03	9.249e-04	2.258e-04	2.088e-04
75	1.231e-03	1.073e-03	2.645e-04	2.357e-04
80	1.479e-03	1.221e-03	3.202e-04	2.666e-04

Table 6.8: *Computation of $W_{1q/2q}$ using the computed weighting function (wf) and the effective attenuation coefficient (α_e) at 1.35GHz and 3.2GHz.*

Chapter 7

Temperature profile reconstruction by multifrequency radiometry

Measurement of the microwave temperature at more than one frequency generates information on the depth variation of the physical temperature distribution. With accurate knowledge of the weighting function estimates of both the relatively small but physiologically important temperature gradients within the human body, and the large, rapidly varying temperature patterns induced during industrial processes can be determined.

7.1 The inverse problem and its solutions

The inverse problem, simply stated is the inversion of equation 7.1 to determine the physical temperature profile (T(**r**)) given known microwave temperatures (T_{mw}(n)) and computed weighting functions w(**r**,n):

$$T_{mw}(n) = \int_{vol} w(\mathbf{r}, n) T(\mathbf{r}) d\mathbf{r} \qquad n = 1, ..., 5 \tag{7.1}$$

where the index n indicates the frequency dependence of the equation. Most researchers currently working on this problem use five frequency bands [25, 26, 46]. In this work attempts to achieve a reasonable solution for the case of only two frequencies are presented.

Although the measurement of the microwave temperature at as many frequencies as possible would appear to provide the best data set for temperature retrieval [59] it may be possible to obtain reasonably accurate temperature profiles for less than five frequencies [26].

The inversion of this equation (7.1), a first order Fredholm equation, is difficult due to several factors. Primarily the problem is "ill-posed" so that small variations in the measured temperatures can lead to large differences in the retrieved temperature profiles. Additionally as two profiles can result in the same radiometric temperatures [24] a unique solution may not exist for each considered configuration. The limited number of "independent" measurements possible also adds to the problems.

Several research groups are working on this problem and the solution methods fall into two main categories, parametric and non parametric methods. The use of *a-priori* estimation of the physical temperature profile [25, 26, 46, 59, 164] reduces the problem to determination of several key parameters of a known profile. Non parametric approaches involve the expansion of the unknown temperature profile in terms of known functions representing the temperature profile. This method proposed primarily by Bardati *et al.* [50, 55, 56, 57] has recently been investigated further by Jacobsen and Stauffer [165]. The applicability of both methods, parametric and non-parametric, with data at two frequencies will be considered further in the following sections.

7.1.1 Problem definition

The discretised form of integral equation 7.1 in terms of frequency (f_n, n=1..N), position in the interior of the body (p'_i, i=1..I), and position on the boundary of the microwave emitting body (p_m, m=1..M) is given as:

$$T^c_{nm} = \sum_i^I w^i_{nm} T_i \qquad \text{with} \qquad \sum_i^I w^i_{nm} = 1. \tag{7.2}$$

Considering the sum of the squares of the differences of the experimentally measured microwave temperatures, T^e_{nm}, and those computed, T^c_{nm}, gives:

$$s = \sum_{nm} (T^c_{nm} - T^e_{nm})^2 \tag{7.3}$$

Upon minimising, by varying the T_j, and setting the equation to zero gives:

$$\sum_i M_{ji} T_i = b_j \qquad \text{or} \qquad M\mathbf{T} = \mathbf{b}. \tag{7.4}$$

for all j. Where $M_{ij} = \sum_{nm} w^j_{nm} w^i_{nm}$ and $b_j = \sum_{nm} w^j_{nm} T^e_{nm}$.

7.1.2 Non parametric solutions

The most obvious method of solution of this equation is to invert matrix M using a standard numerical method, e.g. Singular Value Decomposition. The large condition number of matrix M, however, results in a small number of clustered singular values [165] making this method extremely sensitive to very small changes in the radiometric data (including the effects of rounding errors). One approach to improve the problem and reduce its susceptibility to noise is to employ a regularisation method which transforms the problem to a related well-posed problem [165].

This method, pioneered by Bardati [56, 57] is based on the expansion of the unknown temperature profile in terms of singular functions whose coefficients are obtained from the radiometric data. Some success has been obtained in the reconstruction of temperature distributions in the neck [50] and arm [58] although no direct comparison with measurement has been made.

Further to this Bardati *et al.* [55] consider the case of a cylindrical structure embedded in a high water content phantom with a thermal differential of several degrees. Making use of a four channel radiometer and a number of measurements at different positions at each frequency they were able to reconstruct the position and 2-D thermal map of the embedded cylinder. *A-priori* information in the form of a Sobolev space of thermal functions corresponding to the general shape of the objects was implemented.

Jacobsen and Stauffer [165] employ a related method using Tikhonov regularisation along with Galerkin expansion of the one dimensional temperature profiles for reconstruction of a one dimensional profile. Using a three band radiometer they are able to reconstruct temperature profiles for small temperature gradients. As the gradient increases more frequencies are required. This method relies heavily on specific *a-priori* information

about the thermal distribution (including the position of the maximum temperature and "known" values of the start and end points of the temperature profile) and as such is limited in its applications.

With data at only two frequencies it is unlikely that temperature profiles with gradients of several tens of degrees can be reconstructed well with this method and so it is not considered further.

7.1.3 Optimisation methods

Schaller [166] proposed the solution of equation 7.4 by means of a "pattern-search program". Given an initial estimate of the temperature profile ($T_{1..k}$ where k is a parameterisation of the depth from the antenna aperture) the sum of the squares of the differences (equation 7.3) is minimised by varying each T_k. This optimisation method was applied to a layered phantom of layers related directly to the penetration depth of the measurement frequencies. A further restriction was the necessity to measure at as many frequencies as depth positions. Reasonable reconstruction of a one dimensional local maximum profile over 7 layers was achieved with 10 measurements.

By making use of *a-priori* constraints on the thermal profile to be determined it may be possible to employ a similar method for the cases considered here. An initial estimate of the temperature profile (T_i^0) is made, the "jth equation" is then used to solve for an improved value of T_j^1 as:

$$M_{jj}T_j^1 = b_j - \sum_{i \neq j} M_{ji}T_i^0 = M_{jj}T_j^0 + b_j - \sum_i M_{ji}T_i^0 \tag{7.5}$$

i.e.

$$T_j^1 = T_j^0 + \frac{1}{M_{jj}}\left(b_j - \sum_i M_{ji}T_i^0\right). \tag{7.6}$$

Constrained relaxation of this equation is then possible by iterative improvement with specific *a-priori* constraints (e.g. $T_j > 0$).

7.1.4 Parametric methods

Finally it is possible to determine a solution for the physical temperature profile in a given material by assuming a known form of temperature distribution. This *a-priori* information is then parameterised in some way as to allow estimation of the best fit to the measured data. The main drawback with this approach occurs in the case where the *a-priori* distribution is a bad match for the actual temperature profile, causing possibly large inaccuracies in the result. The high degree of accuracy of the numerical thermal models available limit problems of this nature.

Mizushina *et al.* [59] consider the reconstruction of a one dimensional temperature profile in the human abdomen for hyperthermia treatment thermal monitoring. An assumed temperature distribution of the difference of two exponentials is used, characterised by six parameters, two of which are experimentally determined. This profile is substituted into equation 7.1, along with numerically determined weighting functions, to reduce the problem to a set of linear equations. By minimising an error function, the sum of the square of the differences between the experimental and computed microwave temperatures, the best possible values for each parameter are determined under realistic constraints. In this way confidence levels of 1K - 3K over 0 to 5cm across a 4 layer phantom were obtained for the reconstructed temperature profile at 4, 5 and 6 frequencies.

In a similar vein Maruyma *et al.* [25] apply this method to determine the parameters of a "known" temperature distribution in an infant head. Again a one-dimensional problem is considered where the weighting functions are computed over isothermal layers in the baby brain. The difference of two exponentials is the form assumed for the temperature variation with distance, characterised by three parameters. Further approximations (assuming the position of the peak in the profile, determining the curvature of the temperature profile near the surface) reduce the problem to the determination of two (or one) parameters respectively. Least squares minimisation of the difference between measured and computed temperatures is again used to solve for these parameters. Errors of ≤ 1.5K in central brain temperature make this a feasible option for reconstruction of the brain temperature in infants.

A method very similar to this has been employed by Hand *et al.* [26] again to determine the deep brain temperature in infants. In their approach the temperature distributions within the infant head are numerically determined based on several key parameters (including cerebral blood flow and thermal conductivity). Substitution of one or more computed thermal distributions (based on different values used for these parameters) into equation 7.1 with associated scaling polynomials yields a system of linear equations. The parameters of the scaling functions are then determined by solving this system of equations using singular value decomposition. This method can also be employed to fit a specific temperature profile with varying weighting functions (computed for different dielectric properties) to the measured brightness temperatures. This *a-priori* optimisation method uses the weighting function computed in all three dimensions and gives encouraging results for this application.

Hand *et al.* [26] further investigate the dependence on the resulting profile of errors in several parameters of their model. Of particular interest is the effect of decreases of 10% and 20% of the brain conductivity values. The error in their reconstructed results in both cases is small. The effect of changes to both dielectric constant and permittivity again show a very small effect on the resulting profile. Larger effects are seen for changes in the bolus and skull thickness, factors specific to their problem.

7.2 Reconstruction results

In the experiment considered here linear and quadratic temperature profiles in a mashed potato phantom have been investigated. Clearly with a quadratic temperature profile and measurement at only two frequencies the problem is underdetermined. By assuming the surface temperature to be known this problem can be reduced to the case of two parameter estimation and solutions found. A direct solution in the case of a linear temperature profile is possible with the estimation of either one (gradient only) or two parameters (gradient and intercept).

7.2.1 Parametric estimation of linear profiles

In the first instance the gradient and intercept of the temperature profile produced in the mashed potato are determined directly from the measured microwave temperatures and the computed weighting functions. These results, displayed in Table 7.1 show a reasonable level of agreement between the computed and measured values of the temperature gradient and intercept (surface temperature). As discussed in chapter 5 the uncertainties present in the experimental determination of the physical temperature profile make it difficult to draw strong conclusions on the reconstruction method.

Profile	m_{calc}	m_{meas1}	m_{meas2}	c_{calc}	c_{meas1}	c_{meas2}
1	-671	-743 ± 80	-615 ± 67	26.9	26.6 ± 0.6	24.2 ± 0.6
2	-554	-583 ± 56	-558 ± 54	25.6	25.2 ± 0.6	23.4 ± 0.6
3	-394	-537 ± 52	-478 ± 47	22.5	22.7 ± 0.6	22.1 ± 0.6
4	-354	-474 ± 47	-430 ± 43	21.8	21.8 ± 0.6	21.2 ± 0.5
5	-361	-423 ± 42	-383 ± 39	21.6	20.7 ± 0.5	20.3 ± 0.5
6	-452	-418 ± 51	-392 ± 48	19.8	19.8 ± 0.5	19.5 ± 0.5
7	-363	-336 ± 43	-298 ± 39	18.6	18.8 ± 0.5	18.2 ± 0.5
8	-249	-301 ± 39	-272 ± 37	17.2	18.1 ± 0.5	17.6 ± 0.5
9	-687	-666 ± 68	-574 ± 60	24.7	28.9 ± 0.5	23.6 ± 0.5
10	-572	-572 ± 60	-442 ± 47	22.7	23.4 ± 0.5	22.4 ± 0.5
11	-450	-443 ± 47	-389 ± 42	20.8	22.3 ± 0.5	21.5 ± 0.4
12	-424	-391 ± 42	-350 ± 38	20.3	21.3 ± 0.4	20.7 ± 0.4
13	-242	-364 ± 44	-304 ± 38	20.5	20.5 ± 0.4	19.6 ± 0.4
14	-210	-288 ± 32	-274 ± 31	16.4	17.0 ± 0.5	16.6 ± 0.5
15	-324	-425 ± 52	-392 ± 48	20.8	21.5 ± 0.4	20.3 ± 0.4

Table 7.1: *Reconstructed and measured linear temperature gradients in a mashed potato phantom material. Measurements were made before (meas1) and after (meas2) the microwave reading. One outlier point highlighted.*

For the applications of interest, it is the temperature at several centimetres below the surface that is required and as such the parameter of most relevance is that of the the

gradient. When both gradient and surface temperature are unknown the gradient can be computed as:

$$m = \frac{T_1 - T_2}{W_1 - W_2} \tag{7.7}$$

where T_1 and T_2 are the measured microwave temperatures at the frequencies of 1.35GHz and 3.2GHz and W_1 and W_2 are the integrals of weighting function times z (equation 6.26). Standard error analysis on this equation gives an expression for the error in the gradient, given errors in each of the microwave temperatures and the integrals as:

$$Error \quad m = \sqrt{\frac{dT_1^2}{(W_1 - W_2)^2} + \frac{dT_2^2}{(W_1 - W_2)^2} + \frac{dW_1^2(T_1 - T_2)^2}{(W_1 - W_2)^4} + \frac{dW_2^2(T_1 - T_2)^2}{(W_1 - W_2)^4}}. \tag{7.8}$$

Given the magnitude of each of the components ($dT_1 = 0.5$, $dT_2 = 0.4$, $W_1 \approx$ 1.3e-2 and $W_2 \approx$ 5e-3) even with no error in the computed weighting function integrals the error in the gradient is large (approximately 80 °C/m at 40mm for a gradient close to 700°C/m). For a surface temperature of 27°C this constitutes to an error of close to 3.5°C at a depth of 40mm for a gradient of this nature.

If the surface temperature of the material is assumed known then the gradient can be determined by least squares fitting of the now three data points producing a more accurate measure of the gradient (provided the surface temperature information is accurate). The linear profile parameters obtained by reconstruction in this way (least squares straight line fit to the data) are displayed in Table 7.2. In this case due to the experimental uncertainties the resultant computed gradients are not obviously a better match to the measured data (as expected the surface temperatures are in close agreement). In general, however, an accurately measured surface temperature along with the microwave temperatures would provide the best estimate of the actual profile.

m_{meas1}	m_{comp1}	m_{meas2}	m_{comp2}	c_{meas1}	c_{comp1}	c_{meas2}	c_{comp2}
-743 ± 80	-642	-615 ± 67	-468	26.6 ± 0.6	26.7	24.2 ± 0.6	24.9
-583 ± 56	-531	-558 ± 54	-409	25.2 ± 0.6	25.3	23.4 ± 0.6	24.0
-537 ± 52	-401	-478 ± 47	-362	22.7 ± 0.6	22.7	22.1 ± 0.6	22.2
-474 ± 47	-351	-430 ± 43	-311	21.8 ± 0.6	21.8	21.2 ± 0.5	21.4
-423 ± 42	-301	-383 ± 39	-275	20.7 ± 0.5	20.9	20.3 ± 0.5	20.6
-418 ± 51	-453	-392 ± 48	-434	19.8 ± 0.5	19.8	19.5 ± 0.5	19.6
-336 ± 43	-380	-298 ± 39	-338	18.8 ± 0.5	18.8	18.2 ± 0.5	18.3
-301 ± 39	-316	-272 ± 37	-283	18.1 ± 0.5	17.9	17.6 ± 0.5	17.5
-666 ± 68	-995	-574 ± 60	-608	28.9 ± 0.5	27.9	23.6 ± 0.5	23.9
-572 ± 60	-618	-442 ± 47	-551	23.4 ± 0.5	23.2	22.4 ± 0.5	22.5
-443 ± 47	-558	-389 ± 42	-501	22.3 ± 0.5	22.0	21.5 ± 0.4	21.4
-391 ± 42	-500	-350 ± 38	-456	21.3 ± 0.4	21.1	20.7 ± 0.4	20.6
-364 ± 44	-246	-304 ± 38	-178	20.5 ± 0.4	20.5	19.6 ± 0.4	19.8
-288 ± 32	-255	-274 ± 31	-227	17.0 ± 0.5	16.9	16.6 ± 0.5	16.5
-425 ± 52	-373	-392 ± 48	-289	21.5 ± 0.4	21.3	20.3 ± 0.4	20.4

Table 7.2: *Reconstructed and measured linear temperature gradients in a mashed potato phantom material using the surface temperature (measured before (comp1) and after (comp2) the microwave reading) in the reconstruction. Measurements were made before (meas1) and after (meas2) the microwave reading. One outlier point highlighted.*

7.2.2 Iterative solution for linear temperature profiles

Alternatively one can solve iteritivly equation 7.6 under specific constraints. For the case of a linear temperature profile an obvious constraint of the data would be to ensure that the resulting profile be either increasing or decreasing to suit the situation. Less stringent constraints, e.g. that the resulting profiles fit physical limitations, are also investigated.

Due to the number of uncertainties in the experimental data set, simulated microwave temperatures for a range of profiles were considered. This has the added advantage that a greater range of temperatures could be considered over varying depths of material. The

major disadvantage of using simulated temperatures is that the weighting functions used to compute said simulated temperatures and those used in the reconstruction process are identical. Thus any errors in the computed weighting function as opposed to the real pattern are not taken into account. To consider any effects of this nature and to include the effects of errors in the measured microwave temperatures variations of the simulated temperatures are also tested.

Simulated microwave temperatures, T_n^{mw} were calculated as:

$$T_n^{mw} = \sum_{i=0}^{Imax} W_{i,n} T_i \tag{7.9}$$

where $W_{i,n}$ are the weighting functions at each measurement frequency, n, and T_i is the physical temperature profile in one dimension (from z = i to Imax). Each computed microwave temperature is rounded to one decimal point (i.e. 0.1°C) to introduce a small amount of "noise" (as proposed by Schaller [166]). Variations in each simulated microwave temperature of ±0.2°C are introduced to further investigate the effects of errors in these values.

In particular the weighting functions of two phantom materials are considered, those of 25% protein / saline and those of the mashed potato covering a temperature gradient of 0 to 20°C over 4cm as computed in section 6.1. In each case a plane wave fit to the computed data provided effective attenuation coefficients at each frequency. The attenuation coefficients were α_1=32.31 m^{-1}, α_2=68.65 m^{-1} for the protein / saline phantom and α_1=27 m^{-1}, α_2=92.5 m^{-1} for the mashed potato phantom.

Four linear temperature gradients both increasing and decreasing were considered, m= 500°C/m, 1000°C/m, 1500°C/m and 2000°C/m, with varying surface temperatures of 20°C, 40°C and 100°C. Profiles were reconstructed over varying depths, 2cm, 3cm, and 5cm, within the phantom material with a 1mm resolution.

In the first instance profiles were reconstructed in the absence of any constraint. Latterly the introduction of the constraint that the resulting profile be increasing (or decreasing) was considered. A second constraint which assumed the surface temperature to be known was also employed. The iterative procedure ended when each successive reconstructed profile differed by less than 0.0001°C at each position over ten successive repetitions.

Realistically it is unlikely that from two data points a complete description of the physical temperature with a resolution of 1mm can be determined. Making use of the *a-priori* information of a linear temperature profile, a linear fit can be made to the reconstructed profile and the best fit gradient and intercept values used for comparison. In particular fits are computed by least squares using the *fitexy* function, Press *et al* [147], with errors of 0.1mm and 1°C assumed in each reconstructed point. An initial estimate of the temperature profile of a constant temperature equal to the expected surface temperature plus 20°C was employed in all cases.

7.2.2.1 Results

Initially the effect of reconstructing the temperature over varying depths and gradients for an initial temperature of 40°C with idealised simulated microwave temperatures (those temperatures rounded to 0.1°C). The computed profile parameters, with and without constraints, are listed in Table 7.3. Clearly as the depth over which both the temperature is simulated and the reconstruction is performed increases, the accuracy of the retrieved profile deteriorates. In general as the gradient increases the error in re-computed gradient increases, however as a proportion this error is fairly constant. The introduction of a constraint to ensure that the reconstructed function is decreasing improves the result only for small depths.

The reconstructed profile produced for a phantom of depth 2cm are close to a perfect match for the initial profile. This is as expected, given only a rounding error is in effect in the simulated temperatures, and serves to validate the method. The differences between initial and reconstructed profiles seen for phantoms of greater depth can be explained by considering the attenuation of the weighting function. As the depth increases the weighting function attenuates to a point where from that position on there is no contribution to the simulated temperature. Hence the form of the reconstructed profile past this point has no effect on the temperature and so can take any value. Figure 7.1 displays the reconstructed profiles for gradients of -1000°C/m (Profile 1) and -500 °C/m (Profile 2) for depths of 20mm and 50mm.

Imax (cm)	Initial m	Profile c	No m	constraint c	Decreasing m	constraint c
2	-500	40	-589	40.7	-496	39.9
2	-1000	40	-1110	40.8	-1019	40
2	-1500	40	-1589	40.7	-1494	39.9
2	-2000	40	-2118	40.9	-2014	40
3	-500	40	-547	40.5	-443	39.4
3	-1000	40	-1050	40.5	-941	39.3
3	-1500	40	-1554	40.6	-1433	39.2
3	-2000	40	-2058	40.7	-1925	39.2
5	-500	40	-395	38.3	-340	37.4
5	-1000	40	-825	37.2	-751	36
5	-1500	40	-1255	36.4	-1165	34.9
5	-2000	40	-1699	35	-1596	34

Table 7.3: *Reconstructed linear temperature gradients in a protein / saline phantom material for a range of decreasing gradients and depths. Surface temperature set at 40° C.*

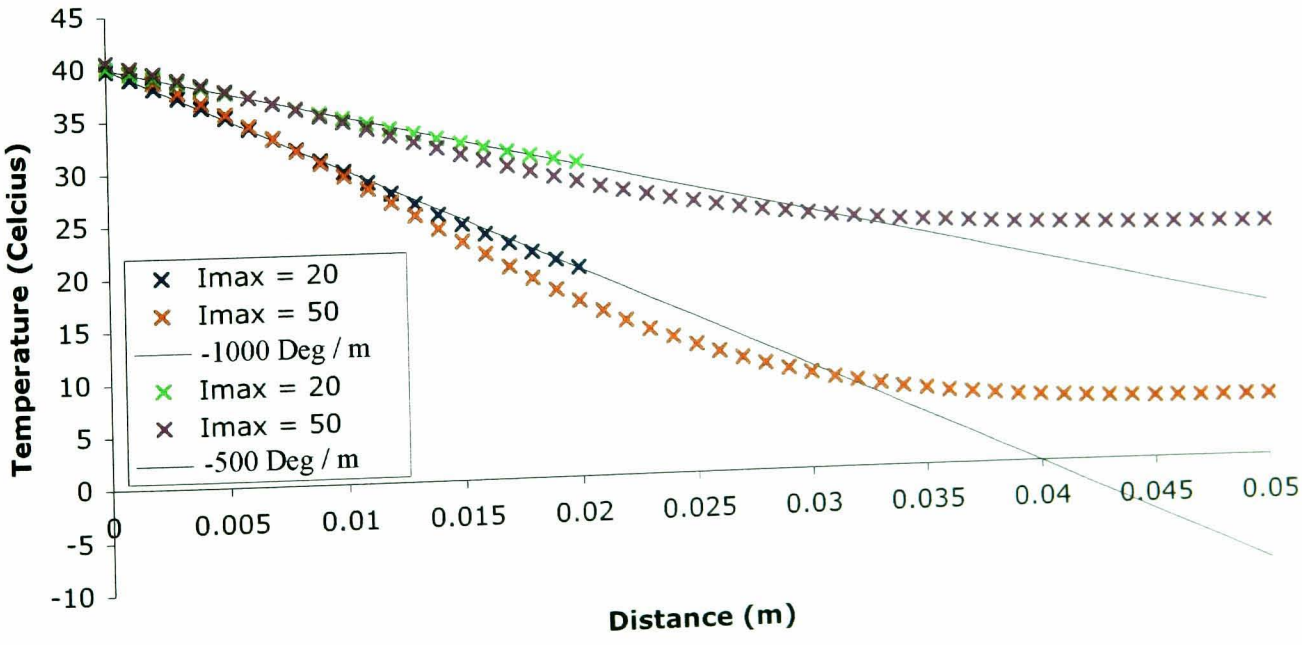

Figure 7.1: *Reconstructed linear temperature profiles for a gradients of -500° C/m and -1000° C/m at different depths.*

It is clear that reconstructing a profile over a depth greater than that which corresponds to the depth at which the lowest frequency weighting function falls to below a limiting value is pointless. In general a depth corresponding to the decrease in amplitude value of this lowest frequency weighting function to one tenth of the maximum value serves as a good guide.

By considering temperature profiles with the same range of gradients and a different initial temperature of 100°C it is clear that the accuracy of the reconstructed profile is dependent entirely on the gradient and phantom depth, compare tables 7.3 and 7.4. Table 7.5 displays the results of the same profile types with increasing gradients. The reconstructed profiles in this case again show good agreement with the initial profiles, even with no constraint in place.

	Initial Profile		Decreasing constraint	
Imax (cm)	m	c	m	c
2	-500	100	-589	100.7
2	-1000	100	-1110	100.8
2	-1500	100	-1589	100.7
2	-2000	100	-2118	100.9
5	-500	100	-395	98.3
5	-1000	100	-825	97.2
5	-1500	100	-1255	96.4
5	-2000	100	-1699	95.7

Table 7.4: *Reconstructed linear temperature gradients in a protein / saline phantom material for a range of decreasing gradients and depths. Surface temperature set at 100°C.*

To test the effect of small changes in the measured microwave temperatures the simulated temperatures are varied by ±0.2°C. The reconstructed profiles with each of the error combinations for a phantom of 2cm deep and a gradient of 1000°C are shown in Figure 7.2. The reconstructed profile parameters for a range of gradients and depths are given in Table 7.6.

Imax (cm)	Initial m	Profile c	No m	constraint c
2	500	40	466	40.2
2	1000	40	1006	40
2	1500	40	1490	40
2	2000	40	2019	39.8
3	500	40	419	40.8
3	1000	40	935	40.7
3	1500	40	1441	40.6
3	2000	40	1947	40.5
5	500	40	332	42.7
5	1000	40	751	43.9
5	1500	40	1176	44.9
5	2000	40	1620	45.5

Table 7.5: *Reconstructed linear temperature gradients in a protein / saline phantom material for a range of increasing gradients and depths. Surface temperature set at 40° C.*

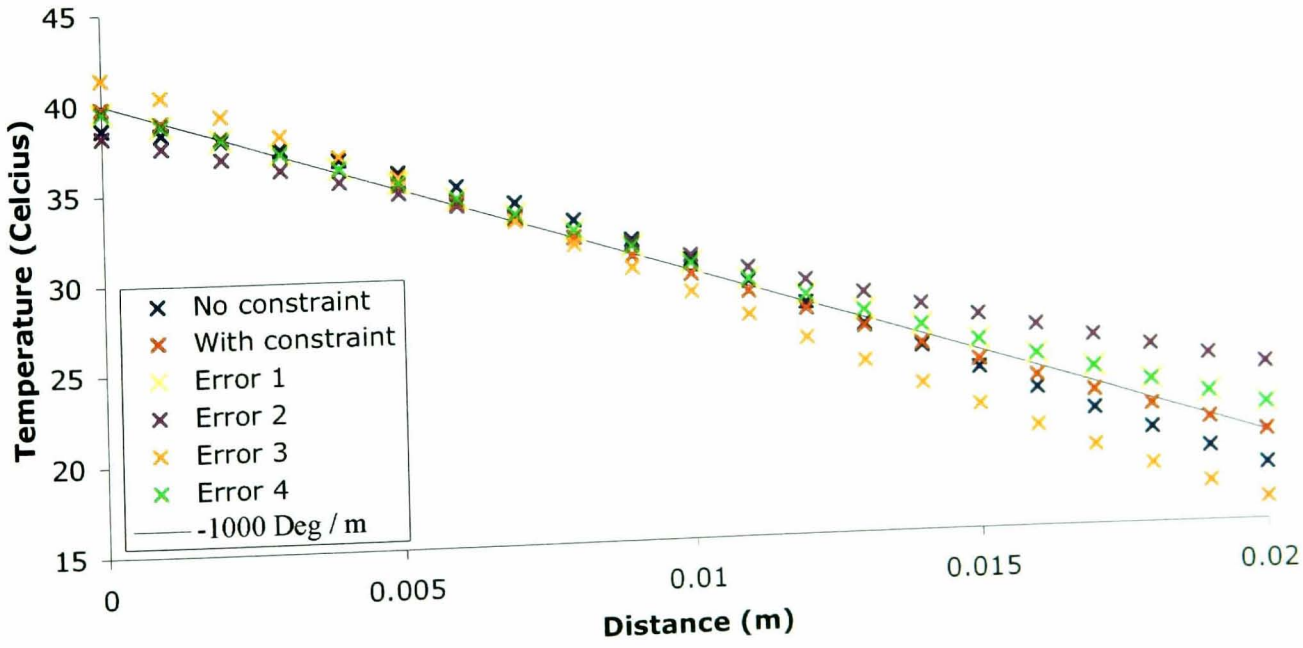

Figure 7.2: *Reconstructed linear temperature profiles for a gradient of 1000° C/m with varying levels of error in the simulated microwave temperatures.*

Initial m	Profile c	Error T_1^{mw}	Error T_2^{mw}	Increasing m	constraint c
-500	40	0.2	0.2	-400	39.6
-1000	40	0.2	0.2	-924	39.7
-1500	40	0.2	0.2	-1399	39.6
-2000	40	0.2	0.2	-1920	39.7
-500	40	0.2	-0.2	-207	38.3
-1000	40	0.2	-0.2	-733	38.1
-1500	40	0.2	-0.2	-1207	38.1
-2000	40	0.2	-0.2	-1730	38.2
-500	40	-0.2	0.2	-783	41.7
-1000	40	-0.2	0.2	-1304	41.8
-1500	40	-0.2	0.2	-1779	41.7
-2000	40	-0.2	0.2	-2299	41.8
-500	40	-0.2	-0.2	-400	39.6
-1000	40	-0.2	-0.2	-924	39.7
-1500	40	-0.2	-0.2	-1399	39.6
-2000	40	-0.2	-0.2	-1920	39.7

Table 7.6: *Reconstructed linear temperature gradients in a protein / saline phantom material for a range of decreasing gradients and depths given errors in the simulated microwave temperature.*

The effect on the reconstructed profile is greatest as expected for the case where the difference from the expected temperatures is largest (i.e. T_1+0.2°C, T_2-0.2°C and vice versa). Clearly even small variations from the exact temperature have a marked effect on the resulting profile, with the effect at the chosen depth corresponding to several degrees.

In a similar manner the effect of errors in the weighting function used for the reconstruction is considered. After generating the simulated microwave temperatures, variations of $\pm 10\%$ are introduced to the attenuation coefficient used to compute the weighting functions for the reconstruction process. As in the case where errors are added to the simulated

temperatures, the largest effects are seen for the maximum change in weighting function. In the case where the weighting function varies by the same amount in each case (i.e.+10%) the reconstructed profiles are as good as with the correct attenuation coefficients. These results are given in Table 7.7 and Figure 7.3 for a gradient of -1000°C/m over a depth of 2cm.

Initial m	Profile c	Error α_1	Error α_2	Increasing m	constraint c
-1000	40	10%	10%	-1067	40.2
-1000	40	10%	-10%	-1264	41.7
-1000	40	-10%	10%	-864	39.1
-1000	40	-10%	-10%	-967	39.9

Table 7.7: *Reconstructed linear temperature gradients in a protein / saline phantom material for a gradient of -1000° C and depth of 2cm given errors in the weighting functions.*

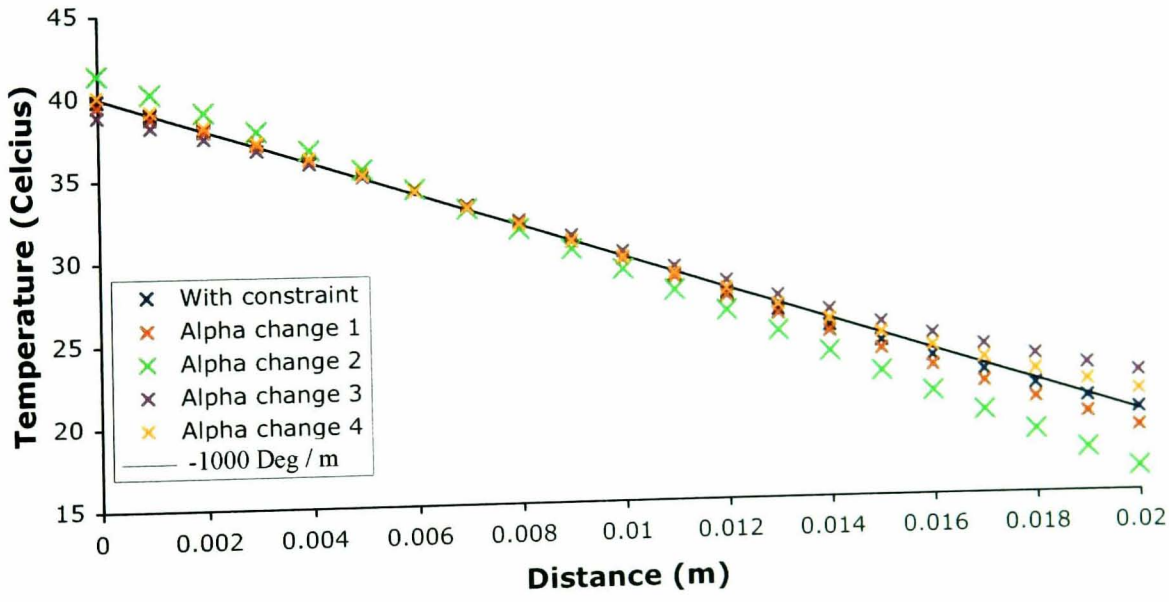

Figure 7.3: *Reconstructed linear temperature profiles for a gradient of -1000° C/m with varying levels of error in the weighting functions used for reconstruction.*

Imposing a further constraint of a known surface temperature to the iterative improvement scheme did not serve to produce better results (Table 7.8) than that of the decreasing constraint alone (compare tables 7.3 and 7.6) for simulated temperatures with and without errors.

Initial Imax (cm)	Profile m	Error T_{mw1} c	Error T_{mw2} m	ST constraint c	gradient	intercept
-1000	40	0	0	none	-1019	40
-1000	40	0	0	T_s	-1027	40.1
-1000	40	0	0	T_s+0.5	-1017	40
-1000	40	0	0	T_s-0.5	-1038	40.2
-1000	40	0.2	0.2	T_s	-927	39.7
-1000	40	0.2	-0.2	T_s	-713	38.1
-1000	40	-0.2	0.2	T_s	-1350	42.2
-1000	40	-0.2	-0.2	T_s	-1128	40.5

Table 7.8: *Reconstructed linear temperature gradients in a protein / saline phantom material for a gradient of -1000° C and depth of 2cm given errors in the simulated microwave temperatures and using a known surface temperature.*

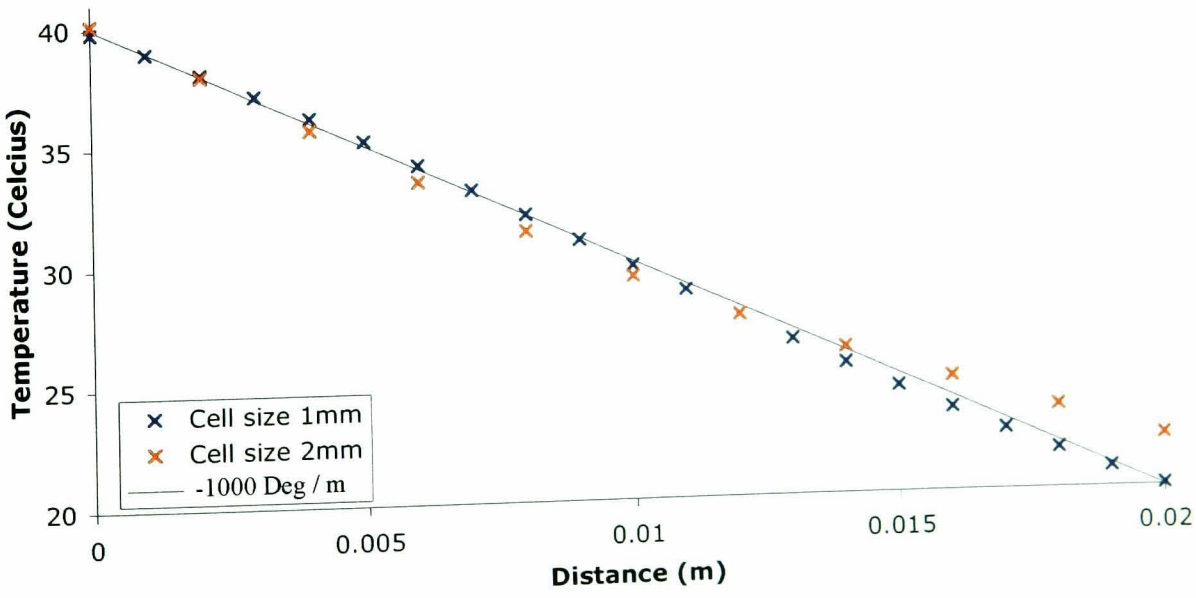

Figure 7.4: *Reconstructed linear temperature profiles for a gradient of -1000° C/m with varying cell spacing.*

To consider the effect of the resolution at which the reconstructed temperature is produced, a spacing of 2mm was compared to the result at 1mm as displayed in Figure 7.4. Results at 2mm are clearly less accurate than at 1mm.

Finally Table 7.9 displays the reconstruction results obtained for the mashed potato phantom material with simulated microwave temperatures. In this case the attenuation of the weighting function at the higher frequency is much greater than the protein/saline phantom example (α_2=92.5 m^{-1} v's α_2=68.65 m^{-1}).

	Initial	Profile	Decreasing	constraint
Imax (cm)	m	c	m	c
1	-500	40	-506	40
1	-1000	40	-1016	40
1	-1500	40	-1440	39.7
1	-2000	40	-2034	40
1.5	-500	40	-447	39.7
1.5	-1000	40	-969	39.8
1.5	-1500	40	-1491	39.9
1.5	-2000	40	-2012	40
2	-500	40	-436	39.5
2	-1000	40	-927	39.4
2	-1500	40	-1392	39.2
2	-2000	40	-1906	39.2
3	-500	40	-343	38.3
3	-1000	40	-772	37.6
3	-1500	40	-1235	37.3
3	-2000	40	-1686	36.9

Table 7.9: *Reconstructed linear temperature gradients in a mashed potato phantom material for a range of gradients and depths.*

The detrimental effect on the reconstructed parameters is clear especially as the phantom

depth increases above 2cm, compare tables 7.9 and 7.3. As the attenuation at the lower frequency is close across the phantom types (α_1=27 m^{-1} v's α_1=32.31 m^{-1}) this detrimental effect can be attributed primarily to the higher frequency measurement and again suggests a limiting reconstruction depth based on the weighting function at 3.2GHz.

7.2.3 Parametric estimation of quadratic temperature profile

In the case of a quadratic temperature profile ($T(z) = az^2 + bz + c$) with measurements at only two frequencies parametric profile reconstruction is underdetermined. If the surface temperature (c) is assumed known then it is possible to directly solve for the remaining quadratic parameters, a and b as:

$$a = \frac{W_{q1}(T_2 - c) - W_{q4}(T_1 - c)}{(W_{q1}W_{q3} - W_{q1}W_{q4})} \tag{7.10}$$

$$b = \frac{W_{q2}(T_2 - c) - W_{q3}(T_1 - c)}{(W_{q2}W_{q4} - W_{q2}W_{q3})} \tag{7.11}$$

where

$$T_1 = aW_{q1} + bW_{q2} + c \qquad \text{and} \qquad T_2 = aW_{q3} + bW_{q4} + c \tag{7.12}$$

The reconstructed parameters of the quadratic profiles measured in chapter 5 are shown in Table 7.10. Exact comparisons here are not possible as an exact surface temperature at the time of microwave measurement is required to reconstruct the quadratic profile. A value for the surface temperature is estimated from those measured before (m1) and after (m2) the microwave reading. Again the time discrepancy between readings at 1.35GHz and 3.2GHz increases the errors. To aid interpretation of these reconstructed parameters the temperature at the centre of the mashed potato phantom is displayed for both the computed and measured profiles. In most cases the central temperature is several degrees less than the measured value. The level of agreement seen, however, suggests that with an improved experimental system encouraging results may be possible.

Considering equations 7.10 and 7.11 with no error in the weighting function an error of 3 to 4 degrees (at 20mm deep) results from measurement uncertainties in the microwave temperatures. As the depth increases this error rapidly increases to close to 10°C at 40mm. Again with measurements at more than two frequencies a better approximation

a_{comp}	b_{comp}	a_{m1}	b_{m1}	a_{m2}	b_{m2}	T_{centre_comp}	T_{centre_m1}	T_{centre_m2}
44916	-1747	33230	-1482	22408	-999	16.6	16.8 ± 1.2	22.1 ± 1.2
33555	-1301	20508	-939	14619	-689	18.6	20.3 ± 1.2	22.9 ± 1.2
16859	-826	29814	-1324	20742	-938	13.7	9.0 ± 1.2	13.1 ± 1.2
27796	-1282	28458	-1256	23306	-1098	12.5	13.4 ± 1.2	14.4 ± 1.2
27445	-1128	18398	-843	14306	-660	12.5	14.4 ± 1.2	16.5 ± 1.2
13212	-559	12117	-545	8161	-368	15.9	15.7 ± 1.2	17.7 ± 1.2
9124	-794	35646	-1527	21879	-993	23.1	19.8 ± 1.2	24.9 ± 1.2
27995	-1113	20426	-915	14348	-659	21.8	22.5 ± 1.2	25.2 ± 1.2

Table 7.10: *Reconstructed and measured quadratic temperature profiles in a mashed potato phantom material. Quadratic profile parameters were determined from measurements made before (m1) and after (m2) the microwave reading.*

of the profile could be estimated. These errors are more significant for smaller temperature variations.

7.2.4 Iterative solution for quadratic profile reconstruction

Reconstruction of quadratic profiles by means of iterative improvement with an appropriate constraint (e.g. function decreases to a point and then increases after a given region) is also possible. A range of quadratic temperature profiles for a protein / saline mixture phantom of depths of 25 and 45mm where the quadratic profile is assumed to have surface temperatures of 35°C and central temperatures ranging from 17 to 30 °C are investigated. Without an initial profile estimate which closely matches the desired profile and the use of strong constraints the reconstructed profile does not match a quadratic function but again follows a linear profile. As a result the iterative solution method is not considered further for quadratic profiles.

7.2.5 Conclusions and limitations - solution by optimisation

Reconstruction of linear profiles by means of an iterative improvement scheme has been investigated for a range of linear temperature gradients and over varying material depths. Making use of simulated microwave temperatures the effects of errors in the computed weighting functions and in the microwave temperatures on the resulting values of gradient and intercept are investigated. Errors of up to 60% in the estimated gradient are observed for small gradients (500°C/m) with the effect reducing to 15% for steeper gradients (2000°C/m).

An important limitation of this solution method is the effect of the depth over which the reconstruction is performed. In the examples considered here the depth over which the simulated temperature is computed is the same as the depth over which the reconstruction is performed. It is clear, however, that the optimum material depth for reconstruction is around 2cm. Thus if the microwave temperature is measured in a material of greater depth (as is likely to be the case) care must be taken in normalisation of the weighting function to ensure that the contribution to the microwave temperature from this greater depth is taken into account when reconstructing the profile. Furthermore for more complex profile shapes (e.g. quadratic) measurements at more frequencies are needed to make this a viable alternative approach.

7.2.6 Conclusions and limitations - direct parameter estimation

Direct computation of the profile parameters generating the measured microwave temperatures for both linear and quadratic profiles in mashed potato has been performed. Given the difficulties with the experimental arrangement the agreement obtained between computed and measured values is encouraging.

The primary limitation in determining the temperature profile by this method is the rigid constraint that the distribution follow a particular shape (linear, quadratic etc). Furthermore uncertainties in the computed weighting functions and measured microwave temperatures can result in errors of several degrees at depths of several cm.

The first problem, that of *a-priori* constrained profile shape does not have a straight forward solution. As the inverse problem is essentially that of using a small number (2 to 5) of data points to fully reconstruct a temperature profile some *a-priori* estimate must always be imposed. Either one constrains the shape of the profile, e.g. Maryuama *et al* [25], and solve for the best fit parameters of this profile or one limits the solution space to a small number of exact thermal distributions and solve for the best combination of these profiles, e.g. Hand *et al* [26].

It seems clear that with measurements at more frequencies the errors in the resulting profile determined by either approach will be reduced. It is important to note, however, that with each additional measurement further uncertainty is introduced in terms of both the computed weighting function and the measured temperature. Considering the case of a linear profile (y=-1000*z+40) measured at 5 frequencies (1.2GHz, 1.65GHz, 2.3GHz, 3.0GHz and 3.6GHz) in cerebrospinal fluid ([25], ϵ_r'=64.8 to 61.8 and σ=1.64 to 3.22 S/m) a plot of measured microwave temperature (T_i) against $\int w_i(z)zdz$ is shown in Figure 7.5. Errors of 5% in the weighting function and 0.5°C in the temperature have been included.

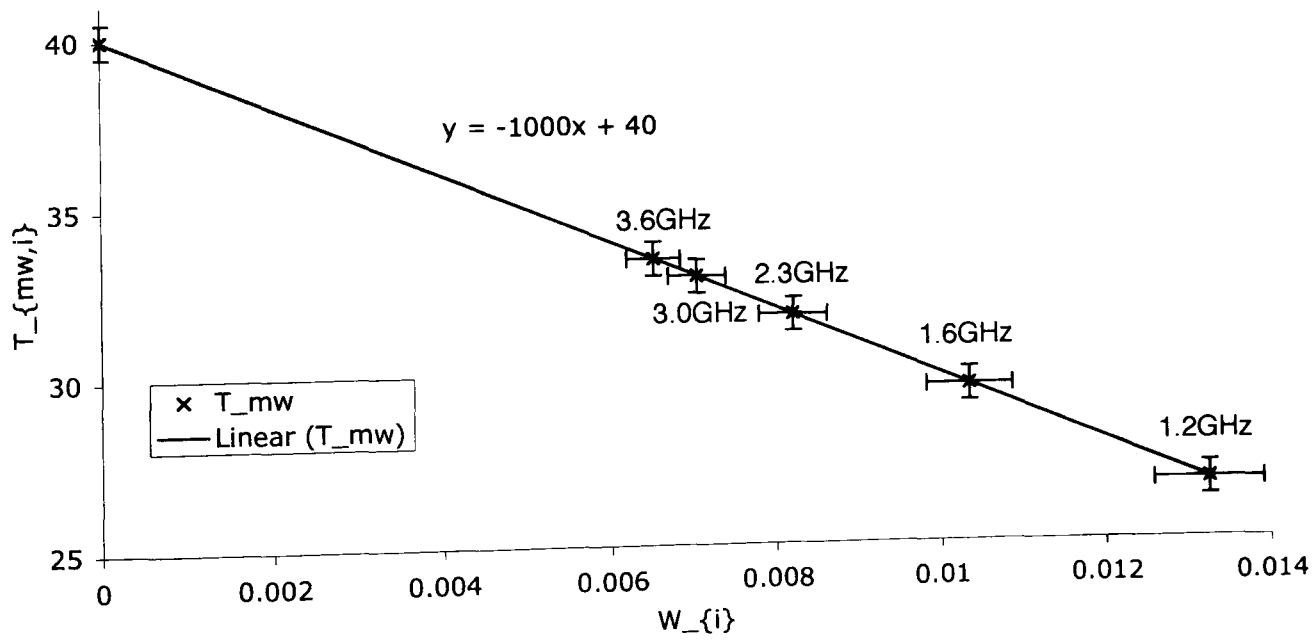

Figure 7.5: *Linear temperature profiles for a gradients of -1000° C/m.*

The importance of a well determined surface temperature is immediately apparent. Further, the data points corresponding to measurements at 3.0GHz and 3.6GHz are so close

that one measure is all but redundant in its effect on the reconstruction result. A good compromise situation would be to have an accurate surface temperature along with measurements at 2 or 3 frequencies (1.35GHz, 3.2GHz and around 2GHz) to minimise the effects of uncertainties in the computed weighting functions.

If an effective attenuation coefficient can be used to fully characterise the weighting function behaviour as a plane wave attenuation then it is possible to fit the measured data to a quadratic form. As described in section 6.2 the microwave temperature can be related to the physical quadratic temperature profile as:

$$T_{mw,i} = \int w(z)T(z)dz = \int 2\alpha e^{-2\alpha z}(az^2 + bz + c)dz \quad (7.13)$$

$$= \frac{a}{2}\frac{1}{\alpha^2} + \frac{b}{2}\frac{1}{\alpha} + c \quad (7.14)$$

where α represents the effective attenuation coefficient. Thus a plot of microwave temperature against the reciprocal of the attenuation coefficient can be used to solve for the parameters of the quadratic profile (assuming enough measurements are available). Figure 7.6 displays such a plot for the 5 frequency situation discussed earlier. Again the need for an accurate surface temperature is obvious along with the conclusion that measurements at 2 or 3 frequencies are required.

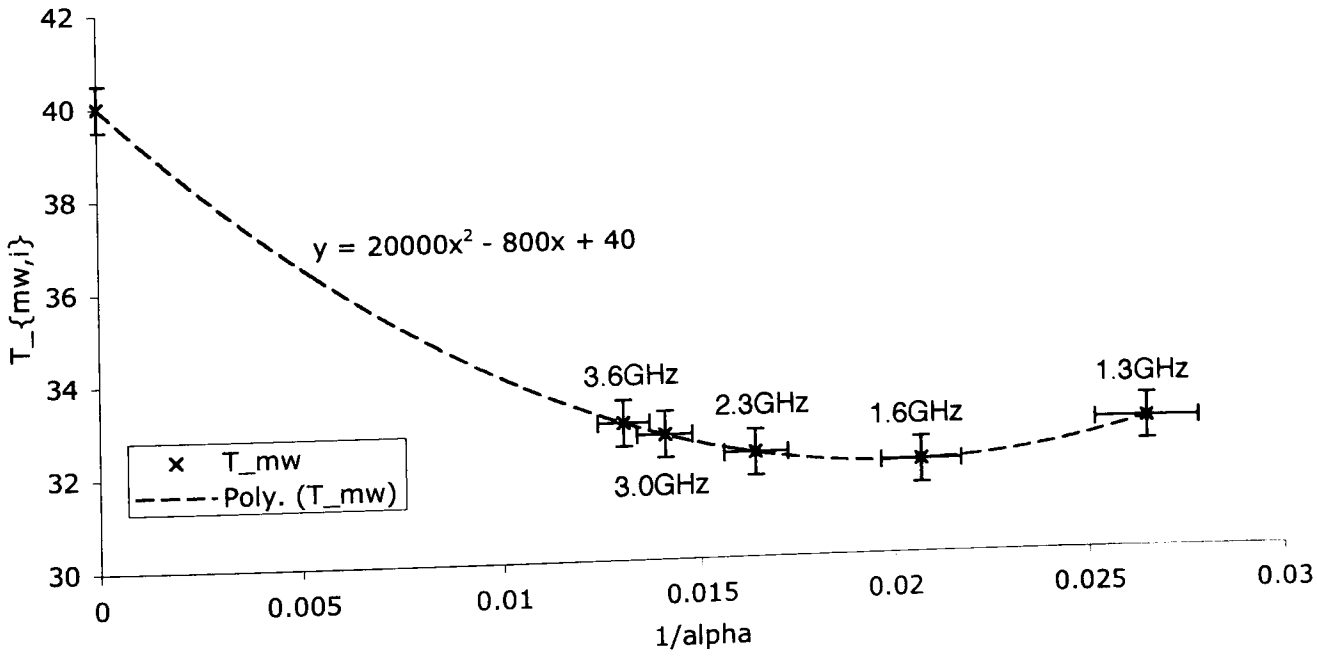

Figure 7.6: *Quadratic temperature profiles for a gradients of -1000° C/m.*

For a phantom material of this nature (where one effective attenuation coefficient is sufficient) a linear profile can also be estimated in the same manner (with a=0, and b = linear gradient the expected result). In this way the strict constraint of a linear function would be lessened.

Chapter 8

Conclusions

The measurement of temperature through the passive detection of microwave radiation from organic materials is a promising method with applications in both medical and industrial fields. Interpretation of the measured microwave signals requires accurate knowledge of the pattern of radiation emission from a particular object. By applying the principle of reciprocity this pattern, the weighting function, can be determined through computation of the near field of the sensing antenna when operated in active mode. A vital component of this computation is a full description of the dielectric behaviour of the emitting body.

In this work the finite difference time domain (FDTD) numerical modelling technique has been investigated for the computational determination of weighting functions for a variety of materials. All FDTD modelling has been performed using the basic electromagnetic simulation tool (BEST) [3] modeller.

8.1 Validation of BEST

Validation of the results of the computational modelling has been achieved primarily by comparing simulation results with experimentally measured values. Experimental results in the form of antenna return loss and impedance measurements, along with directly measured values of the antenna near field, are considered for these comparisons. Additionally

the field forms and numerical values determined for a TE_{01} mode rectangular waveguide were shown to be in excellent agreement with theoretical predictions. Further validation of the BEST modeller for cavity based structures is in preparation [41].

8.1.1 Antenna return loss and impedance comparisons

Simulations of a range of configurations of a monopole radiator above a ground plate were successfully validated by return loss measurements. Furthermore, comparisons of the computed complex impedance of this monopole matched well with published literature. Power reflection comparisons for a monopole probe sourcing a TE_{01} mode waveguide showed reasonable similarity with the measured return loss. Limitations to the modelling in this case were observed, however, by the inability of the model to produce an exact match to the measured values.

8.1.2 Near field comparisons

Direct measurement of the near field of a TE_{11} mode cylindrical antenna has been performed using the non-resonant perturbation technique [133]. Direct comparisons were made for two phantom materials (water and a sucrose solution) with and without the presence of varying thicknesses of dielectric (Tufnol) layers.

The patterns of absorbed power deposition, normalised by maximum amplitude, compare well for all cases considered. The effects of inclusion of the dielectric layers on the measured power distributions are well matched by the simulated patterns. In particular, as shown in Figure 8.1, close to exact agreement is seen for the water phantom with a 3.5 mm dielectric layer at a height of 9mm from the phantom / antenna aperture.

Comparisons of the maximum absolute SAR for non-layered phantom configurations further validate the FDTD modelling. In most cases considered, experiment and simulation values agree well within experimental errors, with an average relative difference of 20%.

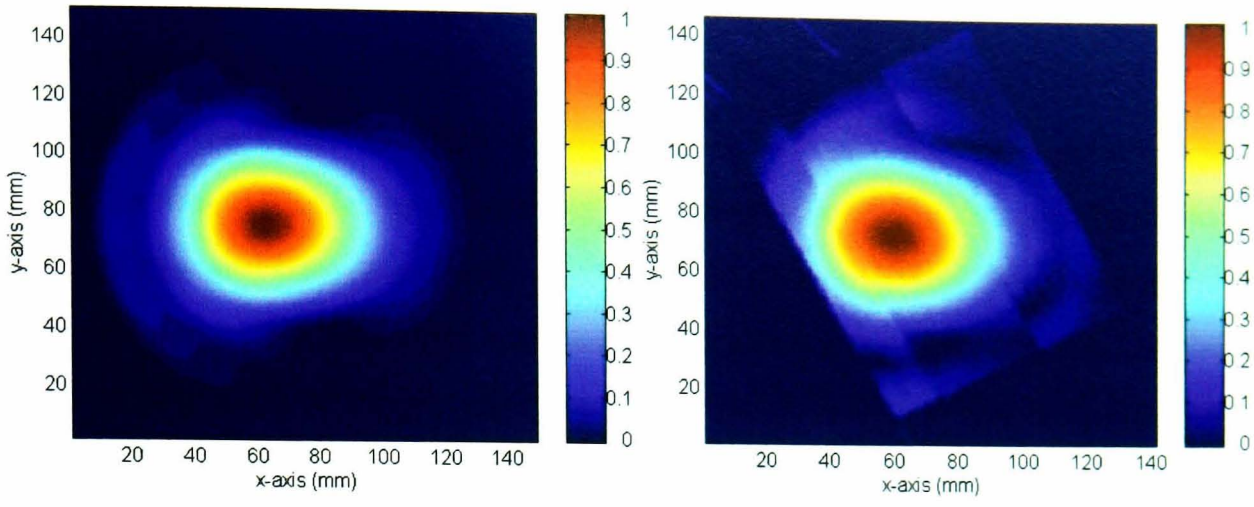

Figure 8.1: *Comparison of normalised simulated and experimental results for a water phantom with the 3.5mm dielectric layer at a height from phantom base of 9mm.*

8.1.3 Microwave temperature comparisons

A final form of validation of the modelling of complex layer phantom materials is performed by comparison of measured microwave temperatures with equivalent simulated temperatures. Linear and quadratic temperature profiles were generated in a phantom material composed of a mashed potato mixture. Measurements of the microwave temperature for a range of profiles were made at 1.35GHz and 3.2GHz. Simulations of the mashed potato phantom were performed at 1.35GHz and 3.2GHz, using a layered structure to simulate the changes in dielectric properties due to the temperature differences. Simulated microwave temperatures were generated using the computed weighting functions and the measured profile parameters.

For linear temperature profiles good agreement was seen for comparisons at 3.2GHz, with a reasonable match at 1.35GHz. Differences between measured and computed temperatures can be accounted for by uncertainties in the experimental procedure and a less accurate knowledge of the dielectric property behaviour at 1.35GHz. For quadratic temperature profiles the agreement is again fair and could be increased by improvements to the experimental procedure.

8.2 Antenna design

Making use of the BEST modeller, a direct contact antenna operating at both 1.35GHz and 3.2GHz was designed by computing the return loss of the antenna for a range of probe positions and sizes in a variety of phantom materials. In this way it was possible to quickly and accurately determine a suitable configuration for each frequency probe that resulted in low levels of power reflection (less than 20% at 1.35GHz and less than 1% at 3.2GHz) for a range of phantom materials. Experimental testing with this antenna confirmed the suitability of the modelled configuration.

8.3 Dielectric property model of mashed potato

In order to use the mashed potato mixture as a test material it was necessary to develop a model of its dielectric behaviour over a range of temperatures at 1.35GHz and 3.2GHz. With this model accurate computation of the weighting function for a range of variations of the potato phantom was possible. The dielectric behaviour of the potato phantom was considered as resulting from three main constituents: water, salt and starch and their interactions.

The dielectric constant, at 1.35GHz and 3.2GHz, has been shown to be well modelled by a Maxwell mixture equation. Any interaction between starch and water has been shown to be negligible for the dielectric constant. Results at 3.2GHz compare favourably to the results of Roebuck [153] and Bengtsson and Risman [162] and to experimental measurements over the temperature range of 0°C to 50°C. At 1.35GHz the results compare reasonably with the limited published data [154] and experiment.

The loss factor at 3.2GHz has been considered in some detail. Literature suggests that the symbiotic effect of adding starch to water serves to keep the loss factor of the mixture constant at the pure water value for starch concentrations of 0 to 25% [161]. In practice, however, a small increase in loss factor as a result of addition of starch was observed. By considering this interaction a model for the potato loss factor at 3.2GHz and 1.35GHz has

been developed. This model uses the loss factor of a pure water solution and incorporates corrections for the presence of salt and for the interaction of starch and water. Comparisons of the results of this model with the results of Roebuck [153] and Land at 3.2GHz and those of Burfoot [154] and Land at 1.35GHz, over a reasonably large temperature range (0 to 50 °C), were favourable.

8.4 Behaviour of the weighting function

The behaviour of the weighting function for a range of phantom materials and configurations was investigated to obtain guidelines as to the effect on the computed weighting function of variations in material dielectric properties and material geometrical structure. Phantom materials of a protein / saline mixture, modelled using Maxwell mixture equations for a range of protein concentrations, were employed to determine the effect of measurement frequency and water binding.

As expected the weighting function behaviour was found to be dominated by the conductivity of the phantom material with the dielectric constant having a much smaller effect. In particular it is worth noting that the inclusion of bound water in the phantom dielectric property model has a marked effect on the computed weighting function. The mashed potato dielectric property model described above was used to demonstrate that changes in the phantom material temperature had a notable effect on the weighting function. Furthermore, it is clear that for the dual-frequency sourcing antenna used for these models, even for the highest water concentrations the assumption that the one dimensional weighting function follows plane wave behaviour will produce significant inaccuracies.

Fitting the one dimensional weighting function to an equivalent plane wave attenuation is applicable primarily in the case where the phantom is single layered only. Assuming a plane wave attenuation of 12% more than the standard penetration depth provides a useful approximation for the weighting functions for the dual frequency antenna developed here (valid for phantom materials where ϵ_r= 35 to 70 and σ= 1 to 1.6 S/m at 1.35GHz and ϵ_r= 35 to 65 and σ = 1.6 to 3.4 S/m at 3.2GHz).

Limitations in the computational modelling of layered structures were demonstrated at 1.35GHz for both continuous and discontinuous variations in dielectric property across layers. The inclusion of intermediate layers with averaged values of dielectric property considerably reduced the instabilities in both cases.

8.5 Temperature reconstruction with two microwave frequency measurements

By measuring the microwave temperature at different frequencies it is possible to reconstruct information on the thermal distribution of the material. Measurements made with the dual frequency antenna of the mashed potato phantom, with quasi-linear and quasi-quadratic temperature profiles, provided estimates of the accuracy with which temperature profile reconstruction could be performed. For both linear and quadratic profiles, the reconstructed temperatures were encouraging, given the experimental problems. In particular, the fact that the measurements at 1.35GHz and 3.2GHz were not made simultaneously as the phantom cooled provided a large source of experimental error.

Using entirely simulated temperatures, the applicability of an optimisation method to reconstruct both linear and quadratic profiles with measurements at two frequencies was investigated. For linear profiles the results were encouraging with minimal constraint on the solution process. Errors in the simulated microwave temperatures and using a modified expression for the weighting function were seen to result in errors of several degrees at the depths of 2cm. For quadratic profiles, however, the level of constraint required is too strong to make the method viable.

Clearly reconstruction of an unknown temperature profile in a phantom material, whether in a medical or industrial application is a challenging problem. It has been demonstrated that with measurements at only two frequencies some success can be achieved by both parametric and iterative solution methods. Furthermore if the surface temperature is accurately known reconstruction of a linear profile is possible.

As any possible solution method is necessarily strongly constrained by *a-priori* estimates of the physical temperature profile, this profile must be very accurately known. Further work in accurately establishing the thermal profiles of the particular products to be measured in industrial applications is required. In particular, uniformity of the thermal distribution in one dimension across the entire source material must be determined.

If the temperature profile is accurately known then the method of Hand *et al.* [26] to compute the best fit weighting function from a small number of alternatives could be employed. In this way errors in the values used for the dielectric properties of the phantom materials could be investigated further.

References

[1] http://radicalacademy.com/philosophicalquotations5.htm, Accessed 15/04/2003.

[2] M. L. Smith, K. Barrie, and D. V. Land. Investigation and validation of FDTD weighting function modelling for microwave radiometric temperature measurment. *Proceedings of IEE Antenna Measurement and SAR*, Loughbourgh University, May 2002.

[3] G. Marrocco and F. Bardati. BEST: a finite-difference simulator for time electromagnetics. *Simulation Practice Theory*, 7(7):279–293, 1999.

[4] D. V. Land. Microwave Radiometry Presentation (Personal). 1999.

[5] John D. Kraus. *Antennas.* McGraw-Hill, Second edition, 1988.

[6] Robert S. Elliot. *Antenna Theory and Design.* Prentice-Hall Inc, 1981.

[7] D. V. Land. Measurement of the effect of dielectric stratification, simulating realistic tissue layering on the behaviour of microwave thermography antennas. *Proceedings of the 2nd International Scientific Meeting Microwaves in Medicine*, pages 233–236, October 1993.

[8] J. B. Hasted. *Aqueous Dielectrics.* Chapman and Hall, London, 1973.

[9] Y. Leroy, M. Mamouni, J. C. Van de Velde, B. Bocquet, and B. Dujardin. Microwave thermometry for noninvasive thermometry. *Automedica*, 8:181–202, 1987.

[10] D. V. Land. A clinical microwave thermography system. *Proceedings of the IEE*, 134:193–200, 1987.

[11] B. Bocquet, J. Van De Velde, A. Mamouni, Y. Leroy, G. Giaux, J. Delannoy, and D. Delvalee. Microwave radiometric imaging at 3GHz for the exploration of breast tumors. *IEEE Transactions on Microwave Theory and Techniques*, 38(6):791–793, June 1990.

[12] M. A. Stuchly and S. S. Stuchly. Dielectric properties of biological substances - tabulated. *Journal of Microwave Power*, 15:19–26, 1980.

[13] H. P. Schwan and K. R. Foster. RF-field interactions with biological systmes: electrical properties and biophysical mechanisms. *Proceedings of the IEEE*, 68:104–113, 1980.

[14] B. Enander and G. Larson. Microwave radiometric measurements of the temperature inside a body. *Electronics Letters*, 317:10–15, 1974.

[15] J. Edrich and P. C. Hardee. Thermometry at millimeter wavelength. *Proceedings of the IEEE*, 62:1391–1392, 1974.

[16] A. H. Barret, P. C. Myyers, and N. L. Sadowski. Detection of breast cancer by microwave radiometry. *Radioscience*, 12:167–171, 1977.

[17] J. Edrich, W. E. Jobe, W. R. Hendeee, H.K. Cacak, and M. Gautherie. Imaging thermograms at cm and mm wavelength. *Annals of the New York Acadamy of the Sciences*, 335(154-160), 1980.

[18] D. V. Land. *Microwave Thermography - A New Medical Technique.* Lochee Publications, 1987.

[19] K. Carr. Microwave radiometry: its importance to detection of cancer. *IEEE Transactions on Microwave Theory and Techniques*, 37:1862–1868, 1989.

[20] E. Fear. Microwave imaging of the breast. *Proccedings of RF Interactions with Humans: Mechanisms, Exposure and Medical Applications*, Insitute of Physics London, February 2003.

[21] A. W. Guy, F . Lehmann J, J. B. Stonebridge, and C. C. Sorensen. Development of a 915MHz direct contact applicator for theraputic heating of tissues. *IEEE*

Transactions on Microwave Theory and Techniques, MTT-26(8):550–556. August 1978.

[22] P. Stauffer. Conformal array applicator for superficial hyperthermia. *Proccedings of RF Interactions with Humans: Mechanisms, Exposure and Medical Applications*. Insitute of Physics London, February 2003.

[23] J. W. Reeves, S. Meeson, M. J. Birch, C. P. Swain, R. F. Feakins, and B. W. Raaymakers. Early results from in vivo tests of a microwave applicator designed to treat barrett's oesophagus. *Proccedings of RF Interactions with Humans: Mechanisms, Exposure and Medical Applications*, Insitute of Physics London, February 2003.

[24] Y. Leroy, B. Bocquet, and A. Mamouni. Non-invasive microwave radiometry thermometry. *Physiological Measurement*, 19:127–148, 1998.

[25] K. Maruyma, S. Mizushina, T. Sugiura, G. M. J. Van Leeuwen, J. W. Hand, G. Marrocco, F. Bardati, A. D. Edwards, D. Azzopardi, and D. Land. Feasibility of noninvasive measurement of deep brain temperatures in newborn infants by multifrequency microwave radiometry. *IEEE Transactions on Microwave Theory and Techniques*, 48(11):2141–2147, November 2000.

[26] J. W. Hand, G. M. J. Van Leeuwen, S. Mizushina, J. Van de Kamer, K. Maruyama, T. Sugiura, D. V. Azzopardi, and A. D. Edwards. Monitoring of deep brain temperature in infants using multi frequency radiometry and thermal modelling. *Physics in Medicine and Biology*, 46:1885–1903, 2001.

[27] D. V. Land, A. J. Gorton, G. Hamilton, B. L. Klauenberg (Editor), and D. Miklavcic (Editor). *Radio Frequency Radiation Dosimetry*, chapter Investigations of Tissue Microwave and Thermal Properties for combined Microwave and Thermal modelling of Body Tissue Regions, pages 85–97. Kluwer Academic Publishers, Netherlands, 2000.

[28] S. Ramo, J. R. Whinnery, and T. Van Duzer. *Fields And Waves In Communication Electronics*. Wiley and Sons, Third edition, 1994.

[29] D. V. Land. Investigations of the behaviour of microwave thermography antennas when coupled to layered tissue regions. *IEE Coloquim "Applications of Microwaves in Medicine" Digest*, 041(Section 7), 1995.

[30] D. V. Land. Microwave radiometry technique for medical and industrial thermometry. *Proccedings of RF Interactions with Humans: Mechanisms, Exposure and Medical Applications*, Insitute of Physics London, February 2003.

[31] R. H. Dickie. The measurement of thermal radiation at microwave frequencies. *The Review of Scientific Instruments*, 17(7):268–275, July 1946.

[32] D. V. Land. An efficient, accurate and robust radiometer configuration for microwave temperature measurement for industrial and medical applications. *Journal of Microwave Power and Electromagnetic Energy*, 36(3):139–153, 2001.

[33] M. Mamouni, J. C. Van de Velde, and Y. Leroy. New correlation radiometer for microwave thermography. *Electronics Letters*, 17(16):554–555, August 1981.

[34] A. Mamouni, Y. Leroy, J. C. Van de Velde, and L. Bellarbi. Introduction to correlation microwave thermography. *Journal of Microwave Power*, 18(3):285–293, 1983.

[35] D. V. Land. Antenna-cavity principles for radiometric temperature measurement. University of Glasgow, 1999.

[36] S. Mizushina, H. Ohba, K. Abe, S. Mizoshira, and T. Sugiura. Recent trends in medical microwave radiometry. *IEICE Transactions on Communications*, E78-B(6):789–798, June 1995.

[37] M. Robillard, M. Chive, Y. Leroy, J. Audet, Ch. Pichot, and J. C. Bolomey. Microwave thermography. Characteristics of waveguide applicators and signatures of thermal structures. *Journal of Microwave Power*, 17(2):97–105, June 1982.

[38] B. Bocquet, A. Mamouni, J. C. Van de Velde, and Y. Leroy. Near field microwave radiometric weighting functions for multilayered materials. *Journal of Electromagnetic Waves and Applications*, 7(11):1497–1514, 1993.

[39] T. Lasri, K. Ridaoui, B. Bocquet, A. Mamouni, and Y. Leroy. Absolute weighting functions for near-field microwave radiometric applications. *Journal of Electromagnetic Waves and Applications*, 13:1237–1265, 1999.

[40] A. J. Gorton. *Measurements and Analysis of the Microwave Dielectric Properties of Human and Animal Tissues.* PhD thesis, University of Glasgow, 1996.

[41] K. Barrie. PhD thesis, University of Glasgow, Manuscript in Progress.

[42] A. Taflove and M. E. Brodwin. Computation of the electromagnetic fields and induced temperatures within a model of the microwave irradiated human eye. *IEEE Transactions on Microwave Theory and Techniques*, MTT-23(11):888–896, November 1975.

[43] D. M. Sullivan, D. T. Borup, and O. P. Gandhi. Use of the finite difference time domain method in calculating em absorbtion in human tissues. *IEEE Transactions on Biomedical Engineering*, BME-34(2):148–157, February 1987.

[44] L. Wu and W. K. Nieh. FDTD analysis of the radiometric temperature measurement of a bilayered biological tissue using a body contacting waveguide probe. *IEEE Transactions of Microwave Theory and Techniques*, 43(7):1576–1583, July 1995.

[45] K. Abe, S. Mizoshira, T. Sugiura, and S. Mizushina. Electromagnetic near fields of rectangular waveguide antennas in contact with biological objects obtained by FD-TD method. *IEICE Transactions on Communications*, E78-B(6):866–870, June 1995.

[46] G. M. J. Van Leeuwen, J. W. Hand, J. B. Van de Kamer, and S. Mizushina. Temperature retrieval algorithm for brain temperature monitoring using microwave brightness temperatures. *Electronics Letters*, 37(6):341–342, March 2001.

[47] A. Mamouni, Y. Leroy, B. Bocquet, J. C. Van de Velde, P. Gelin J. C. Van de Velde, and P. Gelin. Computation of near-field microwave radiometric signals: Definition and experimental verification. *IEEE Transactions on Microwave Theory and Techniques*, 39(1):124–132, January 1991.

[48] K. Ridaoui, A. Mamouni, R. Aït Abdelmalek, B. Boquet, and Y. Leroy. Near field weighting functions for microwave radiometric signals. *IEEE Transactions on Magnetics*, 31(3):2166–2169, May 1995.

[49] E. Cheever, J. B. Leonard, and K. B. Foster. Depth of penetration of fields from rectangular apertures into lossy media. *IEEE Transactions on Microwave Theory and Tecnhiques*, MTT-35(9):865–867, September 1987.

[50] F. Bardati, V. J. Brown, and G. Di Bernardo. Multi-frequency microwave radiometry for retrieval of temperature distributions in the human neck. *The Journal of Photographic Science*, 39:157–160, 1991.

[51] T. Brown and R. M. George. A literature survey of the dielectric properties of foods at microwave frequencies, July 1993. Campden & Chorleywood Food Research Association.

[52] K. S. Cole and R. H. Cole. Dispersion and absorption in dielectrics; i. alternating current characteristics. *Journal of Chemical Physics*, 9:341–351, 1941.

[53] D. V. Land, V. J. Brown, and S. M. Fraser. Clincal testing of combined thermal and microwave radiometric tissue modelling. *The Journal of Photographic Science*, 39:166–169, 1991.

[54] F. Bardati, M. Bertero, M. Mongiardo, and D. Solimini. Singular system ananlysis of the inversion of microwave radiometric data: Applications to biological temperature retrieval. *Inverse Problems*, 3:347–370, 1987.

[55] F. Bardati, V. J. Brown, and P. Tongolatti. Temperature reconstruction in a dielectric cylinder by multi-frequency microwave radiometry. *Journal of Electromagnetic Waves and Applications*, 7(11):1549–1571, 1993.

[56] F. Bardati, M. Bertero, M. Mongiardo, and D. Solomini. Singular system analysis of the inversion of microwave radiometric data: applications to biological temperature retrieval. *Inverse Problems*, 3:347–370, 1987.

[57] F. Bardati, M. Bertero, M. Mongiardo, and D. Solomini. Singular system analysis for the temperature retrieval in microwave thermography. *RadioScience*, 22(6):1035–1041, 1987.

[58] F. Bardati, M. Mongiardo, D. Solimini, and P. Tognolatii. Multispectral microwave radiometry for thermal imaging. *The Journal of Photographic Science*, 37:154–156, 1989.

[59] S. Mizushina, T. Shimizu, K. Suzuki, M. Kinomura, H. Ohba, and T. Sugiura. Retrieval of temperature-depth profiles in biological objects from multi-frequency microwave radiometric data. *Journal of Electromagnetic Waves and Applications*, 7(11):1515–1548, 1993.

[60] L. Bellarbi, A. Mamouni, J. C. Van de Velde, and Y. Leroy. Accurate localisation of thermal gradients in lossy materials by correlation microwave thermography. *Electronics Letters*, 20(10):430–431, May 1984.

[61] T. H. Hubing. Survey of numerical electromagnetic modeling techniques. Technical report, University of Missouri-Rolla;, 1991. Electromagnetic Compatibility Laboratory.

[62] J. W. Strohbehn and R. B. Roemer. A survey of computer simulations of hyperthermia treatments. *IEE Transactions on Biomedical Engineering*, BME-31(1):136–149, January 1984.

[63] G. Schaller, J. Erb, and R. Engelbrecht. Field simulation of dipole antennas for interstitial microwave hyperthermia. *IEEE Transactions on Microwave Theroy and Techniques*, 44(6):887–895, 1996.

[64] E. Gjonaj, M. Bartsch, M. Clemens, S. Schupp, and T. Weiland. High-resolution human anatomy models for advanced electromagnetic field computations. *IEEE Transactions on Magnetics*, 38(2):357–360, March 2002.

[65] R. F. Harrington. *Field Computation by Moment Methods*. New York: Macmillan, Chapter 3, 1968.

[66] R. J. Spiegel. A review of numerical models for predicting the energy deposition and resultant thermal response of human exposed to electromagnetic fields. *IEE Transactions on Microwave Theory and Techniques*, MTT-32:730–746, August 1984.

[67] A. Taflove and M. E. Brodwin. Numerical solution of steady-state electromagnetic scattering problems using the time-dependent maxwell's equations. *IEEE Transactions on Microwave Theory and Techniques*, MTT-23(8):623–630, August 1975.

[68] J. J. H. Wang and J. R. Dubberley. Computation of fields in an arbitrarily shaped hetrogeneous dielectric or biological body by an iterative conjugate gradient method. *IEEE Transactions on Biomedical Theory and Techniques*, 37(7):1119–1124, July 1989.

[69] K. D. Paulsen, D. R. Lynch, and J. W. Strohbehn. Three-dimensional finite, boundary and hybrid element solutions of the maxwell equations for lossy dielectric media. *IEEE Transactions on Microwave Theory and Techniques*, 36(4):682–693, April 1988.

[70] D. Livesay and K. Chen. Electromagnetic fields induced inside arbitrarily shaped biological bodies. *IEEE Transactions on Microwave Theory and Techniques*, MTT-22:1273–1280, December 1974.

[71] K. Chen and B. Guru. Internal EM field absorbed power density in human torsos induced by 1-500MHz EM waves. *IEEE Transactions on Microwave Theory and Techniques*, MTT-25:746–756, September 1977.

[72] H. Chuang. Numerical computation of fat layer effects on microwave near-field radiation to the abdomen of a full-scale human body model. *IEEE Transactions on Microwave Theory and Techniques*, 45(1):118–125, January 1997.

[73] M. N. O. Sadiku. *Numerical Techniques in Electromagnetics.* CRC Press, 1992.

[74] D. R. Lynch, K. D. Paulsen, and J. W. Stohbehn. Finite element solution of maxwell's equations for hyperthermia treatment planning. *Journal of Computational Physics*, 58:246–269, 1985.

[75] A. Taflove. Application of the finite-difference-time-domain method to sinusoidal steady-state electromagnetic-penetration problems. *IEEE Transactions on Electromagnetic Compatibility*, EMC-22(3):191–202, August 1980.

[76] P. J. Dimbylow and O. P. Gandhi. Finite-difference time-domain calculations of SAR in a realistic hetrogeneous model of the head for plane-wave exposure from 600MHz to 3GHz. *Physics in Medicine and Biology*, 36(8):1075–1089, 1991.

[77] P. J. Dimbylow. FDTD calculations of the whole-body averaged SAR in an anatomically realistic voxel model of the human body from 1MHz to 1GHz. *Physics in Medicine and Biology*, 42:479–490, 1997.

[78] P. C. Cherry and M. F. Iskander. FDTD analysis of power deposition patterns of an array of interstitial antennas for use in microwave hyperthermia. *IEEE Transactions on Microwave Theory and Techniques*, 40(8):1692–1699, August 1992.

[79] N. M. Pothecary and C. J. Railton. Finite difference time domain modelling of hyperthermia applicators for cancer therapy. *IEEE Transactions on Microwave Theory and Techniques Digest*, pages 1151–1154, 1993.

[80] T. Samaras, P. J. M. Rietveld, and G. C. van Rhoon. Effectiveness of FDTD in predicing SAR distributions from the lucite cone applicator. *IEEE Transactions on Microwave Theory and Techniques*, 48(11):2059–2063, November 2000.

[81] L. Martens, J. Van Hese, P. P. De Langhe, D. De Zutter, and C. De Wagter. Electromagnetic calculations using the FDTD method for the analysis of waveguide applicators for microwave hyperthermia. *Proceedings of the 22nd European Microwave Conference*, pages 293–298, 1992.

[82] R. H. Johnson, M. P. Robinson, J. L. Green, N. M. Pothecary, and C. J. Railton. Effect of frequency and conductivity on field penetration of electromagnetic hyperthermia applicators. *Physics in Medicine and Biology*, 38:1023–1034, 1993.

[83] A. Hirata, M. Morita, and T. Shiozawa. Temperature increase in the human head die to a dipole antenna at microwave frequencies. *IEEE Transactions on Electromagnetic Compatibility*, 45(1):109–116, February 2003.

[84] D. Dunn, C. Rappaport, and Jr. A. Terzuoli. Fdtd verification of deep-set brain tumor hyperthermia using a spherical microwave source distribution. *IEEE Transactions on Microwave Theory and Techniques*, 44(10):1769–1777, October 1996.

[85] J. Camart, D. Despretz, M. Chive, and J. Pribetich. Modeling of various kinds of applicatiors used for microwave hyperthermia based on the fdtd method. *IEEE Transactions on Microwave Theory and Techniques*, 44(10):1811–1818, October 1996.

[86] J. C. Maxwell. *A treatise on electricity and magnetism.* Clarendon Press, London, 1881.

[87] K. S. Yee. Numerical solution of initial boundary value problems involving maxwell's equations in isotropic media. *IEEE Transactions on Antennas and Propagation*, AP-14(3):302–307, May 1966.

[88] A. Taflove. Review of the formulation and applications of the finite-difference time-domain method for numerical modelling of electromagnetic wave interactions with arbitrary structures. *Wave Motion*, 10(6):547–582, 1988.

[89] G. Marrocco and F. Bardati. BEST basic electromagnetic simulation tool v 2.0, January 1999. User Manual. Universita degli studi di Roma, Tor Vergata.

[90] A. Taflove. *Computational Electrodynamics: The Finite-Difference Time-Domain Method.* Artech House, Boston, 1995.

[91] D. Sullivan. *Electomagnetic Simulation Using the FDTD Method.* IEEE Press, New York, 2000.

[92] K. Kunz and R. Luebbers. *The Finite Difference Time Domain Method for Electromagnetics.* CRC Press, Boca Raton, 1993.

[93] R. Holland, L. Simpson, and K. S. Kunz. Finite difference analysis of EMP coupling to lossy dielectric structures. *IEEE Transactions on Electromagnetic Compatibility*, EMC-22(3):203–209, August 1980.

[94] K. L. Shlager, J. B. Schneider, and A. Taflove (Editor). *Computational Electrodynamics: The Finite-Difference Time-Domain Method*, chapter A Survey of the Finite-Difference Time-Domain Literature. Artech House, Boston, MA, 1998.

[95] K. L. Shlager and J. B. Schneider. A survey of the finite-difference time-domain literature. *IEEE Antennas and Propagation Magazine*, 37(4):39–56, 1995.

[96] R. Holland and Williams. Total-field versus scattered-field finite difference codes: A comparitive assessment. *IEEE Transactions on Nuclear Science*, NS-30(6):4583–4588, 1983.

[97] P. A. Panayiotis and C. A. Balanis. Finite-difference time-domain method for antenna radiation. *IEEE Transactions on Antennas and Propagation*, 40(3):334–340, March 1992.

[98] G. Mur. The modelling of singularities in the finite-difference approximation of the time-domain electromagnetic-field equations. *IEEE Transactions on Microwave Theory and Techniques*, MTT-29(10):1073–1077, October 1981.

[99] J. P. Berenger. A perfectly matched layer for the absorption of electromagnetic waves. *Journal of Computational Physics*, 114:185–200, 1994.

[100] N. V. Kantartzis and T. D. Tsioukis. A comparative study of the berenger perfectly matched layer, the superabsorption technique and several higher-order ABC's for the FDTD algorithm in two and three dimensional problems. *IEEE Transactions on Magnetics*, 32(3):1460–1463, March 1996.

[101] J Berenger. Three-dimensional perfectly matched layer for the absorbtion of electromagnetic waves. *Journal of Computational Physics*, 127:363–379, 1996.

[102] D. S. Katz, E. T. Thiele, and A. Taflove. Validation and extension to three dimensions of the berenger PML absorbing boundary condition for FD-TD meshes. *IEEE Microwave Guided Wave Letters*, 4:269–270, 1994.

[103] P. Zhao. Generalized-material-independent PML absorbers used for the FDTD simulation of electromagnetic waves in 3-D arbitrary anisotropic dielectric and magnetic media. *IEEE Transactions on Microwave Theory and Techniques*, 46(10):1511–1513, October 1998.

[104] K. Abe, S. Mizoshira, T. Sugiura, and S. Mizushina. Electromagnetic near fields of rectangular waveguide antennas in contact with biological objects obtained by FD-TD method. *IEICE Transactions on Communications*, E78-B(6):866–870, June 1995.

[105] P. G. Petropolous. Analysis of exponential time-differencing for FDTD in lossy dielectrics. *IEEE Transactions on Antennas and Propagation*, 45(6):1054–1057, June 1997.

[106] P. G. Petropoulos, L. Zhao, and A. C. Cangellaris. Reflectionless sponge layer absorbing boundary condition for the solution of maxwell's equations with high-order staggered finite difference schemes. *Journal of Computational Physics*, 139:184–208, 1998.

[107] D. Paul, N. M. Pothecary, and C. J. Railton. Calculation of the dispersive characteristics of open dielectric structures by the finite-difference time-domain method. *IEEE Transactions on Microwave Theory and Techniques*, 42(7):1207–1211, July 1994.

[108] J. Nadobny, D. Sullivan, P. Wust, M. Seebass, P. Deulhard, and R. Felix. A high resolution interpolation at arbitrary interfaces for the FDTD method. *IEEE Transactions on Microwave Theory and Techniques*, 46(11):1759–1766, November 1998.

[109] R. Holland. Pitfalls of staircase meshing. *IEEE Transactions on Electromagnetic Compatibility*, 35(4):434–439, November 1993.

[110] D. T. Prescott and N. V. Shuley. A method of incorporating different sized cells in the finite-difference time-domain analysis technique. *IEEE Microwave and Guided Wave Letters*, 2(11):434–436, November 1992.

[111] M.J. White, M.F. Iskander, and Z. Huang. Development of a multigrid FDTD code for three-dimensional applications. *IEEE Transactions on Antennas and Propagation*, 45(10):1512–1517, October 1997.

[112] M. W. Chevalier, R. J. Leubbers, and V. P. Cable. FDTD local grid with material traverse. *IEEE Transactions on Antennas and Propagation*, 45(3):411–421, March 1997.

[113] M. Okoniewski, E. Okoniewska, and M. A. Stuchly. Three- dimensional subgridding algorithm for FDTD. *IEEE Transactions on Antennas and Propagation*, 45(3):422–428, March 1997.

[114] H. Harms, J. Lee, and R. Mittra. A study of the nonorthogonal FDTD method versus the conventional FDTD technique for computing resonant frequencies of cylindrical cavities. *IEEE Transactions on Microwave Theory and Techniques*, 40(4):741–746, April 1992.

[115] Y. Hao and C. J. Railton. Analyzing electromagnetic structures with curved boundaries on cartesian FDTD meshes. *IEEE Transactions on Microwave Theory and Techniques*, 46(1):82–88, January 1998.

[116] T.G. Jurgens, A. Taflove, and K. Umashankar. Finite-difference time-domain modeling of curved surfaces. *IEEE Transactions on Antennas and Propagation*, 40(4):357–365, April 1992.

[117] G. Marrocco, M. Sabbadini, and F. Bardati. FDTD improvement by dielectric subgrid resolution. *IEEE Transactions on Microwave Theory and Techniques*, 46(12):2166–2169, December 1998.

[118] D. P. Rodohan, S. R. Saunders, S. R. Cvetkovic, P. D. Beavis, and R. J. Glover. Parallel simulation of electromagnetic fields for telecommunications applications. *Invited paper to IEEE Singapore Int. Conf. on Communication Systems (ICCS'94)*, pages 435–440, 1994.

[119] D. P. Rodohan and S. R. Saunders. Parallel implementations of the finite difference time domain method. *Second Int. Conf. on Computation in Electromagnetics*, IEE Conf. Pub. No. 384:367–370, 1994.

[120] P. J. Dimbylow. FDTD Calculations of the SAR for a dipole closely coupled to the head at 900MHz and 1.9GHz. *Physics in Medicine and Biology*, 38:361–368, 1992.

[121] P. J. Dimbylow and S. M. Mann. SAR calculations in an anatomically realistic model of the head for mobile phone communication transceivers at 900MHz and 1.8GHz. *Physics in Medicine and Biology*, 39:1537–1553, 1994.

[122] A. Tinniswood, C. M. Furse, and O. P. Gandhi. Power deposition in the head and neck of an antatomically based human body model for plane wave exposures. *Physics in Medicine and Biology*, 43:2361–2378, 1998.

[123] G. M. J.Van Leeuwen, J. J. W. Lagendijk, B. J. A. M. Van Leersum, A. P. M. Zwamborn, S. N. Hornsleth, and A. N. T. J. Kotte. Calculation of change in brain temperatures due to exposure to a mobile phone. *Physics in Medicine and Biology*, 44:2367–2379, 1999.

[124] M. F. Iskander, Z. Yun, and R. Quinteroo-Illera. Polarization and human body effects on the microwave absorbtion in a human head exposed to radiation from handheld devices. *IEEE Transactions on Microwave Theory and Techniques*, 48(11):1979–1987, November 2000.

[125] A. Schiavoni, P. Bertotto, G. Richiardi, and P. Belli. SAR generated by commercial cellular phones - phone modeling, head modeling and measurements. *IEEE Transactions on Microwave Theory and Techniques*, 48(11):2064–2071, November 2000.

[126] P. A. Mason, W. D. Hurt, T. J. Walters, J. A. D'Andrea, P. Gajsek, K. L. Ryan, D. A. Nelson, K. I. Smith, and J. M. Ziriax. Effects of frequency, permittivity, and voxel size on predicted specific absorbtion rate values in biological tissue during electromagnetic field exposure. *IEEE Transactions on Microwave Theory and Techniques*, 48(11):2050–2058, 2000.

[127] A. A. C. De Leeuw, J. J. W. Lagenduk, and P. M. Van Den Berg. SAR distribution of the 'coaxial TEM' system with variable aperture width: measurements and model computations. *International Journal of Hyperthermia*, 6(2):445–451, 1990.

[128] W. G. Scanlon, N. E. Evans, and J. B. Burns. FDTD analysis of close-coupled 418MHz radiating devices for human biotelemetry. *Physics in Medicine and Biology*, 44:335–345, 1999.

[129] Y. Okano, K. Ito, I. Ida, and M. Takahashi. The SAR evaluation method by a combination of thermographic experiments and biological tissue equivalent phantoms. *IEEE Transactions on Microwave Theory and Techniques*, 48(11):2094–2103, November 2000.

[130] H. C. Taylor, M. Burl, and J. W. Hand. Experimental verification of numerically predicted electric field distributions produced by a radiofrequency coil. *Physics in Medicine and Biology*, 42:1395–1402, 1997.

[131] G. P. Rine, T. V. Samulski, W. Grant, and C. A. Wallen. Comparison of two dimensional numerical approximation and measurement of SAR in a muscle equivalent phantom exposed to a 915MHz slab-loaded waveguide. *International Journal of Hyperthermia*, 6(1):213–225, 1990.

[132] J. A. Stratton. *Electromagnetic Theory.* McGraw-Hill, New York. 1941.

[133] D. V. Land. Application of the nonresonant perturbation technique to the measurement of high frequency fields in biological phantom materials. *Electronics Letters*. 24(1):70–72, January 1988.

[134] D. V. Land. Simplified nonresonant perturbation method of measuring aspects of performance of UHF and microwave antennas for biomedical applications. *Electroniocs Letters*, 28(13):1190–1191, June 1992.

[135] S. Gabriel, R. W. Lau, and C. Gabriel. The dielectric properties of biological tissues: III. Parametric modelsfor the dielectric spectrum of tissues. *Physics in Medicine and Biology*, 41:2271–2293, 1996.

[136] G. Marrocco, G. A. Lovisolo, and F. Bardati. A virtual bioelectomagnetic code. *Proccedings of RF Interactions with Humans: Mechanisms, Exposure and Medical Applications*, Insitute of Physics London, February 2003.

[137] G. Marrocco. Private communication, 2000.

[138] D. V. Land. Private communication, 2002.

[139] C. W. Steele. A nonresonant perturbation theory. *IEEE Transactions on Microwave Theory and Techniques*, MTT-14(2):70–74, February 1966.

[140] Spiral Software and MIT. *EasyPlot*, Version 3.2.

[141] MathWorks. *MatLab*, Version 5.0.

[142] W. L. McPherson. *Reference Data for Radio Engineers.* Standard Telephones and Cables Ltd., London, 1958.

[143] B. Bocquet, J. C. Van De Velde, A. Mamouni, and Y. Leroy. An example of thermometry in volume by microwave radiometry. *IEEE Transactions on Biomedical Engineering*, 40(9):990–992, September 1993.

[144] S. Silver (Editor). *Microwave Antenna Theory and Design.* McGraw-Hill, New York, 1949.

[145] Fine Cuisine. Mr Mash, dietry information, 2002.

[146] F. Chen. Uniformly and linearly heating of mashed potatoes. University of Glasgow 2002.

[147] W. H. Press, S. A. Teukolsky, W. T. Vetterling, and B. P. Flannery. *Numerical Recipies in C: The Art of Scientific Computing.* Cambridge University Press, Second edition, Section 15.3. 1993.

[148] E. H. Grant and S. E. Keefe. The dielectric behaviour of aqueous solutions of bovine serum albumin from radiowave to microwave frequencies. *The Journal of Physical Chemistry*, 72(13):4373–4380, 1968.

[149] H. P. Schwan. Electrical properties of tissue and cell suspensions. *Advances in Biological Medical and Physics*, 5:147–209, 1957.

[150] S. R. Smith and K. R. Foster. Dielectric properties of low-water-content tissues. *Physics in Medicine and Biology*, 30(9):965–973, 1985.

[151] A. M. Campbell. *Measurements and Analysis of the Microwave Dielectric Properties of Tissues.* PhD thesis, University of Glasgow, 1990.

[152] S Ryynanen. The electromagnetic properties of food materials: A review of basic principles. *Journal of Food Engineering*, 26:409–429, 1995.

[153] B. D. Roebuck and S. A. Goldblith. Dielectric properties of carbohydrate water mixtures at microwave frequencies. *Journal of Food Science*, 37:199–204, 1972.

[154] D. Burfoot, C. J. Railton, A. M. Foster, and R. Reavell. Modeling the pasteurization of prepared meal with microwaves at 896 MHz. *Journal of Food Engineering*, 30:117–133, 1996.

[155] D. V. Land and A. M. Campbell. A quick accurate method for measuring the microwave dielectric properties of small tissue samples. *Physics in Medicine and Biology*, 37(1):183–192, 1992.

[156] Safeway Plc. Cornflower, dietry information, 2002.

[157] H. F. Cook. A comparison of the dielectric behaviour of pure water and human blood at microwave frequencies. *British Journal of Applied Physics*, 3:249–255. 1952.

[158] D. R. Lide (Editor). *CRC Handbook of Physics and Chemistry.* CRC Press.

[159] P. Cornillon. Use of nuclear magnetic resonance to model thermophysical properties of frozen and unfrozen model food gels. *Journal of Food Engineering*, 25:1–19, 1995.

[160] T Brown and R. M. George. A literature survey of the dielectric properties of foods at microwave frequencies. Technical report, Camden and Chorleywood Food Research Association, 1993.

[161] C. Bircan and S. A. Barringer. Salt-starch interactions as evidenced by viscosity and dielectric property measurements. *Journal of Food Science*, 63(6):983–986, 1998.

[162] N. E. Bengtsson and P. O. Risman. Dielectric properties of foods at 3GHz as determined by the cavity perturbation technique ii. measurements on forrd materials. *Journal of Microwave Power*, 6(2):107–123, 1971.

[163] C. McGregor and J. Nimmo and W. Stothers. *Fundamentals of University Mathematics.* Albion Mathematics and Applications Series. Albion Publishing, 1994.

[164] F. Bardati, G. Lovisolo, S. Nocentini, M. P. Ross, P. Tognolatti, and P. Cordiner. Multi-frequency microwave radiometry for non-invasive transient temperature measurement. *Proccedings of 1st International Scientific Meeting Microwaves in Medicine*, Belgrade 1991.

[165] S. Jacobsen and P. Stauffer. Use of tikhonov regularization on sparce radiometry data for 1-D temperature profile restoration. *IEEE Transactions on Biomedical Engineering*, 50(2):178–188, February 2003.

[166] G. Schaller. Inversion of radiometric data from biological tissue by an optimisation method. *Electronics Letters*, 20(9), 1984.